



**Photo-electrochemical surface  
modification and analysis of dye sensitised  
solar cells**

**Inauguraldissertation**

Zur  
Erlangung der Würde eines Doktors der Philosophie  
Vorgelegt der  
Philosophisch-Naturwissenschaftlichen Fakultät  
Der Universität Basel

Von

William Kylberg

Aus Stockholm, Schweden

Basel, 2008

---

Genehmigt von der Philosophisch-Naturwissenschaftlichen Fakultät

Auf Antrag von

Prof. Dr. E. C. Constable

Dr. E. Figgemeier

Prof. Dr. M. Mayor

Prof. Dr. C. E. Housecroft

Basel, den 14. Oktober 2008

Prof. Dr E. Parlow  
Dekan

---

## Abstract

Photoelectric measurements on a series of ruthenium complexes with 9 different 2,2';6',2''-terpyridine ligands modified by different thienyl substitutions on the 4'-position were performed. Three of the ligands were novel.

With a 2,2':6'2''-terpyridine that has a carboxylic acid group it was possible to attach the complexes to nanocrystalline-TiO<sub>2</sub> surfaces. By changing the anchoring ligands and counter ligands it was possible to tune the efficiency of light to electricity conversion.

Electroactive polymer films were electrochemically deposited from complexes with two of the novel ligands.

The surface bound ruthenium complexes were able to photoelectrochemically polymerise monomers of bis-ethylenedioxythiophene, terthiophene and [Ru(terpy-bisthiophene)]<sup>2+</sup> on the TiO<sub>2</sub> surface. Some photovoltaic activity was seen using the polymerised bis-EDOT as solid-state hole conductor.

A technique to measure the photovoltaic capabilities of dye sensitised TiO<sub>2</sub> thin films was developed using a scanning electrochemical microscope (SECM). It was possible to estimate performance on very small areas of TiO<sub>2</sub> allowing for fast measurements and screening of arrays with different dyes in the future. The technique was dubbed photo-electrochemical microscope (PECM).

Some organic dyes of the imide perylene family were investigated as dyes in DNSC. Some improvements were reached, mainly by changing the attaching group.

---

## Acknowledgements

My thanks go first to my supervisors who gave me the opportunity to work with a wide array of chemistry. Especially I thank Egbert Figgemeier for giving me the opportunity to do a PhD in Switzerland, for his help in general and for interesting scientific discussions. I am also deeply grateful to Edwin Constable and Catherine Housecroft for letting me work in their group at the inorganic department of chemistry in Basel and for access to their unique insight into chemistry.

### *Collaborations and laboratory help*

Thankyou,

Verena Thommen for the AFM images (departement of physics, Basel).

Valerie Jullien for help with synthesis and collaboration.

Ana Hernandez for help with NMR and collaboration.

Marcel Mayor for collaboration with organic dyes.

Connor Brennan, Pirmin Rösle and Ralph Schmitt for mass spectrometry.

Markus Neuburger and Silvia Schaffner for X-ray Crystal data.

Jason Price for help with the crystal structures.

Stefan Graber and Bernhard Jung for computer help.

Biljana Bozic for help with synthesis.

Thanks also to the whole Constable group for friendship and all sorts of help: Jon, Ellie, Valerie, Kate, Emma, Marc, Luki, Paulina, Marjena, Elaine, Jennifer, Swarna, Guoqi, Tao, Sarah, Kevin, Barbara, Amar, Markus, Frank (Hein), Sebastien, Michael, Dan, Liselotte and others.

Many thanks go to Beatrice Erismann, both for administrative help and for being a good friend.

Financial support is gratefully acknowledged from the Schweizer Nationalfonds zur Förderung der wissenschaftlichen Forschung (SNF).

To my darling Monique for support and help with editing, thank you.

Finally I thank my parents for always being there for me and for giving me inspiration and confidence. Also to my brother and sister for their support.

---

## Contents

Abstract

Contents

Abbreviations

### 1 Introduction

1.1 Photoelectrochemical Solar Cells	1
1.1.1 Photovoltaics	1
1.1.2 Dye Sensitised Nanostructured Solar Cells (DNSC)	5
1.2 Photoelectro- and Electro-Chemical Polymerisation	21
1.2.1 Electrochemical Polymerisation	21
1.2.2 Photo-Electrochemical Polymerisation	27
1.2.3 Photophysics and Electrochemistry of Ruthenium (II) Polypyridyl Complexes	31
1.3 Goal	38

Reference list 39

### 2 Experimental Methods

2.1 General Electrochemistry	43
2.2 Scanning Probe Electrochemistry	59
2.2.1 Scanning Electrochemical Microscopy (SECM)	59
2.2.2 Photo-Electrochemical Microscopy (PECM)	65
2.3 Photovoltaic Measurements	68
2.4 Photo-Electrochemical Polymerisation	76

Reference list 82

### 3 Results and Discussion

3.1 Synthesis and Characterisation of Oligopyridine Ligands	84
3.1.1 Terpyridine Ligand Synthesis	84
3.1.2 NMR Spectroscopy	90
3.1.3 Orbital Energy Calculations	92
3.1.4 UV-vis	93
3.1.5 Electrochemistry	94
3.1.6 Crystal-structure	95
3.1.7 Experimental	99

---

3.2 Synthesis and Characterisation of Complexes	115
3.2.1 Metal Complex Synthesis	115
3.2.2 NMR Analysis	118
3.2.3 UV-vis Spectroscopy	122
3.2.4 Electrochemistry	129
3.2.5 Crystal-structure	138
3.2.6 Experimental	142
3.3 Electrochemical and Photo-Electrochemical Polymerisation	165
3.3.1 Electrochemical Polymerisation	165
3.3.2 Photo-Electrochemical Polymerisation	181
3.4 Electrochemistry of Dye Sensitised TiO <sub>2</sub>	193
3.4.1 Cyclic Voltammetry of Dye Sensitised TiO <sub>2</sub>	193
3.5 Photo-Electrochemistry of Metal Complexes	198
3.5.1 Spectroelectrochemistry	198
3.5.2 Photovoltaic Performance of Metal Complexes	203
3.5.3 Four-Electrode PECM Measurements	223
3.6 Photo-Electrochemistry of non-Metal Containing Dyes	237
<b>4 Summary</b>	<b>248</b>
Appendix A	251

---

## Abbreviations

### Chemical

PPI	n-[2-Oxo-2(2-pyridyl)ethyl]pyridinium iodide
KO <sup>t</sup> Bu	Potassium tertiary butoxide
n-BuLi	<i>n</i> -Butyllithium
TBAPF <sub>6</sub>	Tetrabutylammonium hexafluorophosphate
Fc	Ferrocene
Fc <sup>+</sup>	Ferrocenium
TT	2,2':5',2''-Terthiophene
EDOT	3,4-Ethylenedioxythiophene
Bpy	2,2'-Bipyridine
tpy	2,2':6',2''-Terpyridine
tpyS	4'-(2-Thienyl)-2,2':6',2''-terpyridine
tpySS	4'-(2,2'-Bithien-5-yl)-2,2':6',2''-terpyridine
tpySBS	4'-[2,5-(Dithienyl)phenyl]-2,2':6',2''-terpyridine
tpyEDOT	4'-(2-eEthylenedioxythiophene)-2,2':6',2''-terpyridine
EtOH	Ethanol
MeOH	Methanol
MeCN	Acetonitrile
3-MPN	3-Methoxypropionitrile
THF	Tetrahydrofuran
DCM	Dichloromethane
DMF	Dimethylformamide
DMSO	Dimethylsulfoxide
MBI	Methylbenzimidazole
A-sol	MeCN/sat.aqueous KNO <sub>3</sub> /H <sub>2</sub> O, 14/2/1
TLC	Thin layer chromatography
aq	aqueous
sat	saturated
nc-TiO <sub>2</sub>	nanocrystalline titaniumdioxide

### Nuclear Magnetic Resonance (NMR)

COSY	Correlated Spectroscopy
DEPT	Distortionless Enhancement by Polarisation Transfer

---

2D	Two dimensional
s	Singlet
d	Doublet
t	Triplet
q	Quartet
m	Multiplet
b	Broad
dd	Doublet of doublet
ddd	Doublet of doublet of doublet
dt	Doublet of triplet
J	Coupling constant
$\delta$	Chemical shift (ppm)

### **Mass Spectroscopy (MS)**

ES	Electrospray
MALDI	Matrix assisted laser deposition ionisation
TOF	Time-of flight
EI	Electron impact
M	Parent ion mass

### **Infrared Spectroscopy (IR)**

w	weak	s	strong
m	medium	b	broad

### **Ultra-violet Visible Spectroscopy (UV-vis)**

MLCT	Metal to ligand charge transfer
LMCT	Ligand to metal charge transfer
LC	Ligand centred
MC	Metal centred
sh	Shoulder
$\epsilon$	Absorption coefficient
$\lambda$	Wavelength
HOMO	Highest occupied molecular orbital
LUMO	Lowest occupied molecular orbital

### **Electrochemistry**

CV	Cyclic voltammetry
----	--------------------



---

DPV	Differential Pulse Voltammetry
SWV	Square Wave Voltammetry

### **Photovoltaics**

I-V	Current Voltage
$V_{oc}$	Open circuit Voltage
$J_{sc}$	Short Circuit Current density
DNSC	Dye Sensitised Solar Cell
FTO	Fluorine doped SnO <sub>2</sub>
FF	Fill factor

---

# 1 Introduction

## 1.1 Photoelectrochemical Solar Cells

### 1.1.1 Photovoltaics

The first photovoltaic effect where a photo-voltage was observed was in 1839 by Becquerel.<sup>[1]</sup> He measured a small current upon immersing a silver coated platinum electrode immersed in an electrolyte. With the birth of quantum mechanics in the early 1900s a theoretical explanations for the effect was possible. Light could be thought of as packets (quanta) of energy as well as electromagnetic waves. In 1905 Einstein explained the photoelectric effect where high-energy quanta of electromagnetic waves (UV-light) provide enough energy to electrons in a metal to expel them completely from the surface. In normal circumstances when a material absorbs light, an electron is promoted to an excited state upon illumination and then relaxes back to the ground state with the excess energy dissipating as heat or radiation. In a photovoltaic cell, an asymmetry in the device is needed to separate the excited electron and the vacant volume it has left (hole) in order to use the excited electron for work. The early photovoltaic cells consisted of metals and semiconductors pressed together to provide a rectifying barrier (Schottky barrier). An example is copper-copperoxide. Later, in the 1930s, Schottky, Mott and others developed the theory of metal-semiconductor junctions. The modern age of photovoltaic devices began in 1954 when the Bell laboratory accidentally found that silicon, doped with certain impurities, was very sensitive to light. This doping effect eventually resulted in the first practical photovoltaic devices with efficiencies of 6% that were made for spacecraft. In the 1950s techniques were developed to dope crystalline silicon with extra positive charges (or holes) or extra electrons and create so-called p-n junctions. The doping is made by replacing, for example, silicon atoms in the crystal lattice with other elements that have an electron less or an electron more in their valence bands (For example boron or phosphorus in a silicon crystal). These p-n junctions created better rectifying barriers than the Schottky barriers and had better photovoltaic properties. The free carrier pairs (electron-hole pair) are separated

at the junction due to the electric field gradient created at the depletion layer (figure 1.1).<sup>[2]</sup>

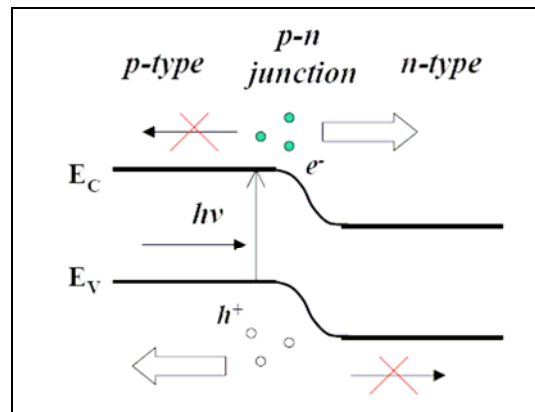


**Figure 1.1** A p-n junction of p-type and n-type material where a potential barrier is created.

The p-n junction then manages the three tasks necessary for a photovoltaic device: charge generation from light absorption, charge separation (separating the hole from the electron) and charge transport.

Over the years several types of solar cells have emerged but silicon remains the foremost photovoltaic material, benefiting from the silicon industry. For the two band solar cell device there is a theoretical limit with an ideal band gap for the maximum conversion efficiency of light with a spectrum like that from the sun. There is a maximum at about 33% for a band-gap of 1.4 eV. In figure 1.2 from reference [3] this relationship is shown together with some semiconductors and their band-gaps.<sup>[3]</sup>

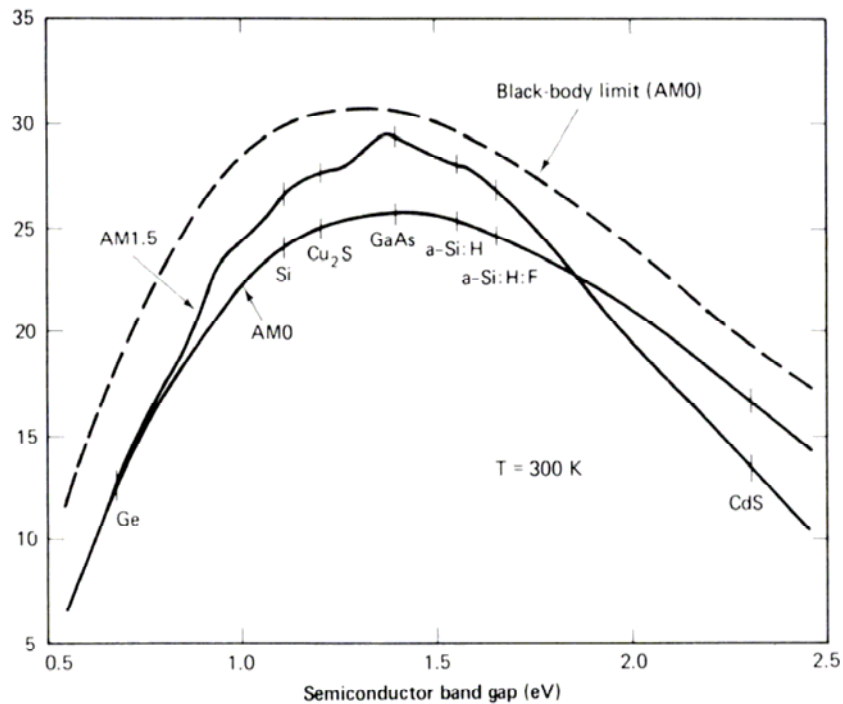


**Figure 1.2** The theoretical maximum conversion efficiencies of single band gap materials in p-n junction type photovoltaic cells depending on their band gap.<sup>[3]</sup>

The two band materials used in photovoltaic devices only absorb light really well when the energy of the light equals or is a bit greater than the band-gap of the material. Photons of less energy are not absorbed and photons of higher are absorbed but lose their excess energy as heat very rapidly and contribute the same energy as a photon with energy equal to the band-gap. The spectrum of solar radiation in figure 1.3 shows the distribution of energy at different wavelengths, which must be taken into account when designing photovoltaic devices.<sup>[2]</sup>

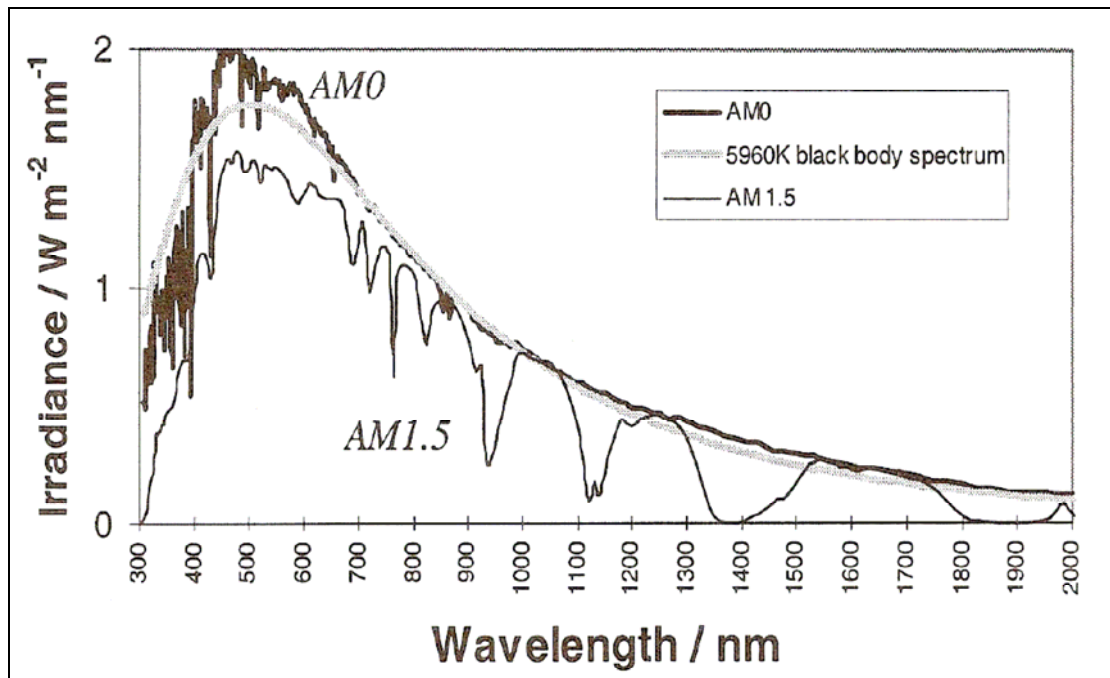


**Figure 1.3** Solar-spectrum that reaches the atmosphere (Air Mass 0), of a black body at 5760 K and of standard terrestrial radiation (Air Mass 1.5).<sup>[2]</sup>

Attenuation of incident sunlight will depend on the length of the light path through the atmosphere and this will in turn depend on the incident angle. The standard solar spectrum is taken when the sun is at an angle of  $42^\circ$ , which is referred to as Air mass 1.5 (AM 1.5) (see figure 1.3). Air mass is defined as  $= 1/\cos\theta$ . The standard terrestrial solar spectrum is defined as the AM 1.5 spectrum normalised to  $1000 \text{ W m}^{-2}$ . Solar simulators use different lamps to approximate the spectrum and the cells can then be placed at a distance that results in an irradiance of  $1000 \text{ W m}^{-2}$ . Examples of lamps used for this are the xenon arc lamp, sulphur lamp or halogen projector lamps. The projector lamps are considerably cheaper than the former lamps and are often used when the more expensive lamps are not available.

The average global irradiance varies from  $100 \text{ Wm}^{-2}$  in northern latitudes, to  $300 \text{ Wm}^{-2}$  in the sunniest places such as some deserts. Another estimate is that the energy flow from the electromagnetic radiation of the sun is  $120\,000 \text{ TW}$  across the earth.<sup>[4]</sup> This far exceeds the energy demands of human society. Sunlight is a diffuse energy source and is not centralised to some specific regions like fossil fuels are. Simple calculations show that an area of land  $0.16\%$  of the total land on earth covered by photovoltaics with  $10\%$  efficiency would provide with  $20 \text{ TW}$ .<sup>[4]</sup> The energy consumption today is  $13 \text{ TW}$  although it is growing fast. The main reason photovoltaic energy conversion is

not used more today is the price to produce them, which until now cannot compete with the price for energy made from fossil fuels. To move away from the relatively expensive silicon cells, alternative photovoltaic technologies are sought after. Thin film technology with amorphous silicon ( $\alpha$ -Si) or combinations of metals is one strategy where the small amount of material needed reduce prices.

One type of solar cell that is promising is based on photoelectrochemical junctions and is referred to as the dye sensitised nanostructured solar cell (DNSC). It is a photovoltaic cell that promises to be cheaper due to cheap materials, less demands on purity and no need for high vacuum equipment. Whereas the p-n junction photovoltaic device relies on electric drift to separate and transport charge, the non p-n junction cells such as the DNSC, rely on carrier diffusion in an electrochemical gradient as there is no general electrostatic field existent.<sup>[2]</sup> The next section will deal with the subject of the DNSC.

### **1.1.2 Dye sensitised Nanostructured Solar Cells (DNSC)**

Light to electric conversion by photoelectrochemical cells has been around as an idea for a long time. After Vogels discovery in 1883 that silver halide emulsions could be sensitised to longer wavelengths with a dye, the same concept was used by Moser to sensitise silver halide electrodes with a dye. Later studies showed that the sensitisation process was mainly due to electron transfer that is also present in the dye sensitised solar cell technology.<sup>[5]</sup>

The first studies in modern photoelectrochemistry were on the semiconductor-electrolyte interface by among others Gerischer.<sup>[6]</sup> The research area was then further stimulated by the oil crisis in 1973. The first attempts at harnessing sun light in photoelectrochemical devices utilised the electric field that exists in the space-charge layer of a semi-conductor in contact with an electrolyte. This electric field can separate charge at the semiconductor/electrolyte interface. The electric field separates hole-electron pairs that have resulted from the absorption of photons of greater energy than the band-gap of the semiconductor. The space-charge layer is further explained below.

### Semiconductor-liquid interface

When a semiconductor is in contact with an electrolyte, the Fermi levels of both phases must become equal. Supposing an n-doped semiconductor, where the  $E_F$  is higher than that of the solution, electrons will flow from the semiconductor to the electrolyte. The excess charge in a semiconductor does not stay on the surface as it does for metals, but is distributed in a space-charge region. The local electrons near the surface are affected but not in the bulk of the semiconductor. This will cause so-called band bending (see figure 1.4). In the case of an n-type semiconductor that accumulates positive charge, the bands will bend “upwards”. An electron in the space-charge region would move toward the bulk under the influence of the existing electric field. An excess hole would move “upward” toward the solution. The semiconductor potential that results in no excess surface charge and thus no band bending is the flat-band potential ( $E_{fb}$ ).

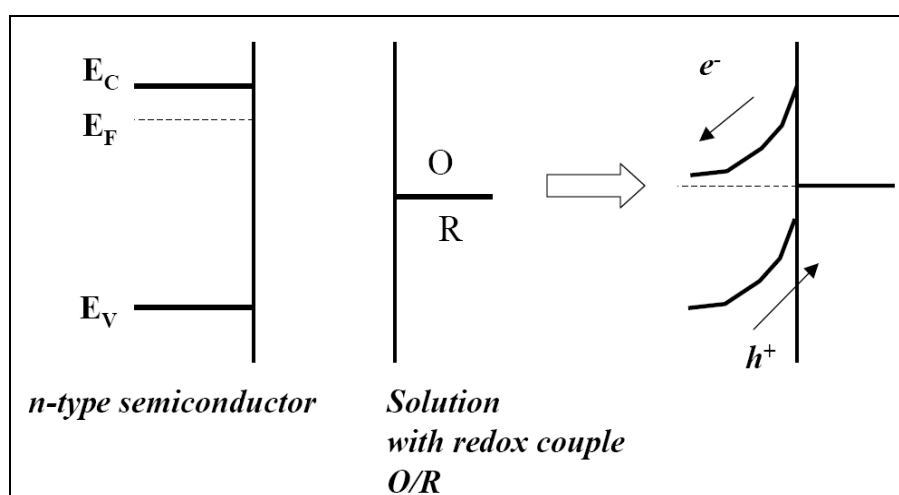


**Figure 1.4** Band bending of valence and conduction bands of n-type semiconductor before (left) and after (right) immersion in solution with a redox couple.

The materials that were used for this purpose were often n-doped semiconductors from group II/VI or III/V elements.  $\text{TiO}_2$  drew attention as a material for water photolysis.<sup>[7]</sup> The problem was the high band gap (e.g. 3.2 eV for  $\text{TiO}_2$  in anatase form) of semiconductors that were stable, which meant they absorbed light in the visible range poorly. The materials with lower band-gaps would photocorrode easily as the band gap is related to the chemical bond strength. The solution was to sensitise the high band gap material with a dye. To maximise the photocurrent a large surface was needed for the monolayer of dye molecules.<sup>[5]</sup> Grätzel and O’regan used mesoscopic semiconductors to increase surface area in photoelectrochemical cells in



1991 with a surprisingly high conversion efficiency of ~7%.<sup>[8]</sup> This is achieved best with TiO<sub>2</sub> but other oxides like ZnO, SnO<sub>2</sub> and Nb<sub>2</sub>O<sub>5</sub> are also useful.<sup>[9-11]</sup> Mesoscopic TiO<sub>2</sub> has remained the most popular choice due to being cheap, abundant and non-toxic. In the nanocrystalline network of mesoscopic TiO<sub>2</sub>, the driving force of the separation of charges is not a space-charge layer. The concentration of dopant impurities is too low and the radii of the particles are too small for a space-layer charge region to form and support an electric field.<sup>[12]</sup> Additionally any electric field in the particles is neutralised by ions in the electrolyte. Consequently there is no band bending and the charge separation must have other driving forces. As will be seen, the kinetics of the system is very important, with high injection rates and low recombination rates crucial for efficient conversion.

As was pointed out earlier, the DNSC relies on diffusion of the charge carriers instead of drift of the charge carriers like in silicon p-n junctions. Concentration gradients in the TiO<sub>2</sub> mesoscopic film drive the electron transport that is best described with a random walk model.<sup>[13-15]</sup> The accepted model of transport is diffusion of electrons between trap states. The kinetics is complex with several parameters determining the diffusion coefficient, such as light intensity, film thickness, particle size and electrolyte composition. The diffusion coefficients reported range between 10<sup>-4</sup> to 10<sup>-8</sup> cm<sup>2</sup> s<sup>-1</sup>. Several groups have found an ambipolar diffusion mechanism to describe the electron transport where the electron diffusion is coupled to cation transport in the electrolyte. Normally the cation concentration is much greater than the electron concentration and only the diffusion coefficient of the electrons through the TiO<sub>2</sub> will determine the transport.<sup>[13]</sup>

## **TiO<sub>2</sub>**

Solids can be classified by their electrical conductivity. The different classes are insulator, conductor, superconducting or semiconductor. Photovoltaic materials mostly belong to the semiconductors. In a conductor the valence band is only partially full and electrons are very easily excited into free electrons. For an insulator the valence band (HOMO) is full and the conduction band (LUMO) is empty and this gap is usually called the band gap. If the band gap is smaller than roughly 3eV the solid can conduct in certain conditions (when free electrons are excited into the conduction band for example at increased temperatures). When the band-gap is between 0.5-3 eV the solid is an intrinsic semiconductor. The conductivity range of these is 10<sup>3</sup>-10<sup>-8</sup>

$\Omega\text{cm}^{-1}$ . Semi-conducting metals come from the Group IV elements like germanium and silicon, and Group III-Group V compounds like gallium arsenide. These are intrinsic semiconductors because their conductivity is a feature of their chemical structure. Metal oxides and sulphides with bandgaps above 3eV form extrinsic semiconductors where the conduction comes from a non-stoichiometric relation of oxygen and the metal ion. Some oxides (e.g.  $\text{TiO}_2$ ) will lose oxygen when heated and become non-stoichiometric with an oxygen deficiency. The oxygen anions that are lost from the titania when heating in air, will be oxidised by the  $\text{Ti}^{4+}$  leaving Ti. These Ti atoms now have 4 extra electrons that they can “donate”. In band theory terms the Ti atoms represent donor levels (figure 1.5). This means that excitation into the conduction band is made easier and subsequently the conductivity reaches semiconductor values.<sup>[16-18]</sup> When the  $\text{TiO}_2$  is sensitised with dye molecules, injection of electrons under illumination leads to “photodoping”, which makes the conductivity sufficient for electron transport to the FTO substrate.<sup>[19]</sup>

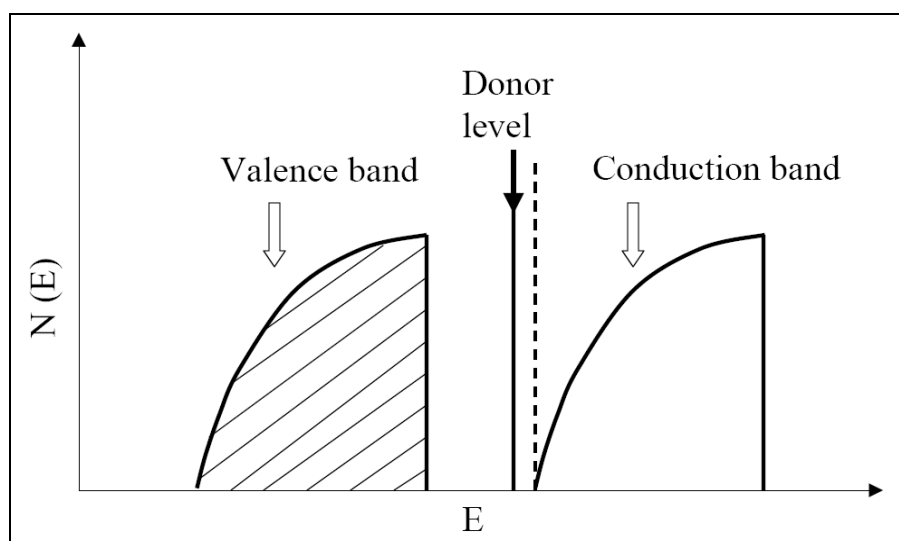


**Figure 1.5** Representation of valence band and conduction band for an n-type semiconductor in band theory. Density of energy levels ( $N(E)$ ) on the Y-axis and energy ( $E$ ) on the X-axis.<sup>[16]</sup>

The flat-band potential ( $E_{fb}$ ) of metal oxides is sensitive to protons and cations in the electrolyte.<sup>[13, 20]</sup> Protonation of the surface leads to a Nernstian dependence on the pH of the  $E_{fb}$ , shifting it positive with increased acidity by  $\sim 59\text{mV/pH}$ . The shift of the  $E_{fb}$  also means the  $\text{TiO}_2$  accepting sites will shift and this has an effect on their overlap with the sensitiser's excited state. This means that in using a semiconductor like  $\text{TiO}_2$  in the DNSC, both the photocurrent and photovoltage will be affected by pH.<sup>[21]</sup> This

effect is also manifested in aprotic solvents when cations are present. In this case the cations are known to intercalate or adsorb with the surface.<sup>[22, 23]</sup> The charge-size ratio of the cation determines the extent of the shift and Redmond and Fitzmaurice found that for cations in an electrolyte with equal activity, the magnitude of positive shift of the  $E_{fb}$  in a DNSC decreased in the order  $Mg^{2+} > Li^+ > Na^+$ .<sup>[24]</sup>

The electronic states of the nanocrystalline (nc)-TiO<sub>2</sub> can be investigated electrochemically by cyclic voltammetry and capacitance measurements. The many sub-states in the bandgap of nc-TiO<sub>2</sub> (see figure 1.6) occur both in the bulk and additionally at the surface in the form of a monoenergetic surface state. Experimentally, an exponential DOS at negative potentials approaching the conduction band (CB) potential is observed with voltammetry.<sup>[25]</sup> As the conduction band potential is reached, there is a large increase in current as the CB of the TiO<sub>2</sub> film is charged.

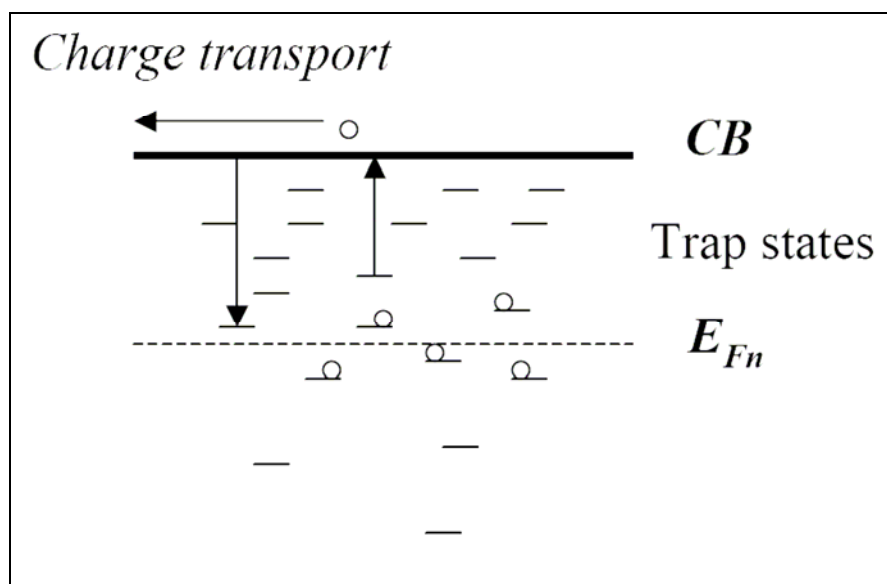


**Figure 1.6** Illustration of trap states below the conduction band (CB) in nc-TiO<sub>2</sub>. The Fermi level ( $E_{Fn}$ ) of the electrons accumulated in the nanoparticles is marked with a dashed line and the electrons with the open circles.

To obtain nanometer sized TiO<sub>2</sub> nanoparticles there are a few main methods. The commercially most common anatase nanoparticles is Degussa P25, which is TiO<sub>2</sub>-powder with 25 nm particle diameters in average, and is synthesized by flame hydrolysis (70% anatase, 30% rutile). Sol-gel preparation of colloidal anatase nanoparticles can, under the right conditions, give a colloid of 10-15 nm in diameter size TiO<sub>2</sub> particles that can be spread on a substrate and sintered at high temperature to

result in transparent thin films.<sup>[26]</sup> Often a polymer such as polyethylene glycol (PEG) is added to the colloid to improve the structural stability of the film. In figure 1.7 there is an AFM image of a TiO<sub>2</sub> nanoporous film made from a Solaronix colloid paste. The thickness of the film is about 6 μm and the particle sizes roughly 20 nm in diameter. The image has a depth profile of 100 nm and the mean roughness is ~10 nm.

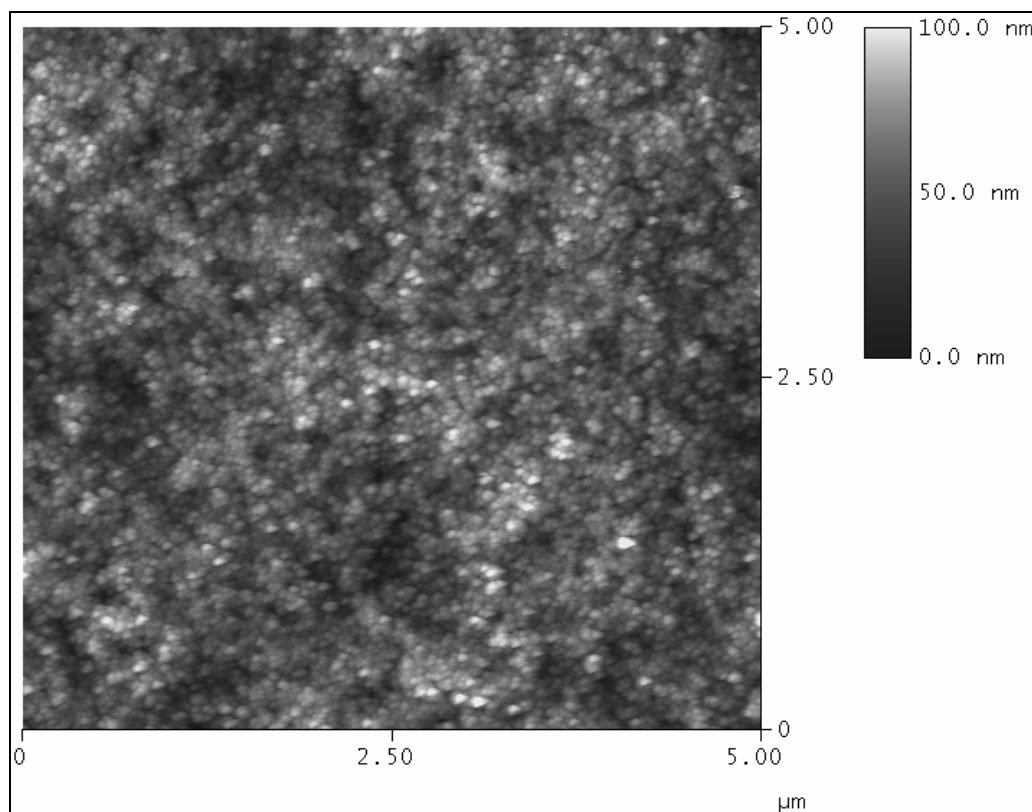


**Figure 1.7** An AFM image of a 5x5 μm area of a nanoporous TiO<sub>2</sub> surface. Image taken by Verena Thommen (Basel university).

The nc-TiO<sub>2</sub> is heated in air at 400-500°C after it has been applied as a thin film on a substrate. The heating will remove organic additives in the colloid and sinter the particles to a mechanically adhering and electrically conducting film. The heating is also needed to partially dehydroxylate the surface to provide a highly reactive surface for dye adsorption. In normal conditions there is both physisorbed and chemisorbed water in the form of acidic hydroxyl groups on the TiO<sub>2</sub> surface. The heating at high temperature results in dehydroxylation. This leads to coordinatively unsaturated and reactive Ti<sup>4+</sup> ions with Lewis acid character. Alcohols are known to adsorb dissociatively on such surfaces. Ethanol will, for example, form alkoxy and hydroxyl groups. Formic acid was found to adsorb in a monodentate fashion on TiO<sub>2</sub>.<sup>[27]</sup> Acids that have been seen to adsorb efficiently to TiO<sub>2</sub> are carboxylic acids, boronic acids

and phosphonic acids. For the DNSC the carboxylic acids work very well although at least two acid groups are needed for the dye in order to not desorb too easily. Phosphonic acids have a stronger bonding but also a lower electron injection rate than the carboxylic acids.<sup>[28]</sup> In figure 1.8 are some of the binding modes that are possible and that have been observed for the carboxylic acid on metal oxides.<sup>[29]</sup>

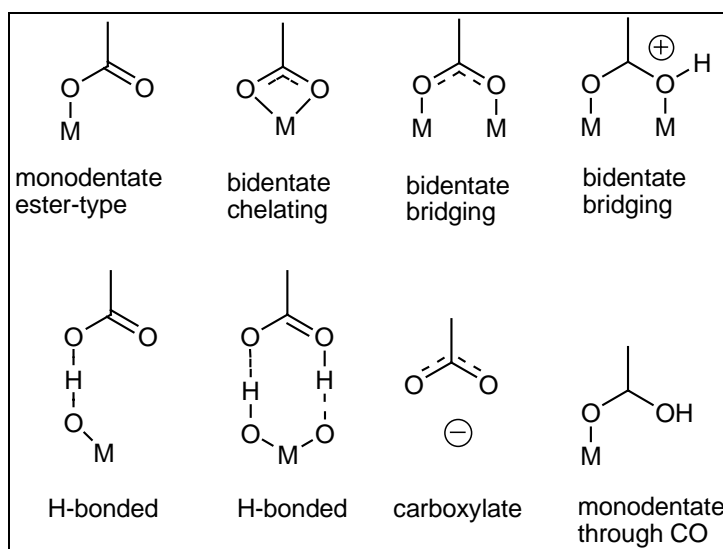


**Figure 1.8** Different binding modes of COOH group to metal oxide (e.g. TiO<sub>2</sub>) as suggested in reference [20].

When a pH neutral solution with dye is used to sensitise the TiO<sub>2</sub>, IR spectroscopic data has suggested a mixture of different bonding modes with both ester type bonds and carboxylate type. By using IR and Raman spectroscopy, Finney *et al.* concluded that a ruthenium bipyridyl-dicarboxylic dye predominately was attached via bidentate or bridging coordination to the Ti ions at the surface.<sup>[30]</sup> In another report, pre-treatments in basic and acidic aqueous solutions led to carboxylate and ester bonding respectively being predominant.<sup>[13]</sup> Hydrogen bonding with hydroxy groups on the surface has also been suggested in models. In conclusion it appears the bidentate bridging between Ti ions and the carboxylate is the most important binding mode.<sup>[31]</sup> It is not yet known exactly how the carboxylic acids or phosphonic acids attach to the TiO<sub>2</sub>, despite a lot of research, but it is clearly very important for good electron injection.<sup>[32]</sup>

### DNOSC basics

The dye-sensitised nanostructured solar cell (DNOSC) is a photo-electrochemical cell consisting of a nanoporous solid semiconductor with an interpenetrating liquid electrolyte that has a redox couple to shuttle ionic charge. The semiconductor is sensitised with a molecular chromophore. The liquid and solid phases are connected to an anode and cathode. As is described below, the combination of these materials lead to photovoltaic conversion with no net chemical change.

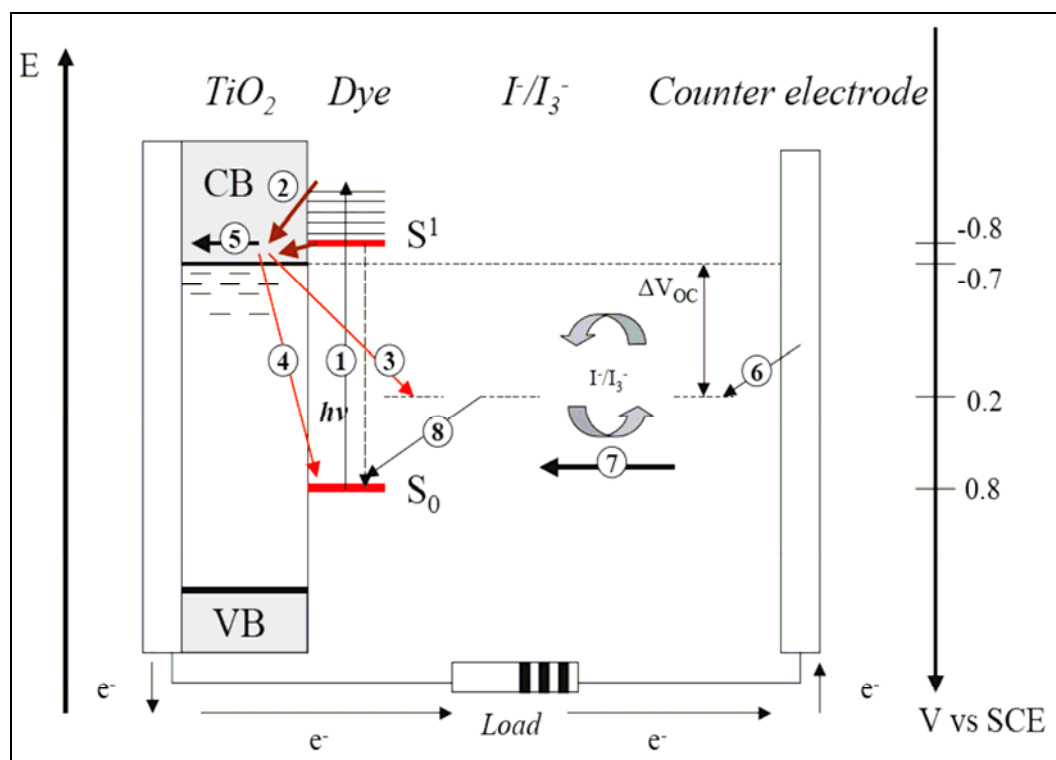


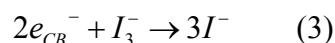
**Figure 1.9** The different processes in the dye sensitised solar cell. The arrows 1 and 3 represent the recombination reactions.

In figure 1.9 the most important steps in the processes of a working DNOSC are labelled. The steps are described together with the kind of time scale involved. The kinetics in the DNOSC is very important, as there is competition between the different processes so the time scales give an indication of where improvements are needed.<sup>[12]</sup>

1. Absorption of photon excites electron into the first excited state. This happens on the  $10^{-15}$  s time scale.
2. Before the excited dye molecule can relax an ultra-fast injection of the electron into the  $\text{TiO}_2$  conduction band can take place in  $10^{-15}$ - $10^{-12}$  s.<sup>[33, 34]</sup>

There is spectroscopic evidence of multiexponential injection kinetics when measuring with transient spectroscopy of the dye on TiO<sub>2</sub>. Although reports have differed they are generally within the same time regimes. An example of life/rise times for different components of the injection kinetics of N3 dye on TiO<sub>2</sub> are <100 fs (29%), 1 ps (25%) and 13 ps (46%).<sup>[35]</sup> Slower components of 100 ps up to 1 ns have also been observed. The faster injection is probably from the vibrationally “hot” excited state and the slower component maybe from the ground-state <sup>3</sup>MLCT.<sup>[36]</sup> While most measurements have been for sensitised films in air or with solvent, Haque *et al.* have measured the injection rate for complete cells. They observed slower half times for the injection rate in efficient complete cells; 150±50 ps compared to 8±2 ps for the film in air. Changing the conduction band level of the TiO<sub>2</sub> by altering electrolyte composition can change the injection rate and the conclusions from the experiments were that the injection rate does not need to be “too” fast (the <100 fs component is unlikely to contribute to device efficiency) and kinetic redundancy can in fact be counter productive.<sup>[37]</sup> Smeigh *et al.* also reported the importance of measuring in complete cells.<sup>[38]</sup>

3. An important recombination process in the cell is the reduction of triiodide in the electrolyte by TiO<sub>2</sub> conduction band electrons. The current density of the recombination depends to a large extent on surface treatments and electrolyte compositions but values lie around 10<sup>-9</sup>-10<sup>-11</sup> A/cm<sup>2</sup> with a time constant of about 10 ms at 1 sun.<sup>[12, 31]</sup> Similar recombination reactions between TiO<sub>2</sub> and solid-state hole conductors is believed to be the main reason for the poor photovoltage in solid-state DNSC.<sup>[39, 40]</sup>



The net reaction of TiO<sub>2</sub> conduction electrons reducing triiodide is seen in equation 3, although dismutation leads to I<sub>2</sub> being the main oxidant.<sup>[39]</sup> It is therefore believed that the initial step is reduction of the I<sub>2</sub> and because there is usually at least a 5-fold excess of iodide and low concentration of I<sub>2</sub>, the recombination is slow.<sup>[41]</sup> The reaction occurs almost entirely in the TiO<sub>2</sub>/electrolyte interface but also to some extent on the SnO<sub>2</sub>:F substrate. To suppress back electron transfer, the recombination centers can be blocked by

e.g. methyl-benzimidazole (MBI) or 4-tert-butylpyridine (4-TBP) or  $\text{Al}_2\text{O}_3$  with resulting increased photovoltages.<sup>[42, 43]</sup>

4. The rate of back reaction from the conduction band or trap states to the ground state of the oxidised dye is much smaller than the injection rate and typically  $\sim 1\mu\text{s}$ . The rapid reduction of the oxidised dye by  $\Gamma^-$  ions in the electrolyte (present in high concentration) means the main back reaction is the previous process, number 3.
5. Electron transport through the nanoporous- $\text{TiO}_2$  is by diffusion and is relatively slow,  $10^{-3}$ - $10^0$  s for  $10\mu\text{m}$  thick films.<sup>[12, 44]</sup>
6. The exchange current of the reduction of  $\text{I}_3^-$  at a platinised TCO counter electrode has been measured to be about  $10^{-2}$ - $10^{-1}$   $\text{A}/\text{cm}^2$ .<sup>[12]</sup>
7. Diffusion through the electrolyte by the redox couple. So far the  $\Gamma^-/\text{I}_3^-$  couple has proven to have the best overall kinetics for photovoltaic performance. One measurement of the diffusion constant for the iodide ion in an 3-MPN electrolyte put it at  $4.0 \times 10^{-6} \text{ cm}^2 \text{ s}^{-1}$ .<sup>[45]</sup> In the DNSC the redox couple  $\Gamma^-/\text{I}_3^-$  leads to a complicated set of reaction including iodide, triiodide and iodide radicals.<sup>[34]</sup>
8. Reduction and regeneration of the oxidised dye by  $\Gamma^-$  occurs on a time scale of  $\sim 10^{-5}$ - $10^{-8}$  s, being faster than the recombination process 4.<sup>[46]</sup> It is also  $\sim 10^8$  times faster than the lifetime of oxidised ruthenium dye N3 in organic solvent in a cyclic voltammetric experiment ( $\geq 1\text{s}$ ). This partly explains this dyes and similar ones ability to sustain 100 million turnovers ( $\sim 20$  years in full sun light) of continuous solar cell performance without performance loss.<sup>[31]</sup>

Important to note in figure 1.9, is that the maximum  $V_{oc}$  is determined by the energy difference (driving force) between the redox-couple potential in the liquid electrolyte (or the HOMO in a solid-state hole-conductor) and the quasi-Fermi level of the  $\text{TiO}_2$ . The quasi-Fermi level (for electrons) is the Fermi level under non-equilibrium conditions such as illumination, which comes from the excited electrons increasing the electron and hole densities. As well as the quasi-Fermi level for electrons there is a corresponding one for the holes. The processes 1-8 above describe the important steps in the photovoltaic functioning of the DNSC. In chapter 2 more will be discussed on measuring the DNSC.



## Dyes

Organic dyes in DNSC are attractive because they are relatively cheap and can have high extinction coefficients. Organic structures that have been popular include porphyrins and phthalocyanines. These molecules were difficult to obtain good photocurrents with, due to absorbance in wrong parts of the spectrum and aggregation respectively. But recently a porphyrin dye reached an efficiency of 7.1%.<sup>[47]</sup> There have been other organic dyes that reach high efficiencies (6-9%) such as coumarin and cyanine dyes, which have donor and acceptor parts. Ito et al. optimised a cell with an indoline type dye to 9.03%, which can be seen in figure 1.10.<sup>[48]</sup>

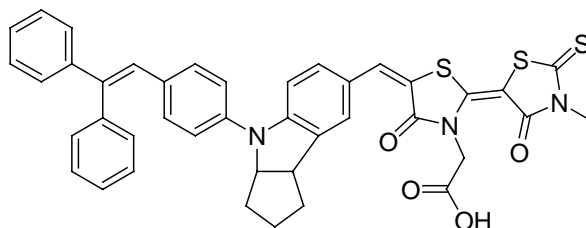


**Figure 1.10** Indoline dye (D149) with  $\eta=9.03\%$ .<sup>[48]</sup>

The problem with organic dyes has been their stability and their tendency to produce reactive radicals after electron injection. In section 3.3 some organic dyes were tested in our lab that have a main structure (naphthalene-diimide) that is relatively stable to light and heat and may provide a route to relatively robust dyes.<sup>[49]</sup>

From the early days of the Grätzel cell it has been metal coordination compounds that have been the most effective dyes for the DNSC.<sup>[12]</sup> Ruthenium has been the metal of choice so far. The ruthenium complexes have a fairly intense metal to ligand charge transfer transition (MLCT) that absorbs light in the visible part of the spectrum (~450-550 nm). Coordinated to bipyridine or terpyridine, the complexes are very stable and the <sup>1</sup>MLCT transition, where the oxidation states change between +II and +III for the ruthenium as the photons are absorbed, is reversible. As well as being stable, the excited electrons are located on the ligands and by using different ligands the electrons can be directed towards the TiO<sub>2</sub>. Carboxylic acid groups on bipyridine, for example, are electron withdrawing and the excited state may be more located on this ligand.<sup>[50]</sup>

Some of the more successful ruthenium dyes are N719, which used to be known as N3 before two of the protons were substituted for *tert*-butylammonium (TBA) cations. The so-called “black dye”, named for its dark green colour, is almost as efficient as

N719 and has a better photoresponse in the near-IR region.<sup>[51]</sup> The protons that were exchanged for TBA groups in N719 were done so to optimize the amount of protons that charge the surface. More protons on the surface will lower the Fermi level (more positive potential) of the TiO<sub>2</sub>, which will enhance the photocurrent but decrease the open circuit voltage. Doing the opposite will have the reverse effect, thus there will be an optimal amount of protons on a dye for an optimal conversion efficiency.<sup>[32]</sup> In figure 1.11 the black dye and N719 are depicted.

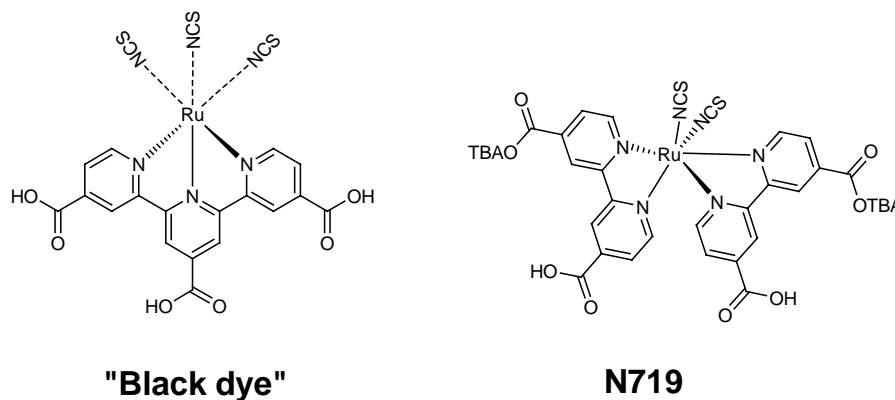


**Figure 1.11** Two ruthenium polypyridine dyes that have proven to be two of the best in DNSCs.

Strategies to improve the cell include extending the conjugation length of the ligands to red shift and increase the optical absorption.<sup>[52]</sup> Another development of ruthenium dyes has been adding hydrophobic groups that are believed to hold potentially damaging water away from the surface. With dye Z-907 the concept of hydrophobic chains connected directly to the dye were tested (see figure 1.12). This appears to improve the stability and repel water molecules especially in cells with solid-state hole conductors.<sup>[53, 54]</sup>

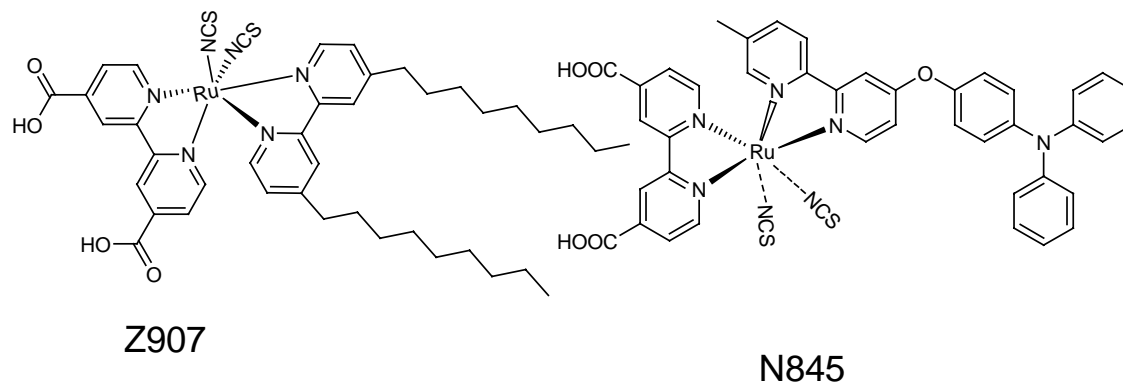


**Figure 1.12** Two ruthenium dyes with modifications to improve stability and electron injection in the DNSC.

The dye N845 in figure 1.12 uses a strategy where the positive charge from the oxidised ruthenium centre is transferred to the electron donating tri-arylamine.<sup>[46]</sup> This strategy to separate the positive charge of the dye away from the TiO<sub>2</sub> surface diminishes back reaction between the hole on the complex and the injected electron. In experiments by Durrant *et al.* the lifetime of the photogenerated charge separated state increased with increased separation (longer bridge) with lifetimes up to 4 s.<sup>[55]</sup> This type of dye shows promise for use in solid-state DNSC.

Another transition metal that has been tested in a coordination compound as molecular sensitiser in DNSC is osmium that has an absorbance band for the spin forbidden <sup>3</sup>MLCT as well as the <sup>1</sup>MLCT due to spin orbit coupling.<sup>[56]</sup> The osmium bipyridine dyes in a report by Sauve *et al.*, showed comparable results with ruthenium analogues.<sup>[56]</sup> For cheaper and more abundant materials a metal such as iron or copper could be used. Iron dyes have been tried but fail mainly due to their weak ligand field splitting that results in low-lying metal centered *e<sub>g</sub>* states that quench the ligand centered MLCT state.<sup>[57-59]</sup>

Copper makes complexes with similar photophysical properties to the ruthenium poly-pyridyls and lately efficiencies of 2.3 % were reported.<sup>[60]</sup> Although there are still question marks about stability, the fact that copper is two orders of magnitude cheaper than ruthenium and much more abundant make it a very interesting alternative. Chlorophylls with Cu<sup>2+</sup>, Mg<sup>2+</sup> and Zn<sup>2+</sup> have been tried as dyes and gave reasonable efficiencies of 2.6 % but were unstable due to transformation to reactive cation radicals upon electron injection while the ruthenium dyes only change oxidation state when the electron is injected.<sup>[61]</sup> Recently however, a publication showed DNSCs with porphyrins with zinc ions that reached efficiencies of 7%.<sup>[47]</sup>

A new development is using so-called quantum dots as sensitizing dyes. By controlling the sizes of nano-particles, the optical properties can be tuned from quantum confinement effects. An advantage of these particles is a very high extinction coefficient. This technology may be important for solid-state cells as a liquid electrolyte would lead to corrosion of the semiconductor nano-particles.<sup>[46]</sup>

In conclusion: The main problem in the quest for cheaper dyes such as completely organic ones or replacing ruthenium with metals like copper seems to be their stability. Increasing the absorption in the near-IR region and improvement of the rectifying properties of the dye (for lower recombination) may independently lead to conversion efficiencies increasing from 10% to 15%.<sup>[31]</sup>

The DNSC is a promising technology but since the nineties when efficiencies of 10% were obtained there have not been any great improvements in efficiency, although some improvements have been made in regards to stability and fabrication. It has been argued that the stability problem is equally if not more important to address than higher efficiency if the DNSC shall contribute to energy production on larger scales.<sup>[62, 63]</sup> Apart from inherent stability issues such as irreversible degradation of dyes and semiconductor, an important contribution would be replacing the liquid electrolyte with a solid-state material to avoid problems of solvent leakage and low temperature crystallisation.

### **Solid-state dye sensitised solar cell**

Several approaches have been made towards solid-state hole-conductors in the DNSC. There have been several publications on using CuI or CuSCN, which are usually cast from solution or vacuum deposited.<sup>[64, 65]</sup> Using CuI as hole transport material (HTM), efficiencies in DNSC between 2.4% and 3.8% have been achieved.<sup>[41]</sup> With the CuI however, there was a problem with strong degradation.<sup>[66]</sup> Cells made with CuSCN had better stability but slightly lower efficiencies of about 1.5%.<sup>[41, 67]</sup> Lately organic p-type semiconductors have been more popular than the inorganic ones. Krüger *et al.* have obtained the efficiencies of up to 3.2% employing the hole transport molecule 2,2',7,7'-tetrakis(N,N-di-p-methoxyphenyl-amine)9,9'-spirobifluorene (spiro OMeTAD, see figure 1.13) together with Li[CF<sub>3</sub>SO<sub>2</sub>]<sub>2</sub>N, 4-tert-butylpyridine and N(PhBr)<sub>3</sub>SbCl<sub>6</sub>. Additionally adding silver ion increased the efficiency. The hole conductor in this case was cast by spin coating.<sup>[68]</sup> A problem with a DNSC using a HTM like the spiro-OMeTAD is that the optimum TiO<sub>2</sub> film thickness is around 2 μm, which means that light absorbance is low.<sup>[69]</sup> Measurements have shown the electron diffusion length in the TiO<sub>2</sub> to be between 10-20 μm, which suggests that getting the HTM into the pores of the TiO<sub>2</sub> is a problem.<sup>[69]</sup>

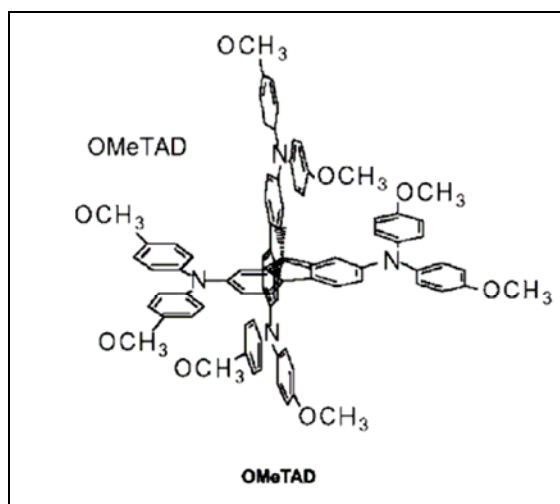


**Figure 1.13** Spiro-OMeTAD that is used as a hole conducting material. The figure is reprinted from<sup>[41]</sup>.

Conducting polymers are known to be good hole transporting materials and can achieve current densities of  $\text{mA cm}^{-2}$ . These materials could then also be useful in a solid-state device. There are some general requirements for a conducting polymer to act as a HTM in a DNSC. For a polymer that is spin casted from solutions onto the  $\text{TiO}_2$ , the wettability is important so that the polymer can penetrate into the pores. Here the molar mass/size can be of importance.<sup>[41, 70]</sup> Other requirements are:

1. The polymeric material must be transparent in the spectral range of the dye so that none of the light is “stolen “ from the sensitising dye. Alternatively if the HTM absorbs light it needs to be as efficient at electron injection as the dye.
2. The deposited HTM should not dissolve or degrade the dye monolayer.
3. The excited state of the sensitiser ( $S^*$ ) must be higher than the conduction band edge of the  $\text{TiO}_2$  for efficient injection and the sensitiser ground-state must be below the upper edge of the valence band of the p-type conducting polymer for efficient hole transfer.

Despite a lot of research, the efficiencies of solid-state DNSC with organic p-type semiconductors remain low, especially under high illumination. The problems are thought to mainly be.<sup>[41, 69, 70]</sup>

- (i) The charge recombination between the HTM and the  $\text{TiO}_2$  conduction band/trap states is high (the dark current). O'Regan *et al.* measured the

recombination to be more than a magnitude of order faster than in the liquid electrolyte cell for a cell with CuSCN.<sup>[71]</sup>

- (ii) The hole-conductors exhibit low conductivity in comparison to inorganic materials. This is mainly due to the disorder of these materials that result in a broad distribution of trap states in the material.
- (iii) Poor connection between the HTM and the adsorbed dye and between the HTM and the counter electrode.
- (iv) Difficulties to fill the pores.

To improve the pore filling (iv) and the connection between the HTM and dye (iii), Yanagida and collaborators have proposed a technique where *in-situ* photo-electrochemically polymerized polypyrrole or poly(3,4-ethylenedioxythiophene) (PEDOT) on TiO<sub>2</sub> as the HTM.<sup>[72]</sup> The first cells were with polypyrrole but in 2004<sup>[73, 74]</sup> PEDOT proved more promising and by 2008<sup>[75]</sup> an efficiency of 2.62% had been reached with PEDOT as HTM using this technique. This is discussed more in section 1.2.2. It is also possible that the organic polymer can act as sensitiser and HTM simultaneously. The major drawback in this method is the short diffusion length of the excitons (excited hole-electron pair) in the polymer, which limits the thickness of the cell. For a spin-coated film the estimated diffusion length is ~20 nm.<sup>[70]</sup> Another possible advantage of replacing the iodide/triiodide redox couple with an HTM such as polythiophene, is a polymer with more positive oxidation potential than the iodide/triiodide couple, which may improve the photovoltage. The iodide/triiodide system loses a large amount of energy (~0.5 eV) during the regeneration of the oxidised sensitiser because of a large potential difference.<sup>[12]</sup> So far however, the solid-state HTM DNSC loses a lot of the potential  $V_{oc}$  to recombination reactions, which the iodide/triiodide liquid electrolyte system does not.<sup>[41]</sup>

Polymer gel and polymer electrolytes may reduce electrolyte evaporation. These have shown good stability at 80°C and efficiencies close to 7%. Unfortunately the ionic diffusion of I<sub>3</sub><sup>-</sup> is slow resulting in a reduced current density. Further research could, however lead to improvements.

Replacing completely or partly the liquid electrolyte with an ionic liquid is another promising method. Efficiencies of up to ~7% and good long term stability have been reached but the viscosity of the ionic liquid results in slow diffusion.<sup>[46, 76, 77]</sup>

## 1.2 Photoelectro- and electro-chemical polymerisation

### 1.2.1 Electrochemical Polymerisation

When Heeger et al. in 1977 showed that poly(acetylene), which is the simplest polyconjugated system, could become conductive by the reaction with bromine or iodine vapours, it was the start of a new field of research.<sup>[78]</sup> Spectroscopic and electrochemical experiments have shown that the reaction was the transformation of neutral polymer chains into polycarbocations with simultaneous insertion of the corresponding number of  $\text{Br}_3^-$  or  $\text{I}_3^-$  anions between the polymer chains in order to counter the positive charge of the doped polymer chain.<sup>[79]</sup> The 1-dimensional organic polymers have band-gaps similar to intrinsic semiconductors. As we shall see, the polymers can possess the electrical, electronic, magnetic and optical properties of either a metal or a semiconductor. They are often called synthetic metals for this. The formation of a HOMO and LUMO arise from the so-called Peierls distortion. For poly(acetylene), for example, the C-C bonds are alternatively slightly longer or shorter and this opens a gap between the fully occupied  $\pi$ -band (valence band) and the LUMO level corresponding to empty  $\pi^*$ -band (the conducting band).<sup>[17, 79]</sup> Many of the polymers are coloured, which is associated with a  $\pi$ - $\pi^*$  transition. There are many ways to synthesise conjugated polymers such as classical polymer chemistry with coordination polymerization and typical organic chemistry procedures. One versatile method is electrochemical polymerization where electrode supported films from small amount of monomer can be prepared and studied. In this work polythiophenes have been used. Thiophene as a monomer has a relatively high oxidation potential so bithiophene and terthiophene can be employed for lower potentials (see table 1.1).<sup>[80]</sup>

**Table 1.1** Oxidation potentials of some monomers that can be polymerized.

Monomer	Oxidation potential (V vs $\text{Fc}^{0/+}$ )*
Thiophene	+ 1.76
Bithiophene	+ 1.00
Terthiophene	+ 0.74
EDOT	+ 1.18
Bis-EDOT	+ 0.53

\*Diaz, et al. J. Electroanal. Chem. 1981, 121, 355<sup>[80]</sup>

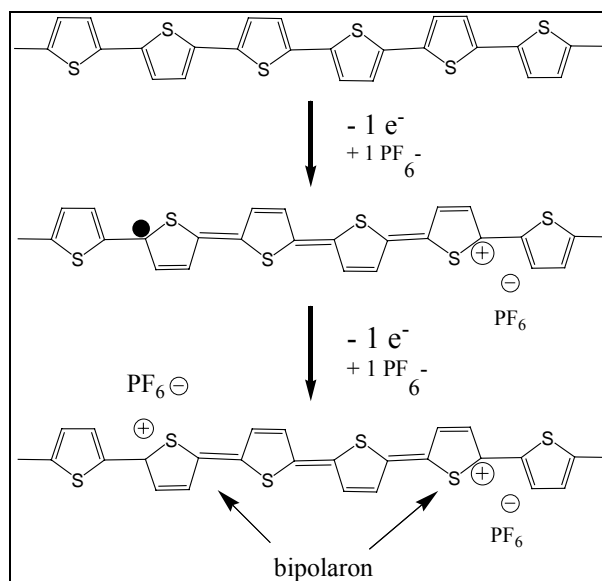


**Figure 1.14** Process of p-doping polythiophene. Reproduced from<sup>[79]</sup>.

The electrochemical p-doping of polythiophenes, involves anodic oxidation of the polymer chains to polycarbonium cations with anions inserting to neutralize the charge. The proposed mechanism: The removal of one electron results in the formation of a radical cation, also known as a polaron in this case. The polaron creates a domain of quinone-type bond sequence within the poly (2,5-thienylene) chain with aromatic bond sequence. A second electron removed may lead to a second polaron or to a spinless bipolaron which is a dication separating the domain of quinone bonds from the aromatic type bonds of the polymer chains (see figure 1.14). By measuring spin-charge correlation with coulometry and EPR in tandem it has been observed that the bipolaron process is the correct one for polythiophene.<sup>[79]</sup> The positive charges of the polycarbonium cations are mobile and make the semiconducting polymer into hole-conductors with conductivities between  $1\text{-}10\text{ Scm}^{-1}$ . In figure 1.15 the spectroelectrochemistry of poly(3-decylthiophene) shows how the absorbance band changes when the anodic potential is increased. The  $\pi\text{-}\pi^*$  transition of the neutral state is bleached and two new bands at wavelengths in the NIR region appear as the potential is increased and the polymer is doped with bipolaron dications. These are ascribed to two bipolaron transitions.<sup>[81]</sup>



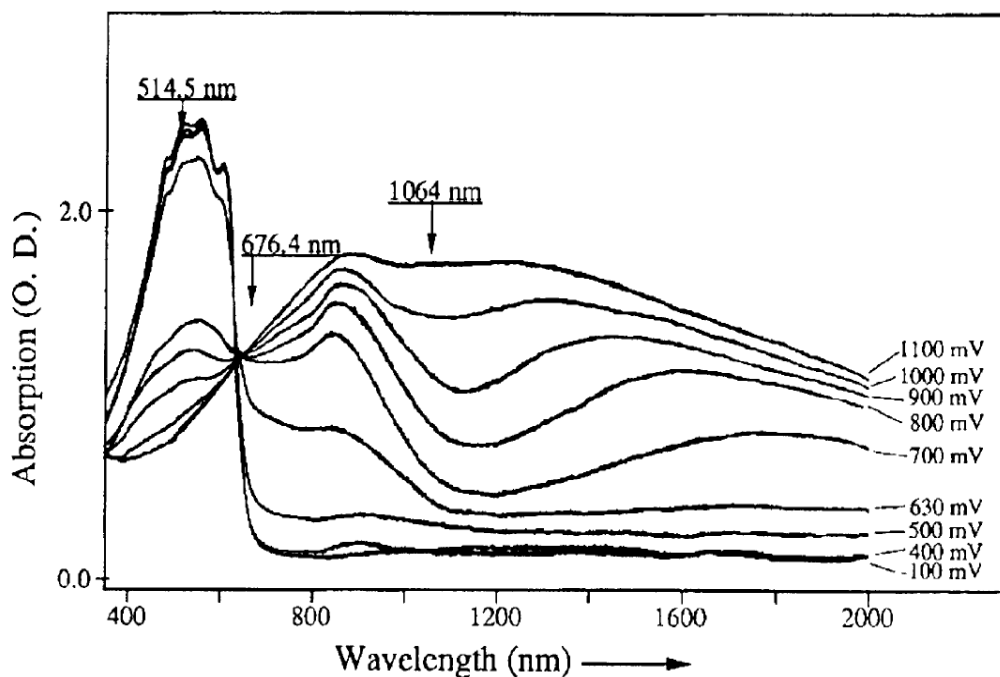


**Figure 1.15** Spectroelectrochemical behaviour of regioregular poly(3-decylthiophene) in 0.1 M  $\text{Bu}_4\text{NBF}_4$ /acetonitrile electrolyte vs Ag/AgCl. Reprinted from reference<sup>[81]</sup>.

The proposed mechanism for the electrochemical oxidative polymerization for heterocyclic monomers such as poly-thiophene is shown in figure 1.16. Experiments on the mechanism of this polymerization have shown that the main route is radical cation coupling with another radical cation.<sup>[82, 83]</sup> Proposed mechanisms for chemical oxidation of thiophenes with for example  $\text{FeCl}_3$  has a monomer being subjected to an electrophilic aromatic substitution from a chemically generated radical cation (RC).<sup>[84]</sup> In electrochemical polymerization the polymer is thought to either grow from initial adsorption or as oligomers that eventually precipitate onto the electrode surface. The growth often proceeds by a nucleation pathway like that for electrodeposited metals. After a monomer has been oxidised to a RC it is thought that the next step is a coupling of two RCs to form a dimer. The electropolymerisation then propagates with successive electrochemical and chemical steps (see figure 1.16). The fast heterogenous electron transfer at the electrode ensures a high concentration of radicals close to the electrode. Electrochemical coupling favours  $\alpha$ - $\alpha$  (2-5) over  $\alpha$ - $\beta$  (2-3/4) coupling (see figure 1.16).<sup>[82, 85]</sup> Other mechanisms have been suggested when two different monomers are present. Wei *et al.* proposed that thiophene in the presence of bithiophene and terthiophene, led to electrophilic aromatic substitution of the radical cations (bi- or ter-thiophene first to oxidize) to the neutral thiophene.<sup>[86]</sup>

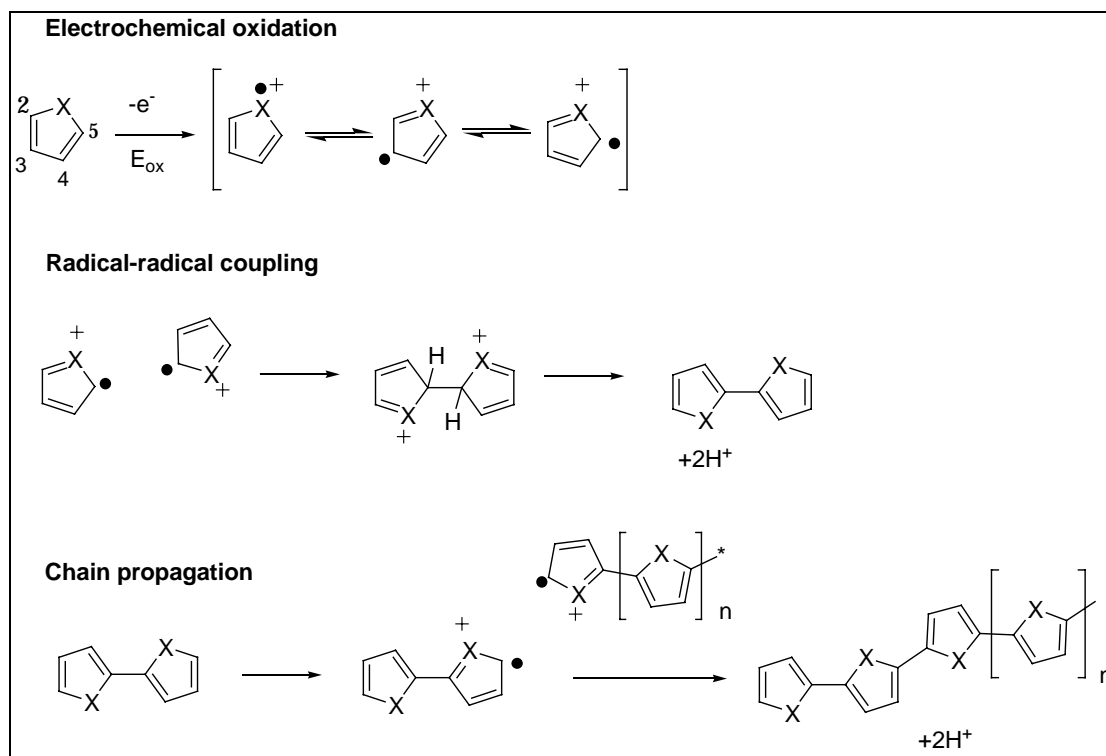


**Figure 1.16** Reaction pathway in electropolymerisation of five-membered heteroaromatics. X = NH, O, or S.

The electrochemical polymerization of ruthenium bis-terpy complexes in this work is probably via the mechanism in figure 1.16 as the coupling groups are the ligands with thiophenes.<sup>[82]</sup> The photo-electrochemical polymerization (PEP) of the monomers by surface adsorbed complexes on TiO<sub>2</sub>, may also proceed by the RC-RC process described in figure 1.16. Alternatively the oxidised dye may initiate an electrophilic aromatic substitution on the monomers in solution as in reference [78]. More on this will be discussed in chapter 2.

A problem with oligo-thiophenes is their poor solubility and the possibility that there will be cross-linking due to unprotected positions. Adding substituents at the 3- and 4-positions can change properties like oxidation potential and solubility. An example is poly(3-hexylthiophene) where the hexyl chains increase the solubility in organic solvents. A polymer that is interesting for different applications is poly(3,4-ethylenedioxythiophene) (see figure 1.17), a material developed by Bayer AG research laboratories in Germany.<sup>[87]</sup> It can be produced by electrochemical oxidation of the monomer or dimer, the dimer having an oxidation potential 0.65 V less positive.<sup>[88]</sup> It is a highly conducting (ca 300 S/cm when p-doped, compared to

Copper with  $10^5$  S/cm) polymer, almost transparent in its oxidised conducting form and additionally shows a high stability in its oxidised form. The ethylenedioxy group protects the  $\beta$ -positions to avoid undesired  $\beta$ - $\beta$  and  $\alpha$ - $\beta$  couplings.<sup>[89]</sup> It has been used in several applications like OLED's and electro-chromic devices.<sup>[90]</sup>

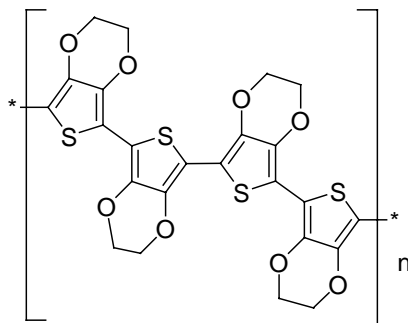


**Figure 1.17** Poly(3,4-ethylenedioxythiophene).

### Conduction in electroactive polymers

As was discussed, the conductivity of conjugated polymers like poly-thiophene is a result of doping the polymer by removing or adding  $\pi$ -electrons and creating carbonium cations within the polymer backbone that are accompanied by ions to neutralize the charge.<sup>[91]</sup> The conductivity is believed to be of a hopping type.<sup>[92]</sup> Diffusion of the counter ion will also be determining for the conductivity.

Electroactive polymers can be divided into three main groups: redox polymers, loaded ionomers and electronically conducting polymers of which PEDOT is an example. The combination of a conjugated polymer together with attached redox centers in redox polymers has been of recent interest. By having the two coupled directly, electronic interactions between the metals d-orbitals and the polymers  $\pi$ -system may modify the properties of both components in interesting ways. An application where this is useful is electrocatalysis.<sup>[93]</sup> The electron transfer between immobilized metal centers on a polymer backbone can occur by three different mechanisms. **1) Outer-sphere** electron transfer between metal centers, **2) Electron transfer through the polymer backbone via metal-metal interactions (superexchange pathway)** and **3) via polymer based charge carriers (e.g. bipolarons)**. For the latter two pathways the bridging ligands energy levels need to be close to that of the redox center. If this is not the case, *outer-sphere* exchange will be the charge transport and a slower electron transport is expected. Using the polymer backbone to directly link redox centers can increase charge transport by two orders of magnitude compared to the analogue

without a conjugated backbone. This is thought to be from superexchange pathways. In figure 1.18 are examples of a conjugated polymer with redox centers.<sup>[93]</sup>

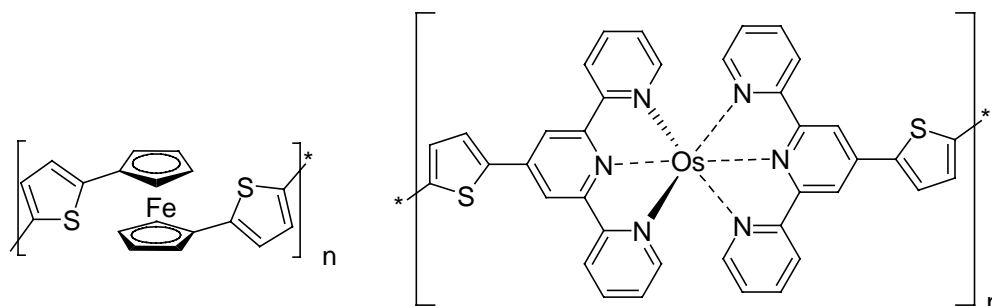


**Figure 1.18** Two examples of metallopolymers.<sup>[93, 94]</sup>

Measurements of the conductivity of the metallopolymers are usually expressed as  $D_e C_M^2$  where  $D_e$  is the effective diffusion constant and  $C_M$  is the concentration of metal centers. The concentration  $C_M$  is usually difficult to know exactly. When describing the conduction mechanisms of materials where there are redox centers on a conjugated polymer there is the complication of two types of conduction. There is the electric conduction along the  $\pi$ -system of the conjugated system and the diffusion of the redox state of the redox centers. These parameters are connected to the so-called redox capacity ( $\rho$ ) of the polymer through equation 5.<sup>[95-97]</sup>

$$D_e = \sigma_e / \rho \quad (5)$$

$D_e$  is the diffusion coefficient of the electrons and  $\sigma_e$  is the dc electron conductivity. The redox capacity of an electroactive material is its ability to store charge at equilibrium potential. To be more exact it is the charge stored at equilibrium per unit volume per infinitesimal change of the potential relative to a reference electrode with the dimensions  $C V^{-1} cm^{-3}$ .<sup>[96]</sup> Experimentally the conduction that is measured is diffusion controlled and is measured electrochemically as a diffusion coefficient derived from *Fick's* equations (described in chapter 2).

## 1.2.2 Photo-Electrochemical Polymerisation

One of the methods mentioned to apply conducting polymer in the solid-state DNSC is by an *in-situ* photo-electrochemical polymerisation (PEP) process where the dye molecules absorb light and then oxidise monomers in solution to produce oxidative coupling. Electrochemical oxidation, as was discussed above, is a well-known method to produce thin films of conducting organic polymers on electrodes. In order to deposit a polymer directly on, or close to the dye molecules on the semiconductor  $\text{TiO}_2$ , and not in contact with the substrate, it is necessary to use a technique such as PEP. Yanagida and his associates have been the pioneers with this process since 1997.<sup>[98]</sup> The first cells from the group of Yanagida used polypyrrole as hole conducting material and ruthenium complexes to photo-oxidise pyrrole monomers.<sup>[72]</sup> The cells had very low efficiencies due partly to the absorption of visible light by the polypyrrole. A better alternative was tested in a paper 2002 when poly(3,4-ethylenedioxythiophene) (PEDOT) was chemically produced from Fe(III) tris-p-toulenesulfonate and EDOT monomer and deposited on dye sensitised  $\text{TiO}_2$ .<sup>[99]</sup> As was discussed, PEDOT has a high transparency in the visible range, relatively high conductivity and good stability at room temperature, which make it a good candidate as hole conducting material for the DNSC.<sup>[73, 89]</sup> This PEDOT DNSC was improved by the *in-situ* polymerisation via the PEP method and using bis-EDOT as monomer in a 2004 publication.<sup>[100]</sup> This was further improved by using the amphiphilic ruthenium dye Z-907 to yield a conversion efficiency of 1.26%.<sup>[101]</sup> In figure 1.19, the concept for this method is outlined. The most important parameter that needs to be considered is that the dye, in its oxidised form, should be able to oxidise the monomer. This is illustrated by the relative potentials of the different energy levels drawn out in figure 1.19. Apart from illumination with a light intensity of about  $20 \text{ mWcm}^{-2}$  it was important to apply a bias potential to the substrate of the  $\text{TiO}_2$  film in order to drain the  $\text{TiO}_2$  from dye injected electrons. The optimal bias potential was found to be at about  $-0.2 \text{ V}$  (vs  $\text{Ag}^+/\text{Ag}$ ).<sup>[73]</sup>

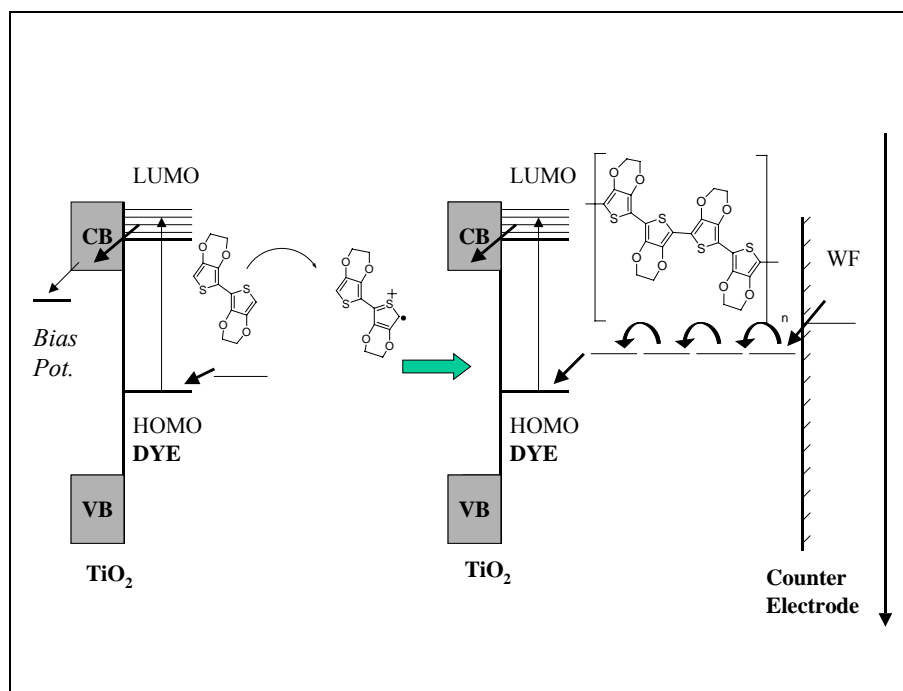


**Figure 1.19** The concept of the photo-electro polymerisation (left) and the DNSC with PEDOT as hole conducting material (right) when under illumination. The solid arrows show the direction of electrons for the two processes. The dashed lines show the main back reactions.

A too positive potential applied to the substrate will oxidize the monomer directly at the FTO substrate. At potentials of 0 to +0.1 V the polymerization was slower and appeared to lead to over-oxidation, which would not be good for the conductivity of the HTM.<sup>[73]</sup>

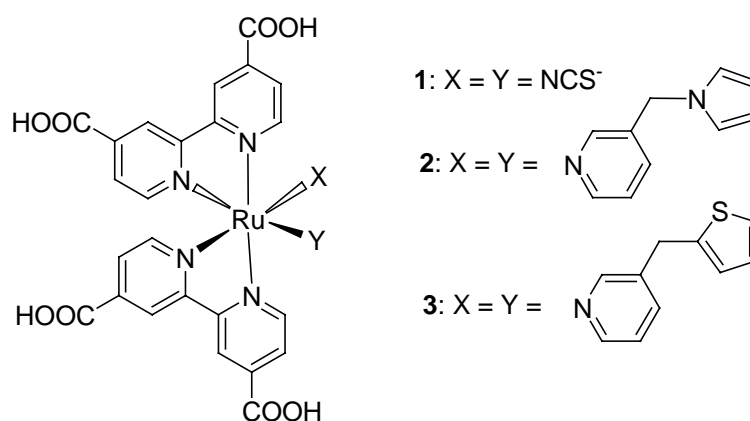


**Figure 1.20** Ruthenium bipyridine complex with different ligands for PEP technique by Yanagida et al.<sup>[73]</sup> Reproduced from reference<sup>[73]</sup>.

Another parameter that Yanagida *et al.* tested was having ligands functionalised with the monomer that is to be polymerised. In figure 1.20 three different ligands on the X and Y positions were made and used in PEP with either pyrrole or bis-EDOT as

monomer in solution. The transient current densities, which have peaks like those in figure 1.21, are believed to first show a nucleation peak followed by diffusion-limited polymerisation.<sup>[73, 102]</sup> In the case of dyes **2** and **3**, the nucleation peaks came earlier than for **1** when pyrrole and bis-EDOT respectively were polymerised. Photovoltaic measurements after the polymerisation showed slightly improved results with dyes **2** and **3**. This suggested that the ligands with pyrrole and thiophene groups were enhancing the charge transport at the dye/PEDOT due to a more intimate coupling. Direct evidence of coupling was not found.<sup>[73]</sup> Later publications showed the optimum thickness to be around 5.8  $\mu\text{m}$  and that the same efficiency (2.6 %) could be reached with Z-907 as with a dye **3** from figure 1.20 (Z-907 being similar to **3** in figure 1.20 but with hydrophobic alkyl chains).<sup>[103-105]</sup>

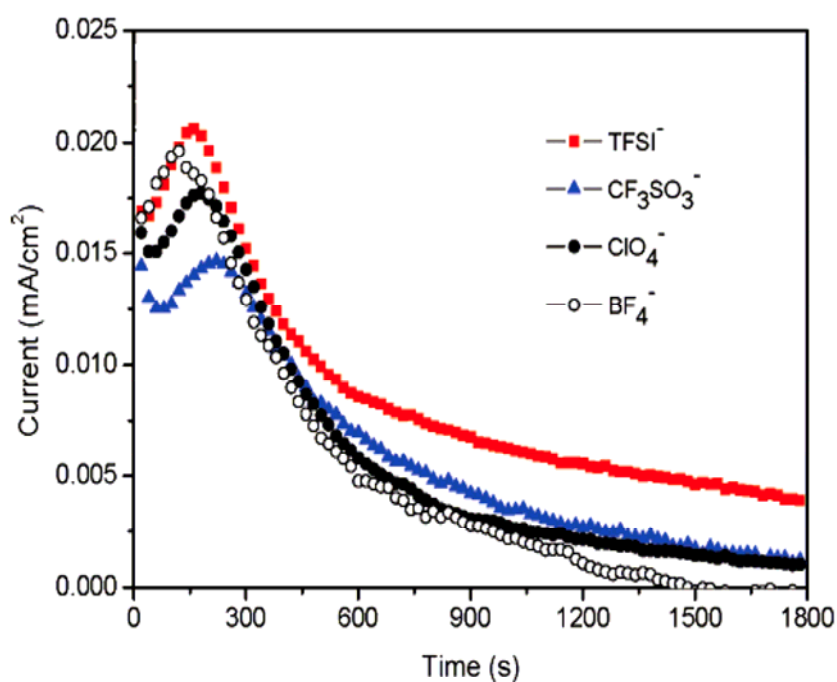


**Figure 1.21** Typical chronoamperometric response to the photo-electrochemical polymerisation (PEP) process from Yanagida *et al.* In this experiment different counter anions were tested.  $\text{Li}^+$  is the cation for all four salts. Reprinted from <sup>[106]</sup>.

In figure 1.21, typical amperometric measurements from the PEP by Yanagida *et al.* are shown.<sup>[106]</sup> In this experiment different anions in the electrolyte were tested. In an oxidative polymerisation, anions will be inserted into the polymer to neutralise the positive charges from the oxidative doping. The ions will be involved in the ionic charge transport that takes place during the experiment and in the conductivity of the

resulting polymers. The conductivities were measured using electrochemical impedance that was fitted with an equivalent circuit for the cell. The conductivities were in the order  $\text{BF}_4^- < \text{ClO}_4^- < \text{CF}_3\text{SO}_3^- < \text{TFSI}$  (bis-trifluoromethanesulfonylimide), which was reflected by the photocurrents and efficiencies showing the same trend. This shows how the choice of anion can influence the photovoltaic performance. As a reason for this, the authors suggested that the higher charge delocalisation on the relatively large anion TFSI compared to especially the  $\text{BF}_4^-$  and  $\text{ClO}_4^-$  anions, allowed the TFSI to induce preferred stacking through the transverse EDOT ring allowing good conduction. In figure 1.21, the peaks of the current curves are thought to indicate nucleation sites from where further growth can proceed.<sup>[106]</sup>

In Yanagidas group the experiments were performed by immersing the dye sensitized  $\text{TiO}_2$  films (which are contacted) in an electrolyte with the monomer. The film is illuminated and the dye molecules will oxidize the monomer after electron injection into the  $\text{TiO}_2$ . After the process the electrode is clipped together with a counter electrode. But other methods have been reported. One elegant experiment with porphyrin dyes, used *in-situ* polymerization of aniline in ready made solar cells by adding the monomer electrolyte to the cell and illuminating ( $\sim 15 \text{ mW cm}^{-2}$ ) it for  $\sim 2.5$  hours with an applied potential of 0 V.<sup>[107]</sup> In figure 1.22 from reference [104], the proposed mechanism of the *in-situ* polymerization is shown. Analysis with MALDI-MS of desorbed product from the electrode indicated porphyrin dye and aniline oligomers but only very faintly dye covalently bonded with oligomers. The photovoltaic measurements for the poly-aniline cell showed an efficiency of 0.8 % compared to the same dye but with  $\text{I}^-/\text{I}_3^-$  electrolyte giving 1.1 % at low light intensities. The main difference was the photocurrent density.

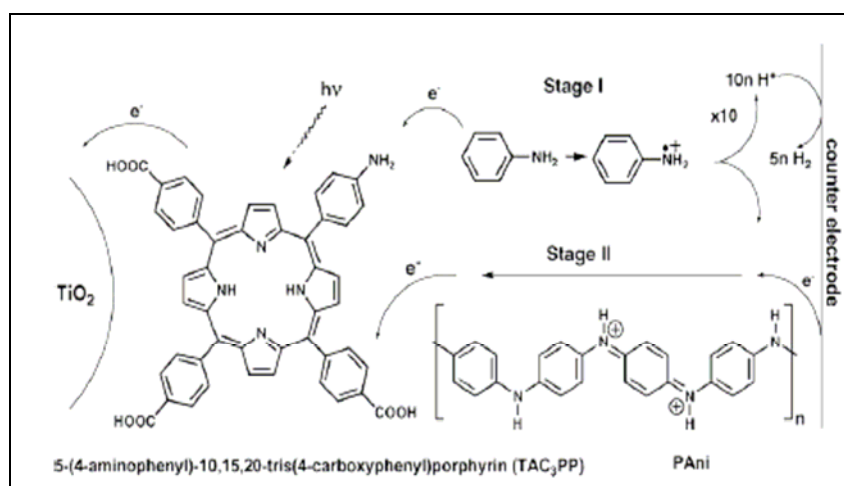


**Figure 1.22** Proposed mechanism scheme for *in-situ* photoelectro-chemical polymerisation.<sup>[107]</sup>



### 1.2.3 Photo-Physics and Electrochemistry of Ruthenium (II) Polypyridyl Complexes

Ever since the chemistry of transition metal complexes was discovered there has been an interest in their spectroscopic and electrochemical properties due to the often-strong absorption of visible light and stability of several oxidation states. As well as academic interest there are technological aspects such as in medicine, display technology and photovoltaics. Ruthenium polypyridyl complexes are interesting as photosensitisers due to their favourable photophysical and electrochemical properties.<sup>[108]</sup> The metal to ligand charge transfer (<sup>1</sup>MLCT) transition (400-600 nm) is usually the dominating absorption in the visible part of the spectrum. It has a reasonably long excited state lifetime (ns- $\mu$ s) and the oxidised and reduced species have good stability. Other metal ions can also be used in complexes for photophysical reasons, such as Os<sup>II</sup>, Co<sup>II</sup>, Ir<sup>III</sup>, Cu<sup>I</sup> and Re<sup>I</sup>.<sup>[109]</sup> In this work mainly ruthenium bis-terpyridine complexes but also a few iron bis-terpyridine complexes are considered. The metal ligand compounds will be referred to as complexes or coordination compound interchangeably.<sup>[110]</sup>

#### Photophysics of Ru<sup>II</sup>/Fe<sup>II</sup> polypyridines

When a molecule absorbs electromagnetic radiation, an excited molecule, with a new electronic state, results. The excited state it is not very stable and the excess energy needs to go somewhere. The photophysical processes for molecules to channel off this energy can be radiative or non-radiative. No chemical changes result but bond lengths and angles differ somewhat in different electronic states. Competing with this are photochemical reactions that lead to chemical changes. The different photophysical processes are drawn out in figure 1.23 in a Jablonski diagram (i.e. a simplified energy diagram of the possible transitions). An important characteristic of the electronic states is their multiplicity. Paired electron spins are singlet states while unpaired electron spins are triplets. Excited triplets are usually lower in energy than the excited singlet.

The initial electronic absorption excites the ground state, S<sub>0</sub> (usually a singlet), to a new electronic state (e.g. S<sub>1</sub>) with the same multiplicity. The transition is a so-called vibronic transition as the excited state is vibrationally excited. The time scale of the

absorption is about  $10^{-15}$  s. An absorption band at room temperature is usually a broad band with several overlapping vibronic (electronic transitions to different vibrational levels) transitions.<sup>[110]</sup>

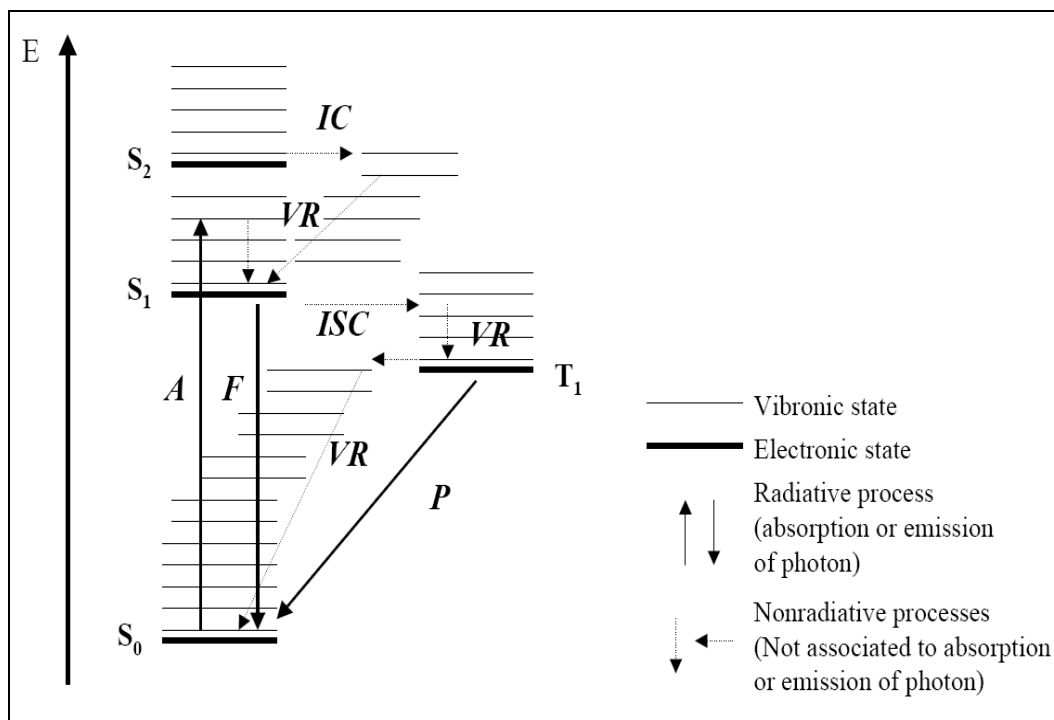


**Figure 1.23** Jablonski diagram depicting molecular states and photophysical processes.

The isoenergetic radiationless transitions between two electronic states having the same multiplicity, is referred to as an internal conversion (IC). When the transition is between two different multiplicities it is an intersystem crossing (ISC). The excited state will lose energy to the surrounding medium by vibrational relaxation (VR) when the molecule collides with neighbouring molecules. Vibrational redistribution within the molecule also is a factor. This mode of nonradiative relaxation has a time scale of 10-100 fs. For large molecules the vibrational relaxation is very rapid so the radiative processes mostly come from the lowest excited states. Fluorescence (F) is between states of the same multiplicity and the time scale for this is  $10^{-9}$ - $10^{-7}$  s. Phosphorescence (P) is a luminescent transition between states of different multiplicity and is therefore a forbidden transition but spin-orbit coupling makes it weakly allowed. Being only weakly allowed, the decay time is longer ( $10^{-6}$ - $10^{-3}$  s) than that of fluorescence.

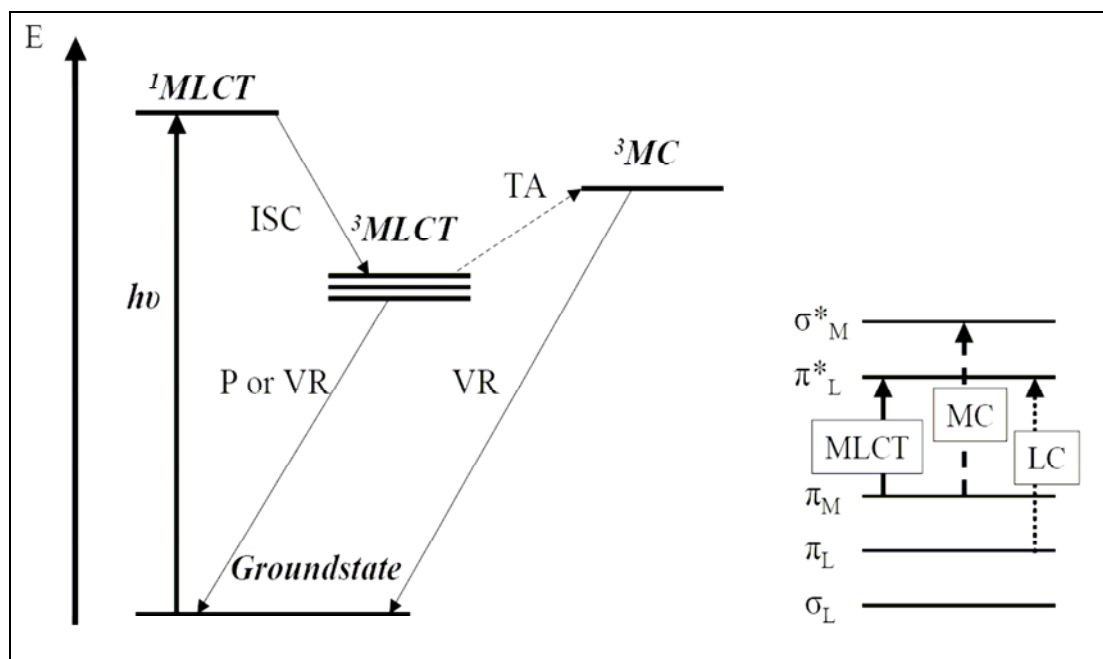


**Figure 1.24** Simplified diagram of the common transitions in polypyridyl ruthenium complexes. The acronyms are the same as earlier in the text. TA is a thermal activation process.

In figure 1.24 a simplified diagram with the dominating transitions in an octahedral ruthenium polypyridyl complex are shown. On the left in figure 1.24 is the MLCT excitation and deactivation and on the right the relative energies of the MLCT, metal centred charge transfer (MC) and the ligand centred (LC) charge transfer transitions.

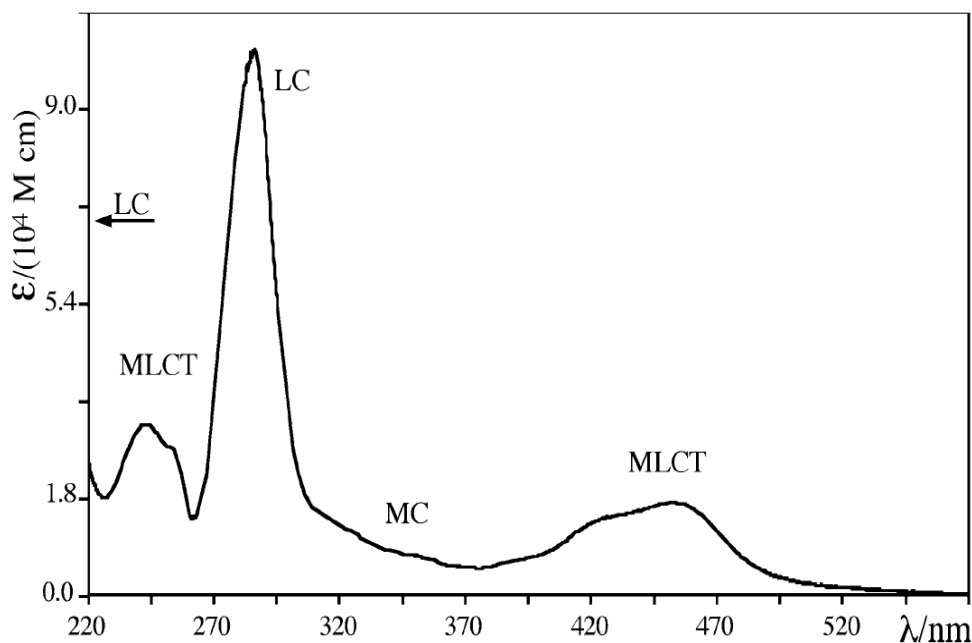


**Figure 1.25** Electronic absorbance spectra of  $[\text{Ru}(\text{bipy})_3]^{2+}$  in ethanol with the important transitions labelled. Figure reprinted from reference<sup>[109]</sup>.

In figure 1.25 the absorbance spectra of  $[\text{Ru}(\text{bipy})_3]^{2+}$  is plotted with extinction coefficient values ( $\epsilon$ ) and the different transitions marked. The ligand centred absorbance ( $\pi\text{-}\pi^*$ ) is usually more intense than for the  $^1\text{MLCT}$ .

$[\text{Ru}(\text{bipy})_3]^{2+}$  compounds have a much more efficient and longer luminescence lifetime at room temperature ( $\Phi \sim 0.04$ ,  $\tau \sim 600$  ns) than the  $[\text{Ru}(\text{terpy})_3]^{2+}$  equivalent ( $\Phi \sim 10^{-5}$ ,  $\tau > 0.3$  ns). This comes mainly from the fact that the bite angle of terpyridine is not as close to the ideal octahedral bite angle of bipyridine.<sup>[110]</sup> With a less octahedral geometry the ligand field is weaker and the metal centered  $^3\text{MC}$  is lowered in energy. A weaker ligand field will thus lead to the anti-bonding metal centered triplet state having a lower energy.<sup>[111]</sup> In the case of iron for example, the weak ligand field moves the  $^3\text{MC}$  below the  $^3\text{MLCT}$  and therefore the MLCT lifetime will be very short (see figure 1.26) and a population of  $e_g^*$  state will direct the excited state away from the ligands and if in the form of a sensitizer on  $\text{TiO}_2$ , away from the  $\text{TiO}_2$  surface. Because the  $e_g^*$  state is anti-bonding it also makes the complex unstable.<sup>[57]</sup> The iron complex  $[\text{Fe}^{\text{II}}(2,2'\text{-bipyridine-4,4'-dicarboxylic acid})_2(\text{CN})_2]$  was reported by Ferrere *et al.* to give quite low photocurrents of  $\sim 0.3$  mA  $\text{cm}^{-2}$  when used in a dye sensitised solar cell.<sup>[57, 59]</sup> As mentioned earlier, the injection of excited electrons is on the femtosecond time scale and the deactivation of the MLCT by the  $^3\text{MC}$  in the iron complex is slightly less rapid (on the ps-fs scale), so the iron complexes should manage to inject some electrons into the  $\text{TiO}_2$  during the first 100 ps or so.

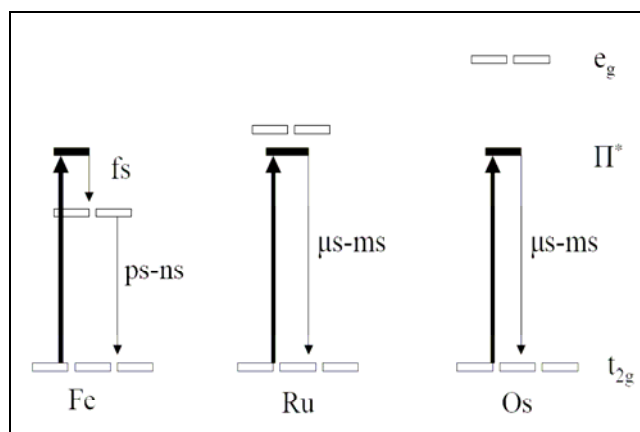


**Figure 1.26** Diagram of the metal d-orbitals and their relation with the LUMO of the ligand for different metal ions with different ligand field strengths. Reproduced from<sup>[57]</sup>.

Figure 1.27 gives a summary of the energy states and electron / energy transfers that are possible for the ruthenium polypyridyl complexes.

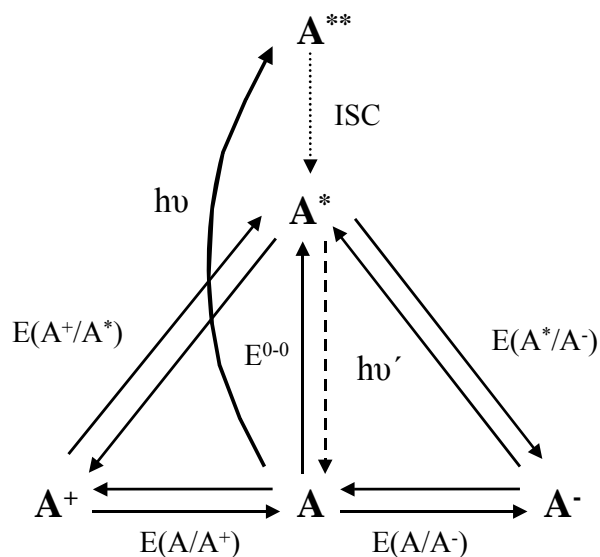


**Figure 1.27** Schematic figure showing the energy states and oxidation states relevant to electron transfer processes.

In competition with the intrinsic deactivation pathways of the excited state, the complex can partake in photochemical reactions. The energy content of the excited state of a molecule make them both a stronger oxidant and stronger reductant than the ground state.<sup>[108]</sup>

As an approximation of the redox potentials of excited state couple, their ground state oxidation potentials together with the zero-zero excitation energy,  $E^{0-0}$ , can be used to calculate them as in equations 1 and 2.

$$E(A^+ / ^*A) = E(A^+ / A) - E^{0-0} \quad (1)$$

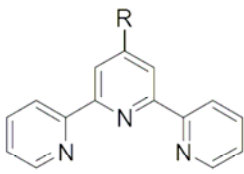
$$E(^*A / A^-) = E(A / A^-) + E^{0-0} \quad (2)$$

The excited state can transfer its excess energy in an energy transfer or transfer the excess energy to chemical energy in an electron transfer. The electron transfer can proceed between covalently linked molecules or in bi-molecular reactions. The electron injection in the DNSC is an electron transfer mostly from  $A^{**}$  and partly from  $A^*$  in figure 1.27. Oxidation of an electron donor by the surface-bound oxidised dye will be from the  $A^+$  relaxed state.

## Electrochemistry of Ru<sup>II</sup>/Fe<sup>II</sup> polypyridines

As was discussed above, the ruthenium polypyridine complexes have interesting possibilities as reactants in the excited state and as redox mediators in reactions involving light. To make these properties possible it is important that the oxidised and reduced forms are stable and reversible. Following the first work on [Ru(bipy)<sub>3</sub>]<sup>2+</sup> many complexes in the ruthenium polypyridine family have been measured electrochemically.<sup>[112]</sup> The main technique has been cyclic-voltammetry (CV) where it is possible to probe the reversibility and stability of oxidation states of the species in solution. Using CV together with other spectroscopic techniques, the location of the acceptor and donor orbitals in the one-electron transfers can be found. In the case of [Ru(bipy)<sub>3</sub>]<sup>2+</sup>, and similarly for metals of the same column in the periodic table, there is a reversible redox process at about +0.96 (vs Fc/Fc<sup>+</sup>) that corresponds to the ruthenium +II and +III oxidation states. Oxidation to the +III states in Fe(II), Ru(II) and Os(II) tris-bipy and bis-terpy complexes form genuine low-spin d<sup>5</sup> configurations from the low-spin d<sup>6</sup> configurations. These metal orbital centered states are inert to ligand substitution.<sup>[108]</sup> The Fe(III) state is not quite as stable as the others but within the time scale of CV experiments (1-100 s) it is reversible. At negative potentials for ligands that are good acceptors, such as bipyridine and terpyridine, there are usually reversible reductions of the ligands. Experiments suggest that the reductions are localised to one ligand and not shared among several. The first oxidation and reduction potentials can be assigned to the HOMO and LUMO of the spectroscopic transitions and therefore there are often correlations between the electrochemical and spectroscopic data.<sup>[108, 113-115]</sup> Examples of CV's for metal polypyridine complexes in this work are shown in chapters 2 and 3.

The reduction and oxidation potentials of the complexes can be changed by substitutions on the ligands. Substituents on the 4'-position of terpyridine ligands may have electron withdrawing or electron donating properties.<sup>[116-118]</sup> Aryl groups are usually weakly donating. Apart from inductive effects other factors can influence. For example, a more conjugated ligand will often be easier to reduce, as is seen for [Ru(bttpy)<sub>2</sub>]<sup>2+</sup> (bt = bis-thiophene) with a first reduction at -1.79 V compared to the unsubstituted [Ru(tpy)<sub>2</sub>]<sup>2+</sup> with -1.90 V.<sup>[94]</sup> The higher conjugation on the ligand lowers the energy of the π\* LUMO and facilitates ligand-centred reduction.



Ruthenium complex		Iron complex	
R Substituent	E <sup>0</sup> /V	R Substituent	E <sup>0</sup> /V
-OH	+ 0.73	-C <sub>4</sub> H <sub>8</sub> N	+ 0.29
-MeS	+ 0.80	-OH	+ 0.55
-bt	+ 0.84	-CH <sub>3</sub> -C <sub>6</sub> H <sub>4</sub>	+ 0.68
-Ph	+ 0.86	-H	+ 0.73
-Py	+ 0.90	-Cl	+ 0.79
-H	+ 0.92	-CH <sub>3</sub> SO <sub>2</sub>	+ 0.90
-Cl	+ 1.00		

**Figure 1.28** Various substituents on the 4'-position of [Ru/Fe(R-terpy)<sub>2</sub>]<sup>2+</sup> complexes with the redox potentials for the M(II)/M(III) process (vs Fc/Fc<sup>+</sup>). The substituent Py is pyridine<sup>[117]</sup> and bt is bis-thiophene.<sup>[94]</sup>

Constable *et al.*<sup>[116, 117]</sup> and Chambers *et al.*<sup>[118]</sup> have found correlations between the Hammett parameters of the substituents and the redox potential of the M(II)/M(III) process in terpyridine complexes. The hammett parameter quantifies the relative inductive strengths of the various substituents with hydrogen as the point of reference. When the substituent is more electron donating the redox potential is less positive and *vice versa* for an electron withdrawing substituent. The reduction potentials of the ligands with electron donating groups are found to be harder to reduce while withdrawing groups decrease the reduction potentials. The longer conjugation of ligands, such as in bi-thiophene terpyridine, has a smaller affect on the redox potential but will generally stabilise the LUMO and lower the reduction potential. In figure 1.28 some redox potentials of complexes with substituents in the 4'-position from references [113-115] and [94] are listed.

When the oxidation potential of a ligand is decreased, it will usually make the redox potential less positive because of its more donating character. In the complex [Ru(ttppy)<sub>2</sub>]<sup>2+</sup> (tt = terthiophene) the oxidation of the terthiophene is overlapping with the redox process.<sup>[94]</sup> Complexes with ligands that oxidise at less positive potentials than the metal redox process have been made with pyrrole or terthiophene substituents on the 4'-position.<sup>[119, 120]</sup> A terthiophene ligand was tested in a heteroleptic complex with an anchoring ligand for use in a DNSC. The idea being that a complex with an oligothiophene may be used in a solid-state cell with polythiophene for better connection between dye and the HTM. Houarner-Rassin *et al.* found that adding an

ethanyl spacer between the terthiophene and the terpyridine improved the photovoltaic performance slightly.<sup>[119]</sup> The LUMO of the ligand without spacer is stabilised by the terthiophene and in the heteroleptic complex the <sup>1</sup>MLCT will involve the terthiophene ligand that is pointing away from the TiO<sub>2</sub> surface. The complexes are shown in figure 1.29. Breaking the conjugation between the terthiophene and terpyridine with an ethanyl spacer seemed to switch the <sup>1</sup>MLCT more towards the anchoring ligand and the TiO<sub>2</sub>.

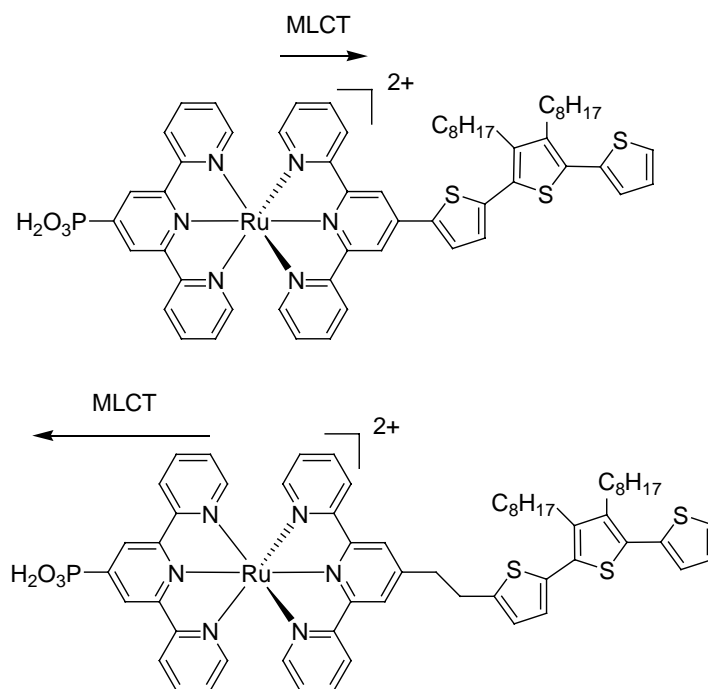


**Figure 1.29** Ruthenium complexes from reference<sup>[119]</sup>. The counter ions are  $2\text{BF}_4^-$ .

### 1.3 Goal

The aim of this project was to design ruthenium bis-terpyridine complexes, which can sensitise nanoporous TiO<sub>2</sub> and photoelectrochemically oxidise monomers that progress to oxidatively couple into polymers. Ultimately the surface bound complexes may be possible to wire to an electrode by growing a polymer between them. For this purpose the complexes were functionalised with different thienyl groups. The affect on the photovoltaic performance from the modifications on the ligands was also of interest with three different anchoring ligands tested.

To investigate the dye sensitised TiO<sub>2</sub> surface, a technique using scanning electrochemical microscopy (SECM) was developed.



## Reference list

- [1] E. Becquerel, *CR* **1893**, 9, 561.
- [2] J. Nelson, *The Physics of Solar Cells*, Imperial College Press, **2003**.
- [3] A. Goetzberger, C. Hebling, H.-W. Schock, *Mater. Sci. Eng., R* **2003**, 40, 1.
- [4] N. Armaroli, V. Balzani, *Angew. Chem. Int. Ed.* **2007**, 46, 52.
- [5] M. Grätzel, *Nature* **2001**, 414, 338.
- [6] H. Gerischer, *J. Electrochem. Soc.* **1966**, 113, 1174.
- [7] H. Tada, H. Honda, *J. Electrochem. Soc.* **1995**, 142, 3438.
- [8] B. O'Regan, M. Grätzel, *Nature* **1991**, 353, 737.
- [9] A. E. Suliman, Y. W. Tang, L. Xu, *Sol. Energy Mater. Sol. Cells* **2007**, 91, 1658.
- [10] A. Furube, M. Murai, S. Watanabe, K. Hara, R. Katoh, M. Tachiya, *J. Photochem. Photobiol., A* **2006**, 182, 273.
- [11] K. Sayama, H. Sugihara, H. Arakawa, *Chem. Mater.* **1998**, 10, 3825.
- [12] A. Hagfeldt, M. Grätzel, *Chem. Rev.* **1995**, 95, 49.
- [13] D. F. Watson, G. J. Meyer, *Coord. Chem. Rev.* **2004**, 248, 1391.
- [14] M. J. Cass, A. B. Walker, D. Martinez, L. M. Peter, *J. Phys. Chem. B* **2005**, 109, 5100.
- [15] J. Nelson, R. E. Chandler, *Coord. Chem. Rev.* **2004**, 248, 1181.
- [16] G. C. Bond, *Heterogeneous Catalysis Principles and Applications*, 2 ed., Oxford Science Publications, **1987**.
- [17] D. F. Shriver, P. W. Atkins, *Inorganic Chemistry*, 3 ed., Oxford University Press, **1999**.
- [18] P. W. Atkins, *Physical Chemistry*, 6 ed., Oxford University Press, **1999**.
- [19] A. Wahl, J. Augustynski, *J. Phys. Chem. B* **1998**, 7820.
- [20] G. Boschloo, H. Lindström, E. Magnusson, A. Holmberg, A. Hagfeldt, *J. Photochem. Photobiol., A* **2002**, 148, 11.
- [21] S. Hao, J. Wu, L. Fan, Y. Huang, J. Lin, Y. Wei, *Sol. Energy* **2004**, 76, 745.
- [22] S. Sodergren, H. Siegbahn, H. Rensmo, H. Lindstrom, A. Hagfeldt, S. E. Lindquist, *J. Phys. Chem. B* **1997**, 101, 3087.
- [23] A. Stashans, S. Lunell, R. Bergstrom, A. Hagfeldt, S. E. Lindquist, *Phys. Rev. B* **1996**, 53, 159.
- [24] G. Redmond, D. Fitzmaurice, *J. Phys. Chem.* **1993**, 97, 1426.
- [25] J. Bisquert, F. Fabregat-Santiago, I. Mora-Sero, G. Garcia-Belmonte, E. M. Barea, E. Palomares, *Inorg. Chim. Acta* **2008**, 361, 684.
- [26] A. Zaban, S. T. Aruna, S. Tirosh, B. A. Gregg, Y. Mastai, *J. Phys. Chem. B* **2000**, 104, 4130.
- [27] M. K. Nazeeruddin, A. Kay, I. Rodicio, R. Humphrybaker, E. Muller, P. Liska, N. Vlachopoulos, M. Gratzel, *J. Am. Chem. Soc.* **1993**, 115, 6382.
- [28] H. Park, E. Bae, J. J. Lee, J. Park, W. Choi, *J. Phys. Chem. B* **2006**, 110, 8740.
- [29] E. Galoppini, *Coord. Chem. Rev.* **2004**, 248, 1283.
- [30] K. S. Finnie, J. R. Bartlett, J. L. Woolfrey, *Langmuir* **1998**, 14, 2744.
- [31] A. Hagfeldt, M. Graetzel, *Acc. Chem. Res.* **2000**, 33, 269.
- [32] M. K. Nazeeruddin, R. Humphry-Baker, P. Liska, M. Gratzel, *J. Phys. Chem. B* **2003**, 107, 8981.
- [33] C. Bauer, G. Boschloo, E. Mukhtar, A. Hagfeldt, *J. Phys. Chem. B* **2001**, 105, 5585.
- [34] C. Bauer, G. Boschloo, E. Mukhtar, A. Hagfeldt, *J. Phys. Chem. B* **2002**, 106, 12693.
- [35] J. R. Durrant, S. A. Haque, E. Palomares, *Coord. Chem. Rev.* **2004**, 248, 1247.

- [36] J. B. Ashbury, R. J. Ellingson, H. N. Ghosh, S. Ferrere, A. J. Nozik, T. Lian, *J. Phys. Chem. B* **1999**, *103*, 3110.
- [37] A. H. Saif, E. Palomares, B. M. Cho, A. N. M. Green, N. Hirata, D. R. Klug, J. R. Durrant, *J. Am. Chem. Soc.* **2005**, *127*, 3456.
- [38] A. L. Smeigh, J. E. Katz, B. S. Brunschwig, N. S. Lewis, J. K. McCusker, *J. Phys. Chem. C* **2008**, *112*, 12065.
- [39] S. Y. Huang, G. Schlichthorl, A. J. Nozik, M. Gratzel, A. J. Frank, *J. Phys. Chem. B* **1997**, *101*, 2576.
- [40] V. P. S. Perera, K. Tennakone, *Sol. Energy Mater. Sol. Cells* **2003**, *79*, 249.
- [41] B. Li, L. D. Wang, B. N. Kang, P. Wang, Y. Qiu, *Sol. Energy Mater. Sol. Cells* **2006**, *90*, 549.
- [42] G. Boschloo, L. Haggman, A. Hagfeldt, *J. Phys. Chem. B* **2006**, *110*, 13144.
- [43] S. A. Haque, E. Palomares, X. P. Cigang, R. J., A. B. Holmes, D. J. R., *SPIE proceedings series* **2003**, *5215*, 9.
- [44] S. Södergren, A. Hagfeldt, J. Olsson, S. E. Lindquist, *J. Phys. Chem.* **1994**, *98*, 5552.
- [45] H. Paulsson, L. Kloo, A. Hagfeldt, G. Boschloo, *J. Electroanalyt. Chem.* **2006**, *586*, 56.
- [46] M. Gratzel, *Inorg. Chem.* **2005**, *44*, 6841.
- [47] W. M. Campbell, K. W. Jolley, P. Wagner, K. Wagner, P. J. Walsh, K. C. Gordon, L. Schmidt-Mende, M. K. Nazeeruddin, Q. Wang, M. Gratzel, D. L. Officer, *J. Phys. Chem. C* **2007**, *111*, 11760.
- [48] S. Ito, S. M. Zakeeruddin, R. Humphry-Baker, P. Liska, R. Charvet, P. Comte, M. K. Nazeeruddin, P. Pechy, M. Takata, H. Miura, S. Uchida, M. Gratzel, *Adv. Mater.* **2006**, *18*, 1202.
- [49] S. Erten, S. Alp, S. Icli, *J. Photochem. Photobiol., A* **2005**, *175*, 214.
- [50] V. Balzani, P. Ceroni, A. Juris, M. Venturi, S. Campagna, F. Puntoriero, S. Serroni, *Coord. Chem. Rev.* **2001**, *219*, 545.
- [51] M. K. Nazeeruddin, P. Pechy, M. Gratzel, *Chem. Commun.* **1997**, 1705.
- [52] M. K. Nazeeruddin, C. Klein, P. Liska, M. Gratzel, *Coord. Chem. Rev.* **2005**, *249*, 1460.
- [53] L. Schmidt-Mende, S. M. Zakeeruddin, M. Gratzel, *Appl. Phys. Lett.* **2005**, *86*.
- [54] M. Gratzel, *Comptes Rendus Chimie* **2006**, *9*, 578.
- [55] J. R. Durrant, S. A. Haque, E. Palomares, *Chem. Commun.* **2006**, 3279.
- [56] G. Sauve, M. E. Cass, G. Coia, S. J. Doig, I. Laueremann, K. E. Pomykal, N. S. Lewis, *J. Phys. Chem. B* **2000**, *104*, 6821.
- [57] S. Ferrere, *Chem. Mater.* **2000**, *12*, 1083.
- [58] S. Ferrere, *Inorg. Chim. Acta* **2002**, *329*, 79.
- [59] S. Ferrere, B. A. Gregg, *J. Am. Chem. Soc.* **1998**, *120*, 843.
- [60] T. Bessho, E. C. Constable, M. Graetzel, A. Hernandez-Redondo, C. E. Housecroft, W. Kylberg, M. K. Nazeeruddin, M. Neuburger, S. Schaffner, *Chem. Commun.* **2008**, 3717.
- [61] A. Kay, R. Humphrybaker, M. Gratzel, *J. Phys. Chem.* **1994**, *98*, 952.
- [62] H. Tributsch, *Coord. Chem. Rev.* **2004**, *248*, 1511.
- [63] E. Figgemeier, *Intern. J. Photoenergy* **2004**, *6*, 127.
- [64] K. Tennakone, G. Kumara, A. R. Kumarasinghe, K. G. U. Wijayantha, P. M. Sirimanne, *Semicond. Sci. Technol.* **1995**, *10*, 1689.
- [65] Q. B. Meng, K. Takahashi, X. T. Zhang, I. Sutanto, T. N. Rao, O. Sato, A. Fujishima, H. Watanabe, T. Nakamori, M. Urugami, *Langmuir* **2003**, *19*, 3572.

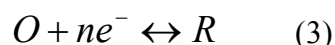
- [66] P. M. Sirimanne, T. Jeranko, P. Bogdanoff, S. Fiechter, H. Tributsch, *Semicond. Sci. Technol.* **2003**, *18*, 708.
- [67] B. O'Regan, F. Lenzmann, R. Muis, J. Wienke, *Chem. Mater.* **2002**, *14*, 5023.
- [68] J. Kruger, R. Plass, M. Gratzel, H. J. Matthieu, *Appl. Phys. Lett.* **2002**, *81*, 367.
- [69] H. J. Snaith, L. Schmidt-Mende, *Adv. Mater.* **2007**, *19*, 3187.
- [70] A. F. Nogueira, C. Longo, M. A. De Paoli, *Coord. Chem. Rev.* **2004**, *248*, 1455.
- [71] B. C. O'Regan, F. Lenzmann, *J. Phys. Chem. B* **2004**, *108*, 4342.
- [72] K. Murakoshi, R. Kogure, Y. Wada, S. Yanagida, *Chem. Lett.* **1997**, 471.
- [73] Y. Saito, T. Azechi, T. Kitamura, Y. Hasegawa, Y. Wada, S. Yanagida, *Coord. Chem. Rev.* **2004**, *248*, 1469.
- [74] Y. Saito, N. Fukuri, R. Senadeera, T. Kitamura, Y. Wada, S. Yanagida, *Electrochem. Commun.* **2004**, *6*, 71.
- [75] Y. K. Kim, Y. E. Sung, J. B. Xia, M. Lira-Cantu, N. Masaki, S. Yanagida, *J. Photochem. Photobiol., A* **2008**, *193*, 77.
- [76] P. Wachter, M. Zistler, C. Schreiner, M. Berginc, U. O. Krasovec, D. Gerhard, P. Wasserscheid, A. Hinsch, H. J. Gores, *J. Photochem. Photobiol., A* **2008**, *197*, 25.
- [77] P. Wang, S. M. Zakeeruddin, M. Gratzel, W. Kantlehner, J. Mezger, E. V. Stoyanov, O. Scherr, *Appl. Phys. A: Mater. Sci. Process.* **2004**, *79*, 73.
- [78] C. K. Chiang, C. R. Fincher, Y. W. Park, A. J. Heeger, H. Shirakawa, E. J. Louis, S. C. Gau, A. G. Macdiarmid, *Phys. Rev. Lett.* **1977**, *39*, 1098.
- [79] A. Pron, P. Rannou, *Prog. Polym. Sci.* **2002**, *27*, 135.
- [80] A. F. Diaz, J. Crowley, J. Bargon, G. P. Gardini, J. B. Torrance, *J. Electroanal. Chem.* **1981**, *121*, 355.
- [81] G. Louarn, M. Trznadel, J. P. Buisson, J. Laska, A. Pron, M. Lapkowski, S. Lefrant, *J. Phys. Chem.* **1996**, *100*, 12532.
- [82] P. Audebert, P. Hapiot, *Synth. Met.* **1995**, *75*, 95.
- [83] G. Tourillon, F. Garnier, *J. Electroanal. Chem.* **1982**, *135*, 173.
- [84] M. R. Andersson, D. Selse, M. Berggren, H. Jarvinen, T. Hjertberg, O. Inganas, O. Wennerstrom, J. E. Osterholm, *Macromolecules* **1994**, *27*, 6503.
- [85] R. John, G. G. Wallace, *J. Electroanal. Chem.* **1991**, *306*, 157.
- [86] W. Yen, C. C. Chan, T. Jing, G. W. Jang, K. F. Hsueh, *Chem. Mater.* **1991**, *3*, 888.
- [87] B. AG, in *Eur. Patent 339 340*, **1988**.
- [88] S. Akoudad, J. Roncali, *Synth. Met.* **1998**, *93*, 111.
- [89] L. Groenendaal, F. Jonas, D. Freitag, H. Pielartzik, J. R. Reynolds, *Adv. Mater.* **2000**, *12*, 481.
- [90] S. Kirchmeyer, K. Reuter, *J. Mater. Chem.* **2005**, *15*, 2077.
- [91] A. J. Heeger, *Angew. Chem., Int. Ed. Engl.* **2001**, *40*, 2591.
- [92] E. Johansson, S. Larsson, *Synth. Met.* **2004**, *144*, 183.
- [93] P. G. Pickup, *J. Mater. Chem.* **1999**, *9*, 1641.
- [94] J. Hjelm, R. W. Handel, A. Hagfeldt, E. C. Constable, C. E. Housecroft, R. J. Forster, *J. Phys. Chem. B* **2003**, *107*, 10431.
- [95] C. G. Cameron, B. J. MacLean, P. G. Pickup, *Macromol. Symp.* **2003**, *196*, 165.
- [96] C. E. D. Chidsey, R. W. Murray, *J. Phys. Chem.* **1986**, *90*, 1479.
- [97] P. G. Pickup, W. Kutner, C. R. Leidner, R. W. Murray, *J. Am. Chem. Soc.* **1984**, *106*, 1991.

- [98] Y. Saito, T. Azechi, T. Kitamura, Y. Hasegawa, Y. Wada, S. Yanagida, *Coordination Chemistry Reviews* **2004**, *248*, 1469.
- [99] Y. Saito, T. Kitamura, Y. Wada, S. Yanagida, *Synth. Met.* **2002**, *131*, 185.
- [100] Y. Saito, N. Fukuri, R. Senadeera, T. Kitamura, Y. Wada, S. Yanagida, *Electrochemistry Communications* **2004**, *6*, 71.
- [101] N. Fukuri, Y. Saito, W. Kubo, G. K. R. Senadeera, T. Kitamura, Y. Wada, S. Yanagida, *J. Electrochem. Soc.* **2004**, *151*, A1745.
- [102] S. Asavapiriyant, G. K. Chandler, G. A. Gunawardena, D. Pletcher, *J. Electroanal. Chem.* **1984**, *177*, 245.
- [103] A. J. Mozer, Y. Wada, K. J. Jiang, N. Masaki, S. Yanagida, S. N. Mori, *Appl. Phys. Lett.* **2006**, *89*.
- [104] K. J. Jiang, N. Masaki, J. B. Xia, S. Noda, S. Yanagida, *Chem. Commun.* **2006**, 2460.
- [105] Y. K. Kim, Y. E. Sung, J. B. Xia, M. Lira-Cantu, N. Masaki, S. Yanagida, *Journal of Photochemistry and Photobiology a-Chemistry* **2008**, *193*, 77.
- [106] J. B. Xia, N. Masaki, M. Lira-Cantu, Y. Kim, K. J. Jiang, S. Yanagida, *J. Am. Chem. Soc.* **2008**, *130*, 1258.
- [107] H. S. Kim, C. C. Wamser, *Photochem. Photobiol. Sci* **2006**, *5*, 955.
- [108] A. Juris, V. Balzani, F. Barigelletti, S. Campagna, P. Belser, A. Vonzelewsky, *Coord. Chem. Rev.* **1988**, *84*, 85.
- [109] V. Balzani, G. Bergamini, S. Campagna, F. Puntoriero, in *Photochemistry and Photophysics of Coordination Compounds I, Vol. 280*, Springer-Verlag Berlin, Berlin, **2007**, pp. 1.
- [110] M. Gerloch, E. C. Constable, *Transition metal chemistry*, VCH, **1994**.
- [111] E. A. Medlycott, G. S. Hanan, *Coord. Chem. Rev.* **2006**, *250*, 1763.
- [112] Tokeltak.Ne, Hemingwa.Re, A. J. Bard, *J. Am. Chem. Soc.* **1973**, *95*, 6582.
- [113] A. A. Vlcek, E. S. Dodsworth, W. J. Pietro, A. B. P. Lever, *Inorg. Chem.* **1995**, *34*, 1906.
- [114] A. A. Vlcek, *Electrochim. Acta* **1968**, *13*, 1063.
- [115] C. E. Housecroft, A. G. Sharpe, *Inorganic Chemistry*, 3 ed., Prentice Hall, **2007**.
- [116] E. C. Constable, A. W. T. Cargill-Thompson, D. A. Tocher, M. A. M. Daniels, *New J. Chem.* **1992**, *16*, 855.
- [117] E. C. Constable, A. W. T. Cargill-Thompson, *J. Chem. Soc., Dalton Trans.* **1994**, 1409.
- [118] J. Chambers, B. Eaves, D. Parker, R. Claxton, P. S. Ray, S. J. Slattery, *Inorg. Chim. Acta* **2006**, *359*, 2400.
- [119] C. Houamer-Rassin, E. Blart, P. Buvat, F. Odobel, *J. Photochem. Photobiol., A* **2007**, *186*, 135.
- [120] M. Beley, D. Delabouglise, G. Houppy, J. Husson, J. P. Petit, *Inorg. Chim. Acta* **2005**, *358*, 3075.

## 2 Experimental methods

### 2.1 General electrochemistry<sup>[1-3]\*</sup>

Electrochemistry is the study of the relationship between chemical change and electrical work. The fundamental laws of electrochemistry can be divided into two main parts, a thermodynamic and a kinetic part. The most common situation in electrochemistry is a dissolved molecule in an electrolyte together with a solid electrode. The chemical and electrical processes that occur at the electrode/solution interface when there is charge transfer between the phases, is then studied. The simplest example is electron transfer between the oxidized species, O and the reduced species, R, when they are both in solution.



In figure 2.1 are the different steps in a general electrode reaction that describe what happens to the reaction in equation 3.  $O_{\text{bulk}}$  is the oxidised species in the bulk solution that is reduced at the electrode surface to the reduced form R. After mass transport through the solution to an area near the electrode surface the species undergoes reduction (or oxidation). Adsorption to the surface before the electron transfer may occur. The reduction process takes place at the cathode while oxidations take place at the anode. With the metal complexes in this work, the oxidations and reductions are in most cases not accompanied by adsorption. \*Most of the information on electrochemistry in this chapter is from references [1-3].

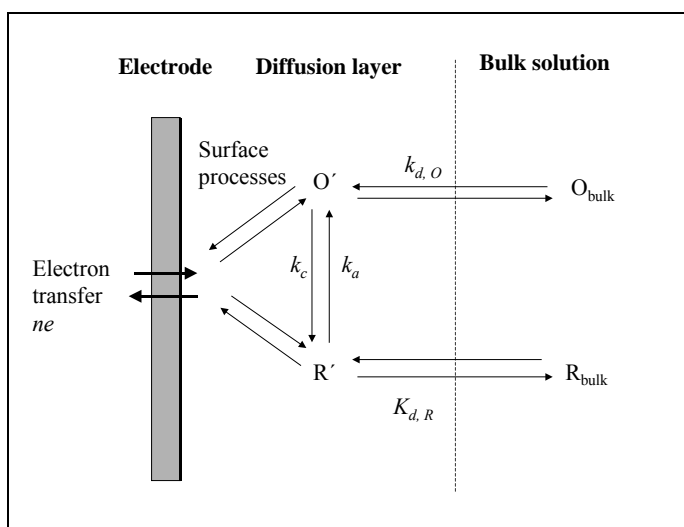


**Figure 2.1** Pathway of a general electrode reaction.

### Thermodynamics in electrochemistry

The Nernst equation relates the equilibrium potential at the electrode surface to the activities of the reduced and oxidized species.

$$E_{eq} = E^0 + \frac{RT}{nF} \ln \frac{a_O}{a_R} \quad (4)$$

$E^0$  is the standard electrode potential of the electrochemical reaction when the species have equal activities,  $R$  is the gas constant,  $T$  the temperature (in most cases room temperature),  $n$  the amount of electrons in the process,  $F$  is Faradys constant and  $a_O$  and  $a_R$  are the activity constants. In most experiments it is convenient to measure in concentration rather than activities and so the formal potential,  $E^{0'}$ , is more commonly used. The formal potential is defined in equation 5 and it leads to  $a=c\gamma$  where  $\gamma$  is the activity coefficient. One of the advantages of using concentration in place of activity is that the current is directly proportional to the concentration.

$$E^{0'} = E^0 + \frac{RT}{nF} \ln \frac{\gamma_O}{\gamma_R} \quad (5)$$

In a galvanic cell where two half-cells are connected, the cell potential can be expressed as in equation 6.

$$E_{cell} = E_{Cathode}^0 - E_{Anode}^0 \quad (6)$$

The electromotive force present in a galvanic cell is directly connected to thermodynamics by equation 7. In equation 7, the maximum amount of work that is available, without resistance losses in the circuit, can be calculated.

$$\Delta G = -nFE \quad (7)$$

The free energy can in turn be related to the enthalpy, entropy and the electron transfer rate constant of the reaction by (8):

$$\Delta G = -nFE = \Delta H^0 - T\Delta S^0 = -RT \ln K \quad (8)$$

### The solid-liquid interface

The potential-current behaviour of an electrode in electrochemistry can in theory be an ideally polarizable electrode (IPE) or an ideally non-polarizable electrode (IPNE). In an IPE there should be no charge transfer upon change of potential but a real electrode cannot behave as an IPE over the whole range of a solvent potential window. Certain combinations of electrode and solvent can however approach this

behaviour. Such an electrode is called the working- or indicator- electrode. The opposite, an IPNE, where the potential remains constant during passage of current, is also only possible within a limited potential window. Such an electrode is used as a reference electrode.

Since no charge can pass through the IPE when a potential is applied, the interface between the electrode and the liquid acts as a parallel plate capacitor (where two metal plates with opposing charge have a dielectric material sandwiched between them). When the electrode is immersed into an electrolyte and there is an applied potential, there will be a net charge on the surface that will attract charge of opposite polarity. The whole collection of dipoles and ions that amass at the electrode-electrolyte interface is called the electrochemical double layer. Figure 2.2 shows the concepts of the double layer with an inner layer of specifically adsorbed solvent molecules and ions from the electrolyte salt. This layer is often referred to as the Helmholtz layer. The solvated ions in the diffuse layer only interact with the electrode through long-range electrostatic forces and are usually described as non-specifically adsorbed.

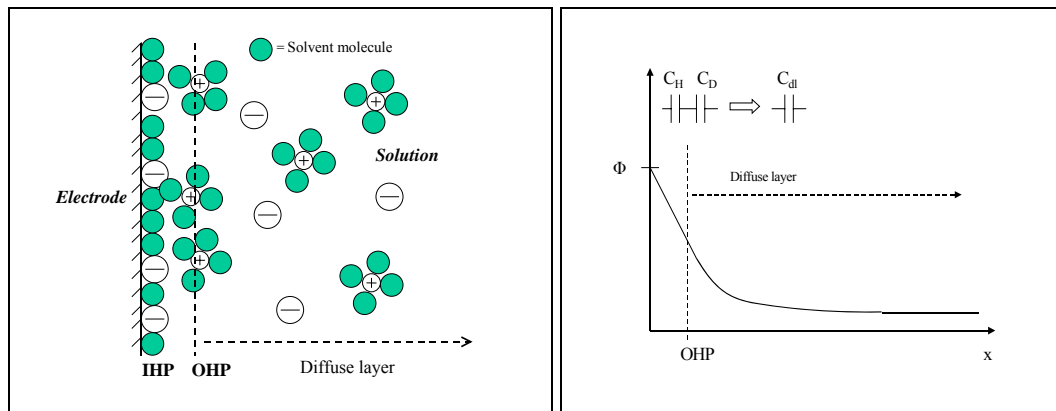


**Figure 2.2** A schematic picture of the Helmholtz double layer under conditions where the electrode adsorbs anions. IHP is the *inner Helmholtz plane* and OHP is the *outer Helmholtz plane*. In the box to the right presents the Gouy-Chapman–Stern model where the double layer is modelled with capacitors in series for the Helmholtz layer ( $C_H$ ) and the diffuse layer ( $C_D$ ) to combine into the total capacitance ( $C_{dl}$ ).

The Gouy-Chapman model relates the potential decay between the electrode surface and the bulk solution through equation 9.

$$\phi = \phi_0 e^{-\alpha x} \quad (9)$$

In equation 9,  $x$  is the distance and  $\kappa$  is regarded as the reciprocal of the characteristic thickness of the diffuse layer via equation 10,

$$\kappa = \left( \frac{2n^0 z^2 e^2}{\epsilon \epsilon_0 kT} \right)^{1/2} \quad (10)$$

where  $n^0$  is the number concentration of each ion in the bulk,  $z$  is the magnitude of the charge of each ion,  $\epsilon_0$  is the permittivity of free space,  $\epsilon$  is the dielectric constant and  $k_B$  is the Boltzmann constant. In a 0.1 M solution of a 1:1 electrolyte in acetonitrile ( $\epsilon = 37.5$ ) the diffuse thickness is 13.8 Å. The thickness is a lot thinner than the diffusion layers for typical faradic experiments and electrochemically deposited polymers. It becomes thicker with lower concentrations of electrolyte.

### Microscopic models of charge transfer

To model the charge transfer at the electrode and understand what affects the rates of electron-transfer, there are a few models that have been developed for heterogeneous electron transfer. A useful distinction is dividing reactions into *outer-sphere* and *inner-sphere* electron-transfer reactions. Heterogenous *inner-sphere* reactions require a close contact between the electrode and the reactant and involve specific adsorption of the species. Reduction of oxygen in water and the oxidation of hydrogen at Pt are *inner-sphere* reactions. In *Outer-sphere* reactions the reactants and products do not interact strongly with the electrode surface and are generally at a distance of at least a solvent layer from the electrode.

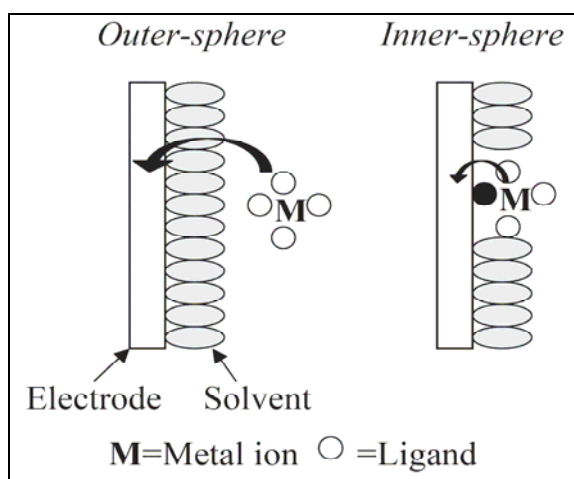


**Figure 2.3** The outer-sphere and inner-sphere reactions of a heterogeneous reaction where metal complexes in solution are oxidized at an electrode. The darker ligand of the inner-sphere reaction indicates a specifically adsorbed ligand that acts as a bridge with the metal center.



The classic Marcus theory, that aims to explain rates of electron transfer between a donor and an acceptor, is the most widely used theory for electron transfer reactions. Most microscopic models, including the Marcus theory, have the aspect of assuming that the reactants and products do not change their configurations during the actual act of transfer. This comes from the Franck-Condon principle that says the nuclear positions do not change on the scale of electronic transitions. It is also necessary the transition be isoenergetic as it is radiationless. Marcus theory is built on the Arrhenius equation (equation 11) with a frequency factor ( $\nu$ ) and an exponential with activation energy ( $E_A$ ), gas constant ( $R$ ) and temperature ( $T$ ).

$$k_{ET} = \nu \exp(-E_A / RT) \quad (11)$$

For the activation energy a reorganisation energy ( $\lambda$ ) along with the standard free energy of the reaction ( $\Delta G^0$ ) are determining as shown in equation 12.

$$E_A = \frac{(\Delta G^0 + \lambda)^2}{4\lambda} \quad (12)$$

The reorganisation energy can be divided into two parts, an *outer-sphere component* ( $\lambda_{\text{out}}$ ) that take into account the reorganisation of solvent and surrounding media, and an *inner-sphere component* ( $\lambda_{\text{in}}$ ), which is a measure of the geometrical changes (bond angles and lengths) of the reactant as it reaches the product state. Metal complexes, like the iron and ruthenium bis-terpyridine ones in this work, undergo very small or negligible changes to the geometry as they are reduced and oxidised around their redox potential, therefore the more important contribution to the reorganisation component is  $\lambda_{\text{out}}$  for these compounds. The frequency factor,  $\nu$ , is a measure of the electronic coupling between the states and is affected by the distance. The Marcus theory thus says that a nuclear term and an electronic term govern the rate of electron transfer. The nuclear term is dependent on solvent, temperature and thermodynamic conditions while the electronic part is distance dependent.

Other models have been made of the electron transfer. Among others, Gerischer contributed to models that were based on distribution of states to describe the processes at the electrode with a species in solution. The electrode, which is a conductor, will have a certain Fermi energy. The Fermi level ( $E_F$ ) is the maximum energy that the electrons in the electrode can have when the material is at absolute zero temperature. The filling of states at thermal equilibrium is described by the Fermi function,  $f(E)$ , as shown in equation 13.

$$f(E) = \{1 + \exp[(E - E_F) / kT]\}^{-1} \quad (13)$$

Equation 13 is the probability that an electron occupies the state  $E$ .  $T$  is temperature in degrees Kelvin and  $k$  is Boltzmann's constant. From equation 13 it can be seen that electron occupancy is close to unity below and close to zero above  $E_F$ . There is a band of states around  $E_F$  of about  $4kT$  with intermediate occupation (about 100 mV at 25°C). To reduce a species, the  $E_F$  of the electrode needs to be moved to a higher energy than the LUMO and to oxidise it to a lower energy than the species HOMO (see figure 2.4). The energies of the corresponding orbital the O and R species together make up a pair with a redox potential. It should be noted that both the redox potential and Fermi level correspond to the electrochemical potentials of the electrons and only differ in terminology.<sup>[4]</sup>

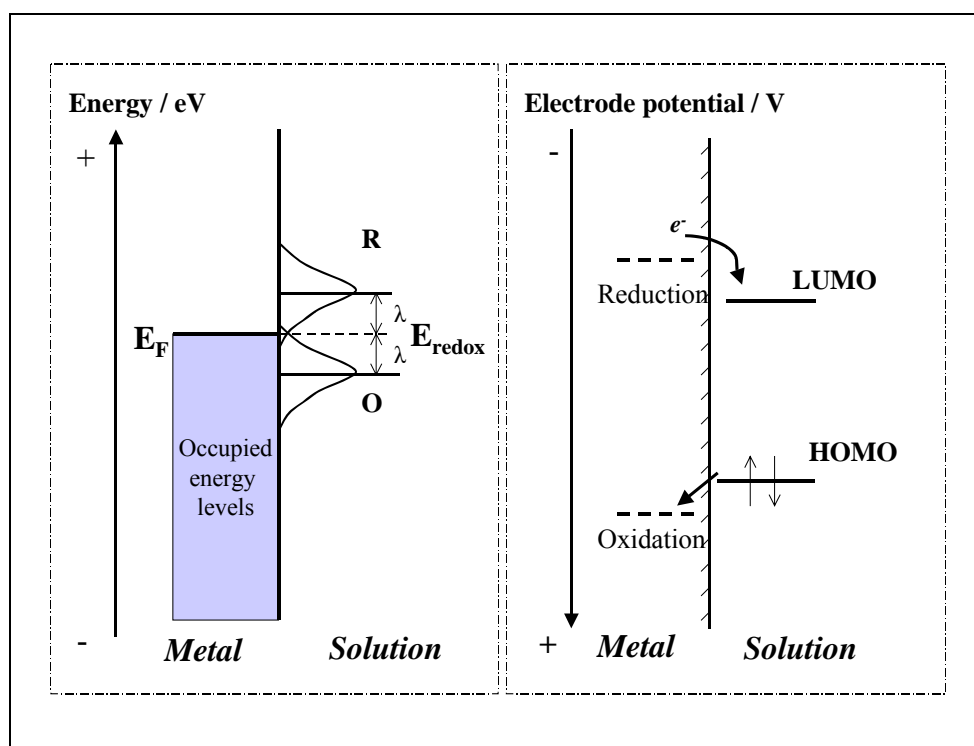


**Figure 2.4** Energy and potential levels of the electrode/electrolyte interface.

In figure 2.4, diagrams of the energy levels of the electrode (a conductor) are related to the energy levels of the redox potential of the molecule in solution. On the left side the electrode potential is applied at the redox potential of the molecule and  $\lambda$  is the reorganization energy. The reduced and oxidised molecules polarize the solvent in different ways and this is the main reason for the reorganization energy. As was mentioned, the ruthenium terpyridine complexes in solution have mainly a  $\lambda_{out}$

contribution to the reorganization energy for the reversible redox processes. The metal-based redox process has only a small reorganization energy.

### Mass transport

Mass transport of material in a solution occurs from differences in electrical or chemical potential between two locations or from movement of a volume through the solution. The three modes are divided into:

*Migration*: Movement of a charged body in a gradient of electrical potential.

*Diffusion*: Movement of a species in a gradient of chemical potential (*i.e.*, a concentration gradient).

*Convection*: Caused by stirring or hydrodynamic transport. The convection can be natural (caused by density gradients) or forced (stirring). Stagnant regions, laminar flow and turbulent flow characterize it.

The mass transfer to the electrode is governed by the *Nernst-Planck equation*, which is written for 1 dimensional mass transfer along the x-axis as in equation 14.

$$J_i(x) = -D_i \frac{\delta C_i(x)}{\delta x} - \frac{z_i F}{RT} D_i C_i \frac{\delta \phi(x)}{\delta x} + C_i v(x) \quad (14)$$

$J_i(x)$  is the flux of species  $i$  at a distance  $x$  from the surface,  $D_i$  is the diffusion coefficient ( $\text{cm}^2\text{s}^{-1}$ ),  $\delta C_i(x)/\delta x$  is the concentration gradient,  $\delta \phi(x)/\delta x$  is the potential gradient,  $z_i$  and  $C_i$  are the charge and concentration of species  $i$  and  $v(x)$  is the velocity of the transport along the axis. The three terms on the right hand side represent the contributions of diffusion, migration and convection, respectively, to the flux. To simplify the mathematical models of the current flux in electrochemical measurements, one or two of the contributions are usually made negligible. The main equations in dynamic electrochemistry (when working with transient potentials) assume that migration and convection are suppressed. Preventing stirring and vibrations in the electrochemical cell minimizes convection. Adding an excess of supporting electrolyte (about 100 times the species concentration) leads to most of the current (through the bulk solution) being transported by the electrolyte ions and only a very small part (<1%) of the flux of the species is by migration. Eliminating these two contribution leads to an expression for the transport only by diffusion. *Fick's second law* describes the change in concentration of species  $i$  with time. The formulation in equation 15 is general for all geometries of electrode.

$$\frac{\delta C_i}{\delta t} = D_i \nabla^2 C_i \quad (15)$$

In equation 15,  $\nabla^2$  is the laplacian operator and different geometries give different forms of the operator. The transport of the material that will react at the electrode is determining the current flux and is thus very important in formulating equations for the currents. As well as the geometric parameters, there are different boundary conditions for different voltammetric experiments that will give different equations. In this work macro-disk electrode and ultra-microelectrode geometries will be important.

### Dynamic electrochemistry

Combining the kinetic and thermodynamic parts for the rate of electron transfer at an electrode/solution interface for a reduction of an oxidised species to its reduced form give an expression for the net current density that is referred to as the Butler-Volmer equation (equation 16).

$$j = j_a - j_c = j_0 \left[ \exp \frac{(1-\alpha)n_a F \eta}{RT} - \exp \frac{-\alpha n_a F \eta}{RT} \right] \quad (16)$$

In equation 16 the current density ( $j$ ) is determined by the transfer coefficient ( $\alpha$ ) and the over-potential ( $\eta$ ) that is applied. This relation is very important as it, or a variation of it, is used to treat almost every problem concerning heterogenous kinetics. The overpotential,  $\eta = E - E^0$ , is an important term in electrochemistry and refers to the additional potential, beyond the thermodynamical potential, needed to induce a reaction at a certain rate. This differs for different electrode materials. For example mercury is said to have a high overpotential for hydrogen evolution.

The concentration gradients in an electrode process are created by the consumption of electroactive species at the electrode surface. An interesting situation is when  $(\delta c / \delta t) = 0$ . This is a so-called steady-state response with the current not changing with time. This can be achieved with *e.g.* microelectrodes.

The measurement of the current after a step in the potential is applied is called chronoamperometry. The step is from a potential where no species reacts to one where all the species that reach the electrode react. For a planar electrode (with *Fick's*

second law for this geometry) the current response with time is described by the Cottrell equation:

$$i(t) = \frac{nFAD_o^{1/2}C_o^*}{\pi^{1/2}t^{1/2}} \quad (17)$$

The current  $i$  is measured as a function of the electrode area  $A$ , bulk concentration  $C_o$  of the species and the diffusion constant  $D_o$ . The Cottrell equation is important in pulse voltammetry where voltage steps are applied. Another application is using it to evaluate the diffusion constant,  $D_o$ , if the other parameters are known, by plotting  $i$  with  $t^{-1/2}$ .

In chronocoulometry the total amount of charge that is passed is measured with time according to the integrated Cottrell equation:

$$Q = \frac{2nFAD_o^{1/2}C_o^*t^{1/2}}{\pi^{1/2}} + Q_{dl} + Q_{ads} \quad (18)$$

There will be contribution from the double layer ( $Q_{dl}$ ) and from any molecules that might be adsorbed ( $Q_{ads}$ ) at the applied voltage. An advantage of coulometry over amperometry is that it is less disturbed by random electric noise. Also it is easier to separate the effect of charging at the electrode from the faradic charge of interest.

### Faradic and non-faradic processes

When a charge is transferred across the electrode/liquid interface the process is called a faradic process. Oxidation and reduction are faradic and result in anodic and cathodic currents respectively. Non-faradic currents arise from adsorption, desorptions and restructuring of the surface. In an electrochemical measurement the double layer of the indicator electrode needs to be charged before the applied potential is reached. This means that the applied potential cannot be reached instantaneously. By considering a potential step to the IPE as an RC circuit problem where the resistance ( $R_s$ ) is in series with the capacitance ( $C_d$ ), the charging current can be described by equation 19. Equation 19 relates the behaviour of the charging current with time after the potential step ( $\Delta E$ ).

$$i_c = \frac{\Delta E}{R_s} e^{-t/(R_s C_d)} \quad (19)$$

When the potential is changed continuously in a linear fashion, as in cyclic voltammetry, there is a charging current ( $i_c$ ) that depends on the rate of the changing potential ( $v$ ). The relation is described in equation 20.

$$i_c = \nu C_{dl} \quad (20)$$

In figure 2.5 a cyclic voltammogram of a metal complex adsorbed to a surface shows faradic current for the oxidation and reduction of the metal center and non-faradic current elsewhere. To measure fast faradic processes it is necessary to minimise the product  $R_S C_{dl}$ , also referred to as the *cell time constant*. This can be done using high concentration of electrolyte for a low series resistance ( $R_S$ ) or a microelectrode for lower double layer capacitance ( $C_{dl}$ ).

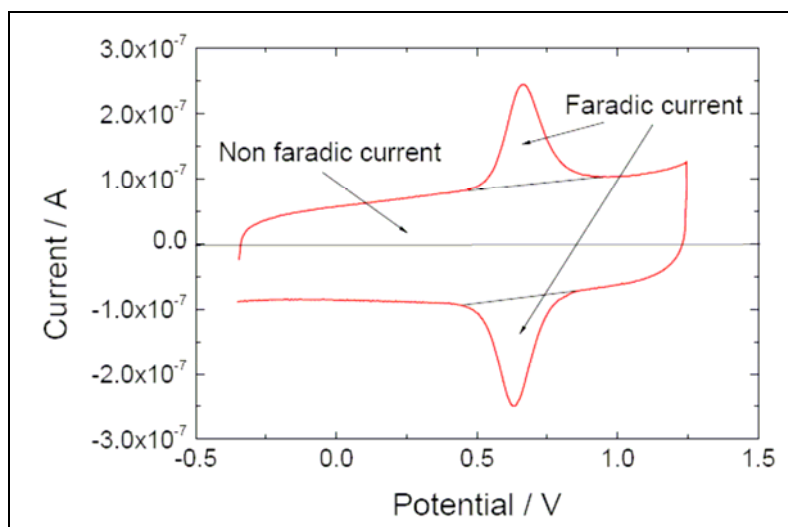


**Figure 2.5** CV of surface bound Os complex on a Pt microelectrode. The  $\text{Os}^{2+}/\text{Os}^{3+}$  process is visible as the faradic current.

### Electrochemical techniques

In electro-analysis there are essentially three types of measurements. In (a) conductimetric measurements the solution resistance is measured to obtain information on ion concentrations. Potentiometric (b) measurements measure the equilibrium potentials of an electrode against a reference using a high impedance voltmeter. By tailor making the electrode material to be more sensitive to certain ions the technique can be selective. A common example is the pH meter with a particular sensitivity to protons. Amperometry and voltammetry (c) both use a potentiostat to control the potential of the electrode and measure the current. In amperometry a fixed potential is set and the resulting current is measured. As will be discussed, steady state convection allows a constant current to be measured if the concentration is uniform. A steady state current is measured in flowing streams of electrolyte or by microelectrodes and can be useful when probing how concentrations change with time. Voltammetry is a

technique that is said to be dynamic because the applied potential is changed while a current is measured.

The electrochemical methods in this work are voltammetric/amperometric. There are different waveforms of the applied potentials in voltammetry. Linear sweep methods have an applied potential that is changed in a linear way, although modern digitally controlled potentiostats apply many small steps to approximate the analogue linear potential change. One of the most informative techniques is cyclic voltammetry (CV), where the potential is cycled between two potentials. Kinetic and thermodynamic information on the electroactive species can be gathered from the current and potential of the peaks.

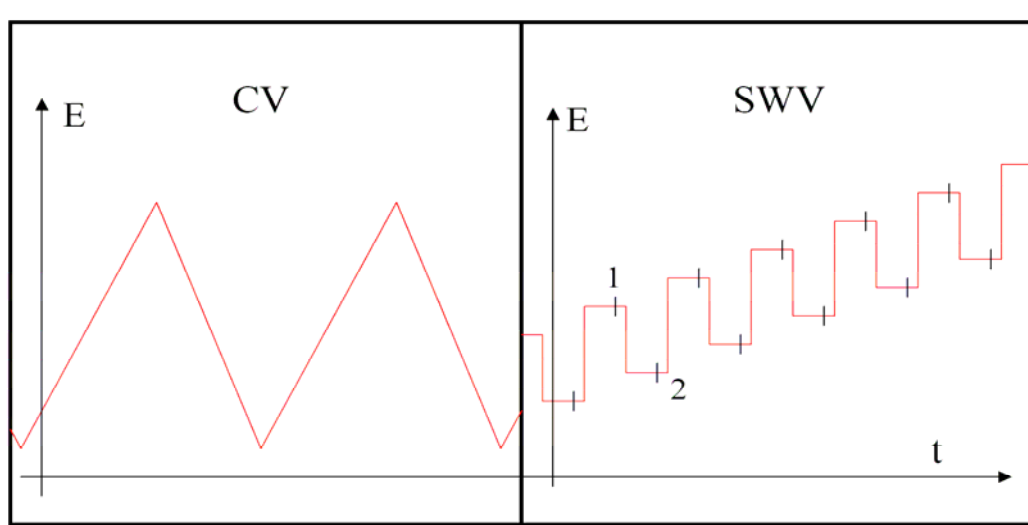


**Figure 2.6** The potential functions for cyclic- and square wave-voltammograms with time. Points 1 and 2 in the SWV represent the points where the current is measured.

### Cyclic voltammetry

In cyclic voltammetry (CV) the current is measured constantly during the cycling of voltage. In Figure 2.6 the potential function with time is shown. The technique is very useful to gather information on the redox chemistry of the species. A typical CV of a reversible process is shown in figure 2.7A with some of the important values marked. The reversibility of the compounds can be diagnosed from a CV and thermodynamic data as seen in points 1 and 2 below.

1. Peak potential separation should be close to  $59/n$  mV for a reversible process.
2. The ratio of peak current values of the anodic and cathodic ( $i_a/i_c$ ) should equal 1.

In contrast to the non-faradic current (equation 20), the faradic current is proportional to the square root of the scan rate through the Randles-Sevcik equation

$$i_p = (2.69 \times 10^5) n^{3/2} A D_o^{1/2} C_o^* \nu^{1/2} \quad (21)$$

In equation 21 the current is at 25°C with  $A$  in  $\text{cm}^2$ ,  $D_o$  is  $\text{cm}^2\text{s}^{-1}$ ,  $C_o^*$  in  $\text{molcm}^{-3}$  and  $\nu^{1/2}$  in  $\text{V/s}$ . By measuring the peak current at different scan rates, values for the diffusion constant can be calculated.

When the species has formed a monolayer on the electrode surface and is measured upon in an electrolyte without other electroactive substances, the current response will look like the curve in figure 2.7B. Ideally, for an adsorbed reversible nernstian species, the peak potentials for the anodic and cathodic currents will have no separation and the peak current will be proportional to the scan rate and surface coverage as in equation 22. The total width at half-height,  $\Delta E_{p,1/2}$ , of the cathodic or anodic waves should be 90.6 mV (at 25°C, equation 23).

$$i_p = (9.39 \times 10^5) n^2 \nu A \Gamma_o^* \quad (22)$$

$$\Delta E_{p,1/2} = 3.53 \frac{RT}{nF} = \frac{90.6}{n} \text{mV} \quad (23)$$

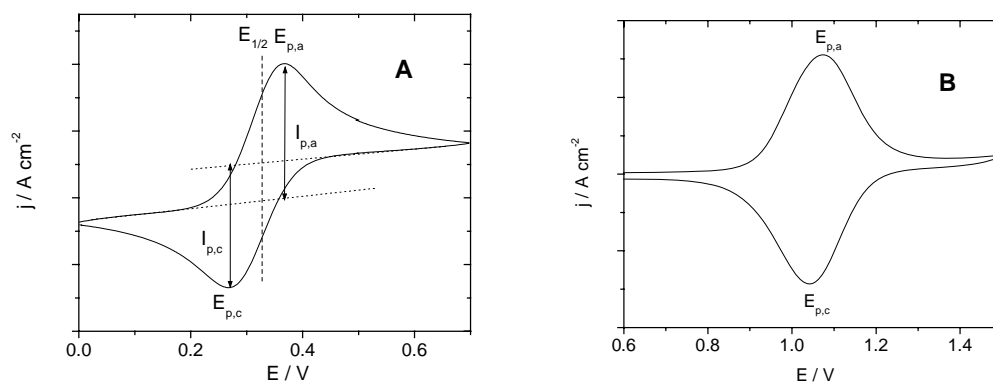


**Figure 2.7** Close to ideal CV for a reversible process of a molecule in solution (A). Close to ideal CV for a reversible process of a molecule adsorbed to a surface (B). The locations of some of the relevant values are marked.



### Pulse voltammetry

In pulse techniques the applied potential is changed in steps or pulses. Differential pulse voltammetry (DPV) and square wave voltammetry (SWV) are useful when overlapping peaks in linear sweep measurements need to be better resolved and the charging current reduced.

In figure 2.6, the SWV measurements are done at points 1 and 2 of the potential-time function and the difference between the forward current (1) and reverse currents (2) is plotted. In this way the  $E_p$  will appear between the  $E_{p,a}$  and  $E_{p,c}$  (formal redox potential) and the charging current can be discriminated.

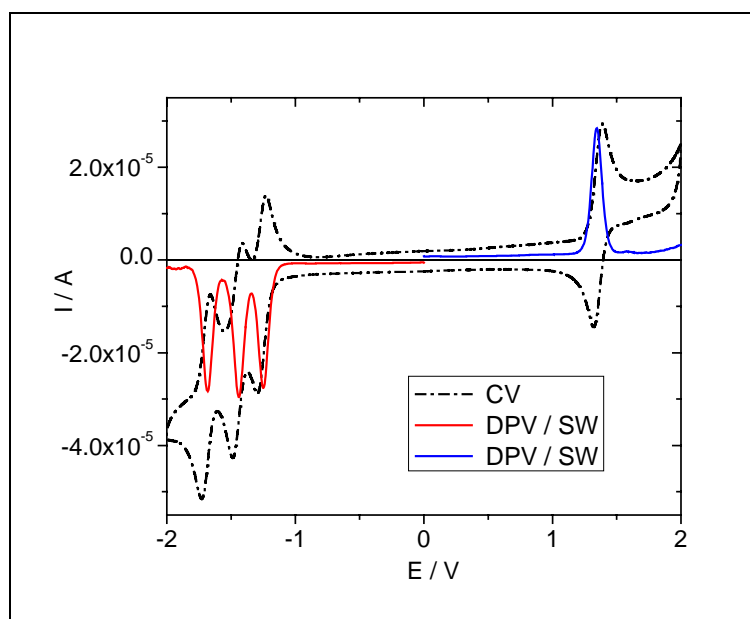


**Figure 2.8** CV of  $[\text{Ru}(\text{bipy})_3]$  in MeCN overlapped with the SW voltammograms (blue and red).

In figure 2.8 a cyclic voltammogram of  $[\text{Ru}(\text{bipy})_3]^{2+}$  in acetonitrile is overlapped with SW voltammograms in the same solution. The lack of charging current enhances the sensitivity of the measurement and peaks that may be difficult to resolve in a CV are more visible in SWV and DPV. As previously stated, the  $E_p$  of the SWV is very close to the formal potential / halfway potential of the CV. In DPV the peak potential for a reversible system is shifted according to equation 24.

$$E_p = E_{1/2} - \frac{\Delta E}{2} \quad (24)$$

In SWV the potential is shifted in the scan direction by an amount of  $|\Delta E/2|$  from  $E_p$  of the DPV. The value of  $\Delta E$  is usually 10-20 mV for DPV so the shift for SWV is smaller than for DPV and not more than about 10 mV. SWV can be much faster than

DPV due to the DPV technique needing time for the capacitive currents to dissipate before measuring the potential.<sup>[2]</sup>

### Solvents

Acetonitrile (MeCN) was used for most voltammetric measurements in solution. It is an aprotic solvent and has a moderate dielectric constant ( $\epsilon = 36$ ) to dissolve supporting electrolyte salts like TBAPF<sub>6</sub> and LiClO<sub>4</sub>. The potential window with dry solvent and glassy carbon or platinum electrodes is about + 2.3 to - 2.5 V (vs. SCE).

Dichloromethane (DCM) is a suitable solvent to stabilise radical cations. Radical cations are sensitive to nucleophilic attack and solvents that contain donor electron pairs are good nucleophiles. Hence, solvents that are Lewis bases destabilise radical cations.<sup>[3]</sup> DCM has negligible Lewis base properties. In chapter 3 the electrochemistry of complexes in DCM with ligands that can be oxidised to radical cations show electro-deposition and possible polymerisation while the same experiments in MeCN do not lead to electro-deposition.

3-Methoxypropionitrile (3-MPN) was used for some of the photo-oxidation experiments as it has a relatively high vapour pressure allowing non-enclosed experiments to be made with a not too high rate of evaporation.

There may be slight differences in oxidation / reduction potentials of organic molecules to radicals depending on solvent. The reduction potential relative to a reference electrode can be expressed as in equation 25 where  $EA$  is the electron affinity of the neutral molecule in the gaseous state and  $\Delta G_{solv}$  the difference in free energy of solvation of the neutral molecule ( $R$ ) and its' radical anion ( $R^{\cdot-}$ ) ( $\Delta G_{solv} = \Delta G_R - \Delta G_{R^{\cdot-}}$ ).  $K$  is a constant.

$$E_{1/2} = EA + \Delta G_{solv} - K \quad (25)$$

The Born theory (equation 26) relates the Gibbs energy of solvation to the charge, size and the dielectric constant ( $\epsilon_r$ ) of the solvent. The change of  $\Delta G_{solv}$  for the neutral molecule is negligible because no strong charge-dipole interactions are expected and thus the changes in  $\Delta G_{solv}$  are dominated by the solvation energy of the radical anion. This also holds for radical cations.

$$\Delta G_{solv} = \frac{Z_i^2 e^2 N_A}{8\pi\epsilon_0 r_i} \left( 1 - \frac{1}{\epsilon_r} \right) \quad (26)$$

## Potentials

The reference electrode that was used in the solution electrochemistry was the silver wire, a quasi-reference electrode, with added ferrocene as an internal reference. For some of the experiments that needed a fixed potential the  $\text{Ag}/\text{Ag}^+$  reference was used. To avoid liquid junction potentials and unwanted water contamination in electrochemical experiments, organic solvents were used instead of water in the  $\text{Ag}/\text{Ag}^+$  reference-electrode. To work in organic solvents  $\text{AgNO}_3$  salt was used. Reference-electrodes with 3-MPN and MeCN were prepared.

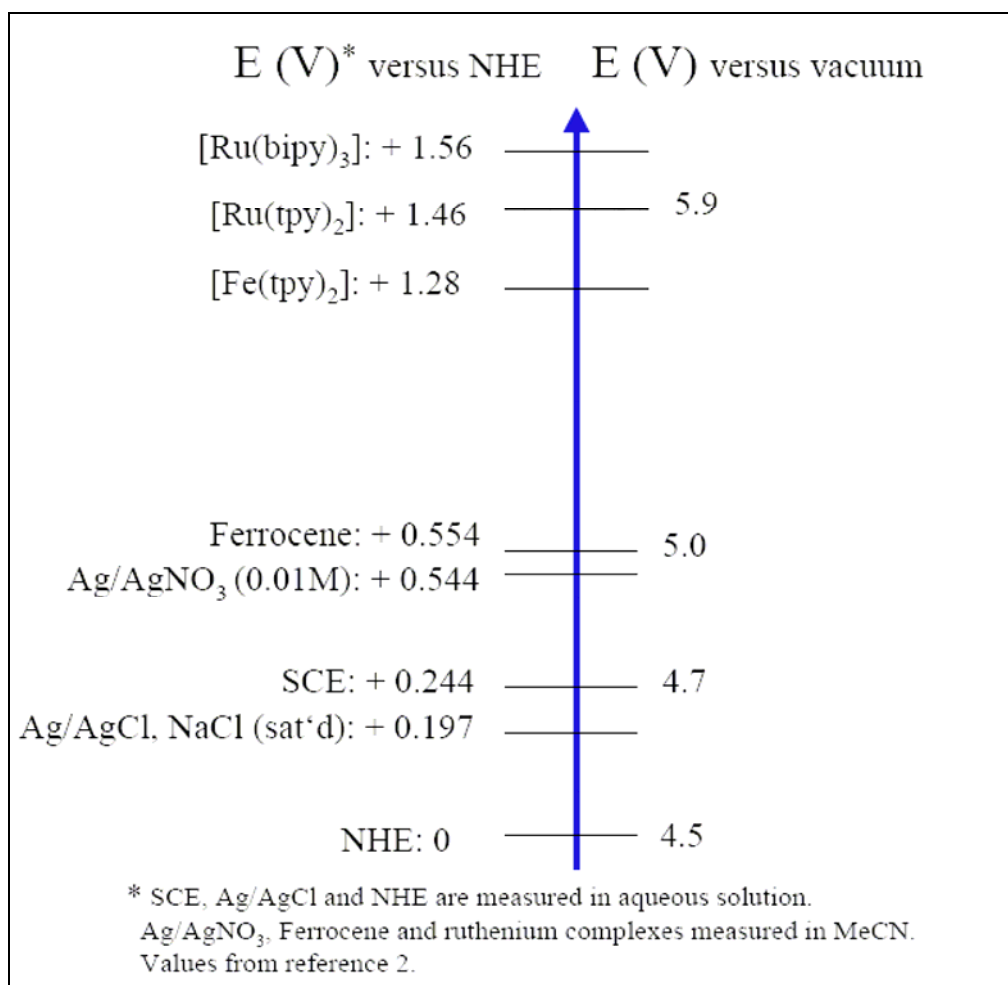


**Figure 2.9** Some potentials that are pertinent to this work with their relative values.<sup>[1]</sup>

In figure 2.9 the different reference electrode potentials are compared. On the right side are the absolute potentials (i.e., vs. the potential of a free electron in vacuum) for some of the compounds. The work functions for semi-conductors and metals are usually quoted at their absolute potential and when comparing it can be practical to use this value. The absolute potential of the NHE can be estimated at  $4.5 \pm 0.1$  V, which is based on certain extrathermodynamic assumptions, such as the amount of

energy involved in moving a proton from the gas phase into an aqueous solution.<sup>[1]</sup> With this value, the standard potentials of other redox couples and reference electrodes can be expressed on the absolute scale.

### Experimental set-up

In figure 2.10 the typical three-electrode set-up for the voltammetric experiments. The potential is measured between the reference and the working electrodes. The current is transported between the working and auxiliary electrodes by ionic transport.

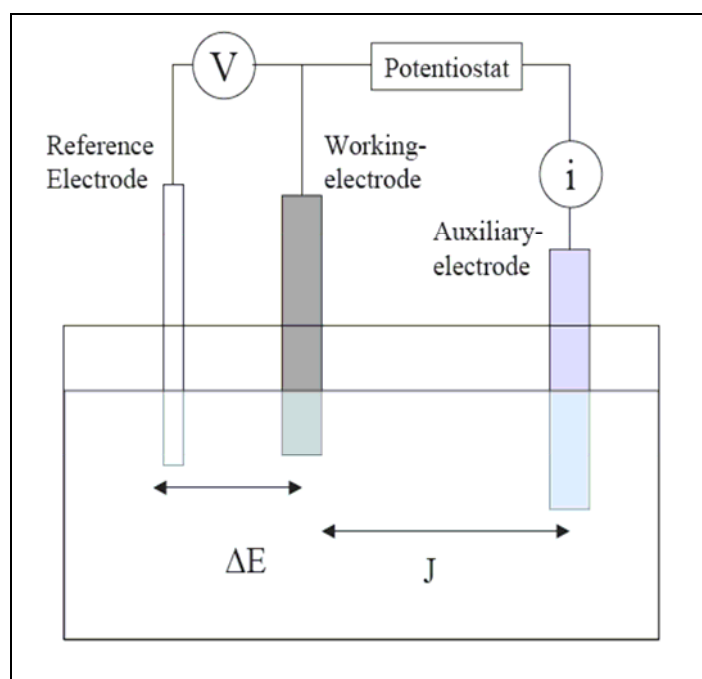


**Figure 2.10** A three-electrode-setup connected to a potentiostat with the electrodes in a cell.

### Experimental details

Electrochemical measurements were performed with an Eco Chemie Autolab PGSTAT 30 system using glassy carbon or platinum working and platinum auxiliary electrodes with a silver wire as quasi-reference; the working electrode was polished with aluminium oxide powder (0.3 micrometer) before use; purified  $\text{CH}_3\text{CN}$  (Fluka) was used as solvent and 0.1 M  $[\text{nBu}_4\text{N}][\text{PF}_6]$  as supporting electrolyte. Potentials are quoted versus the ferrocene/ferrocenium couple ( $\text{Fc}/\text{Fc}^+ = 0.0 \text{ V}$ ), and all potentials were referenced to internal ferrocene added at the end of each experiment.

## 2.2 Scanning Probe Electrochemistry

### 2.2.1 Scanning Electrochemical Microscopy (SECM)

Scanning electrochemical microscopy (SECM) was born from two techniques in the early 1980's when both Scanning Tunneling Microscopy and the ultra microelectrode (UME) were introduced.<sup>[1, 5, 6]</sup> After an initial period with few publications when the theory was established there has been an explosion in papers related to SECM in the last 10 years. The SECM allows one to control a microelectrode in 3-dimensions with sub micrometer precision often in relation to a surface. CH Instruments commercial versions have a minimum spatial resolution of 1.6 nm.

The UME is complimented with a counter electrode, reference electrode and, if needed, a second working electrode to bias the substrate. To monitor the microelectrode tip and position in relation to the surface a microscope video camera is connected. Figure 2.11 illustrates the SECM set-up used in the work presented here.

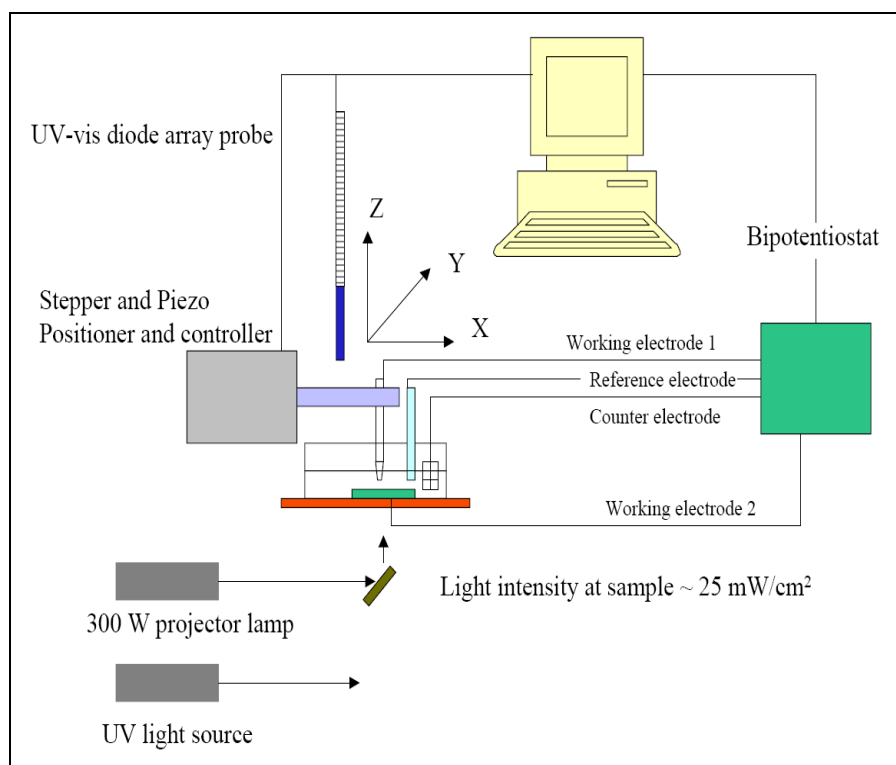


**Figure 2.11** Schematic picture of SECM set-up.

### Microelectrodes (UME)<sup>[1]</sup>

Electrodes with dimensions smaller than 10 $\mu\text{m}$  were developed in the late 1970's and went under the name ultramicroelectrodes (UME). The definition of a microelectrode is a diameter of less than 100 $\mu\text{m}$ . The microelectrodes used in this work were 10 $\mu\text{m}$  and 25 $\mu\text{m}$  in diameter.

In contrast to the semi-infinite current that is measured in voltammetry at a disk electrode with millimetre diameter, the current at a microelectrode can reach a steady state current very rapidly (within 10ms). This allows a constant current to be measured according to equation 27. At scan rates low enough, a CV with a UME results in a sigmoidal curve shapes for reversible metal complexes and steady state currents for the +II and +III species.

$$i_{ss} = 4nFD_oC_o^*r_o \quad (27)$$

In equation 27 the current is in amperes,  $n$  is the number of electrons in the process,  $F$  is Faradys constant,  $D_o$  the diffusion constant,  $C_o^*$  the bulk concentration and  $r_o$  the radius of the electrode. The  $O$  is added to highlight that it is for the oxidised or reduced form, which depends on whether the current is anodic or cathodic.

### Measurements

There are two main forms of operation that have been developed for the SECM. When close (within a few tip radii) to a surface that is much larger than the diameter of the electrode, the anodic or cathodic current that is generated from probing a species (e.g. an oxidising potential to probe the reduced form) will be perturbed by two effects. The first is the blocking of the species by the surface, which will decrease the current. This may be counteracted by a surface that can regenerate the species that is being probed (e.g. the oxidised form is reduced by the surface) and an increase in the current is observed. These phenomena are used in positive and negative *feedback mode* and was first developed by Bard *et al.*<sup>[7, 8]</sup> Using the *feedback mode*, conductivity can be estimated by the measurements described below. It is also possible to work in *collection mode* where the electrode is held close to the substrate at a potential where electroactive products produced at the substrate are detected at the tip. This mode is used in the PECM measurements described further below.

### Approach curve measurements

In the *feedback mode* of the SECM, the UME can be approached towards a surface at the same time as it is probing an electroactive species. Using the ferrocinium/ferrocene ( $\text{Fc}^+/\text{Fc}$ ) redox couple in the measurement, as a redox mediator, is common because it is a reasonably inert redox couple.<sup>[9-12]</sup> Applying, for example, a potential to the UME that will oxidise the ferrocene produces a steady-state current that can be monitored. The local concentration of ferrocene and ferrocinium will be perturbed close to the UME tip. The bulk part of the surface under investigation has a surface potential ( $E_{bulk}$ ) that is poised by the relative concentrations of oxidised (O) and reduced (R) species in the bulk solution. A potential dependent model that was proposed by Whitworth *et al.*<sup>[13]</sup> uses the potential differences that arise directly beneath the UME tip in predicting the conductivity. A local change in redox concentration close to the surface will set up a potential difference ( $\Delta E$ ) between this area and the bulk surface.

$$\Delta E = E_{bulk} - E_s \quad (28)$$

In equation 29 the local potential at the film/solution boundary  $E_s$  is given by the Nernstian equation for a reversible one-electron (or hole) transfer process:

$$E_s = E_s^{0'} + \frac{RT}{F} \ln \left( \frac{C_{Ox,int}}{C_{Red,int}} \right) \quad (29)$$

where  $E_s^{0'}$  is the formal of the redox couple. The potential difference defined in equation 28 affects the current at the UME by influencing the first-order potential dependent rate constant,  $k$ , of the electron transfer at the film/solution interface:

$$k = k' \exp(-\alpha F \Delta E / RT) \quad (30)$$

The change in current at the UME is then proportional to the rate constant  $k$  and the concentration of reduced species at the interface compared to the initial concentration. The current measured by the UME tip consists of one component due to hindered diffusion of Red ( $i_{hind}$ ) and one due to the current through the film ( $i_{film}$ ). Current from the hindered diffusion is known and  $i_{film}$  is readily deduced ( $i_{tip} = i_{hind} - i_{film}$ ). The resistance (inverse of conductivity) of the film can then be determined via a relationship from the gradient of a plot of  $(E_s - E_s^{0'})$  versus  $i_{film}$ .<sup>[13]</sup> If the corresponding conductivity cell geometry is known, the conductivity can then be calculated with the obtained resistance.

The basic approach curve experiment is explained in figure 2.12 where it can be seen that the steady-state current needs a bulk solution around it to “feed” the current. Blocking the surface in any way will perturb the current.

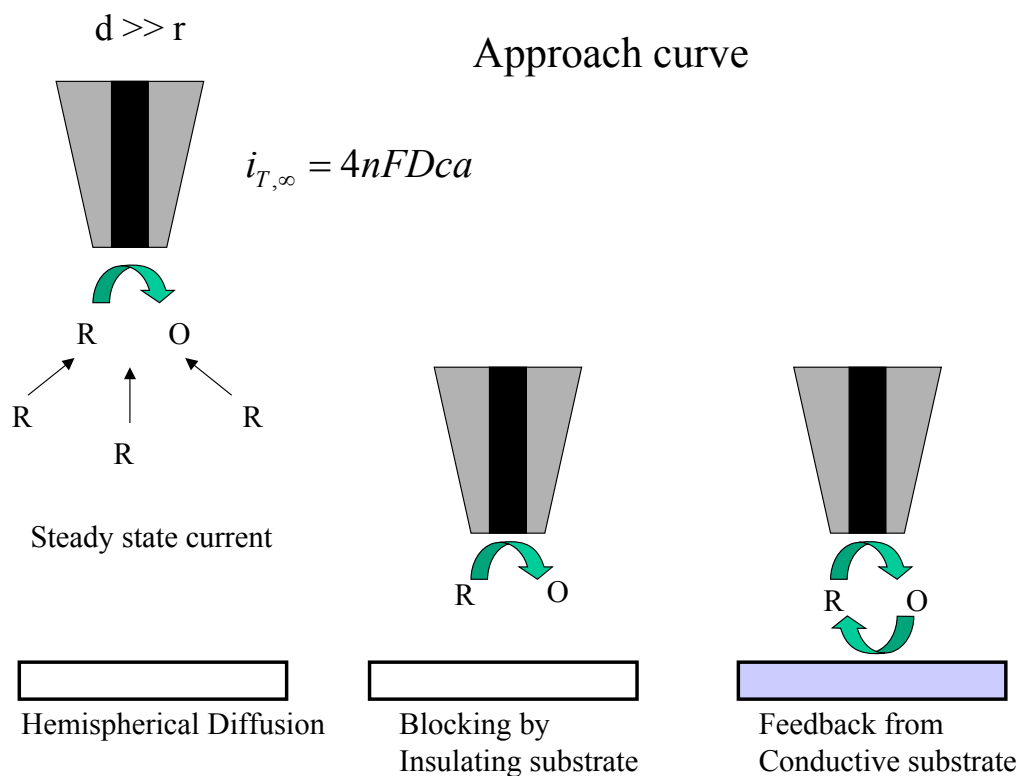


**Figure 2.12** Depiction of the different processes during an approach curve experiment. The platinum wire inside the electrode can be seen as the black rectangle. Figure reproduced from <sup>[1]</sup>.

When the UME approaches a surface, shown in figure 2.12, there are two outcomes. At a distance of a few radii (of the UME), the redox mediator can be blocked from diffusing in towards the electrode surface. This will diminish the current until it is zero when the electrode has reached the surface. If the surface can regenerate the reduced species there will be a feedback effect and the current may increase instead of dissipate as the UME tip approaches the surface. A conducting surface will give a clear increase of current but other less conducting surfaces will result in less dramatic increases. In figure 2.13 the theoretical curves for a perfectly conducting surface and a perfectly insulating surface are shown.<sup>[6]</sup> The curves are calculated by numerical approximation where only the normalised current (Tip current,  $I_{tip}$ , divided by current far from surface,  $i_0$ ) and the normalised distance (Tip distance,  $d$ , divided by electrode radius,  $a$ ) affect the current.<sup>[14]</sup> The model can be modified to include finite kinetics,



either reversible or irreversible, for heterogenous kinetics. The current will then be dependent on probing over-potential, diffusion constants of redox mediator and rate constants determined by the films resistance (or conductivity).

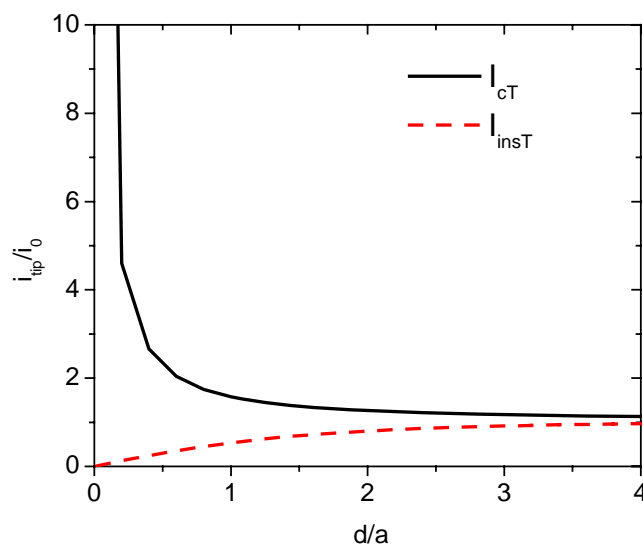


**Figure 2.13** Approach curve response for a perfectly conductive surface (black line,  $I_{cT}$ ) and for a perfectly insulating surface (red line,  $I_{insT}$ ). The curve for the insulating surface decreases to zero current while it increases to infinity for the conductive surface.

Conductivity measurements were used as one of the tools to characterise the different surfaces in this work. The electro-active polymers were probed when possible and the compact  $\text{TiO}_2$  under-layer was characterised by this technique to control how well it insulates. In figure 2.14 there is a schematic picture of how a surface with a monolayer of redox couples may transport charge laterally to compensate for the oxidation of surface bound molecules beneath the UME.<sup>[10, 15]</sup> In this example, the monolayer consists of a redox compound that can reduce oxidised  $[\text{Ru}(\text{terpy})_2]^{2+}$ . As will be seen in chapter 3, the monolayer could consist of linked  $[\text{Fe}(\text{terpy})_2]^{2+}$  complexes with the  $\text{Fe}^{+II}$  centres having a lower redox potential than the ruthenium redox mediator and may thus be able to reduce the oxidised ruthenium complex. In ideal conditions the approach curve measurement should be done for a homogeneous monolayer and exhibit relatively fast charge transport.<sup>[15]</sup> For measurement of a 2-D lateral charge transport the thickness of the film should be thin compared to the radius of the UME. This is in order to avoid polarisation in the z-direction and so that cross film conduction can be discriminated.

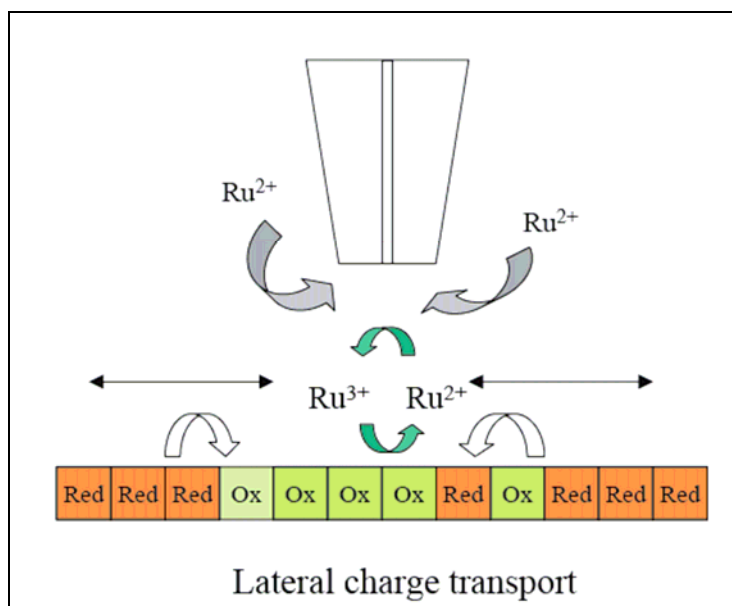


**Figure 2.14** A schematic figure of a monolayer of redox centers on a surface that may allow for charge transport via electron hopping between centers of different oxidation state. Reproduced from <sup>[15]</sup>.

### Experimental details

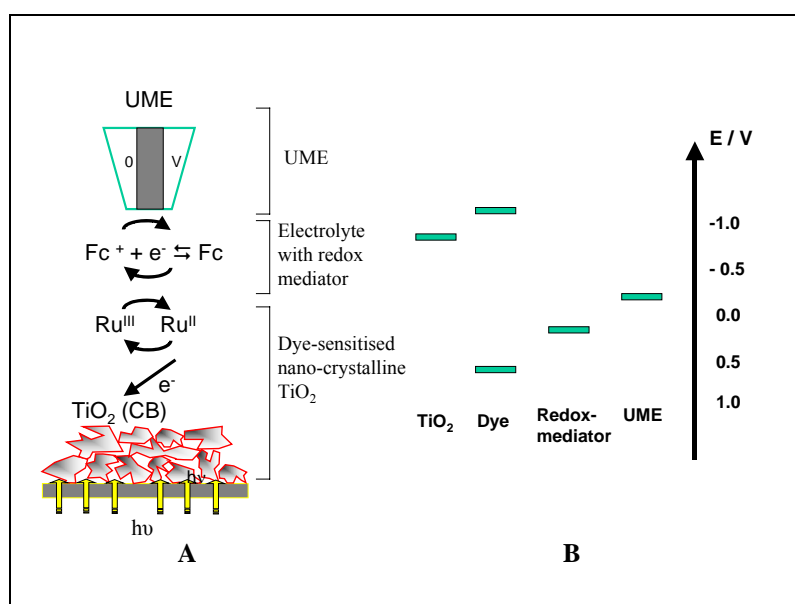
The instrument in this work is a CH instrument 900B. The electrodes are connected to a bipotentiostat with a current range of 1 pA to 10 mA and a stepper / piezo motor is used to control the UME.

The microelectrodes were prepared by first polishing with 0.3  $\mu\text{m}$   $\text{Al}_2\text{O}_3$  particles followed by sonication in deionised water for 10 minutes. The polished electrodes were electrochemically cleaned by cycling in 0.5 M  $\text{H}_2\text{SO}_4$  between potential limits chosen to first oxidize and then to reduce the surface of the platinum electrode. Excessive cycling was avoided in order to minimize surface roughening. The real, or microscopic, surface area of microelectrodes was found by calculating the charge under the oxide desorption peaks. Before removing the electrode from the cell, the potential was then held in the double layer region at a sufficiently negative value to ensure complete reduction of any surface oxide. Finally, the electrode was cycled between 0 and 0.9 V in 0.1 M  $\text{LiClO}_4$  until hydrogen desorption was complete. By dividing the geometric area of the electrode surface by the microscopic surface area, a value referred to the surface roughness factor was calculated. Typically the surface roughness factor was between 1.5 and 3.0.

## 2.2.2 Photo-Electrochemical Microscopy (PECM)

In this project the SECM set-up was used to study photo-electrochemical processes on surfaces. Mostly only the vertical distance above the surface (z-axis) was used in these measurements so the technique for this was designated as *Photo-Electrochemical Microscopy (PECM)*.

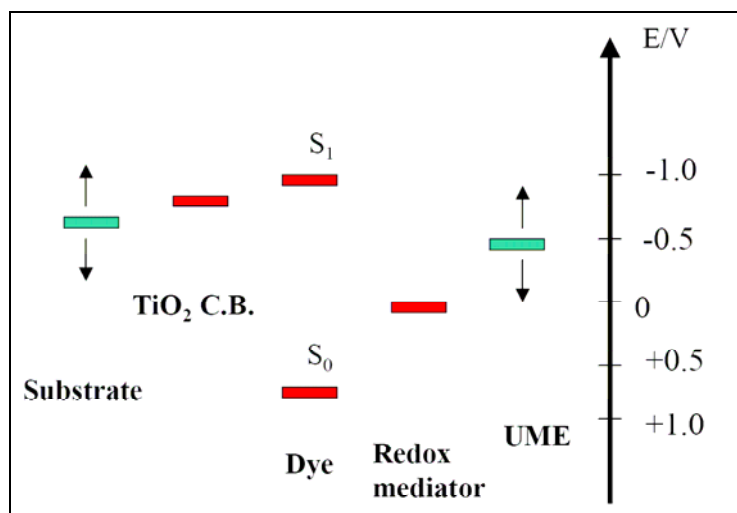
According to the energy scheme in scheme 2.1, illumination should trigger electron injection from the adsorbed dye into the  $\text{TiO}_2$  conduction band and leave the dye in an oxidised state. A suitable redox mediator then regenerates the dye. In most cases for the dye sensitised solar cell it is the  $\text{I}^-/\text{I}_3^-$  couple. Upon illumination  $\text{I}_3^-$  is produced when the excited dye oxidises  $\text{I}^-$  and is detected at the microelectrode as a cathodic current. The current is due to an applied potential to the UME that has a negative potential relative to  $\text{I}^-/\text{I}_3^-$  couple. Depending on the applied potential on the glass substrate of the  $\text{TiO}_2$  film the photocurrent changes. The  $\text{I}^-/\text{I}_3^-$  redox reactions consist of several different species but together result in a redox couple that can transport charge through the electrolyte.<sup>[16]</sup>



**Scheme 2.1** Working principles (A) and Energy levels (B) in the photoelectrochemical experiment.<sup>[9]</sup>

Schemes 2.1 and 2.2 describe the energy levels involved in the SECM measurements. It is possible to adjust the potentials of the substrate glass supporting the  $\text{TiO}_2$  and the platinum tip of the microelectrode. This allows one to measure the currents and potentials of the anode and cathode separately and simultaneously. By applying an

external potential to the substrate of the nc-TiO<sub>2</sub> at a value high (positive) enough, it is possible to assure complete separation of all charge carriers (in this case the majority carriers, electrons, and holes). At this potential the current under illumination will cease to increase with increasing external potential and only increase with increased photon flux.<sup>[17]</sup>



**Scheme 2.2** Energy levels of SECM set-up where substrate and UME potentials are variable.

In the PECM measurements both the dark current and the photo current will have absolute values. The relative current will be the addition of the two currents. In figure 2.15 the three different current values that the PECM measurement will process are pointed out. The blue line represents the current that is measured.

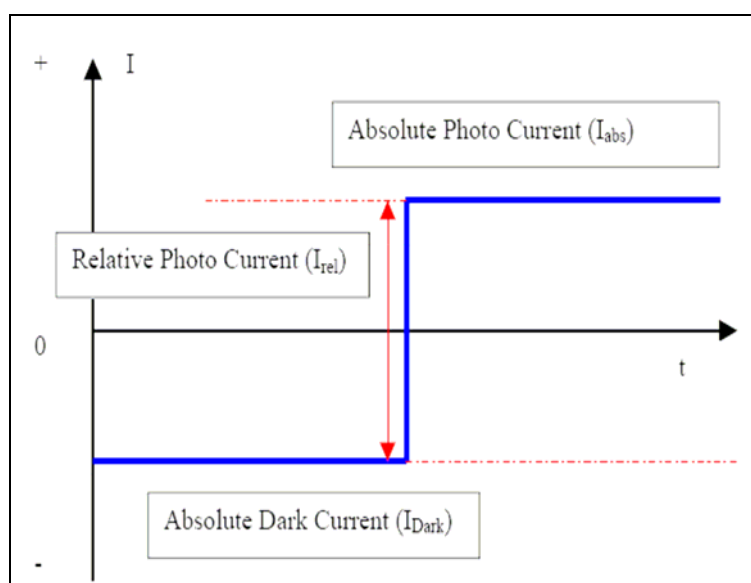


**Figure 2.15** The currents and their designations in a PECM measurement.

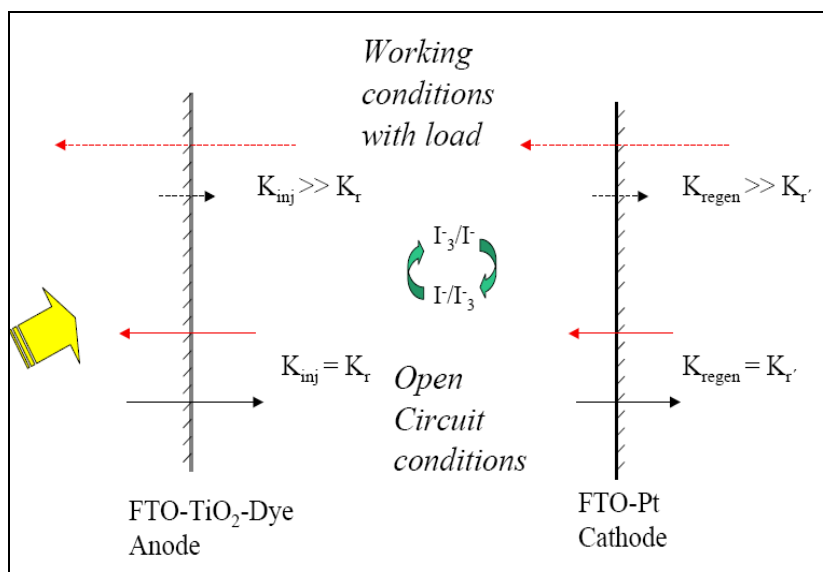


**Figure 2.16** Diagram showing the rates of electron injection and recombination.  $K_r$  and  $K_r'$  are recombination rates for the dark current while  $K_{inj}$  is the injection rate. The red arrows represent the processes where the anode and cathode titles are correct.

In figure 2.16, a conceptual diagram of the processes in the DNSC under working conditions, when there is a load connected to the electrodes, and under open circuit conditions where no net current flows and the voltage is at its maximum are depicted. As is seen in figures 2.16 and 2.17, under open circuit conditions, the rate constant of the electron injection and the rate of recombination are equal and the net current under illumination is 0. In the PECM the applied potentials of the FTO glass and the Pt-electrode can both be set to approximate these conditions by finding at what potential the current under illumination is 0.

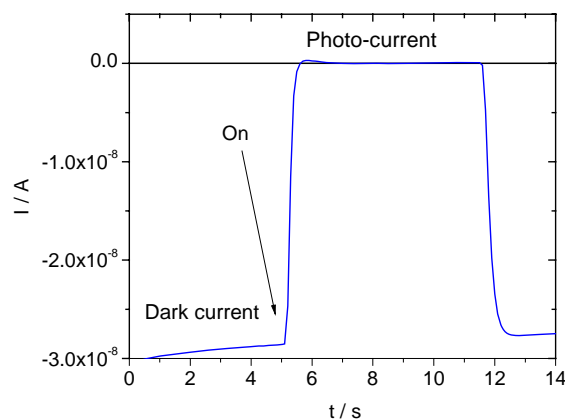


**Figure 2.17** An example of how the current response may look for a UME measurement.

## 2.3 Photovoltaic Measurements<sup>[18]\*</sup>

Photovoltaic cells convert the light they absorb to electrical energy. To measure the conversion efficiency, there are some standard techniques. Measuring the current voltage characteristics (I-V curve) upon illumination is the main characterisation of a solar cell.<sup>[18]</sup> In this case the light source is a constant white light that simulates solar light conditions e.g. from an ELH halogen lamp.<sup>[19]</sup> From an I-V measurement (see figure 2.18) the open circuit voltage ( $V_{OC}$ ) and the short circuit current ( $I_{SC}$ ) can be derived and a maximum power point can be found between the two. The overall efficiency ( $\eta_{global}$ ) can be calculated from equation 31.

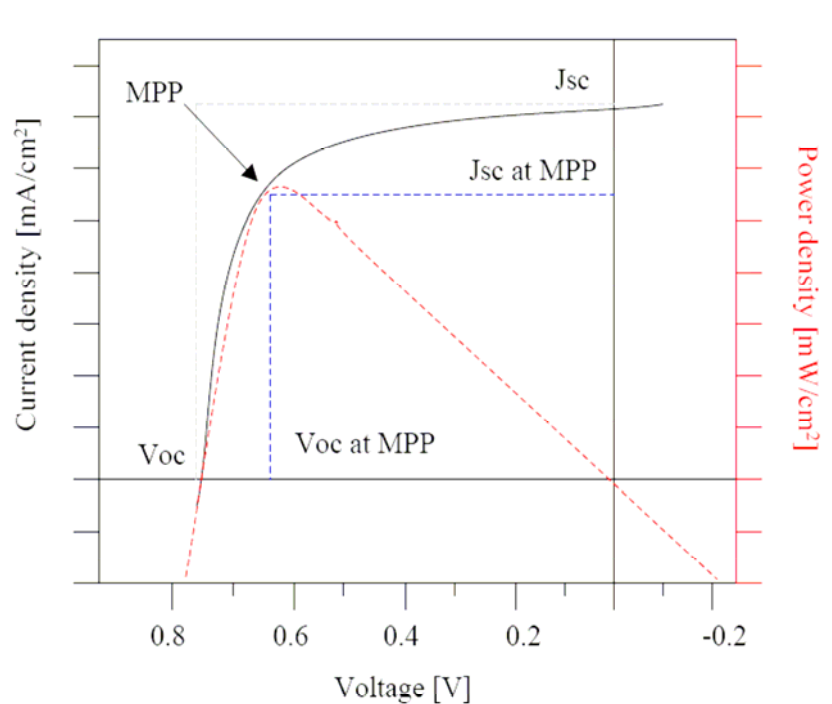


**Figure 2.18** The black line outlines a typical I-V curve where the maximum power point is used to calculate the global efficiency. The red dashed curve is the power density ( $\text{mWcm}^{-2}$ ) ( $P=I*V$ ). MPP=Maximum Power Point.

From measuring the current at different voltages of a photovoltaic device under illumination and obtaining an I-V curve as in figure 2.18, it is possible to calculate the global conversion efficiency of light to electric work from equation 31.

\*Much of the information on physics of photovoltaics is from reference [18].

$$\eta_{global} = \frac{i_{ph} \times V_{OC} \times ff}{I_S} \quad (31)$$

In equation 31 for global efficiency,  $i_{SC}$  (A) is the short circuit current,  $V_{OC}$  (V) is the open circuit voltage,  $ff$  is the fill factor and  $I_S$  (W) is the intensity of the impinging light. The Standard Test Condition (STC) for solar cells is the Air Mass 1.5 spectrum, and a normalised incident power density of  $1000 \text{ W m}^{-2}$  at a temperature of  $25^\circ\text{C}$ . The value of the Fillfactor ( $ff$ ) is a number between 0 and 1. For a perfect photovoltaic cell,  $ff=1$ , *i.e.* the I-V curve in figure 2.18 would have a rectangular shape and  $\text{MPP} = J_{sc} \times V_{oc}$ .

Photovoltaic devices can be compared to simple equivalent circuits like that in figure 2.19 in order to analyse their properties.<sup>[18]</sup> Included in the circuit are two parasitic resistances, a resistance in series ( $R_S$ ) and a shunt resistance ( $R_{SH}$ ) in parallel.  $R_S$  is the resistance of the materials and contacts, mainly the electrolyte, TCO substrate and the Pt counter electrode. The series resistance is particularly problematic at high current densities, for instance under concentrated light illumination.  $R_S$  should ideally be 0.  $R_{SH}$  arises from current leakage through the cell and around the edges of the device. It should be high for good photovoltaic performance. Equivalent circuits for the DNSC have been modified due to a slightly more complex system but for illustrating resistance effects figure 2.19 is sufficient.<sup>[20, 21]</sup> Figure 2.20 shows the effect on the I-V curves of  $R_S$  and  $R_{SH}$ .

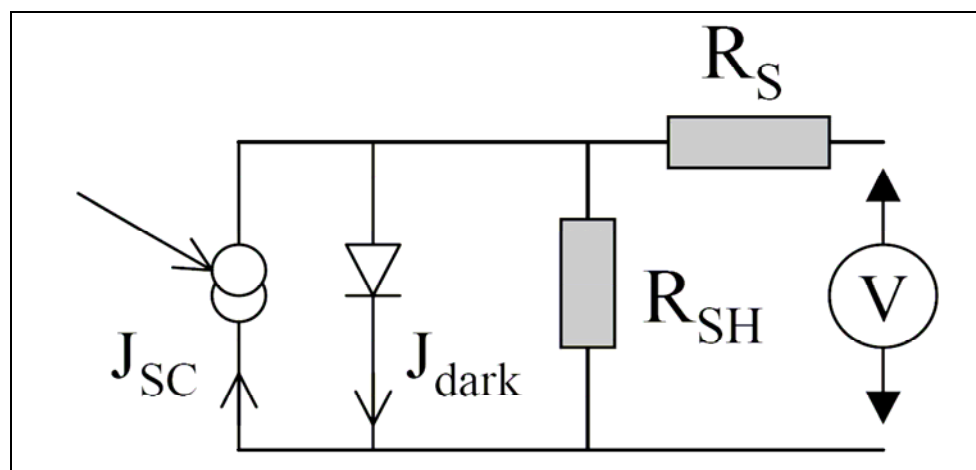


**Figure 2.19** Simple equivalent circuit model for conventional p-n junction photovoltaic cells. This model includes a series resistance ( $R_S$ ), a shunt resistance ( $R_{SH}$ ), a photocurrent ( $J_{SC}$ ) and a diode.<sup>[18, 21]</sup>

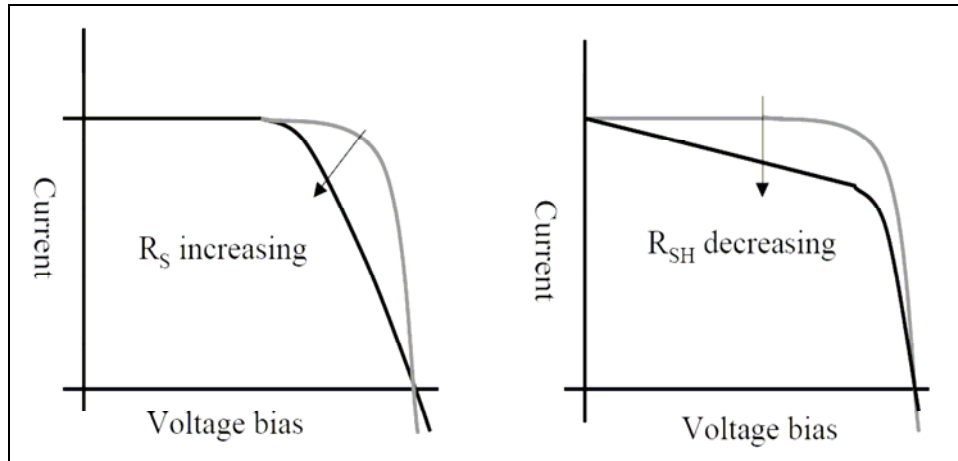


**Figure 2.20** Impact of  $R_S$  (left) and  $R_{SH}$  (right) on shape of I-V curves.<sup>[18]</sup>

Another technique that is often used is the measurement of incident photon to electron conversion efficiency (*IPCE*) where the photocurrent is measured in monochromatic light so that a spectrum of wavelengths can be measured. The *IPCE* is defined as the number of electrons generated by light in the external circuit divided by the number of incident photons. The *IPCE* ( $\lambda$ ) curve is defined in equation 32.

$$IPCE(\lambda) = \frac{1240 \times J_{SC}}{\lambda \phi} \quad (32)$$

$\lambda$  is the wavelength,  $J_{SC}$  is the short circuit photocurrent density ( $A\ cm^{-2}$ ) and  $\Phi$  is the incident radiative flux ( $W\ m^{-2}$ ). From the *IPCE* spectrum it is then possible to see the amount of photocurrent generated at different parts of the solar spectrum. Comparing with the intensity from the light source the result is given in percent. Another important parameter is the light harvesting efficiency (*LHE*) of the dye sensitised  $TiO_2$ . It is the proportion of light that is absorbed (between 0-1) at wavelength  $\lambda$ .

$$LHE(\lambda) = 1 - 10^{-A} \quad (33)$$

In equation 33,  $A$  is the absorbance of the film at wavelength  $\lambda$ . The *IPCE* and the *LHE* for photons of the wavelength  $\lambda$  are related by the equation below:

$$IPCE(\lambda) = LHE(\lambda) \phi_{inj} \eta_{coll} \quad (34)$$

where  $\Phi_{inj}$  is the quantum yield for the electron injection from the excited sensitizer to the conduction band of the semiconductor metal oxide and  $\eta_{coll}$  is the electron collection efficiency at the anode.

When a load on the cell is present, a potential difference between the electrodes develops, which creates a current in the opposite direction of the photocurrent and the net current is reduced from the short circuit value. This reverse current is usually



referred to as the *dark current*. The term *dark current* comes from the current flow in the cell in the dark when a voltage bias is applied. Measuring the I-V characteristics in the dark gives an approximation of the amount of *dark current* in an illuminated cell.

### Electrolyte

The main ingredients of the electrolytes are LiI and I<sub>2</sub>, which forms the redox couple I/I<sub>3</sub><sup>-</sup>. As an additive, MBI (1-Methylbenzimidazole) is added to increase the *V<sub>oc</sub>*. To replace some of the LiI, an ionic salt of iodide, MBII (1-Butyl-3-methylimidazolium Iodide), is added. The MBII additive gave a slight improvement in performances of both *V<sub>oc</sub>* and *J<sub>sc</sub>*. In this work two electrolytes have been used but mainly *Standard 2*:

*Standard 1*: 0.5 M LiI, 0.05 M I<sub>2</sub> and 0.5 M MBI;

*Standard 2*: 0.1 M LiI, 0.05 M I<sub>2</sub>, 0.5 M MBI and 0.6 M MBII;

### Dyes

N719 (Solaronix) is used as a standard to compare with the complexes synthesised in this work.<sup>[22, 23]</sup> In figure 1.11 (chapter 1) N719 is depicted. It is widely recognised as one of the best dyes for the DSNSC and has a reported efficiency of 10%. For the bis-terpy complexes MeCN was used as solvent while the N719 used ethanol in 0.2 mM concentrations.

### TiO<sub>2</sub>

The commercial nanocrystalline (nc) TiO<sub>2</sub> colloid paste Ti-Nanoxide T from Solaronix was used in this work. To calculate a rough estimate of the real surface area for the TiO<sub>2</sub> films, a 1.1x5.4 cm (5.94 cm<sup>2</sup>) TiO<sub>2</sub> thin film (2 scotch layers) of Ti-Nanoxide T was prepared and then removed from substrate. The particles recovered from the film were weighed as being ~4.35 mg. That means 1 cm<sup>2</sup> (projected area) = 0.73 mg. Ti-Nanoxide from Solaronix has 13 nm anatase particles with a surface area of 120 m<sup>2</sup>/g (BET as measured by Solaronix). For sintered thin films made from P25 (25 nm diameter), values 30 or 40 m<sup>2</sup>/g are reported. The value from Solaronix, that translates to 1 projected cm<sup>2</sup> = 876 cm<sup>2</sup>. The necking during sintering will probably reduce the exposed surface area somewhat. Reported factors of roughness for TiO<sub>2</sub> films have been even greater than 1000 for film thickness of 8 μm.<sup>[24]</sup>

Terpyridine is about 9.4 Å (crystal structure) wide. One terpyridine dye molecule takes up about 9.4x9.4 Å<sup>2</sup> = 88.4 Å<sup>2</sup> = 8.84 x10<sup>-15</sup> cm<sup>2</sup> in area. Reported projected

area of N3 is  $180 \text{ \AA}^2$ .<sup>[25]</sup> For  $100 \text{ nmol/cm}^2$  (projected) coverage, a bis-terpyridine molecule needs  $532 \text{ cm}^2$  and for  $200 \text{ nmol/cm}^2$  it needs  $1065 \text{ cm}^2$ . This can be compared to measurements in chapter 3 where the terpyridine complexes have surface coverages of projected area of between  $\sim 50\text{-}200 \text{ nmol/cm}^2$ . For N719, the area needed at  $110 \text{ nmol/cm}^2$  (measured coverage in chapter 3) is  $1192.4 \text{ cm}^2$ . This means a surface area of  $163.3 \text{ m}^2/\text{g}$ , which is higher than the  $120 \text{ m}^2/\text{g}$  used in the estimation of surface area. Inaccuracies in the measurements (e.g. the weighing) or aggregation of dye molecules may explain the deviance.

### TiO<sub>2</sub> underlayer

To prepare the substrate with a compact TiO<sub>2</sub> under-layer in order to insulate it from electroactive species, spray pyrolysis was used. Following literature procedures, a titanium(IV) bis(acetylacetonate) 0.5 M solution in isopropanol and ethanol was prepared and sprayed onto a glass substrate that was heated to  $450^\circ\text{C}$  and left to heat for 30 minutes (see figure 3.2).<sup>[26]</sup> The control of the layer thickness is difficult but for 10x2 seconds a layer thickness of about 10-50 nm thick is obtained.

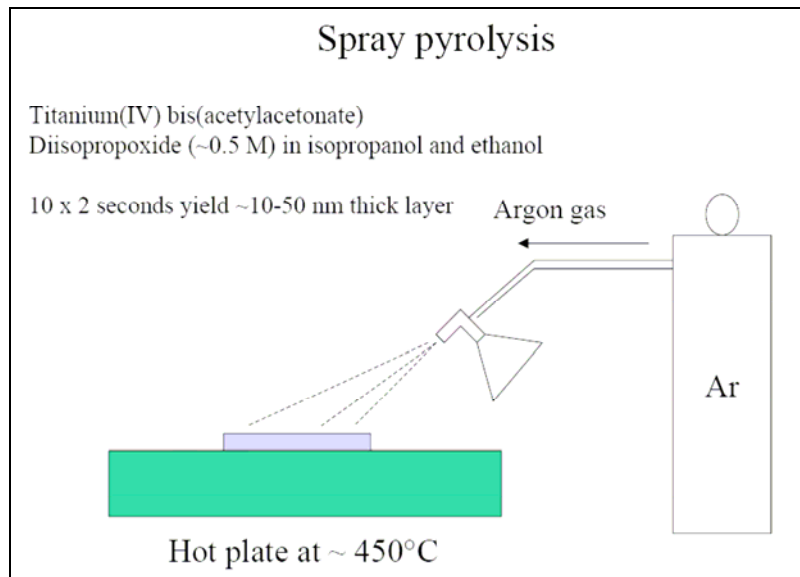


**Figure 2.21** The procedure for preparing a thin compact TiO<sub>2</sub> layer on a FTO glass substrate.

To characterize the under-layer and control that it insulates the FTO surface well, AFM and electrochemical measurements were undertaken. In figure 2.22, AFM images of the underlayer and the nc-TiO<sub>2</sub> are compared. The underlayer appears to consist of compact aggregates of smaller particle while the nc-TiO<sub>2</sub> is composed of

discrete spherical particles. Control images of bare FTO were taken. CVs of dye sensitized nc-TiO<sub>2</sub> films on FTO substrates with and without a compact under-layer in figure 2.23 indicate that there is no contact between dye molecules close to the FTO and the actual FTO when the compact under-layer is present.

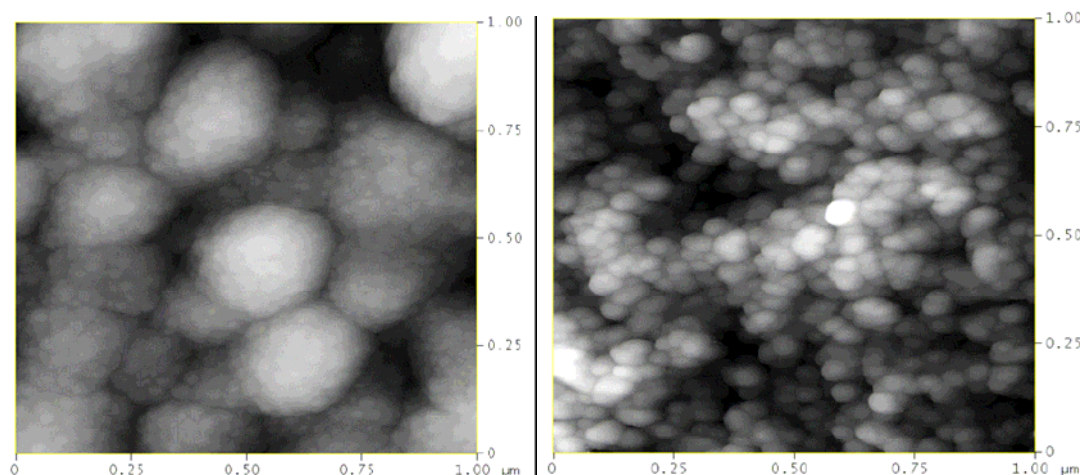


**Figure 2.22** AFM images of TiO<sub>2</sub> compact layer (left) and mesoscopic TiO<sub>2</sub> thin film (right).

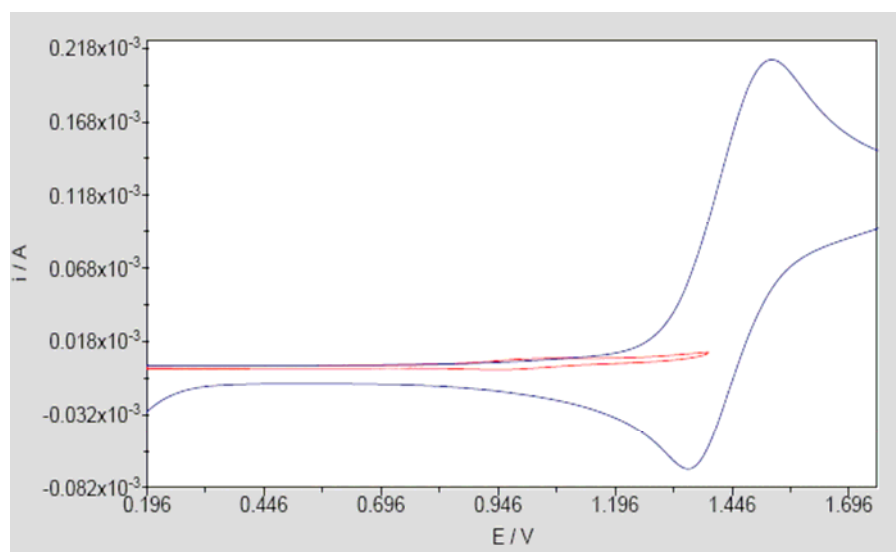


**Figure 2.23** CV of dye sensitized TiO<sub>2</sub> with (red) and without (blue) a compact TiO<sub>2</sub> under-layer. The experiment was performed in MeCN (0.1 M TBAPF<sub>6</sub>) with Ag wire reference.

To further establish the insulation that the compact under-layer provides, approach curve experiments with the SECM were made on a bare and a compact under-layer modified FTO substrate. Figure 2.24 shows the typical result from several measurements. The bare FTO displays a positive feedback as the distance is

decreased, which indicates a conductive surface. The FTO with compact under-layer however, shows a negative feedback curve indicating an insulating surface.

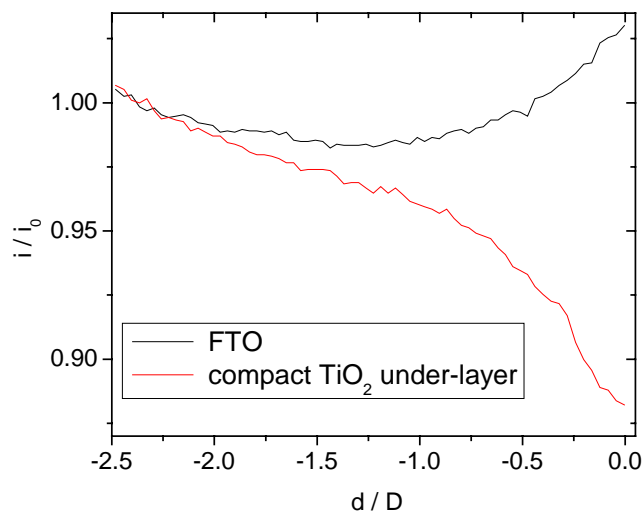


**Figure 2.24** SECM approach curve of FTO substrate with (red line) and without (black line) compact TiO<sub>2</sub> under-layer. The Pt UME diameter was 25 $\mu$ m and the electrolyte 0.5 mM ferrocene in 3-MPN (0.1 M TBAPF<sub>6</sub>).

### Solar cell preparation

Glass pieces with a conducting surface (F-doped SnO<sub>2</sub>, FTO, Hartford glass company, Tec 8, 8 $\Omega$ /cm<sup>2</sup>) were cut to 0.9 x 2.0 cm and cleaned with water and ethanol. Transparent nanoporous TiO<sub>2</sub> films were prepared by doctorblading a colloidal paste (Solaronix Nanooxide-T, colloidal anatase) on to the conductive glass substrates. Two layers of scotch tape were used as spacers. The TiO<sub>2</sub> film area was 0.9 x 0.5 cm.

The films were left to dry (~20 minutes) and then heated on a heat plate at 450°C for 30 minutes. The heating enables contaminations (such as the added polymer in the colloid paste) to be burnt off and substantial “particle necking” that increases the contact between particles. As well as this the surface is dehydroxylated leaving reactive Ti<sup>3+</sup> centers that can react with the carboxylic acid groups.<sup>[27]</sup> The TiO<sub>2</sub> film is then submersed into a solution of the dye while still hot (~80°C) overnight to avoid re-hydroxylation of the surface.

The film thickness, which was measured with a profilometer (Dektak), was 6.0  $\pm$  0.5  $\mu$ m. There is always an optimum film thickness in the DNSC. For efficient collection

of electrons at the electrode, it is necessary that the thickness  $d$  is smaller than  $L_n$ , the electron diffusion length in  $\text{TiO}_2$ .<sup>[28]</sup> The electron diffusion length is obtained from:

$$L_n = \sqrt{D_e \tau_r} \quad (35)$$

where  $D_e$  and  $\tau_r$  are the electron diffusion constant and electron lifetime respectively. This has to be balanced with the light absorption for optimal light conversion. Often, for the best cells, around 10-12  $\mu\text{m}$  is optimal.<sup>[23]</sup>

To estimate the coverage or amount of dye on the surface, the extinction coefficient adsorbed to  $\text{TiO}_2$  is assumed to be the same as it is in solution. The absorbance of the adsorbed dye can be measured because the  $\text{TiO}_2$  film is transparent. Using a rearranged form of the Beer-Lambert law (equation 36) for the  $\text{TiO}_2$  films (equation 37) the number of moles of dye per  $1 \text{ cm}^2$  on the  $\text{TiO}_2$  surface was calculated.

$$OD = \varepsilon \times l \times C \quad (36)$$

$$OD = \varepsilon \times (t \times 10^{-4}) \times [x / (t \times 10^{-7})] \quad (37)$$

In equation 35  $t$  is the thickness (in  $\mu\text{m}$ ) of the sample films and  $x$  is the number of dye molecules in the cube of  $1 \text{ cm} \times 1 \text{ cm} \times t \mu\text{m}$  (in mol). The number of moles of dye per projected  $\text{cm}^2$  of  $\text{TiO}_2$  film can be calculated using equation 38.

$$x = OD / (\varepsilon \times 10^3) \quad (38)$$

This method was compared to another one where the dye is desorbed afterwards in a slightly basic solution of EtOH, and the amount determined by UV-vis. This method is probably more accurate at high coverages. In figure 2.25 three films with different coverages are first measured as they are on  $\text{TiO}_2$  and then desorbed. At higher coverages, where  $A > 2.0$  for the dye sensitised  $\text{TiO}_2$  films, the measurement on the sensitised films underestimates the amount of dye on the surface (if we assume that the extinction coefficients are the same on the surface as in solution) compared to the method of desorbing first. Physical limitations of measuring absorbance values when  $A > 2.0$  may contribute to the inaccuracy.

To evaluate the dye coverage by using  $x$  from equation 38, one needs to approximate the surface area the dye will take up and the real surface area of the mesoscopic  $\text{TiO}_2$ . Using equation 39 the surface coverage in percentage can be approximated. A complete monolayer would mean  $y$  equalling 100%.

$$y = x \times Na \times s / A \times 100 \quad (39)$$

In equation 39,  $N_a$  is Avogadro number,  $s$  is the area occupied by one molecule of the dye and  $A$  is the real surface area for  $1 \text{ cm}^2$   $\text{TiO}_2$  film.

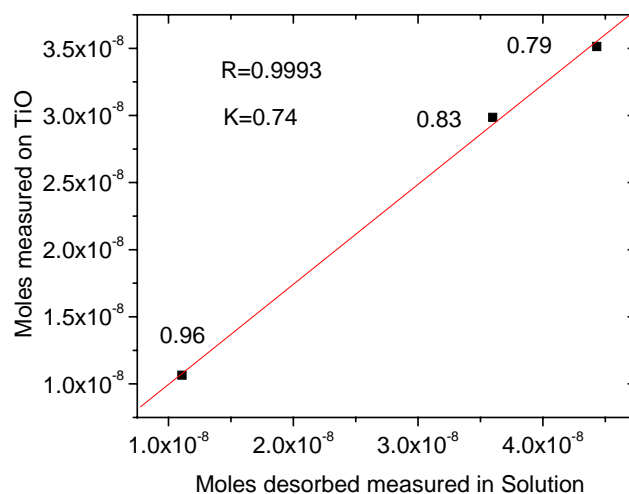


**Figure 2.25** A plot of the moles of dye on  $\text{TiO}_2$  measured by UV-vis either directly on the surface (Y-axis) and those measured after desorption (X-axis). The numbers by the points are the ratios of X-value/Y-value.

Cathode electrodes were made from FTO glass pieces of the same dimensions as the anodes. A few of drops of a 5mM  $\text{H}_2\text{PtCl}_4$  isopropanol solution were spread on. After the solvent had evaporated the glass is heated at  $\sim 380^\circ\text{C}$  for 15 minutes to deposit a platinum coating.<sup>[29]</sup> The photo-anode and the counter electrode were assembled using Surlyn (Dupont) plastic between the electrodes and heating it to  $110\text{-}120^\circ\text{C}$  while pressing them together.

## 2.4 Photo-Electrochemical Polymerisation

To polymerise conducting polymers close to the dye molecules with good contact and deep in the pores of the  $\text{TiO}_2$ , photo-electrochemical polymerisation (PEP) at the surface of the  $\text{TiO}_2$  could be an effective method. As discussed in chapter 1 there are requirements on the dye and monomers in the experiments if polymerisation by the dye is to be successful. The first requirement is that the dye on the surface needs to have an oxidation potential higher than that of the monomer to be capable of oxidising the monomer and cause coupling between monomers or between the dye and

monomer. In figure 2.26 the relative position of the energy levels are depicted in a system where the oxidised dye (after  $S_1 \rightarrow \text{TiO}_2^{\text{C.B.}}$ ) can be reduced by the ligand and the ligand in turn oxidises the monomer in solution. The blue arrow represents the excitation of the dye molecule by a photon and the red arrows represent first the electron injection into the  $\text{TiO}_2$ , then the oxidation of the ligand and finally the oxidation of the monomer.

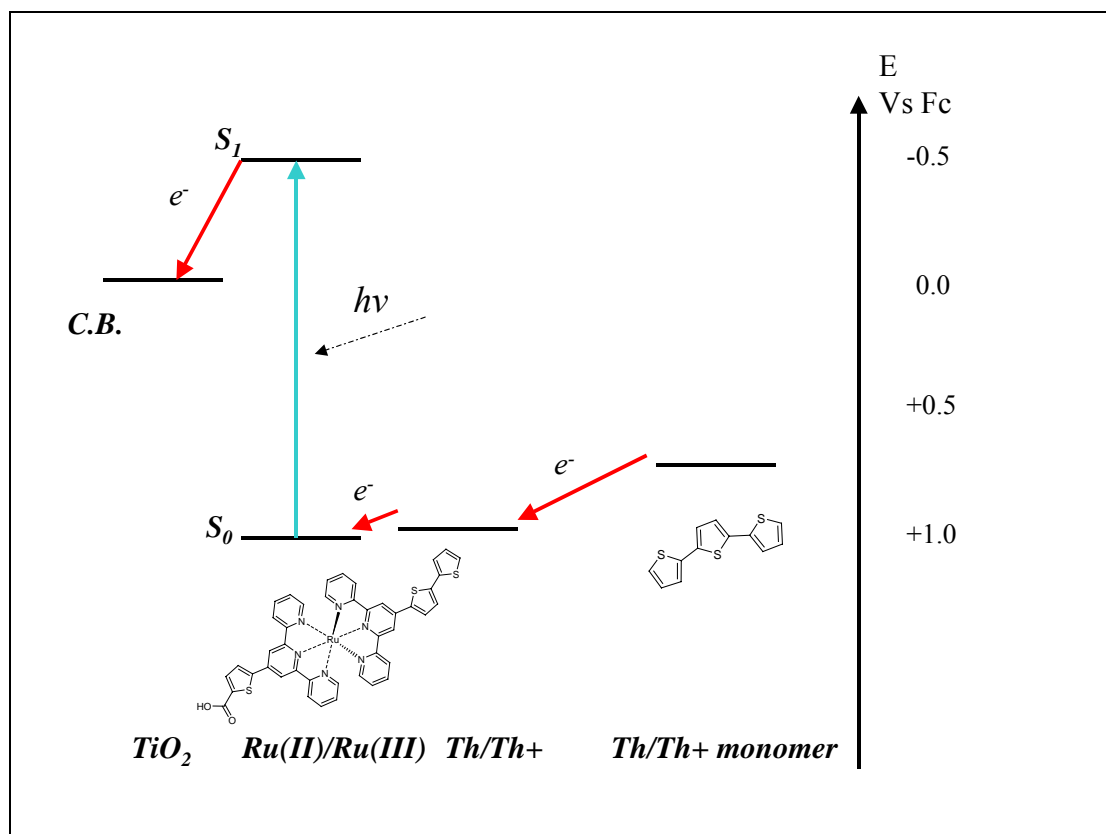


**Figure 2.26** Energy diagram of the relative energy levels of the  $\text{TiO}_2$ , surface attached dye molecule and the monomers oxidation potential.

From the electrochemical measurements in section 3.2 the oxidation potentials of the bi-thienyl ligands in different complexes are partly mixed with the ruthenium +II/III process but also have a part separate and at more positive potentials. Figure 2.26 has the bi-thienyl ligand oxidation potential lower than the ruthenium process to show the concept but the potentials are in reality more equal. If there is oxidation of the monomer in solution by the dye there may be two different initial events. In figure 2.27 there are two simplified mechanisms, (1) the ruthenium center is in its +III oxidation state and the monomer is oxidised directly by this, alternatively (2) the ligand with the bi-thienyl group is oxidised by the ruthenium III and the radical cation

of the ligand is able to oxidise the monomer. Because the entire ligand is conjugated there it is probable that the process will be a mixture of these two proposed paths.

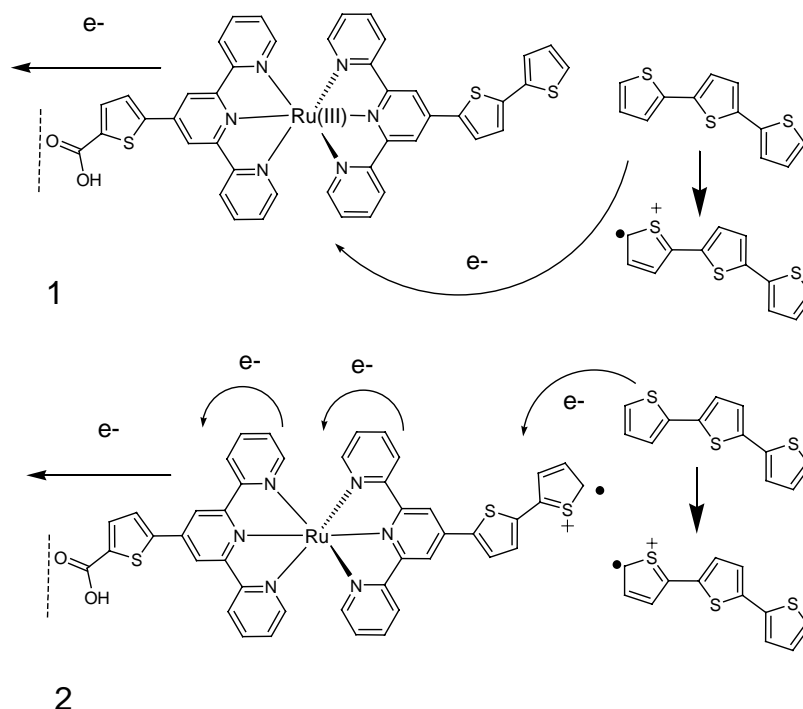


**Figure 2.27** The possible outcomes of electron injection from excited dye. A monomer, that has a low enough oxidation potential, may be oxidised by the ruthenium metal center (1). The ruthenium (III) may oxidise the bis-thienyl ligand, which in turn oxidises the monomer (2).

The presumed mechanism of oxidative coupling in thienyl monomers is two radical cations coupling in the  $\alpha$ -position (chapter 1). This mechanism suggests that the monomers are oxidised (by the oxidised complex) and remain radicals until they meet other cation radical monomers and couple. Alternatively an oxidised ligand radical cation may undergo an electrophilic attack on a neutral monomer and couple to them in the same process.

There are several material parameters to take into account when combining several components and phases into a single photo-electrochemical cell. In figure 2.28 some of the parameters in making a solid-state dye sensitised solar cell are shown. On the  $\text{TiO}_2$  there is an adsorbed dye molecule with a part that is pointing away from the  $\text{TiO}_2$ . The group that is pointing away should be something that may couple strongly with the hole transporting material (HTM) that is between the two electrodes. On the counter electrode (cathode) side, the material that is reducing the hole-conducting polymer, should have a Fermi level that allows the regeneration of the hole



conducting polymer. At the  $\text{TiO}_2$ /dye interface where the HTM polymer is formed, it is important that the oxidised dye can be reduced by the HTM. As Haque *et al.* found, the extra electrochemical potential needed to drive the extraction of photo-generated holes is at least 0.2 eV (equation 40).<sup>[30]</sup> But a bigger difference in this driving force will decrease the open circuit voltage of the DNSC so a good balance is needed.

$$\Delta G_{(\text{dye-HTM})} = E(\text{HTM}^+ / \text{HTM}) - E(\text{Dye}^+ / \text{Dye}) \quad (40)$$

The free energy difference is inhomogeneously broadened from local variations in the electrostatics of the interface and they need to have a large average  $\Delta G_{(\text{dye-HTM})}$  in order to achieve high hole-transfer yield. PEDOT has an oxidation potential of about  $\pm 0$  V (vs  $\text{Fc}/\text{Fc}^+$ ), which is slightly more positive than the  $\text{I}/\text{I}_3^-$  couple ( $\sim -0.2$  V) and is closer to the oxidation potential of the ruthenium dyes ( $\sim +0.85$  V) but further from the  $\text{TiO}_2$  conduction band, which may give a higher  $V_{OC}$ . In figure 2.28 some examples of the materials that are used when preparing a solid-state DNSC are shown (Counter electrode materials together with their work functions).

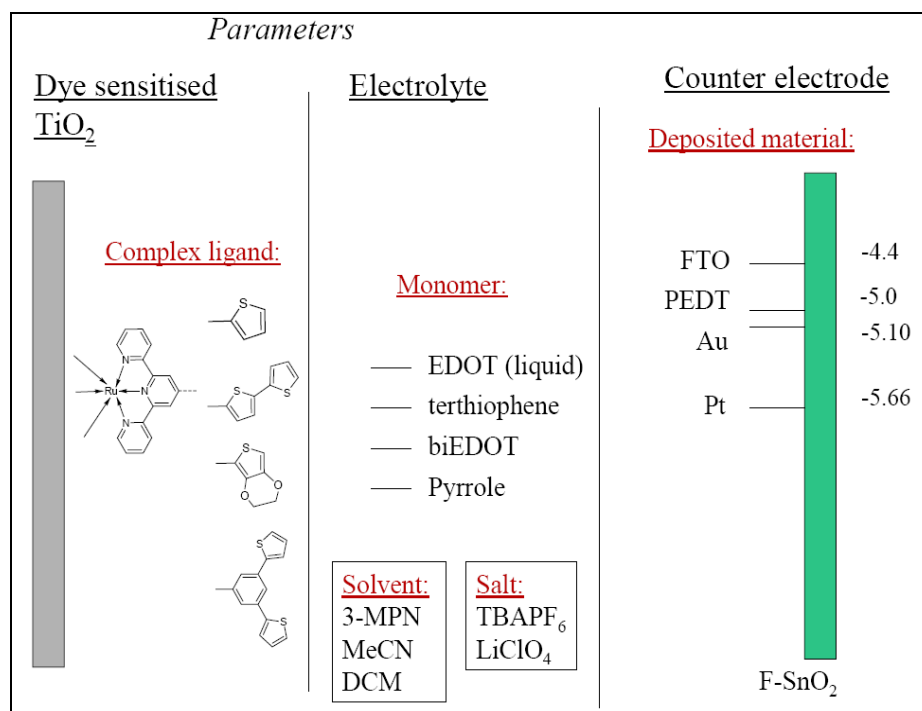


**Figure 2.28** The different parameters that are relevant when setting up the photo-electrochemical polymerisation and eventual solid-state DNSC. The work functions of the materials on the right are in eV where the energy quoted is that required to remove an electron from the material.

Also the solvent and salts that are used for the monomer are important. In chapter 1 an example from the literature showed how the anion in anodic polymerisation has an affect on conductivity of the deposited polymer. The solvent can also affect the

effectiveness of the polymerisation when radicals are involved.<sup>[3]</sup> The experimental conditions of the PEP were tested in four different configurations. In figure 2.29, where the four different configurations used in this work are listed, (1) involves first polymerisation on TiO<sub>2</sub> in monomer solution and then assembling the photo-anode with a counter electrode<sup>[31]</sup>, (2) uses *in-situ* polymerisation where the monomer solution is injected into the complete cell and illumination under short-circuit conditions may oxidise monomer and (3) is like (2) but the electrodes are pressed together instead of a spacer connecting the electrodes before the monomer solution is injected.<sup>[19]</sup> With method (1) it may be difficult to contact the polymer with the counter electrode. Evaporation of a metal to contact the polymer is probably necessary but was not available in this work. The position of the light source can be from glass side and/or the TiO<sub>2</sub> side. In methods (2)-(4) the polymer HTM may contact better with the counter electrode, as the PEP is performed with the counter electrode in close proximity.

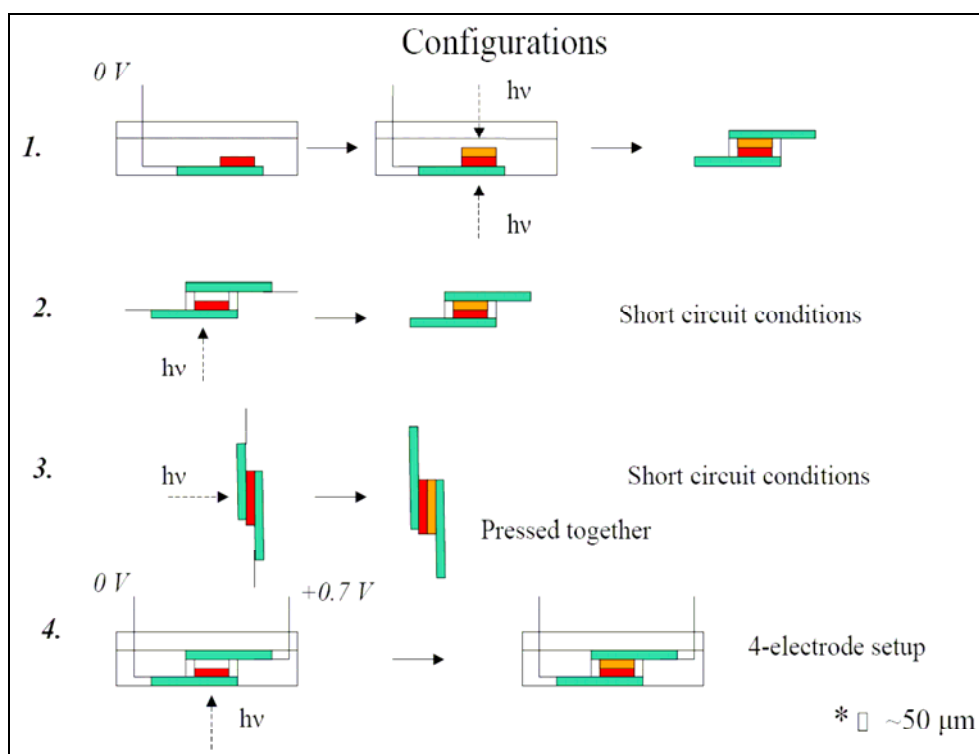


**Figure 2.29** The four experimental configurations of the photoelectrochemical polymerisation (PEP). Red blocks symbolise the dye sensitised TiO<sub>2</sub> and the yellow blocks the polymerised HTM.

The method in configuration (1) is that of the experiments by Yanagida *et al.*<sup>[32]</sup> Method (3), from figure 2.29, was previously proposed and tested by Kim *et al.* with a

porphyrin dye and aniline monomer.<sup>[19]</sup> Figure 2.30 shows the mechanism that was proposed for the *in-situ* methods (2) and (3) similar to that in reference [19]. Connecting the cell to a potentiostat under short circuit conditions may be the most effective as the current flow should be at its maximum. Illumination through either side or both is needed to inject electrons and have an oxidised dye that can oxidise monomer in the electrolyte.

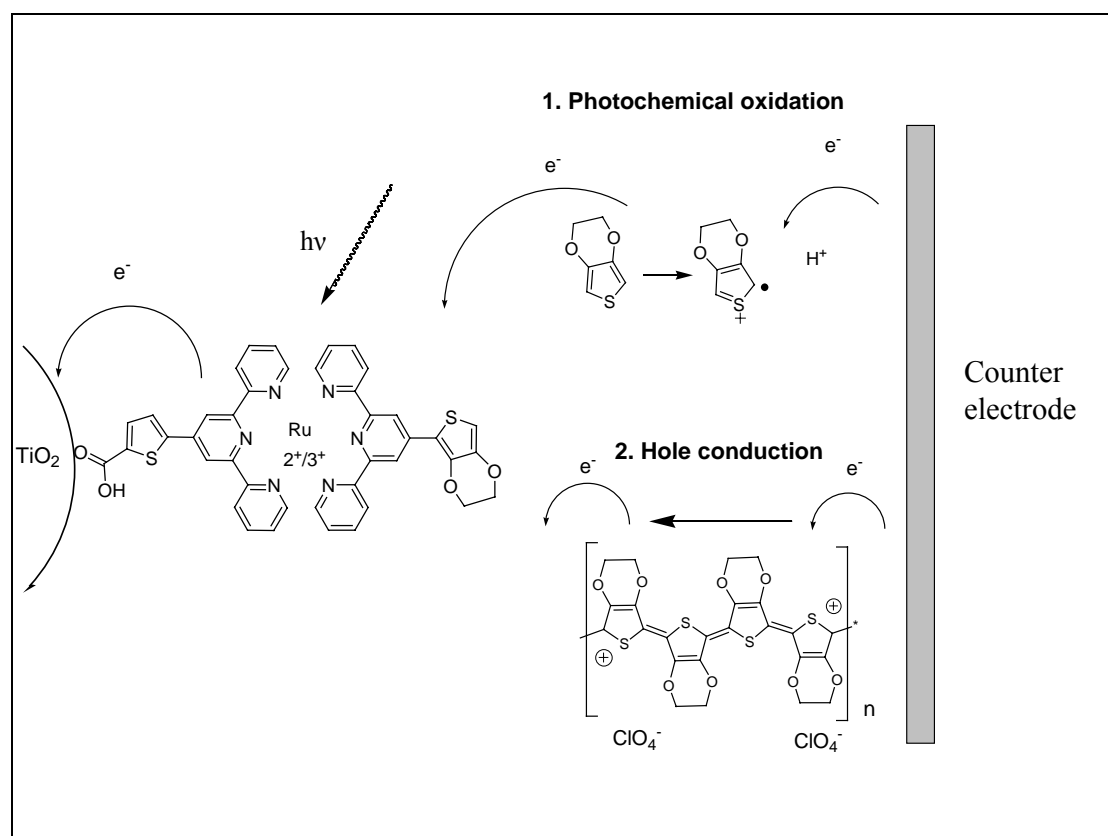


**Figure 2.30** The concept of *in-situ* photochemical oxidation where the reaction could take place in a cell under short circuit conditions.

In figure 2.29, configuration (4) is similar to configuration (3) but with the added possibility of applying a potential to the cathode electrode in order to electrochemically polymerise monomer (EDOT in this case) at the same time as the photo-oxidation at the photo anode. This technique may promote connection of the hole conducting material with the counter electrode in a better way than the other configurations. The drawbacks in methods (2) and (4) is the thickness of the Surlyn spacer ( $\sim 50 \mu\text{m}$ ) that is much thicker than the expected diffusion length ( $< 100 \text{ nm}$ ) of charge carriers in the polymer HTM.

## Reference list

- [1] A. J. Bard, F. L. R., *Electrochemical Methods, Fundamentals and Applications*, 2 ed., Wiley, **2001**.
- [2] C. M. A. Brett, A. M. Oliveira-Brett, *Electroanalysis*, Oxford University Press, **1998**.
- [3] D. T. Sawyer, A. Sobkowiak, R. L. R., *Electrochemistry for chemists*, 2 ed., **1995**.
- [4] H. Reiss, *J. Phys. Chem.* **1985**, *89*, 3783.
- [5] A. L. Barker, M. Gonsalves, J. V. Macpherson, C. J. Slevin, P. R. Unwin, *Analyt. Chim. Acta* **1999**, *385*, 223.
- [6] P. Sun, F. O. Laforge, M. V. Mirkin, *Phys. Chem. Chem. Phys.* **2007**, *9*, 802.
- [7] J. Kwak, A. J. Bard, *Analyt. Chem.* **1989**, *61*, 1794.
- [8] J. Kwak, A. J. Bard, *Analyt. Chem.* **1989**, *61*, 1221.
- [9] B. Bozic, E. Figgemeier, *Chem. Commun.* **2006**, 2268.
- [10] V. Ruiz, P. Liljeroth, B. M. Quinn, K. Kontturi, *Nano Lett.* **2003**, *3*, 1459.
- [11] J. Zhang, A. L. Barker, D. Mandler, P. R. Unwin, *J. Am. Chem. Soc.* **2003**, *125*, 9312.
- [12] R. R. Gagné, A. K. Koval, G. C. Lisensky, *Inorg. Chem.* **1980**, *19*, 2854.
- [13] A. L. Whitworth, D. Mandler, P. R. Unwin, *Phys. Chem. Chem. Phys.* **2005**, *7*, 356.
- [14] M. V. Mirkin, M. Arca, A. J. Bard, *J. Phys. Chem.* **1993**, *97*, 10790.
- [15] D. Mandler, P. R. Unwin, *J. Phys. Chem. B* **2003**, *107*, 407.
- [16] C. Bauer, G. Boschloo, E. Mukhtar, A. Hagfeldt, *J. Phys. Chem. B* **2002**, *106*, 12693.
- [17] M. Neumann-Spallart, *Chimia* **2007**, *61*, 806.
- [18] J. Nelson, *The Physics of Solar Cells*, Imperial College Press, **2003**.
- [19] H. S. Kim, C. C. Wamser, *Photochem. Photobiol. Sci* **2006**, *5*, 955.
- [20] F. Fabregat-Santiago, J. Bisquert, G. Garcia-Belmonte, G. Boschloo, A. Hagfeldt, *Sol. Energy Mater. Sol. Cells* **2005**, *87*, 117.
- [21] N. Koide, A. Islam, Y. Chiba, L. Y. Han, *J. Photochem. Photobiol., A* **2006**, *182*, 296.
- [22] M. K. Nazeeruddin, S. M. Zakeeruddin, R. Humphry-Baker, M. Jirousek, P. Liska, N. Vlachopoulos, V. Shklover, C. H. Fischer, M. Gratzel, *Inorg. Chem.* **1999**, *38*, 6298.
- [23] M. K. Nazeeruddin, R. Splivallo, P. Liska, P. Comte, M. Gratzel, *Chem. Commun.* **2003**, 1456.
- [24] M. Gratzel, *Curr. Opin. Coll. & Interface Sci.* **1999**, *4*, 314.
- [25] A. Fillinger, B. A. Parkinson, *J. Electrochem. Soc.* **1999**, *146*, 4559.
- [26] L. Kavan, M. Gratzel, *Electrochim. Acta* **1995**, *40*, 643.
- [27] M. K. Nazeeruddin, A. Kay, I. Rodicio, R. Humphry-Baker, E. Muller, P. Liska, N. Vlachopoulos, M. Gratzel, *J. Am. Chem. Soc.* **1993**, *115*, 6382.
- [28] M. Gratzel, *Inorg. Chem.* **2005**, *44*, 6841.
- [29] A. Hagfeldt, B. Didriksson, T. Palmqvist, H. Lindstrom, S. Sodergren, H. Rensmo, S. E. Lindquist, *Sol. Energy Mater. Sol. Cells* **1994**, *31*, 481.
- [30] S. A. Haque, T. Park, A. B. Holmes, J. R. Durrant, *Chem. phys. chem.* **2003**, *4*, 89.
- [31] J. B. Xia, N. Masaki, M. Lira-Cantu, Y. Y. Kim, K. J. Jiang, S. Yanagida, *J. Phys. Chem. C* **2008**, *112*, 11569.

- [32] Y. Saito, T. Azechi, T. Kitamura, Y. Hasegawa, Y. Wada, S. Yanagida, *Coord. Chem. Rev.* **2004**, 248, 1469.

## 3 Results and Discussion

### 3.1 Synthesis & Characterisation of Oligopyridine Ligands

#### 3.1.1 Terpyridine Ligand Synthesis

Oligopyridines, especially 1,10-phenanthroline, 2,2'-bipyridine and 2,2':6',2''-terpyridine, have been widely used as metal binding units in supramolecular chemistry.<sup>[1-3]</sup> Coordination compounds formed with metal ions offer a route to obtaining complexes with interesting photochemical and electrochemical properties.<sup>[2, 4, 5]</sup> Substitution in the 4'-position is a useful and straightforward way to modify the ligand and change these properties.<sup>[6]</sup>

This chapter describes the modification of 2,2':6',2''-terpyridines at the 4'-position with a variety of aryl groups and particularly with thienyl-based functional groups. Three of the ligands below are new (**2**, **6** and **8**). The synthetic methods for ligands **3** and **9** differ slightly from the methods in previous literature.<sup>[7-9]</sup>

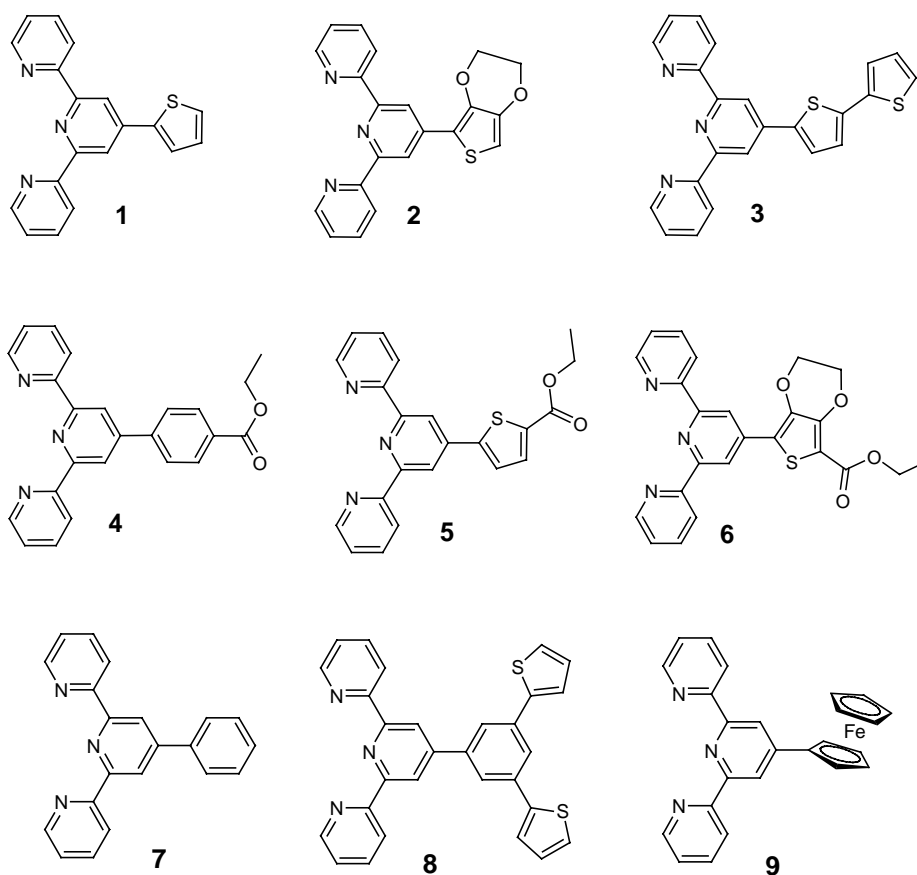
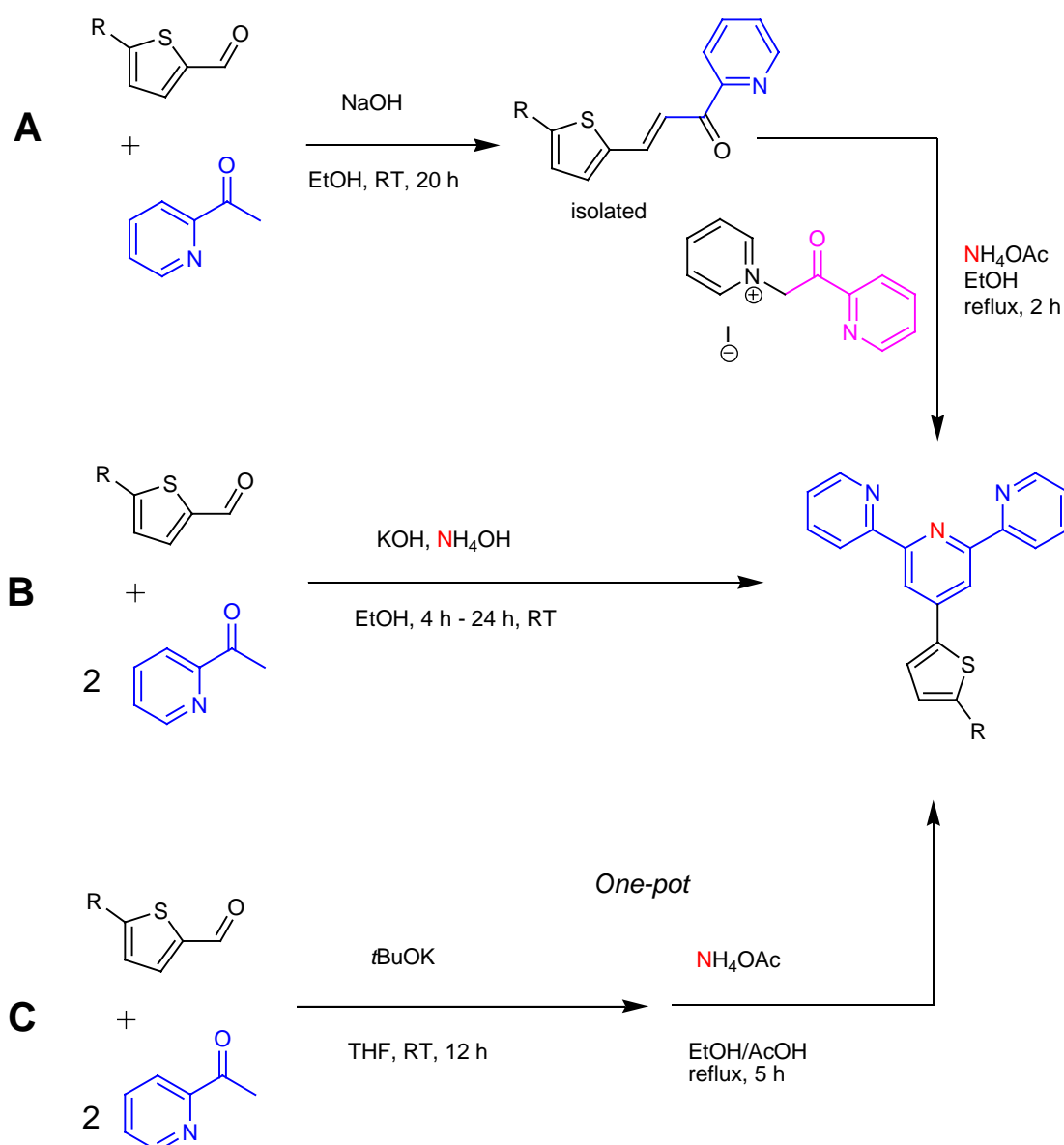


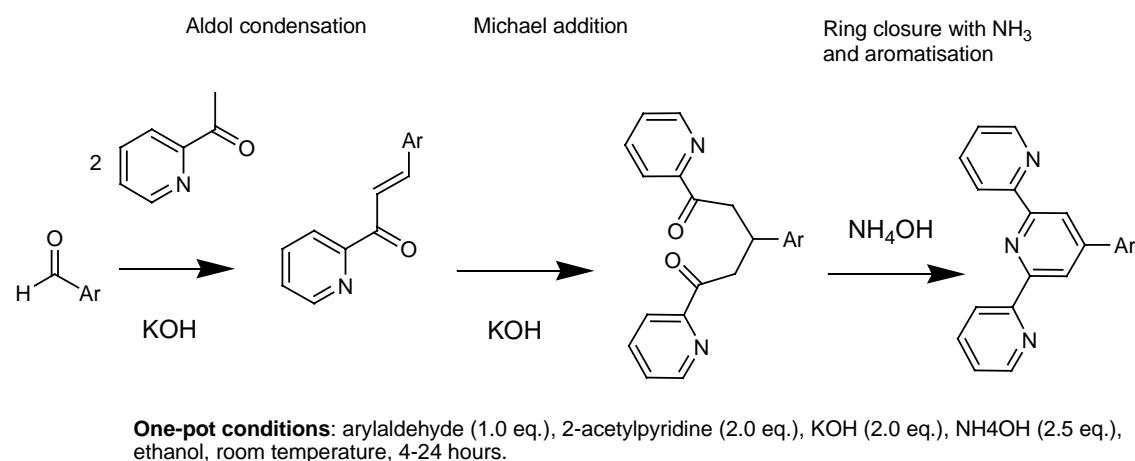
**Figure 3.1** At position 4' modified 2,2':6',2''-terpyridines.

The most common methods for the synthesis of 4'-substituted terpyridines are based on the condensation of two equivalents of 2-acetylpyridine with an aryl aldehyde.<sup>[10, 11]</sup> Scheme 3.1 outlines three methods towards 4'-aryl-2,2':6',2''-terpyridines when aryl is a thienyl-group.<sup>[3, 5]</sup> In the so-called Kröhnke synthesis<sup>[12]</sup> (method A, scheme 3.1), the product of initial aldol condensation, an enone, is isolated. Michael addition of N-[2-oxo-2(2-pyridyl)ethyl]pyridinium iodide (PPI) to this enone gives a diketone at reflux temperature in ethanol. The *in-situ* formed diketone then reacts in the presence of a nitrogen source (such as ammonia) to form the central pyridine ring. A corresponding one-pot, two-step reaction sequence involving KO<sup>t</sup>Bu as the base for enolate formation has been reported (method C).<sup>[13, 14]</sup>



**Scheme 3. 1** Three main synthetic routes to obtain a terpyridine ligand with thienyl group on the 4'-position.

Wang and Hanan developed a straightforward and efficient synthesis for 4'-aryl-2,2':6',2''-terpyridines (method **B**).<sup>[11]</sup> In this work, method **B**, was applied in most of the synthesis of the aryl-terpyridines. A general procedure with the main intermediates is depicted in scheme 3.2. The reaction was relatively clean and recrystallisation from MeOH/CHCl<sub>3</sub> was usually sufficient to afford pure products.

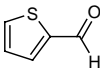
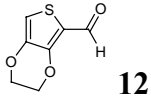
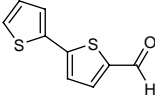
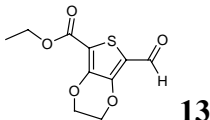
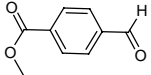
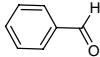
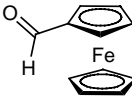
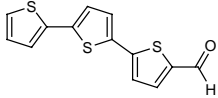
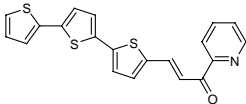
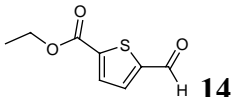


**Scheme 3.2** Synthesis of 4'-arylated 2,2':6',2''-terpyridines by the method of Wang and Hanan.<sup>[11]</sup> Ar = aryl group.

The method was efficient for the terpyridines involving monothienyl (**1**), bithienyl (**2**), ethylenedioxythienyl (**3**) and carboxy-aryl (**4** and **6**) groups, which are introduced by the corresponding aldehydes. An attempt was made with a terthiophene aldehyde but the reaction stopped at the enone. The terthiophene enone was isolated and subjected to the reaction once more without success. The problem could be due to poor solubility of the enone. An attempt to change the solvent to THF for better solubility did not help and higher temperatures led to polymerisation. In table 3.1 the results and unoptimised yields from the synthesis of the 4'-aryl-2,2':6',2''-terpyridines are listed. The references on the entry numbers refer to publications where the respective terpyridine have been reported.



**Table 3.1** Results of the synthesis of 4'-arylated terpyridines (method **B**): according to scheme 3.2.

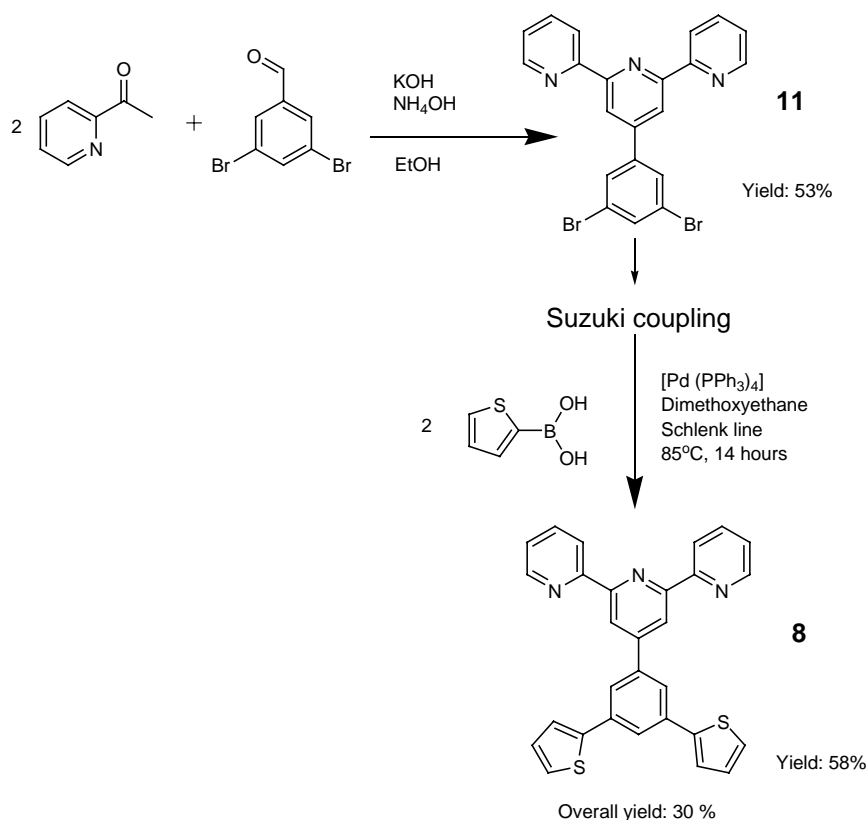
Entry	Aldehyde	Product	Yield
1 <sup>[9]</sup>		<b>1</b>	22%
2		<b>2</b>	41%
3 <sup>[13]</sup>		<b>3</b>	41%
4		<b>6</b>	44%
5 <sup>[15]</sup>		<b>4 (acid)<sup>a</sup></b>	48%
6 <sup>[16]</sup>		<b>7</b>	40%
7 <sup>[7]</sup>		<b>9</b>	49%
8		enone 	No terpyridine formed
9 <sup>b</sup>		<b>5</b>	29%

<sup>a</sup> Hydrolysis of the methyl ester occurred under reaction conditions and acidic work-up yielded the acid.

<sup>b</sup> Synthesis according to method A, scheme 3.1.

Coupling reactions like the Stille and Suzuki coupling are also frequently used in order to prepare modified polypyridine ligands.<sup>[17, 18]</sup> For ligand **8**, the two thienyl groups were added in a Suzuki coupling to the readily synthesised 4'-(3,5-dibromophenyl)-terpyridine **11**, as can be seen in scheme 3.3. The terpyridine **11** and two equivalents of thiophene-2-boronic acid were reacted in refluxing DME in an

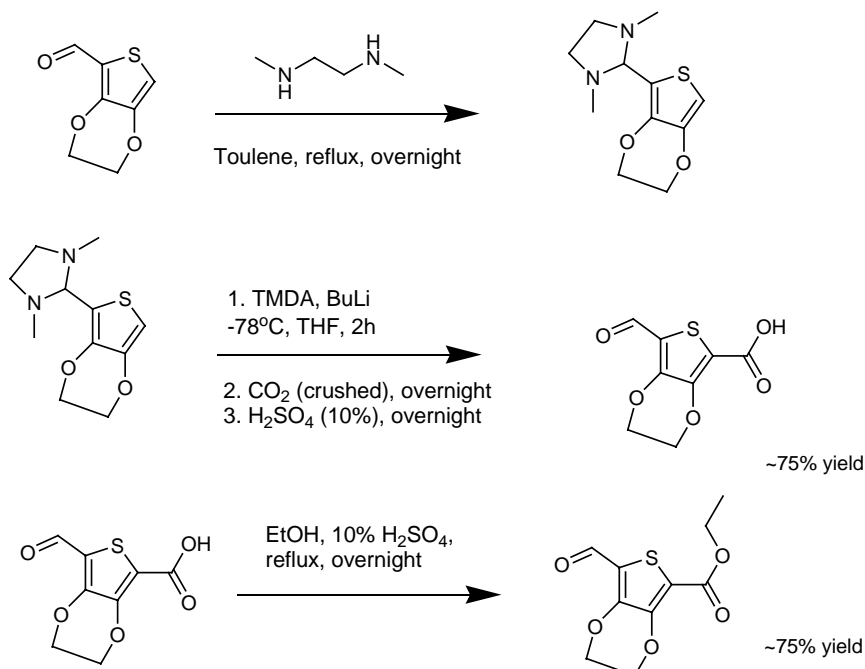
oxygen free environment with a palladium catalyst.<sup>[18]</sup> These Suzuki coupling conditions led to the product **8** in 58% yield.



**Scheme 3.3** Suzuki coupling of two boronic-acid functionalised thiophenes with one dibromophenyl functionalised terpyridine in the presence of a palladium catalyst.<sup>[18]</sup>

Some of the aldehydes mentioned above had to be synthesised. The aldehydes for ligands **1**, **3**, **4**, **7** and **9** could be purchased commercially but the aldehydes **12-14** for ligands **2**, **5** and **6** were prepared. Aldehyde **12** was synthesised by the Vilsmeier-Haack reaction.<sup>[19]</sup> To synthesise aldehydes **13** and **14**, a carboxyl group had to be introduced at the 5 position of the corresponding 2-formyl-thiophene derivative (commercial 2-formyl-thiophene or aldehyde **12**). Scheme 3.4 shows the procedure for such a functionalisation. First, the aldehyde group was protected with *N,N'*-dimethylethylenediamine. Metallation with *n*-BuLi was followed by treatment of the lithiated intermediate with CO<sub>2</sub>, either under a flow of CO<sub>2</sub> gas or with crushed dry ice, to form the carboxylate.<sup>[20, 21]</sup> Under acidic conditions the aldehyde function was deprotected and the carboxylic acid was isolated in good yield. Due to poor solubility, the acid was transformed to the ethyl ester for further use in terpyridine synthesis. The esterification was performed in two different manners. The reaction with ethyl iodide in DMF led to poor yields. However, the carboxylic acid could be efficiently

esterified in EtOH with diluted aqueous H<sub>2</sub>SO<sub>4</sub> under reflux. The isolated formyl-thiophene-carboxylic ester can then be condensed with two 2-acetylpyridines to form a 4'-terpyridine derivative.



**Scheme 3.4** Procedures to synthesise 2'-formyl-5-carboxylate-ethylester-thiophene.<sup>[20]</sup>

The thiophene oligomers, 2,2'-bithiophene and 2,2':6',2''-terthiophene were commercially available but bis-ethylenedioxythiophene (bis-EDOT) was synthesised according to literature.<sup>[22, 23]</sup> Ullmann coupling of EDOT monomer with BuLi and CuCl<sub>2</sub> gave the bis-EDOT in moderate yield.

### 3.1.2 NMR Spectroscopy

$^1\text{H}$ -NMR and  $^{13}\text{C}$ -NMR spectroscopy were used to analyse 2,2':6',2''-terpyridine ligands. All the  $^1\text{H}$ -NMR peaks could be assigned by using the 2-dimensional techniques COSY and NOESY. In the COSY experiment, it is possible to identify J-coupled hydrogens. Using this technique, the thiophene peaks of the bi-thienyl groups were elucidated. To verify some peaks, the NOESY spectra can be useful to measure couplings of hydrogens close in space. The spectra were also compared to literature examples of similar ligands and between each other for full assignment.<sup>[13]</sup> The 2,2':6',2''-terpyridine peaks are all deshielded by the  $\pi$ -system of the 2,2':6',2''-terpyridine and appear in the  $\delta$  7-9 ppm range.<sup>[24]</sup> Thienyl peaks often appear in the same range. Other peaks, for example from the dioxyethylene bridge, have peaks in the  $\delta$  3-6 ppm range. The acids have very poor solubility and are difficult to measure in the protonated form. They were instead measured as ethyl esters but the 4'-(4-carboxyphenylacid)-2,2':6',2''-terpyridine was measured in DMSO and a broad peak at about  $\delta$  13 ppm can be assigned to the proton of the  $\text{CO}_2\text{H}$  group. Figure 3.2 is a typical spectrum of a 4'-substituted terpyridine in  $\text{CDCl}_3$ .

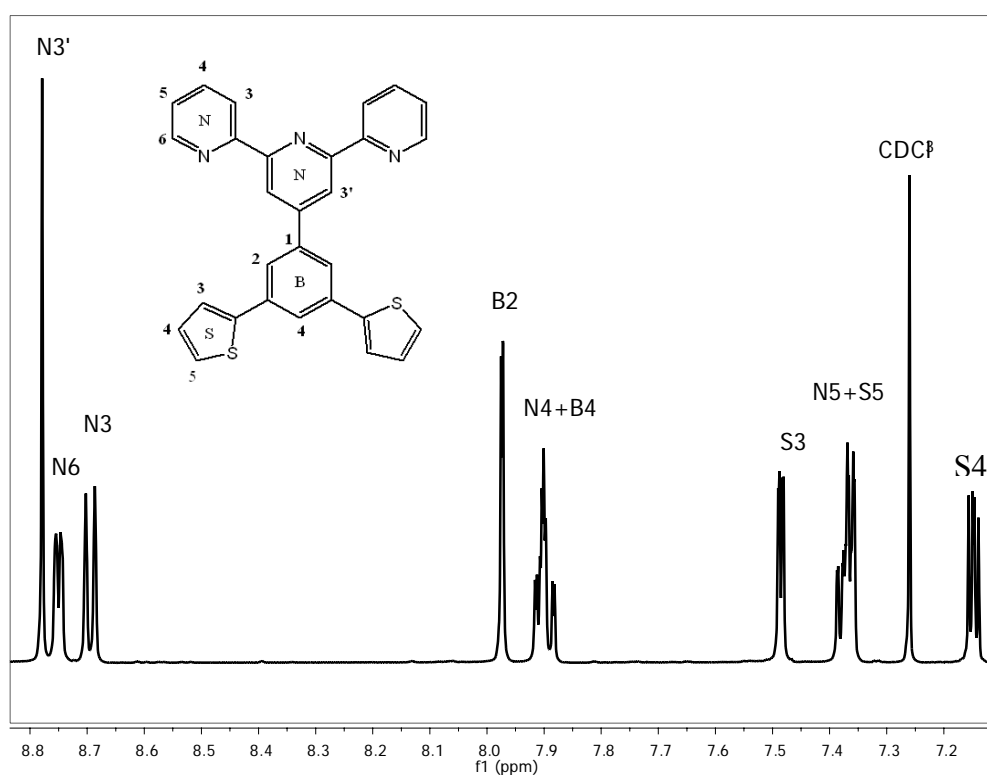


**Figure 3.2**  $^1\text{H}$ -NMR of 2,2':6',2''-terpyridine with substitution on the 4' position (ligand **8**). The solvent peak from chloroform is also visible.

The assignment of  $^{13}\text{C}$ -NMR peaks was harder due to the lower sensitivity of  $^{13}\text{C}$  compared to that of  $^1\text{H}$ . Some of the carboxylate ligands were not soluble enough for well-resolved carbon spectra. Quaternary carbons were distinguished by cross-reference with the DEPT spectra, which only plots tertiary and secondary (inverted) carbons. With the HMBC technique the coupling with hydrogens of neighbouring carbons can be measured and thus enables elucidation of the quaternary carbon peaks. The remaining carbons that are bonded to hydrogens can be assigned when using HMQC to find which carbon is bonded to which hydrogen (which were already assigned). As with the  $^1\text{H}$ -NMR spectra comparing the peaks with confirmed spectra of similar compounds in the literature assists in the assigning of peaks.

### 3.1.3 Orbital Energy Calculations

Molecular orbital calculations on the ligands to calculate their orbital energies were performed with Hyperchem 7<sup>TM</sup> using semi-empirical PM3 geometry and AM1 energy optimization software. The results are in table 3.2. The HOMO energy level can be compared to the first oxidation potential and the LUMO with the first reduction potential. The values from the calculations follow the electrochemical trends from Table 3.4 (chapter 3.1.5) for the ligands **1**, **2** and **3** but the exact values are probably not very reliable. The 2,2':6',2''-terpyridine with a 2,2'-bithienyl has the lowest oxidation and reduction potentials while unsubstituted 2,2':6',2''-terpyridine has the highest LUMO but the calculated HOMO is lower than that of ligand **1**. The band gap between the LUMO and HOMO energy levels is comparable to the lowest optical transition of the ligand. This also follows the trend with the UV-vis data from Table 3.3 (chapter 3.1.4).

**Table 3.2** Molecular orbitals were calculated with semi-empirical PM3 geometry and AM1 energy optimisation. (Potentials are referenced to vacuum.)

Ligand	HOMO (eV)	LUMO (eV)	$\Delta E$ (eV)
tpy	-9.058	-0.644	8.414
tpyS	-9.085	-0.727	8.358
tpySS	-8.608	-1.041	7.567
tpyEDOT	-8.896	-0.731	8.165

### 3.1.4 UV-vis

The terpyridine ligands have the usual 2,2':6',2''-terpyridine transitions at around 280 nm. The thienyl-modified terpyridines have a third peak at a slightly longer wavelength. The mono-thienyl ligand appears to have a transition that can be assigned to the thienyl group and is visible as a shoulder on the terpyridine transition at 280 nm. The bi-thienyl transition is red shifted compared to the mono-thienyl and appears as a large band at 354 nm.

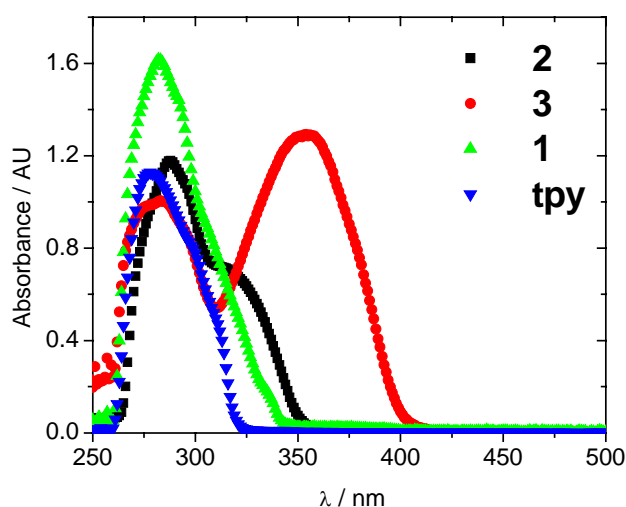


**Figure 3.3** UV-vis spectra of 2,2':6',2''-terpyridine, **1**, **2** and **3** in MeCN. The monothienyl ligand has a shoulder at about 325 nm and the bithienyl has a peak at 354 nm.

Extension of the thiophene substituent extends conjugation and therefore red shifts the  $\pi\text{-}\pi^*$  transition.<sup>[25]</sup> Ligand **2** (TpyEDOT) has a large shoulder at 314 nm attributed to the EDOT. The UV-vis peaks of **1-3** are listed in table 3.3.

**Table 3.3** Lowest UV-vis absorption peaks of the thiophene substituted ligands in acetonitrile.

Compound	terpyridine $\pi\text{-}\pi^*$ , $\lambda/\text{nm}$ ( $\epsilon / 10^4 \text{ M}^{-1} \text{ cm}^{-1}$ )	thiophene $\pi\text{-}\pi^*$ , $\lambda/\text{nm}$ ( $\epsilon / 10^4 \text{ M}^{-1} \text{ cm}^{-1}$ )
tpyS ( <b>1</b> )	282 (6.9)	310 (5.0)
tpySS ( <b>3</b> )	284 (6.5)	354 (8.7)
tpyEDOT ( <b>2</b> )	287 (8.3)	314 (7.0)

### 3.1.5 Electrochemistry

Cyclic and square wave voltammetric measurements on the 2,2':6',2''-terpyridine ligands show the typical reduction peaks for 2,2':6',2''-terpyridine.<sup>[14, 26]</sup> Oxidation peaks for the thienyl-substituted ligands are oxidations to radical cations. In the time scales and conditions of the measurements the reactions are irreversible.

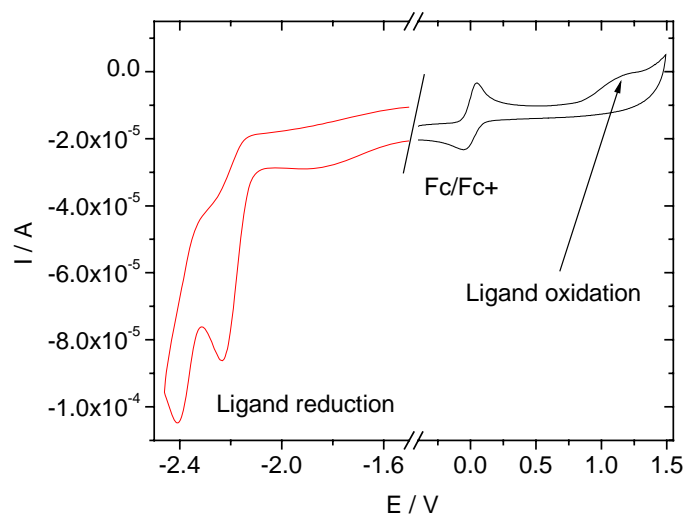


**Figure 3.4** CV at 0.1 V/s of ligand **2** in MeCN with ferrocene as internal reference and 0.1 M TBAPF<sub>6</sub> as supporting electrolyte.

The two terpyridine reduction peaks and the oxidation peak are at more extreme potentials than when coordinated with a metal ion. Some of the ligands were very difficult to dissolve thus making it hard to get clear voltammograms. Other problems were surface adsorption or polymerisation. Oxidation of unsubstituted terpyridine in acetonitrile has previously been measured at  $\sim +1.7$  V (vs. Fc/Fc+) and reduction at  $-1.8$  V and  $-2.8$  V (vs. Fc/Fc+).<sup>[26]</sup> The oxidation and reduction potentials of ligands **1**, **2**, **3** and **8** are listed in table 3.4.



**Table 3.4** Oxidation and reduction potentials of terpyridine ligands measured in MeCN or DCM using square wave voltammetry (SWV). All potentials are quoted versus the ferrocene redox couple.

Compound	Ox. SW (V)	Red. SW (V)
<b>1</b>	+ 1.28	- 2.5
<b>3</b>	+ 1.10	- 2.16, - 2.40
<b>2</b>	+ 1.15	-2.45, -2.61
<b>8</b>	+1.29	- 2.59

### 3.1.6 Crystal-structure

The crystal structure of **8** was obtained from single crystals that were grown by slowly evaporating  $\text{CHCl}_3$  solution. The asymmetric unit consisted of one molecule with no internal symmetry. In figure 3.5 the number scheme connectivity is shown. Even though from this angle the ligand appears flat, there is twisting between the rings. There are torsion angles between the phenyl and the thiophenes of  $31.54^\circ$  (C21-C20-C26-C27) and  $18.49^\circ$  (C17-C18-C22-C23). The phenyl group on position 4' in **8** has a torsion angle with the pyridine of  $40.08^\circ$  (C9-C8-C16-C21) and  $38.14^\circ$  (C7-C8-C16-C17). This is a larger angle than for crystal structures of thienyl ( $8.9^\circ$ )<sup>[27]</sup> and bithienyl on the 4' positions, which would suggest less conjugation for **8** than for the thienyl substituted terpyridines.<sup>[14, 27]</sup> Torsion angles from crystal structures of modified 4'-phenyl-2,2':6',2''-terpyridine of around  $30^\circ$  have been reported and the torsion angle is explained by the steric interactions between the protons of C7/C9 and C17/C21.<sup>[15], [28]</sup>

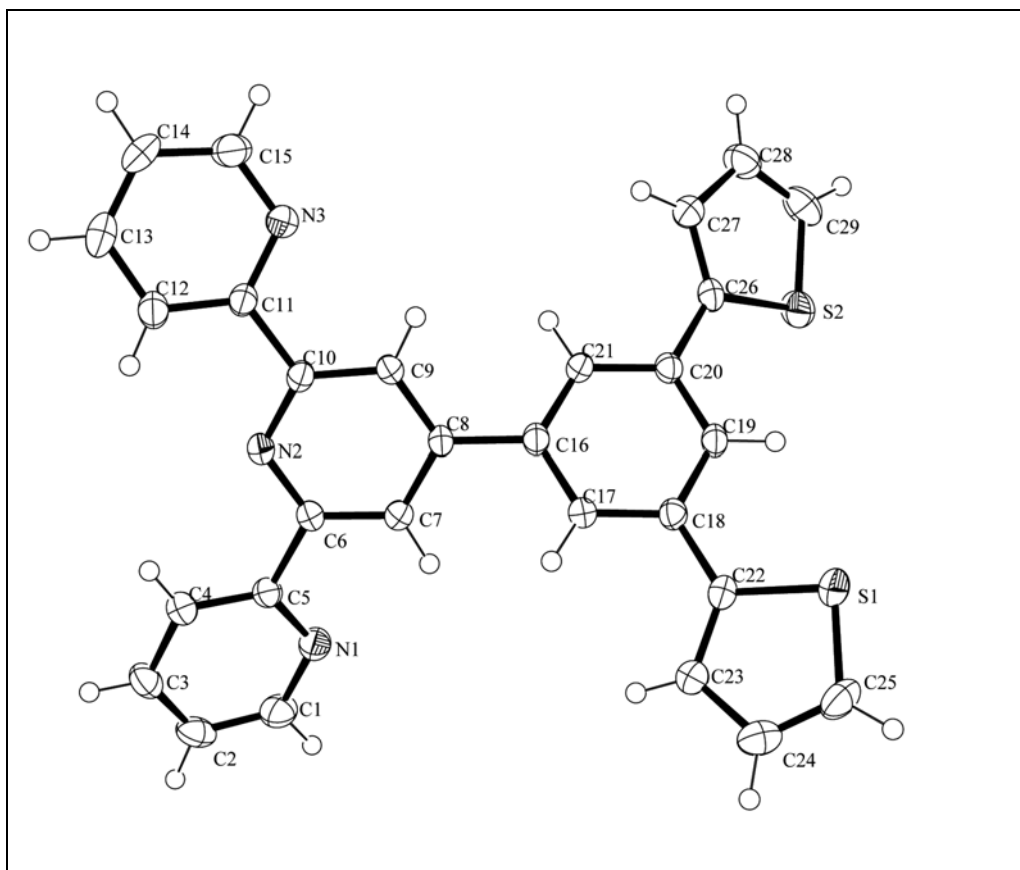


**Figure 3.5** Crystal structure of **8** where the molecules are plotted as thermal ellipsoids at 50% probability level. (i)  $x-1/2, y+1/2, -z+1$

The ligands form 1-dimensional weakly hydrogen bonded polymers where the main connective force is an interaction between the N1 nitrogen of the terpyridine and the  $\alpha$ -proton of the S1 thiophene. The distance between the nitrogen (N1) and the carbon (C25) of the  $\alpha$ -proton is 3.441(3) Å (N--H-C) and the angle is 135.67°.

There is a helical sub-structure along the b-axis of the unit cell (figure 3.6). The helical structures are interleaved and offset  $\pi$ - $\pi$  interactions exist between the helices (see figure 3.7).<sup>[29]</sup>

**Table 3.5** Selected bond lengths and angles from the crystal structure of **8**.

Atoms	Length (Å)	Atoms	Angle (°)
N2-C6	1.338(2)	S1-C25-C24	111.27(15)
N2-C10	1.344(2)	S2-C29-C28	111.90(15)
C8-C16	1.483(2)	N1-C5-C6	116.42(15)
C26-S2	1.7297(17)	N3-C11-C12	122.39(16)
C22-S1	1.7246(17)	C18-C19-C20	121.46(15)

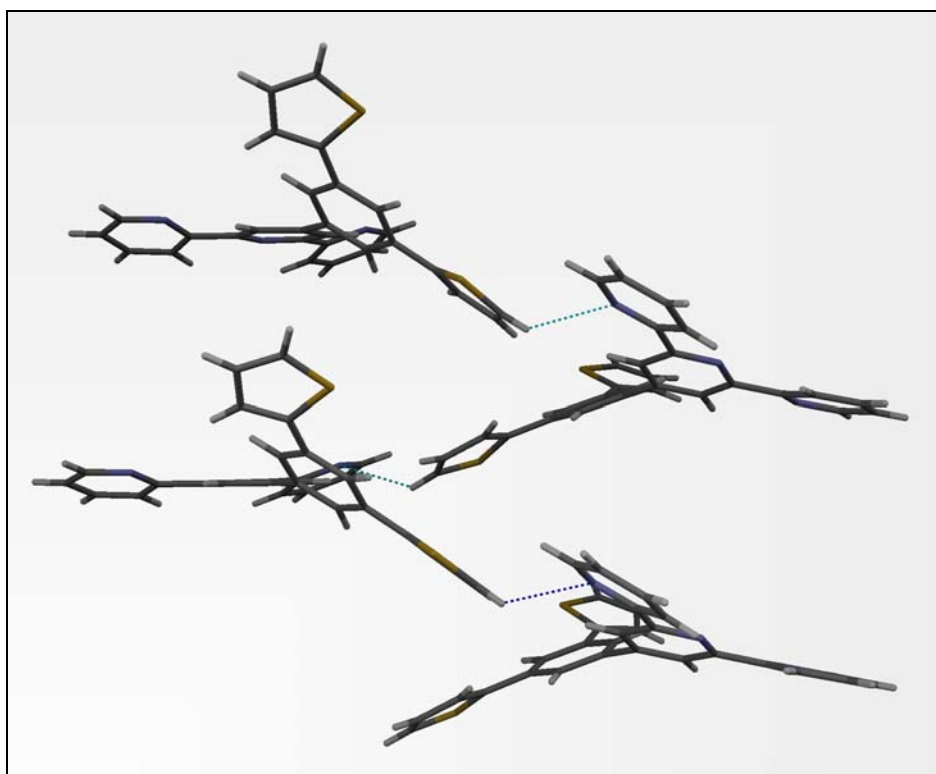


**Figure 3.6** 1-dimensional polymer of ligand **8** crystal structure with the short contact between S1 and N1 marked as blue dotted lines.

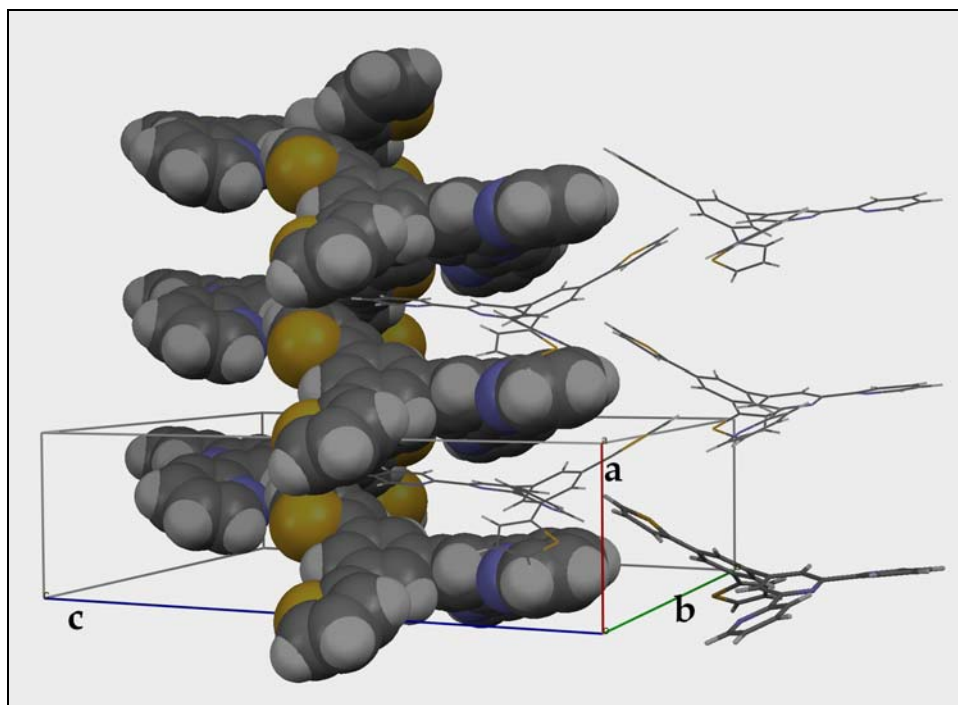


**Figure 3.7** The interpenetrating helices of ligand **8** with one helix displayed as a space filling model and two other spirals as stick models that stack between the twists. The unit cell is included.

**Further analysis**

MALDI-TOF mass spectroscopic measurements were performed on all the ligands to confirm their masses. This technique was useful to verify that a molecule with the expected mass is present but does not allow quantitative determination of any impurities in the sample.

Most of the ligands were measured with IR spectroscopy. This technique is useful to check for the characteristic absorptions of terpyridines, thiophenes and carboxylates. The C=O bond of the aldehydes and carboxylates for example, appear at about 1650  $\text{cm}^{-1}$  and 1600  $\text{cm}^{-1}$  respectively.

Elemental analysis was used for the new ligands. This requires that any solvent is included in the mass percentage calculation or removed prior to the measurement.

### 3.1.7 Experimental

1. 2,2'-Bi(3,4-ethylenedioxy)thiophene
2. 1,3-Dibromo-5-terpyridylbenzene
3. 4'-(2-Thienyl)- 2,2':6',2''-terpyridine, tpyS (**1**)
4. 4'-(2-Ethylenedioxythiophene)- 2,2':6',2''-terpyridine, tpyEDOT (**2**)\*
5. 4'-(2,2'-Bithien-5-yl)- 2,2':6',2''-terpyridine, tpySS (**3**)
6. 4'-4-(Benzoicacid)- 2,2':6',2''-terpyridine (**4**)
7. 4'-(2,5-Ethyl-carboxylate-thienyl)-terpyridine, tpySCOOEt (**5**)
8. 2-Formyl-ethylenedioxythiophene
9. 2-Formyl-5-ethylcarboxylate-ethylenedioxythiophene
10. 4'-(2-Ethylenedioxythiophene)-2,2':6',2''-terpyridine-carboxylate-ethylester, tpyECOOEt (**6**)\*
11. 4'-(Phenyl)- 2,2':6',2''-terpyridine, tpyPh (**7**)
12. 4'-[2,5-(Dithiophene)phenyl]- 2,2':6',2''-terpyridine, tpySBS (**8**)\*
13. 4'-(2-Ferrocene)- 2,2':6',2''-terpyridine (**9**)

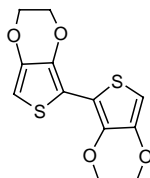
\*Novel ligands

**2,2'-Bi(3,4-ethylenedioxy)thiophene, bi-EDOT**

Previously reported in references [22, 23].

Formula: C<sub>12</sub>H<sub>10</sub>O<sub>4</sub>S<sub>2</sub>

Formula weight: 282.4



4.00 g (28.2 mmol) of EDOT in THF was cooled to  $-78^{\circ}\text{C}$ . To the solution 12.5 ml (31 mmol) n-BuLi was added dropwise. Then 4.17 g (31 mmol) CuCl<sub>2</sub> was added in one portion to the reaction and the flask was taken out of the ice bath. After gentle heating to  $40^{\circ}\text{C}$  for 4 hours the reaction was stopped. A blue residue was filtered off. Water and hexane was added and the organic phase was collected and the solvent evaporated. The blue solid that was left was dissolved in DCM and put through silica column to filter off remaining Cu-salts. The product was a greyish powder. MALDI-TOF spectrometry showed biEDOT signal but also evidence of the trimer.

Yield: 1.9 g, 6.73 mmol (48%)

<sup>1</sup>H-NMR (CDCl<sub>3</sub>, 250 MHz):  $\delta$  = 6.25 (s, 2H), 4.31 (m, 4H, CH<sub>2</sub>O), 4.22 (m, 4H, CH<sub>2</sub>O);

MALDI MS *m/z* (calc.): 283.6 (283.3, [M-H]<sup>+</sup>);

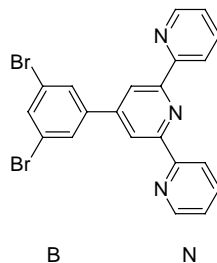
IR (solid, cm<sup>-1</sup>): 3125w, 2947w, 2914w, 2866w, 1566m, 1466s, 1435s, 1360s, 1171m, 1142m, 1055s, 949m, 897s, 864m, 700m, 650s;

**1,3-Dibromo-5-terpyridylbenzene**

Previously reported in reference [18].

Formula:  $C_{21}H_{13}Br_2N_3$

Formula weight: 467.2



0.43 ml (3.8 mmol) 2-acetylpyridine and 500 mg 1,3-dibromo-5-benzaldehyde (1.9 mmol) were stirred together in a mixture of 40 ml EtOH and 10 ml THF. KOH pellets, 0.29 g (3.8 mmol), and 5.5 ml (4.8 mmol) aqueous  $NH_3$  were added to the solution. The reaction was stirred overnight at room temperature. The solution went from clear red brown to yellow with white precipitate. The solid was finally collected by filtration and washed with EtOH.

Yield: 470 mg, 1.00 mmol, (53%)

$^1H$ -NMR ( $CD_3CN$ , 400 MHz):  $\delta$  = 8.73 (d,  $J$  = 4.76 Hz, 2H, N3), 8.66 (d,  $J$  = 7.97 Hz, 2H, N6), 8.64 (s, 2H, N3'), 7.94 (d,  $J$  = 1.70 Hz, 2H, B2+B6), 7.88 (td,  $J$  = 1.78, 7.75, 7.86 Hz, 2H, N4), 7.73 (t,  $J$  = 1.69 Hz, 1H, B4), 7.36 (ddd,  $J$  = 1.12, 4.79, 7.44 Hz, 2H, N5);

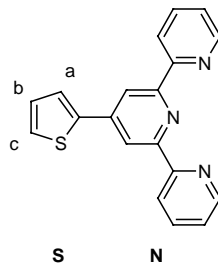
**MALDI MS**  $m/z$  (calc.): 467.7 (467.2)

**4'-(2-thienyl)-2,2':6',2''-terpyridine, tpyS (1)**

Previously reported in references [27, 34].

Formula: C<sub>19</sub>H<sub>13</sub>N<sub>3</sub>S

Formula weight: 315.4



3.0 ml (26.7 mmol) 2-acetylpyridine was added to a solution of 1.25 ml (13.4 mmol) thiophene-2-carboxaldehyde in 60 ml EtOH. 2.04 g (26.5 mmol) KOH pellets and aq. NH<sub>3</sub> (36 ml, 29%, 31.0 mmol) were added to the solution. The solution was stirred for 4 hours at room temperature. During this time a light blue solid precipitated. This was not pure product and the reaction was continued overnight. A white solid precipitated during the night and was collected and washed with EtOH. The white solid was clean and did not need further purification.

Yield: 0.92 g, 2.9 mmol, (22%)

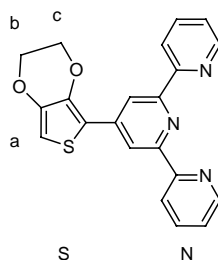
<sup>1</sup>H-NMR (CDCl<sub>3</sub>, 400 MHz): δ = 8.74 (d, J= 4.78 Hz, 2H, N6), 8.69 (s, 2H, N3'), 8.64 (d, J= 7.96 Hz, N3), 7.88 (td, J= 1.80, 7.73, 7.83 Hz, 2H, N4), 7.78 (dd, J= 1.13, 3.67 Hz, 1H, S<sup>a</sup>), 7.46 (dd, J= 1.10, 5.05 Hz, 1H, S<sup>c</sup>), 7.36 (ddd, J= 1.19, 4.79, 7.48 Hz, 2H, N5), 7.17 (dd, 3.69, 5.05 Hz, 1H, S<sup>b</sup>);

<sup>13</sup>C-NMR (CDCl<sub>3</sub>, 400 MHz): δ = 156.4 (N2'/N2, quat), 149.4 (N6, tert), 143.7 (N4', quat), 142.1 (S, quat), 137.1 (N4, tert), 128.5 (S<sup>b</sup>, tert), 127.4 (S<sup>c</sup>, tert), 126.0 (S<sup>a</sup>, tert), 124.1 (N5, tert), 121.6 (N3, tert), 117.4 (N3', tert).



**4'-(2-ethylenedioxythiophene)-2,2':6',2''-terpyridine, tpyEDOT (2)**Formula: C<sub>21</sub>H<sub>15</sub>N<sub>3</sub>O<sub>2</sub>S

Formula weight: 373.4



1.32 ml (11.76 mmol) 2-acetylpyridine and 1 g ethylenedioxythiophene aldehyde (5.88 mmol) were stirred together in 50 ml EtOH. KOH pellets, 0.93 g (11.77 mmol), and 17.1 ml (14.7 mmol) aqueous NH<sub>3</sub> were added to the solution. The reaction was stirred for 4 hours at room temperature. The solution went from clear yellow to orange with precipitate. The solid was collected by filtration and washed with EtOH (3x10 ml). Recrystallised from CHCl<sub>3</sub>-MeOH mixture. NMR showed the enone had formed. The enone was then added to a solution of 2-acetylpyridine in EtOH. KOH pellets and aqueous NH<sub>3</sub> were once again added in the same proportions. The reaction was left over night and the product filtered off and washed with EtOH.

Yield: 0.9 g, 2.4 mmol, (41%)

<sup>1</sup>H-NMR (CD<sub>3</sub>CN, 500 MHz, COSY): δ = 8.77 (s, 2H, N3'), 8.73 (d, J= 4.70 Hz, 2H, N6), 8.62 (d, J= 7.95 Hz, 2H, N3), 7.86 (td, J= 1.73, 7.72, 7.79 Hz, N4, 2H,), 7.34 (ddd, J= 0.93, 4.80, 7.31 Hz, 2H, N5), 6.47 (s, S<sup>a</sup>, 1H), 4.45 (m, 2H, S<sup>b</sup>), 4.29 (m, 2H, S<sup>c</sup>);

<sup>13</sup>C-NMR (CD<sub>3</sub>CN, 500 MHz, DEPT, 500 MHz): δ = 156.6 (N2'/N2, quat), 156.0 (N2'/N2, quat), 149.3 (N6, tert), 142.7 (S2, quat), 142.5 (S3, quat), 141.3 (S4, quat), 137.0 (N4, tert), 123.9 (N5, tert), 121.5 (N3, tert), 117.1 (N3', tert), 115.6 (N4', quat), 100.7 (S5, tert), 65.3 (Sc, sec), 64.7 (Sb, sec);

**Anal.** Calcd for C<sub>21</sub>H<sub>15</sub>N<sub>3</sub>O<sub>2</sub>S: C, 67.54; H, 4.05; N, 11.25; found; C, 67.18; H, 4.22; N, 11.00 %

**MALDI MS** *m/z* (calc.): 374 (373.4, [M-H<sup>+</sup>]);

**IR** (solid, cm<sup>-1</sup>): 3110w, 3067w, 2926w, 1580m, 1562m, 1537m, 1495s, 1466m, 1394m, 1358m, 1173m, 1077s, 910m, 789s, 731m, 650s, 611s;

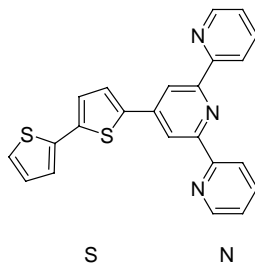
**Anal.** Calcd for C<sub>23</sub>H<sub>15</sub>N<sub>3</sub>S<sub>2</sub>: C, 69.50; H, 3.80; N, 10.57; found; C, 66.82; H, 3.63; N, 9.80 %

**4'-(2-bithienyl)-2,2':6',2''-terpyridine, tpySS (3)**

Previously reported in reference [14].

Formula: C<sub>23</sub>H<sub>15</sub>N<sub>3</sub>S<sub>2</sub>

Formula weight: 397.5



1.32 ml (11.76 mmol) 2-acetylpyridine and 1.05 g bithiophenethiophene aldehyde (5.88 mmol) were stirred together in 50 ml EtOH. KOH pellets, 0.93 g (11.77 mmol), and 17.1 ml (14.7 mmol) aqueous NH<sub>3</sub> were then added to the solution. The reaction was stirred for 4 hours at room temperature. Solution went from clear yellow to orange with precipitate. The reaction was left over night. A light yellow solid had precipitated and was collected by filtration and washed with EtOH (3x10 ml). Recrystallisation in MeOH/CHCl<sub>3</sub> afforded the clean product.

Yield: 0.9 g, 2.4 mmol, (41%)

<sup>1</sup>H-NMR (CD<sub>3</sub>CN, 400 MHz): δ = 8.75 (dm, J=3.91 Hz, 2H, N6), 8.67 (s, 2H, N3'), 8.65 (d, J=7.95 Hz, 2H, N3), 7.91 (td, J=5.90, 1.72 Hz, N4, 2H), 7.71 (d, J=1.18 Hz, 1H, S<sup>a</sup>), 7.37 (ddd, J=1.14, 4.80, 7.47 Hz, N5, 2H), 7.27 (m, 2H, S<sup>b+c</sup>), 7.24 (d, J=3.84 Hz, 1H, S<sup>e</sup>), 7.06 (dd, J=3.65, 5.05 Hz, 1H S<sup>d</sup>);

**MALDI MS** *m/z* (calc.): 398 (398, [M-H]<sup>+</sup>);

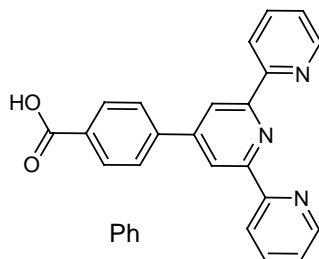
**IR** (solid, cm<sup>-1</sup>): 3063w, 2983w, 1749w, 1597w, 1580m, 1564m, 1458m, 1396m, 1225w, 1043w, 1009m, 987m, 878m, 837m, 785s, 714s, 683m, 667m, 658m;

**4'-(4-carboxyphenyl)- 2,2':6',2''-terpyridine (4)**

Previously reported in reference [15].

Formula: C<sub>22</sub>H<sub>15</sub>N<sub>3</sub>O<sub>2</sub>

Formula weight: 353.4



In a minimum of water 5 ml NH<sub>3</sub> (30%) and 2.44 g NaOH (61 mmol) were dissolved. The solution was added to a mixture of 5 g (30.5 mmol) 4-formyl-benzaldehyde methyl ester and 6.84 ml (61 mmol) 2-acetyl pyridine in 125 ml EtOH. When NaOH was added, the solution turns yellow and then after about one hour red. The reaction was stirred over night in an open flask to let oxygen in. To the yellow suspension, 250 ml water is added to dissolve all. Addition of concentrated HCl precipitates a white solid. The solid is filtered off and washed with water and ethanol.

Yield: 5.2 g, 14.7 mmol, (48 %)

<sup>1</sup>H-NMR (DMSO, 400 MHz): δ = 13.19 (br s, 1H, COOH), 8.80 (d, J=4.80 Hz, 2H, N6), 8.79 (s, 2H, N3'), 8.71 (d, J= 7.96 Hz, 2H, N3), 8.14(d, J=8.40 Hz, 2H, Ph), 8.07 (d, J= 8.80 Hz, 2H, Ph) 8.05 (dt, J=1.7, 7.7 Hz, 2H, N4), 7.56 (ddd, J= 1.11, 4.80, 7.49 Hz, 2H, N5);

**MALDI MS** *m/z* (calc.): 354 (353.4, [M-H<sup>+</sup>])

**UV-vis**, λ<sub>max</sub> (nm), ε (\*10<sup>3</sup> l mol<sup>-1</sup>cm<sup>-1</sup>): 274 nm (30.0), 317 nm (7.5);

**Ester formation**

100 mg (0.28 mmol) of 4'-(4-carboxyphenyl)- 2,2':6',2''-terpyridine were added to 50 ml EtOH with 5 ml H<sub>2</sub>SO<sub>4</sub> and left to stir overnight. Water with AcOEt was added and the solvent removed *in vacuo* to leave precipitated product.

Yield : 82 mg, 0.21 mmol (75%)

<sup>1</sup>H-NMR (CDCl<sub>3</sub>, 400 MHz): δ = 8.74 (s, 2H, N3'), 8.72 (ddd, J= 0.89, 1.77, 4.78 Hz, 2H, N3'), 8.66 (dt, J= 1.01, 7.97 Hz, 2H, N6), 8.16 (d, J= 8.62 Hz, 2H, Ph), 7.94 (d, J= 8.62 Hz,

2H, Ph), 7.87 (dt,  $J = 1.83, 7.68$  Hz, 2H, N4), 7.35 (ddd,  $J = 1.19, 4.79, 7.48$  Hz, 2H, N5), 4.41 (q,  $J = 7.13, 7.14$  Hz, 2H, CH<sub>2</sub>), 1.42 (t,  $J = 7.14$  Hz, 3H, CH<sub>3</sub>);

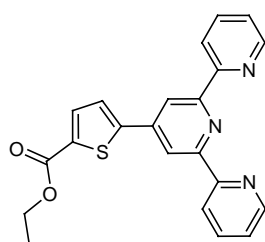
**MALDI MS**  $m/z$  (calc.): 382 (381.4, [M-H<sup>+</sup>])

**Anal.** Calcd for C<sub>24</sub>H<sub>19</sub>N<sub>3</sub>O<sub>2</sub>: C, 75.57; H, 5.02; N, 11.02; found; C, 74.87; H, 4.97; N, 11.14 %

#### 4'-(2,5-ethyl-carboxylate-thienyl)-2,2':6',2''-terpyridine, tpySCOOEt (5)

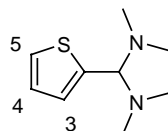
Formula: C<sub>22</sub>H<sub>17</sub>N<sub>3</sub>O<sub>2</sub>S

Formula weight: 387.5



#### 5 Steps:

1



#### 2-dimethylethylenediamine-thiophene (DEA-S)

To a round bottomed flask, 8.41 g (7 ml, 75 mmol) 2-formyl-thiophene, was added to 75 ml of toluene. 6.61 g (8 ml, 75 mmol) 2-dimethylethylenediamine was added dropwise and the solution stirred at reflux for 1 night. The toluene was dried off *in vacuo* to yield 6.33 g of an oil.

To purify the oil, the two starting materials were distilled off and 2.5 g (13.8 mmol) of the desired product (dimethylethylenediamine protected thiophene) was isolated.

Yield: 2.5 g, 13.8 mmol, (18%)

**<sup>1</sup>H-NMR** (CDCl<sub>3</sub>, 250 MHz):  $\delta = 7.30$  (d, 1H, S5), 7.05 (d,  $J = \text{Hz}$ , 1H, S3), 6.93 (t,  $J = \text{Hz}$ , 1H, S43), 3.62 (s, 1H, CH), 3.38 (d,  $J = \text{Hz}$ , 2H, CH<sub>2</sub>), 2.52 (d,  $J = \text{Hz}$ , 2H, CH<sub>2</sub>), 2.23 (s, 6H, CH<sub>3</sub>)

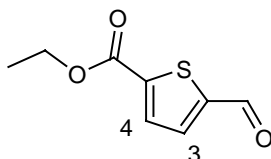
2

2-carboxylic acid-5-formyl-thiophene

In an oven dried round bottom flask, 2.5g (13.8 mmol) DEA-S, 1.83 ml (13.8 mmol) TMEDA and 200 ml distilled THF were cooled with CO<sub>2</sub> ice (-78°C). Then 8.63 ml (13.8 mmol) BuLi (1.6 M) were carefully added. The reaction was stirred for two hours at -78°C overnight. The solution had turned light pink. CO<sub>2</sub> was bubbled through solution over night at room temperature (alternately crushed CO<sub>2</sub> ice can be mixed with compound). Then H<sub>2</sub>SO<sub>4</sub> (10%) was added to the solution to protonate the carboxylate and deprotect aldehyde and left to stir overnight. The product was extracted from acidic water with DCM (6x70 ml). Solvent was dried with NaHSO<sub>4</sub>. The DCM was evaporated to give 2-carboxylic acid-5-aldehyde-thiophene as a reddish powder. The compound was re-crystallised in 75 ml / 75 ml Hexane / ethylacetate.

Yield: 0.6 g, 3.8 mmol (28%);

3

2-ethyl-carboxylate-5-formyl-thiophene

The 2-carboxylic acid-5-aldehyde-thiophene (0.6 g, 3.8 mmol) was put in a flask with 0.62 ml (7.6 mmol) ethyl-Iodide, 2 g Na<sub>2</sub>CO<sub>3</sub> (18.9 mmol) and 10 ml DMF to stir overnight (The esterification could also be done by putting the product in ethanol and adding ~1 ml H<sub>2</sub>SO<sub>4</sub> and stirring for ~2 nights).

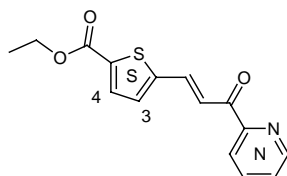
The ester was extracted with 20 ml H<sub>2</sub>O and 3x10 ml ethyl acetate. The product was then dried over Na<sub>2</sub>SO<sub>4</sub> and the solvent evaporated *in vacuo*. The final product had a brown colour.

Yield: 0.5 g, 2.7 mmol, (71%)

<sup>1</sup>H-NMR (CD<sub>3</sub>Cl<sub>3</sub>, 250 MHz): δ = 9.87 (s, 1H, CHO), 7.74 (d, J= 3.92 Hz, 1H, S3), 7.68 (d, J= 3.91 Hz), 4.24 (q, J= 7.14 Hz, 2H, CH<sub>2</sub>), 1.21 (t, J= 7.14 Hz, 3H, CH<sub>3</sub>)

**MALDI MS** *m/z* (calc.): 183.4 (184.2);

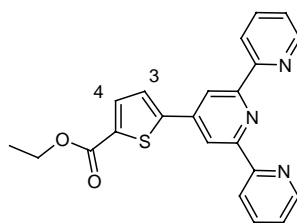
4



#### 2-ethyl-carboxylate-thiophene-pyridine enone

0.32 ml 2-acetylpyridine was added to a solution of 0.5 g (2.7 mmol) 2-ethyl-carboxylate-5-aldehyde-thiophene in 7 ml dry EtOH. Then 0.76 ml DEA (2.5 eq.) was added dropwise under stirring. The reaction was refluxed over night under N<sub>2</sub>. After reflux the product was collected and purified by silica chromatography (eluent: CH<sub>2</sub>Cl<sub>2</sub>). The product came out as yellow powder.

5



#### 4'-(2,5-ethyl-carboxylate-thienyl)-terpyridine

387 mg (1.35 mmol) 2-ethyl-carboxylate-thiophene-pyridine enone was put in a round bottom flask together with 445 mg (1.35 mmol) PPI and 4g dry NH<sub>4</sub>OAc (4 eq.) in 20 ml dry ethanol. The solution was refluxed over night under N<sub>2</sub>. A white product was isolated.

Yield: 150 mg, 0.39 mmol (29%)

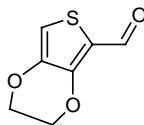
<sup>1</sup>H-NMR (CDCl<sub>3</sub>, 500 MHz): δ = 8.73 (m, 4H, N3'+N6), 8.64 (d, J= 7.90 Hz, 2H, N3), 7.88 (t, J= 7.64 Hz, 2H, N4), 7.84 (d, J= 3.71 Hz, 1H, S<sup>4</sup>), 7.74 (d, J= 3.70 Hz, 1H, S<sup>3</sup>), 7.37 (m, 2H, N5), 4.40 (q, J= 7.11 Hz, 2H, CH<sub>2</sub>), 1.39 (t, J= 7.11 Hz, 3H, CH<sub>3</sub>);

<sup>13</sup>C-NMR (CDCl<sub>3</sub>, 500 MHz): δ = 162.1 (COOEt, quat), 156.2 (S<sup>5</sup>, quat), 155.9 (N2, quat), 149.3 (N6, tert), 148.2 (N4', quat), 142.7 (N2', quat), 136.8 (N4, tert), 134.5 (S<sup>2</sup>, quat), 134.2 (S<sup>4</sup>, tert), 126.0 (S<sup>3</sup>, tert), 124.1 (N5, tert), 121.3 (N3, tert), 117.5 (N3', tert), 61.6 (CH<sub>2</sub>), 14.5 (CH<sub>3</sub>).

**MALDI MS** *m/z* (calc.): 388.2 (387.5, [M-H<sup>+</sup>]);

**2-formyl-ethylenedioxythiophene**

Previously reported in reference [19].

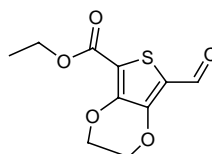


To a dry round bottom flask, 1.5 g (10.5 mmol) EDOT and 1.65 ml DMF (21.4 mmol) were added to 25 ml dry DCE. The solution was then cooled to 0°C. To the cooled solution, 1.65 ml (17.7 mmol) POCl<sub>3</sub> was added dropwise under nitrogen atmosphere. The solution was refluxed for two hours and it turned red/orange. When the solution had cooled to room temperature, sodium acetate (1 M) was added which gave a phase separation. The organic phase was separated with DCM and washed 3 times with water and dried over Na<sub>2</sub>SO<sub>4</sub>. Evaporation of solvent yields a brown oil, which was purified by column chromatography on silica (eluent: CH<sub>2</sub>Cl<sub>2</sub>) giving a yellow solid (200 mg, 1.18 mmol, ~8%). The water phase eventually gave a yellow solid. Filtration of the solid and washing with water yielded 2.08 g (0.0122 mol, 82%) of a yellow solid.

Total yield: 1.61 g, 9.45 mmol (~90%)

<sup>1</sup>H-NMR (CD<sub>3</sub>CN, 400 MHz): δ = 9.88 (s, 1H, CHO), 6.78 (s, 1H), 4.34 (m, 2H, CH<sub>2</sub>O), 4.25 (m, 2H, CH<sub>2</sub>O).

IR (solid, cm<sup>-1</sup>): 1645s (C=O)

**2-formyl-5-ethylcarboxylate-ethylenedioxythiophene**

To a round-bottom flask with 20 ml toluene, 0.96 g (5.6 mmol) 2-formyl-ethylenedioxythiophene was added. Under stirring, 0.5 g (0.6 ml di-methyl-ethylenediamine) was added dropwise. Under N<sub>2</sub> atmosphere the solution was refluxed over night under Dean-Stark conditions. After reflux there was about 3 ml water in the trap. The reaction was stopped and the toluene evaporated *in vacuo*.

Distilled THF (~60ml) with 1.3 g (5.42 mmol) of the DMEDA protected 2-formyl-EDOT, was cooled in dry ice bath to -78°C. TMEDA (3.39 ml) was added under stirring and then nBuLi (1.6 M) (5.42 mmol) was added carefully to the solution. The solution went from clear yellow to clear red brown. The reaction was stirred for 2 hours and then left to reach room

temperature. The solution was then poured onto a slurry of dry-ice (CO<sub>2</sub>) and ether. Thereafter it was left to stir overnight. Upon reacting with the CO<sub>2</sub> slurry the reaction turned a thick red. The solvents were removed *in vacuo* and the residue stirred with 10% w/w H<sub>2</sub>SO<sub>4</sub> (aq.) for 12 hours. The reaction was stopped and 0.9 g (4.2 mmol, ~75% yield) of a dark brown powder is collected.

0.604 ml (7.47 mmol) C<sub>2</sub>H<sub>5</sub>I and 0.8 g (3.73 mmol) of the 2-formyl-5-ethylcarboxylate-ethylenedioxythiophene were added to 10 ml DMF together with 1.95 g (18.65 mmol) NaCO<sub>3</sub>. The reaction was stirred overnight at room temperature. The reaction was stopped and then extracted with water (10 ml) and 3x10 ml ethylacetate. A dark brown organic phase was dried over Na<sub>2</sub>SO<sub>4</sub> and the solvent removed to leave a dark brown solid.

Yield: 0.4 g, 1.65 mmol (44%)

Total yield: 0.4g, 1.65 mmol (29%)

<sup>1</sup>H-NMR (CD<sub>3</sub>CN, 400 MHz): δ = 9.95 (s, 1H, CHO), 4.38 (m, 4H, C<sub>2</sub>H<sub>4</sub>O<sub>2</sub>), 4.30 (q, J= 7.12 Hz, 2H, CH<sub>2</sub>), 1.31 (t, J= 7.12 Hz, CH<sub>3</sub>);

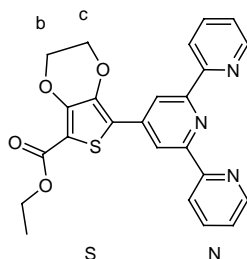
**MALDI MS** *m/z* (calc.): 243.2 (243, [M-H]<sup>+</sup>);



**4'-(2,5-ethyl-carboxylate-ethylenedioxythienyl)-2,2':6',2''-terpyridine, tpyEDOTCOOEt (6)**

Formula: C<sub>24</sub>H<sub>19</sub>N<sub>3</sub>O<sub>4</sub>S

Formula weight: 445.5



0.37 ml (3.3 mmol) 2-acetylpyridine and 400 mg ethylenedioxythiophene ethyl carboxylate aldehyde (1.65 mmol) were stirred together in 20 ml EtOH. KOH pellets, 0.26 g (85%, 3.3 mmol), and 4.80 ml (4.13 mmol) aqueous NH<sub>3</sub> (29%) were added to the solution. The reaction was stirred overnight at room temperature. The solution went from dark brown to form brown precipitate. The solid was collected by filtration and washed with EtOH (3x10 ml).

Yield: 330 mg, 0.74 mmol, (45%)

<sup>1</sup>H-NMR (CDCl<sub>3</sub>, 500 MHz): δ = 8.82 (s, 2H, N3'), 8.74 (d, J= 3.93Hz, 2H, N6), 8.62 (d, J= 7.94Hz, 2H, N3), 7.87 (td, J= 7.60, 1.82 Hz, 2H, N4), 7.35 (ddd, J= 1.47, 4.82, J= 6.00Hz, 2H, N5), 4.48 (s, 4H, S<sup>b+c</sup>), 4.36 (q, J= 7.12Hz, 2H, CH<sub>2</sub>), 1.39 (t, J= 7.13Hz, 3H, CH<sub>3</sub>);

<sup>13</sup>C-NMR (CDCl<sub>3</sub>, 500 MHz, DEPT 500 MHz): δ = 161.3 (COOEt, quat), 156.3 (N2'/N2, quat), 156.2 (N2'/N2, quat), 149.4 (N6, tert), 146.2 (S2/S3/S4, quat), 140.0 (S2/S3/S4, quat), 137.0 (N4, tert), 124.1 (N5, tert), 121.5 (N3, tert), 117.9 (N3', tert), 100.2 (S5, quat), 65.3 (Sc, sec), 64.9 (Sb, sec), 61.2 (CH<sub>2</sub>), 14.6 (CH<sub>3</sub>);

**Anal.** Calcd for C<sub>21</sub>H<sub>15</sub>N<sub>3</sub>O<sub>2</sub>S: C, 64.71; H, 4.30; N, 9.43; found; C, 63.75; H, 4.38; N, 8.62 %

**MALDI MS** *m/z* (calc.): 447.5 (446.5, [M-H]<sup>+</sup>), 485.5 (485.5, [M-K]<sup>+</sup>);

**IR** (solid, cm<sup>-1</sup>): 3059w, 2982w, 2937w, 1707s, 1582s, 1539m, 1504m, 1468m, 1435m, 1357s, 1275s, 1246m, 1219m, 1094s, 1070s, 1026m, 791m, 658m;

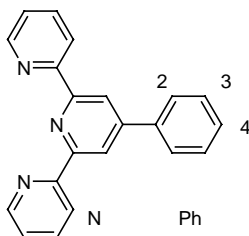
**mp:** 253-256°C

**4'-(phenyl)-2,2':6',2''-terpyridine, tpyPh (7)**

Previously reported in reference [10].

Formula: C<sub>21</sub>H<sub>15</sub>N<sub>3</sub>

Formula weight: 309.4



2.51 g 2-Acetylpyridine (21 mmol) was added to a solution with 1.10 g (10.4 mmol) benzaldehyde in 50 ml EtOH. 1.60 g (21 mmol) of KOH pellets were then added together with 30 ml (26 mmol) aqueous NH<sub>3</sub> (29%). The solution was stirred at room temperature for 4 hours. The off-white solid that had precipitated was collected and washed with EtOH. Recrystallising the product from CHCl<sub>3</sub>-MeOH (1:1) yielded a white solid.

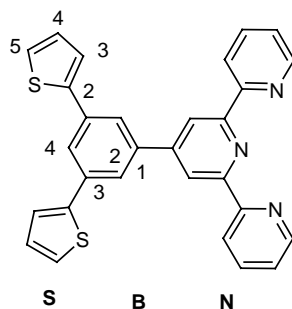
Yield: 1.30 g, 4.20 mmol, (40%)

<sup>1</sup>H-NMR (CDCl<sub>3</sub>, 400 MHz): δ = 8.74 (s, 2H, N3'), 8.73 (m, 2H, N6), 8.67 (d, J= 7.95 Hz, 2H, N3), 7.90 (m, 4H, Ph3+N4), 7.51 (t, J= 7.27 Hz, 2H, Ph2), 7.46 (t, J= 7.25 Hz, 1H, Ph4), 7.35 (ddd, J= 1.21, 4.79, 7.47 Hz, 2H, N5);

**MALDI MS** *m/z* (calc.): 310 (309, [M-H<sup>+</sup>]);

**4'-[2,5-(dithienyl)phenyl]-2,2':6',2''-terpyridine, tpySBS (8)**Formula: C<sub>29</sub>H<sub>19</sub>N<sub>3</sub>S<sub>2</sub>

Formula weight: 473.6



In a schlenk tube, 400 mg (0.86 mmol) of 3,5-dibromobenzene-4'-2,2':6',2''-terpyridine and 242 mg 2-boronic acid-thiophene (1.89 mmol) were dissolved in 10 ml 1,2-dimethoxyethane. The solution was degassed with three freeze-pump-thaw cycles (vacuum pump) and then placed under nitrogen. In another schlenk tube sodium carbonate, 272 mg (2.57 mmol) in a minimum of water was degassed under vacuum. A small amount of the catalyst, Pd(PPh<sub>3</sub>)<sub>4</sub>, was added to the first schlenk tube, followed immediately by the sodium carbonate solution using a syringe. After stirring at room temperature for 1 hour, the temperature was increased to 85° and the reaction left overnight.

TLC on alumina (eluent: 70% hexane, 30% ethyl acetate) showed that the starting material was consumed and one new spot present after 22 hours. The solvent was removed under reduced pressure to leave a crude solid. A mixture of water and DCM (20ml:20ml) was added to dissolve the solid. The organic phase was collected and cleaned with 3 x 25 ml 0.1 M NaOH. A precipitate was formed in the DCM, which was collected as a white solid (161 mg). <sup>1</sup>H-NMR showed clean product. The rest of the DCM was dried with potassium carbonate and evaporated *in vacuo* to yield a grey solid. The solid was recrystallised in methanol to yield more of the desired product as a greyish solid (75 mg).

Yield: 236 mg, 0.498 mmol, (58%)

<sup>1</sup>H-NMR (CD<sub>3</sub>CN, 400 MHz, COSY): δ = 8.76 (s, 2H, N3'), 8.73 (d, J=3.96Hz, 2H, N6), 8.67 (d, J=Hz, 2H, N3), 7.95 (d, J=1.60Hz, 2H, B2), 7.88 (m, 3H, N4+B4), 7.46 (d, J=2.58Hz, 2H, S3), 7.35 (m, 4H, N5+S5), 7.13 (dd, J=3.62, 5.04 Hz, 2H, S4);

<sup>13</sup>C-NMR (CD<sub>3</sub>CN, 500 MHz, DEPT 500 MHz): δ = 156.2 (N2', quat), 156.1 (N2, quat), 150.0 (B1, quat), 149.2 (N6, tert), 143.5 (B3, quat), 140.4 (N4', quat), 137.0 (N4, tert), 135.9 (S2, quat), 128.2 (S4, tert), 125.5 (B4, tert), 124.3 (B2, tert), 124.5 (N5, tert), 124.0 (S3, tert), 121.5 (N3, tert), 119.2 (N3', tert);

**Anal.** Calcd for  $C_{29}H_{19}N_3S_2 \cdot 1 H_2O$ : C, 70.85; H, 4.31; N, 8.55; found; C, 70.85; H, 3.83; N, 8.45 %

**MALDI MS**  $m/z$  (calc.): 475 (475,  $[M+H]^+$ ), 947 (948,  $[2M+H]^+$ );

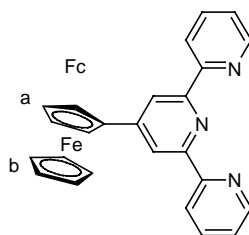
**IR** (solid,  $cm^{-1}$ ): 3093w, 3068w, 3007w, 1602w, 1578s, 1545m, 1468s, 1445m, 1385s, 1265m, 1240m, 1124m, 995s, 835s, 791s, 752m, 741m, 694s, 652s, 621s;

#### 4'-(2-ferrocene)-2,2':6',2''-terpyridine (9)

Previously reported in reference [7].

Formula:  $C_{25}H_{19}FeN_3$

Formula weight: 417.3



810 mg (3.8 mmol) and 0.84 ml (3.8 mmol) 2-acetylpyridine were dissolved in 50 ml EtOH in a round bottom flask. Under stirring, 0.6 g KOH and 11 ml  $NH_3$  (30%) were added to the reaction. The clear yellow solution turned red. The reaction was left over night to stir at room temperature. After ~14 hours a precipitate had formed. The solid was collected on a Frit and washed with EtOH. The ligand was then recrystallised in  $CHCl_3/CH_3OH$  (1:1). A TLC on aluminium with  $CH_2Cl_2$  showed one yellow/red spot.

Yield: 830 mg, 2.00 mmol (49%)

$^1H$ -NMR ( $CDCl_3$ , 400 MHz):  $\delta$  = 8.75 (d,  $J$  = 4.49 Hz, 2H, N3), 8.66 (d,  $J$  = 8.06 Hz, 2H, N6), 8.52 (s, 2H, N3'), 7.87 (t,  $J$  = 8.00, 2H, N4), 7.35 (m, 2H, N5), 5.02 (s, 2H,  $Fc^a$ ), 4.47 (s, 2H,  $Fc$ ), 4.10 (s, 5H,  $Fc^b$ );

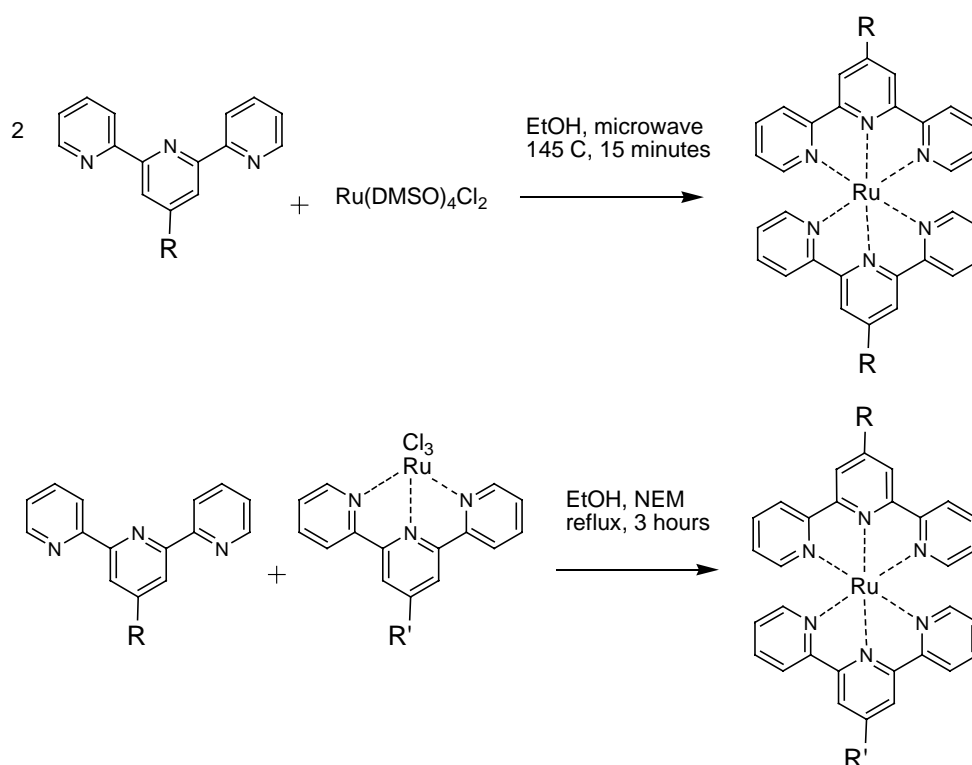
**MALDI MS**  $m/z$  (calc.): 416.7 (417.1,  $[M-H]^+$ );

## 3.2 Synthesis & Characterisation of Complexes

### 3.2.1 Metal Complex Synthesis

Ruthenium and iron complexes were formed from the 2,2':6',2''-terpyridine ligands in different combinations. New compounds were made from combinations of the new ligands with the already reported ones. Heteroleptic compounds made with one anchoring group and the ligand **3** or **9** were also not found in the literature.

#### General procedures for ruthenium complexes



**Scheme 3.5** Synthesis procedures for obtaining homoleptic (upper) and heteroleptic (lower) bis-terpyridine ruthenium complexes.

Scheme 3.5 outlines the main synthetic routes to synthesise the homoleptic and heteroleptic complexes that were prepared in this work and are described in the following paragraphs.

### Homoleptic complexes

Ligand coordination with metal complexes was performed with microwave heating or in the oil bath at reflux. The homoleptic ruthenium compounds were synthesised from  $[\text{Ru}(\text{DMSO})_4\text{Cl}_2]$ . The complexes were most efficiently made in a Biotage 8 microwave reactor at  $145^\circ\text{C}$  in EtOH for 15 minutes. After the reaction, adding aqueous solution of excess  $\text{NH}_4\text{PF}_6$  to the solution precipitated the  $\text{PF}_6^-$  salt. The precipitate is filtered off through Celite on a frit and washed with water, ethanol and ether. The compound is then redissolved in MeCN and the solvent evaporated with a rotavap under reduced pressure. TLC on silica is used to confirm that there is one major product. In many cases column chromatography (silica) is necessary to obtain the pure compound. The eluent for the chromatography and TLC is usually MeCN, saturated  $\text{KNO}_3$  (aq.) and  $\text{H}_2\text{O}$  in a 14:2:1 ratio (A-sol). The products were characterised by NMR, IR, UV-vis, ES-MS and electrochemistry.

### Heteroleptic complexes

The heteroleptic compounds were synthesised by first making  $[\text{RtpyRuCl}_3]$  from mixing  $\text{RuCl}_3 \cdot 3\text{H}_2\text{O}$  and tpyR in a 1:1 ratio in ethanol and refluxing for 3 hours. This results in insoluble  $[\text{RtpyRuCl}_3]$ , which is isolated and used without further characterisation.  $[\text{RtpyRuCl}_3]$  is then mixed with 1 equivalent of counter ligand in ethanol together with a few drops of a reducing agent such as N-ethylmorpholine.<sup>[30]</sup> The reaction is usually complete after three hours at reflux. Refluxing too long can result in scrambling of the complex. The product is precipitated and isolated in the same way as the homoleptic complexes. The yields were not optimised and varied between 40-90 %.

### Hydrolysis of ethyl carboxylates

The complexes with a terpyridine carboxylate were usually made with the carboxylate ester. The esters are easier to handle and their solubility in EtOH and MeCN is better than for the carboxylic acids. The isolated ester was later base hydrolysed to yield the free acid. The standard procedure, which has previously been reported<sup>[9]</sup>, was to dissolve the complex (~10-20 mg) in a small amount of MeCN (~2 ml) and then add 1 ml NaOH (2 M) while stirring. The next step was heating to  $80^\circ\text{C}$  for ~3 hours. After cooling to room temperature, a few drops of  $\text{HPF}_6$  were added before precipitating the complex with  $\text{NH}_4\text{PF}_6$  and finally filtering it off through celite and

re-dissolving in MeCN. The solvent can then be removed *in vacuo*. Adding the  $\text{HPF}_6$  hopefully protonates the carboxylate and avoids the formation of a sodium salt.

The acid proton is very difficult to detect, as there is often a fast exchange of protons in solvents.<sup>[24]</sup> In  $^1\text{H-NMR}$ , for example, the complex with a carboxylic acid does not exhibit the broad proton signal from the acidic proton. The free ligand, 4'-4-(carboxylicacid-benzyl)-2,2':6',2''-terpyridine, has a  $^1\text{H-NMR}$  peak for the  $\text{CO}_2\text{H}$  proton at  $\delta=13.19$  ppm (DMSO) but not when it is coordinated, which suggests an increased acidity when the ligand is coordinated.<sup>[15]</sup>

### General procedures for iron complexes

Two equivalents of the 2,2':6',2''-terpyridine ligand were added to the iron salt,  $[\text{Fe}(\text{H}_2\text{O})_6][\text{BF}_4]_2$ , in a 1:1 mixture of MeOH and MeCN and stirred for as long as necessary. The colour of the complex appears as the coordination takes place. Most of the compounds only need 15 minutes but more bulky and less soluble ligands like **8** need longer times to completely coordinate. The yields are usually high (80-90%). The work up is like that of the ruthenium complexes. Only the homoleptic iron complexes were prepared, as the labile nature of the iron (II) ion complex leads to a statistical mixture of species in solution when more than one ligand is present.<sup>[31, 32]</sup>

### 3.2.2 NMR Analysis

All the complexes were dissolved in  $\text{CD}_3\text{CN}$  for NMR measurements. Although some of the acids were difficult to dissolve, spectra were obtained albeit with poorer resolution. Figure 3.8 shows the typical upfield shift of the N6 proton when the 2,2':6',2''-terpyridines coordinate in a  $^1\text{H}$ -NMR measurement.<sup>7</sup> This is due to the change from the *trans, trans* conformation observed in the free ligand (Fig. 1) to *cis, cis* in the coordinated ligand.<sup>[15]</sup> The N6 proton is closer to the shielding effect of the opposing ligand when it is in *cis, cis* conformation. The proton at N4 is shifted slightly downfield due to the changes in the electron density of the terpyridine  $\pi$ -cloud and the charge from the metal cation as is the N3' proton. The thienyl proton shifts are all shifted downfield probably due to the deshielding effect when the charge of the metal decreases the electron density around the ligand.<sup>[14]</sup>

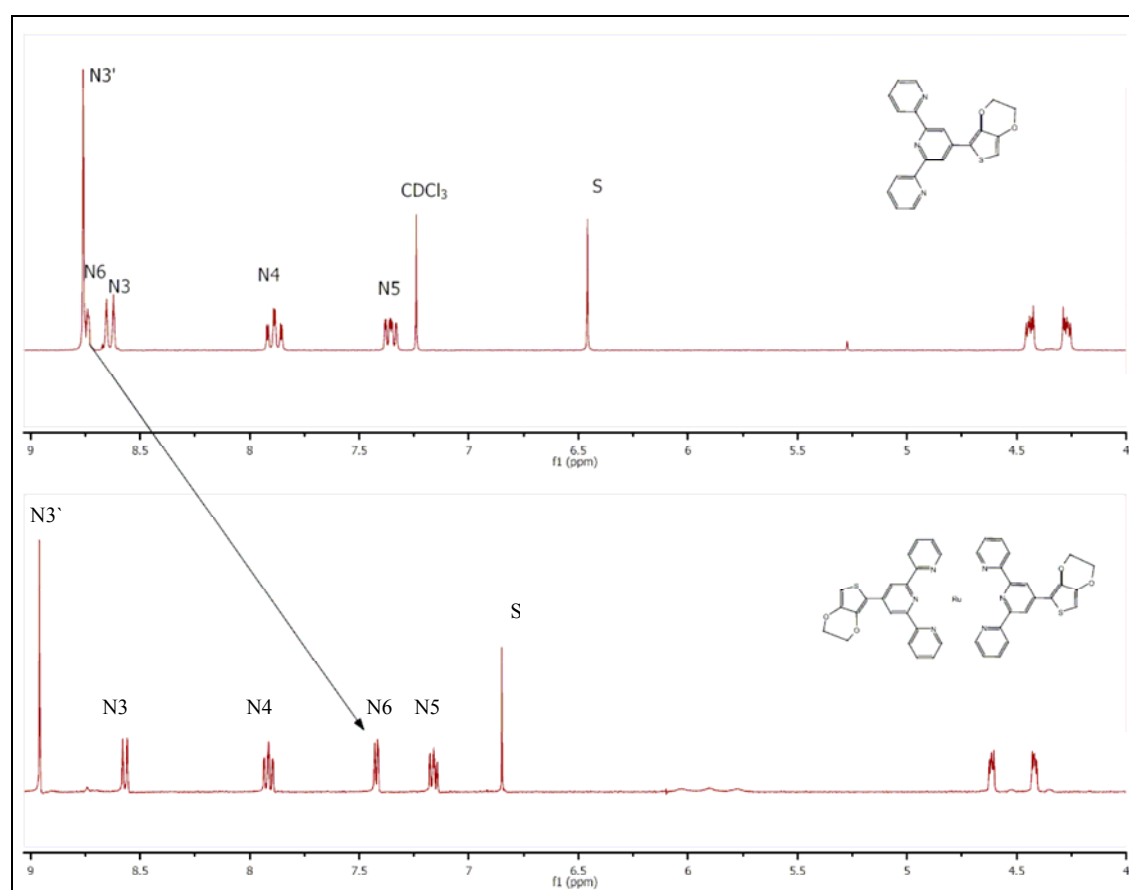


**Figure 3.8**  $^1\text{H}$ -NMR (400MHz) spectrum of ligand **2** in  $\text{CDCl}_3$  and of  $[\text{Ru}(\mathbf{2})_2][\text{PF}_6]_2$  complex in  $\text{CD}_3\text{CN}$ . The most notable difference between the two spectra is the up-field shift of the N6 proton, which was typical for the  $[\text{Ru}(\text{tpy})_2]^{2+}$  complexes.



$^1\text{H}$ -NMR spectra were recorded for all the complexes. Ruthenium (II) complexes with thienyl-substituted terpyridines have earlier been reported in the literature and the assignment of peaks from these publications could be used as reference.<sup>[14, 33]</sup> When necessary, the 2-D technique COSY is needed to assign the peaks. An example is shown in figure 3.9, where a COSY spectrum on the heteroleptic complex  $[(\mathbf{3})\text{Ru}(\mathbf{5})][\text{PF}_6]_2$  is used to elucidate the thienyl proton peaks. The homoleptic compounds exhibit peaks that are unchanged from the heteroleptic compound, so a comparison of  $[(\mathbf{3})\text{Ru}(\mathbf{5})][\text{PF}_6]_2$  with  $[\text{Ru}(\mathbf{5})_2][\text{PF}_6]_2$  is useful in separating peaks from ligands  $\mathbf{5}$  and  $\mathbf{3}$ . In figure 3.9, the COSY spectrum indicates that a proton of the thienyls couple to two neighbouring protons. An assignment of this peak to the S7 (middle proton of terminating thienyl) proton can then be assumed. In the bi-thienyl ligand the bridging thiophene protons were downfield compared to the terminal thiophene. In the anchoring ligand with a thiophene bridge, the carboxylate oxygens deshield the protons shifting them a little downfield. Also to note in figure 3.9 are the two peaks from the N3'-protons of the two ligands in the heteroleptic complex. This is a good indication of a heteroleptic compound. Another point to make on figure 3.19 in the 1-D spectrum, are the two N3 doublets appearing as a triplet. In this case the two doublets signals overlap and appear as a triplet.

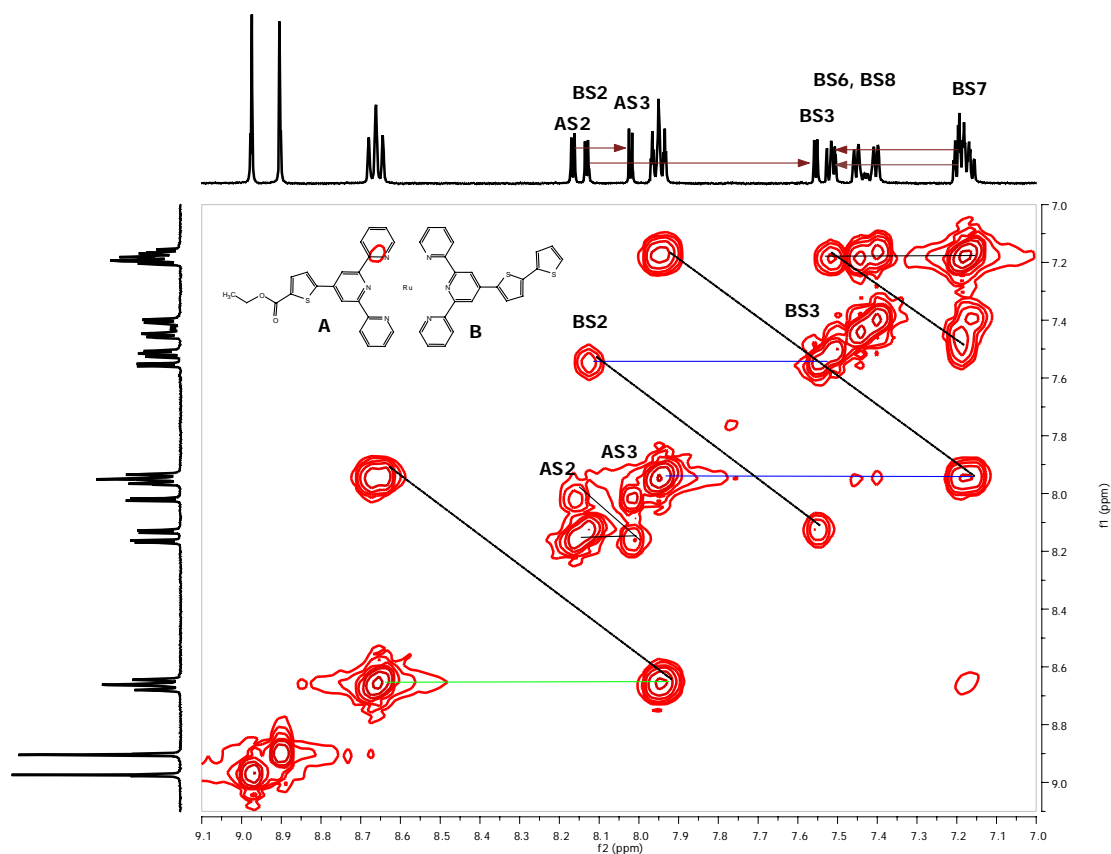


**Figure 3.9 A**  $^1\text{H}$ - $^1\text{H}$  COSY spectrum showing the coupling between some of the hydrogens to elucidate the assignment of the hydrogens. In the figure the thienyl protons are highlighted but the couplings between the terpyridine protons are also visible. The measurement was done in  $\text{CD}_3\text{CN}$  at 298 K at 500 MHz.

For the new compounds,  $^{13}\text{C}$ -NMR spectra, in combination with DEPT, to distinguish tertiary, quaternary and secondary carbons, were measured.<sup>[13]</sup> As was discussed for the ligands, HMQC and HMBC are also used to help assign the carbon peaks. Due to poorer solubility of some of the complexes, it was difficult to assign all the carbon peaks (less intense than the proton peaks). In the literature there are many similar structures with full characterisation that were used for comparison and reference.

### Mass spectrometry

The most common mass spectrometric technique for metal complexes is electrospray ionisation (ESI) because of its relatively non-destructive nature, allowing detection of the whole complex with or without counter ion (only charged species will be detected). The isotope distribution of the mass spectra can be calculated with Bruker Daltonics Dataanalysis™ (ESI-MS prediction software) and compared to the measured spectra. In the case of ruthenium (II) and iron (II) complexes, most of the complexes gave peak packages for the complex with one PF<sub>6</sub> counter ion ([M-PF<sub>6</sub>]<sup>+</sup>) and for the compound without any counter ion ([M-2PF<sub>6</sub>]<sup>2+</sup>). The peaks are plotted as *m/z* and the separation between the peaks in the isotope pattern is *1/z*. An example of the spectra of [M-PF<sub>6</sub>]<sup>+</sup> for the complex [(tpy)Ru(**8**)]PF<sub>6</sub>]<sub>2</sub> is seen in figure 3.10. ESI-MS is for most applications not useful in quantitative measurements and only indicates that a molecule with the reported mass/charge ratio is present.

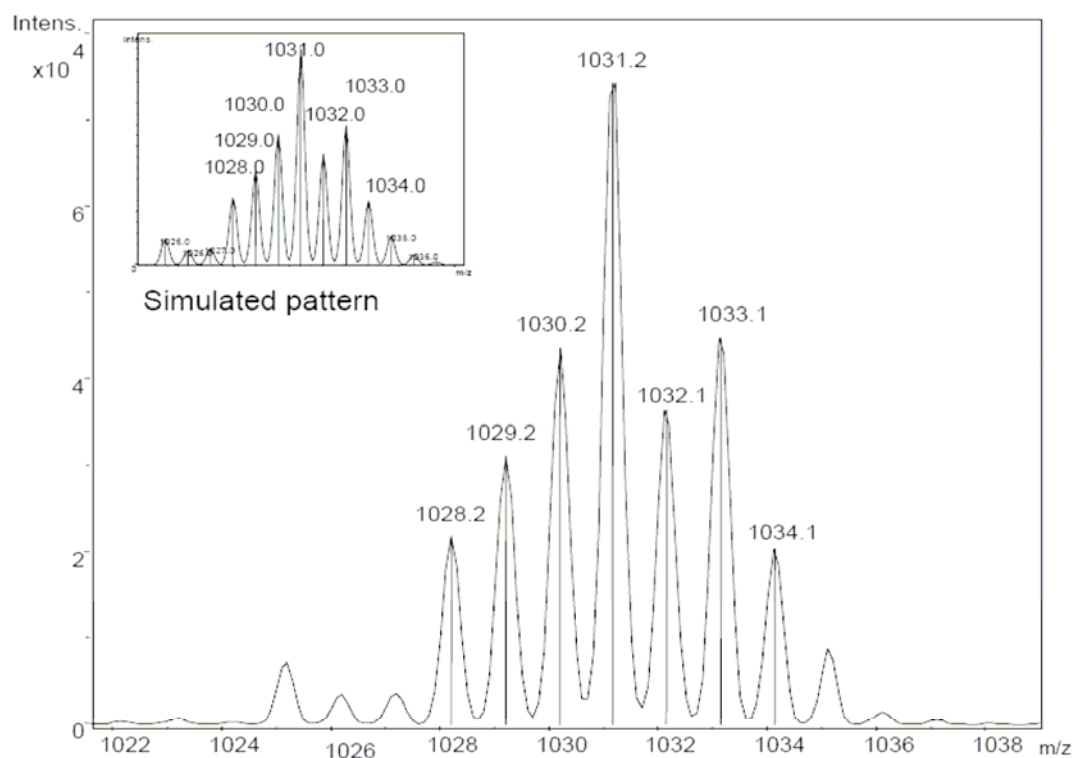


**Figure 3.10** ESI-MS spectrum of [(tpy)Ru(**8**)]PF<sub>6</sub>]<sub>2</sub> for the [M-PF<sub>6</sub>]<sup>+</sup> species. The separation between the peaks is 1 for the +1 charged species.

### 3.2.3 UV-vis Spectroscopy

All the metal-complexes that were prepared exhibited electronic spectra that were dominated by metal-to-ligand charge transfer ( $^1\text{MLCT}$ ) in the visible part of the spectrum and ligand centered ( $^1\text{LC}$ )  $\pi\text{-}\pi^*$  and  $\text{n-}\pi^*$  transitions in the near UV part (see figure 3.11). The ‘forbidden’ d-d transitions (parity rule) of transition metal complexes are not visible in the iron (II) or the ruthenium (II) compounds. The forbidden  $^3\text{MLCT}$  transition is also not visible as it is in, for example, osmium complexes where spin orbit coupling (heavier nucleus) relaxes the spin-conservation rule.<sup>[2, 4]</sup>

Complexes with the core  $[\text{Ru}(\text{tpy})_2]^{2+}$  and substituents on the 4'-position have been reported to show a red shift of the  $^1\text{MLCT}$  band in comparison to the parent  $[\text{Ru}(\text{tpy})_2]^{2+}$  complex both for electron donating and withdrawing substituents.<sup>[34]</sup> The thiophene groups on the 4'-position of the terpyridines in this work, and earlier publications, also show an effect on the extinction coefficient of the  $^1\text{MLCT}$  transition. These effects result from a combination of the lower lying energy of the LUMO of thiophenes and the extended conjugation. Adding a thiophene moiety to the terpyridine is also known to increase the emission lifetimes of complexes compared to the parent ruthenium bis-terpyridine compound by 1-2 orders of magnitude.<sup>[35]</sup>

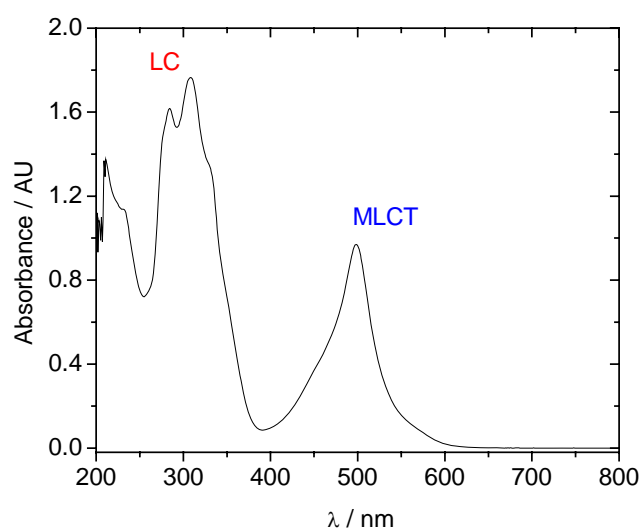


**Figure 3.11** UV-vis spectrum of  $[(2)\text{Ru}(4)]\text{[PF}_6\text{]}_2$  in MeCN with labels for the MLCT and LC transitions.

A reason for the improved luminescence of the ruthenium (II) complexes with thienyl modified terpyridines is the increased energy gap between the  $^3\text{MLCT}$  and  $^3\text{MC}$  ( $^3\text{MLCT}$  stabilised and  $^3\text{MC}$  destabilised), which decreases the deactivation of the ligand centred triplet state by the metal centred triplet state.<sup>[4, 28]</sup> Luminescence lifetime measurements were performed on the ruthenium homoleptic terpyridine carboxylate ester complexes (ligands **3**, **4** and **5**) in acetonitrile at 298 K. The complex with phenyl spacer had a lifetime  $< 2$  ns while the thiophene and EDOT spacers prolonged the lifetime to 51 and 56 ns respectively, which is in line with earlier reports that attribute prolonged luminescence lifetimes to thiophene substituents.<sup>[35]</sup> The UV-vis spectra of these carboxylate complexes are plotted in figure 3.12 and show the peak shift and extinction coefficient being influenced by the spacer. The EDOT group has the greatest effect in comparison with  $[\text{Ru}(\text{tpy})_2]^{2+}$ . More discussion on the photophysics of ruthenium oligo pyridine complexes is found in section 1.2.

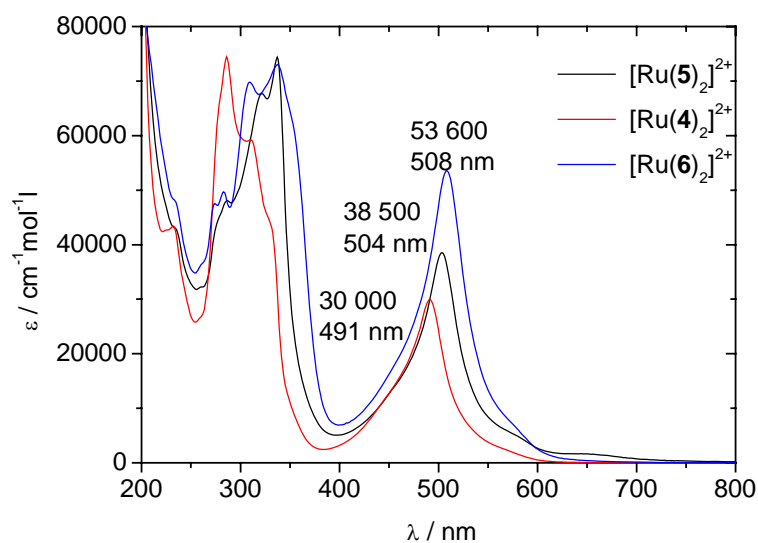


**Figure 3.12** UV-vis spectra of three homoleptic ruthenium complexes in MeCN. The Y-axis plots the extinction coefficient value.

**Table 3.6** UV-vis absorbance data from measurements in MeCN.

Compound	MLCT $\lambda_{\max}$ , /	LC	LC	LC
	nm ( $\epsilon / 10^4, \text{M}^{-1}$ $\text{cm}^{-1}$ )	/ nm ( $\epsilon / 10^4, \text{M}^{-1}$ $\text{cm}^{-1}$ )	/ nm ( $\epsilon / 10^4, \text{M}^{-1}$ $\text{cm}^{-1}$ )	/ nm ( $\epsilon / 10^4, \text{M}^{-1}$ $\text{cm}^{-1}$ )
[Ru(tpy) <sub>2</sub> ] <sup>2+</sup> *	475 (1.2)		307 (5.2)	270 (6.0)
[(tpy)Ru( <b>2</b> )] <sup>2+</sup>	491 (4.4)	328sh (8.6)	308 (12.2)	272 (7.1)
[Ru( <b>2</b> ) <sub>2</sub> ] <sup>2+</sup>	506 (6.0)	332sh (3.0)	307 (8.0)	282 (3.6)
[Ru( <b>4</b> ) <sub>2</sub> ] <sup>2+</sup>	491 (3.0)	329sh (4.5)	311 (5.9)	287 (7.4)
[Ru( <b>5</b> ) <sub>2</sub> ] <sup>2+</sup>	504 (3.9)	337 (7.4)	320 (6.8)	287 (4.8)
[Ru( <b>6</b> ) <sub>2</sub> ] <sup>2+</sup>	508 (5.4)	337 (7.3)	309 (7.0)	283 (5.0)
[(tpy)Ru( <b>8</b> ) <sub>2</sub> ] <sup>2+</sup>	483 (2.2)		307 (8.8)	287
[Ru( <b>8</b> ) <sub>2</sub> ] <sup>2+</sup>	490 (3.1)		309sh (9.1)	289 (9.5)
[Ru( <b>3</b> ) <sub>2</sub> ] <sup>2+</sup> *	510 (0.6)	370 (0.6)	308 (0.7)	274
[Ru( <b>1</b> ) <sub>2</sub> ] <sup>2+</sup> *	490 (2.6)	330sh (4.8)	310 (6.9)	282 (4.0)

\*Data from reference [14].

The UV-vis absorbance data for the homoleptic complexes (additionally [(tpy)Ru(**2**)]<sup>2+</sup> and [(tpy)Ru(**8**)]<sup>2+</sup>) is presented in table 3.6. As mentioned, all substituted 2,2':6',2''-terpyridines give red shifted MLCT bands compared to the parent [Ru(tpy)<sub>2</sub>]<sup>2+</sup> complex. The red shift of a heteroleptic complex with one unsubstituted terpyridine ligand is about half way in between the wavelengths of the homoleptic complex and [Ru(tpy)<sub>2</sub>]<sup>2+</sup>. In fact the wavelength maxima of all the heteroleptic complexes are superpositions of the homoleptic complexes as has been reported in earlier literature.<sup>[14]</sup> The extinction coefficients are increased in comparison to the [Ru(tpy)<sub>2</sub>]<sup>2+</sup> complex except for [Ru(**3**)<sub>2</sub>]<sup>2+</sup> where the absorbance decreases.

**Table 3.7** Absorbance maximum of MLCT band and the emission band maximum. Measurements were performed in MeCN. Lifetime measurements only done for ruthenium complexes with **4**, **5** and **6**.

Compound	Absorption max (nm)	Fluorescence (nm)**	$\tau$ (ns)
[Ru( <b>4</b> ) <sub>2</sub> ] <sup>2+</sup>	491	658	2
[Ru( <b>5</b> ) <sub>2</sub> ] <sup>2+</sup>	504	687	51
[Ru( <b>6</b> ) <sub>2</sub> ] <sup>2+</sup>	508	690	56
[Ru( <b>1</b> ) <sub>2</sub> ] <sup>2+*</sup>	499	664	
[Ru( <b>2</b> ) <sub>2</sub> ] <sup>2+</sup>	510	675	
[Ru( <b>8</b> ) <sub>2</sub> ] <sup>2+</sup>	490	651	
[Ru( <b>3</b> ) <sub>2</sub> ] <sup>2+*</sup>	514	715	

\* Data from reference [14].

\*\* Excitation at absorption maximum.

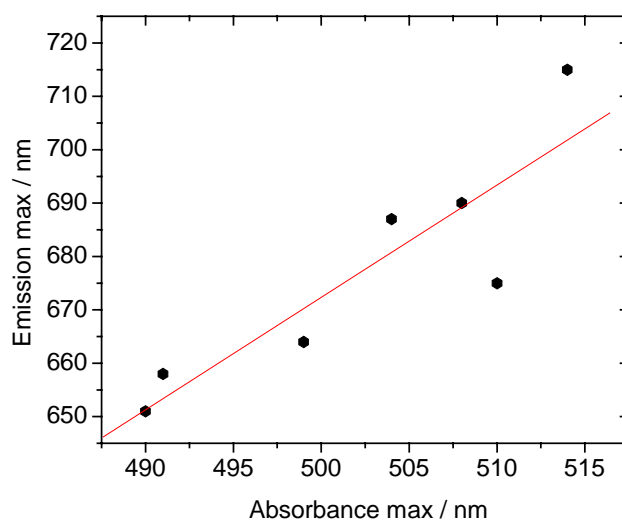


**Figure 3.16** The values of the wavelengths of the absorption maximums and emission maximums from table 3.9.

A plot of the maximum absorbance and emission wavelengths from table 3.7 in figure 3.16 shows how the two values follow each other and that the difference ( $\lambda_{\max}^{\text{Em}} - \lambda_{\max}^{\text{Abs}}$ ) does not differ much between the different complexes.

### Complexes with a carboxylate ligand

The complexes with carboxylic acid groups have an MLCT maximum that shifts, for some of the complexes, depending on whether it is protected with an ethyl group or

not. Upon hydrolysis of the ethyl ester the peak is red shifted between 0 and 5 nm. The extinction coefficient does change slightly but no consistent trend can be found. Table 3.8 has all the relevant data of the MLCT absorbance and emission data for the complexes with an anchoring group (dyes).

**Table 3.8** MLCT maximum of the dyes as ethyl ester, acids and adsorbed to TiO<sub>2</sub>. The emission maximum for the dyes is used to calculate the E<sub>0-0</sub>. Measurements performed in MeCN.

Compound	MLCT $\lambda_{\max}$ ester /nm ( $\epsilon / 10^4 \text{ M}^{-1}\text{cm}^{-1}$ )	MLCT $\lambda_{\max}$ acid /nm ( $\epsilon / 10^4 \text{ M}^{-1}\text{cm}^{-1}$ )	Emission /nm	MLCT $\lambda_{\max}$ , on TiO <sub>2</sub> /nm
[(tpy)Ru(4)] <sup>2+</sup>		483 (1.2)	652	489
[(tpy)Ru(5)] <sup>2+</sup>	489 (2.7)	491 (2.5)	690	496
[(1)Ru(4)] <sup>2+</sup>		495 (1.1)	662	488
[(1)Ru(5)] <sup>2+</sup>	498 (3.9)	502 (4.0)	673	507
[(1)Ru(6)] <sup>2+</sup>		504 (4.1)	675	507
[(3)Ru(4)] <sup>2+</sup>	502 (3.6)	503 (3.5)	658	505
[(3)Ru(5)] <sup>2+</sup>	507 (3.3)	509 (3.0)	718	514
[(2)Ru(4)] <sup>2+</sup>	498 (3.3)	501 (3.1)	668	503
[(2)Ru(5)] <sup>2+</sup>	505	505 (3.6)	675	507
[(2)Ru(6)] <sup>2+</sup>	507 (3.7)	508 (3.8)	694	514
[(9)Ru(4)] <sup>2+</sup>	490 (4.1)	491	-	494
[(8)Ru(4)] <sup>2+</sup>	490	491 (3.0)	652	495

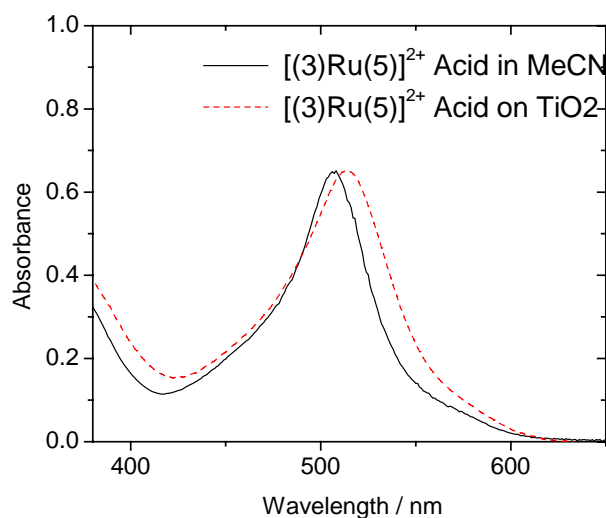


**Figure 3.17** UV-vis absorbance of dye in solution (MeCN) and adsorbed to TiO<sub>2</sub> surface.



The absorption spectra of the dye-sensitised TiO<sub>2</sub> films were measured as described in chapter 2. Upon adsorption of the carboxylated dyes on TiO<sub>2</sub> surfaces there was a slight red shift and broadening of the MLCT peak. In figure 3.17 an example with [(**3**)Ru(**5**)]<sup>2+</sup> is shown but the effect is similar for all the other dyes. The only exception was [(**1**)Ru(**4**)]<sup>2+</sup> that had a slight blue shift (495→488 nm). The C-O-Ti bridge that is formed upon adsorption increases the overlap of the ligand π\* orbital and Ti(3d) orbital manifold, which may lower the LUMO of the anchoring ligand and in doing so decreases the MLCT band-gap.<sup>[36, 37]</sup> Charge transfer transitions such as the <sup>1</sup>MLCT in metal complexes show shifting absorbance maxima depending on the polarity of solvent (solvatochromism) in which they are dissolved.<sup>[38]</sup> Binding to the TiO<sub>2</sub> may have a similar effect, indeed complex [(**3**)Ru(**5**)]<sup>2+</sup> had an <sup>1</sup>MLCT band maximum at 515 nm in DCM while the maxima in MeCN is 508 nm. The red shift with a less polar solvent is what has generally been seen in literature.<sup>[38]</sup> Scattering of light by the TiO<sub>2</sub> nano-particles should also be taken into account. The lower wavelength light will be scattered more than the longer wavelengths (Rayleigh scattering) possibly resulting in distortion of the peaks. Contradicting this is the absorption spectra of the adsorbed ester. TiO<sub>2</sub> films were immersed in solutions of either the ester or the acid form of the complex [(**3**)Ru(**5**)]PF<sub>6</sub>]<sub>2</sub>. The acid adsorbs well with a good coverage but the ester adsorbs less (Abs.= ~0.3) and has the same λ<sub>max</sub> (508 nm) as that of the ester in solution and not as red shifted as that of the adsorbed acid (514 nm). Another possibility to consider is that the MLCT consists of a number of overlapping absorptions and small shifts can be due to changes in intensity of these components.<sup>[2]</sup>

### Iron (II) complexes

The iron (II) complexes have absorbance maximums at longer wavelengths than the ruthenium complexes but there appears to be no emission from the iron complexes. This is expected due to the deactivating  $^3\text{MC}$  state that greatly reduces the emission lifetime.<sup>[39]</sup> The iron 4'-substituted terpyridine complexes show the same trend in absorbance maximum red shift as the equivalent ruthenium complexes. The MLCT maxima and ligand centered (LC) maximum wavelengths are tabulated in table 3.9 together with their extinction coefficients.

**Table 3.9** UV-vis absorbance data for iron homoleptic complexes in MeCN.

Compound	MLCT $\lambda_{\text{max}}$ , /nm ( $\epsilon / 10^4 \text{ M}^{-1} \text{ cm}^{-1}$ )	LC ( $\epsilon / 10^4 \text{ M}^{-1} \text{ cm}^{-1}$ )	LC ( $\epsilon / 10^4 \text{ M}^{-1} \text{ cm}^{-1}$ )	LC ( $\epsilon / 10^4 \text{ M}^{-1} \text{ cm}^{-1}$ )
$[\text{Fe}(\text{tpy})_2]^{2+}$ *	511 (1.2)		318 (5.2)	280 (3.4)
$[\text{Fe}(\mathbf{1})_2]^{2+}$	577 (4.6)	340 (7.2)	325 (8.7)	283 (7.2)
$[\text{Fe}(\mathbf{3})_2]^{2+}$	589 (8.2)	391 (9.4)	318 (3.8)	280 (4.8)
$[\text{Fe}(\mathbf{2})_2]^{2+}$	580 (5.1)		317 (8.7)	283 (8.1)
$[\text{Fe}(\mathbf{8})_2]^{2+}$	569 (2.6)		314 (9.2)	286 (7.2)
$[\text{Fe}(\mathbf{4})_2]^{2+}$	570 (2.3)		322 (4.1)	286 (7.8)

\* Data from reference [27].

### 3.2.4 Electrochemistry

Most of the 4'-substituted terpyridine metal complexes were soluble in acetonitrile allowing good electrochemical measurements to be carried out in solution. The compounds with acid groups were harder to dissolve but the solubility was adequate to obtain the oxidation and reduction potentials. All the ruthenium compounds showed a reversible ruthenium II/III redox process at about 0.9 V vs. ferrocene. At negative potentials two quasi-reversible processes at about -1.5 and -1.8 V vs. ferrocene for the two reductions of the terpyridine ligands were present.<sup>[40]</sup> The reduction potentials shift similarly depending on the ligand. Homoleptic iron complexes with the same ligand set were measured and showed similar shifts. Figure 3.18 shows an example of a CV of a  $[\text{Ru}(\text{terpy})_2]^{2+}$  complex in  $\text{CH}_3\text{CN}$ .

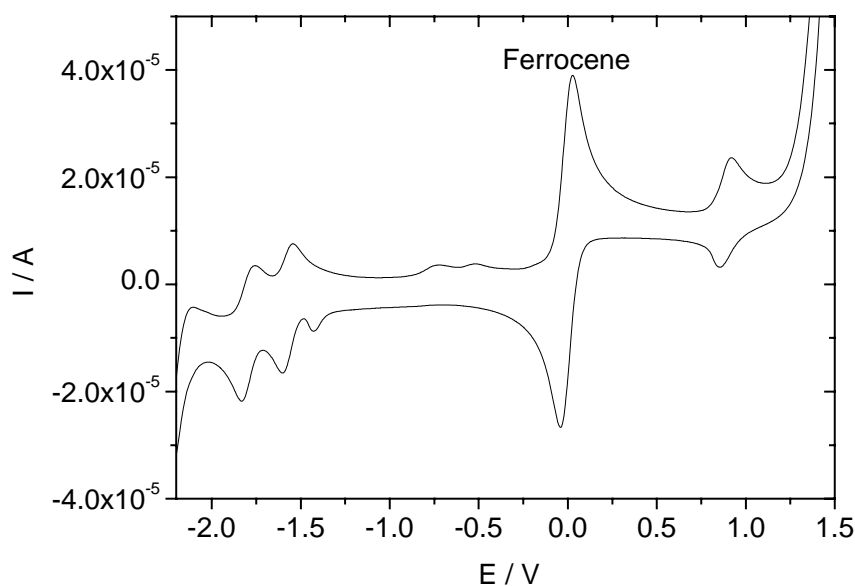


**Figure 3.18** Above is a typical CV of a ruthenium bis-terpyridine complex with the ferrocene / ferrocinium redox process included. Measurement made in  $\text{CH}_3\text{CN}$  (0.1 M  $\text{TBAPF}_6$ ) with glassy carbon electrode at 100 mV/s.

For the compounds with terpyridine ligands functionalised with oligo thienyl groups, there is a second oxidation after the ruthenium peak, which is assumed to be oxidation of the oligo thienyl group.<sup>[41]</sup> The oxidation of the thiophene group is an irreversible process and in acetonitrile, in the case of ligands **3** and **8**, it leads to some deposition/polymerisation. Changing to a non-nucleophilic solvent like CH<sub>2</sub>Cl<sub>2</sub> facilitates electro-deposition or electro-polymerisation and multiple layers of polymer film can be formed on the electrodes.<sup>[26]</sup> This is further described in section 3.3.

For the complexes with the ruthenium II/III process close in energy to the oxidation of the ligand substituent, the oxidation processes overlap and are difficult to distinguish even with square wave (SWV) or differential pulse voltammetry (DPV).<sup>[13]</sup> As can be seen in figure 3.19 the ligand oxidation is partly overlapping. SWV can help in elucidating the processes and establish the charge ratios of the processes. In section 3.3 this will be further discussed. In the iron complexes the II/III process is more separated from the thiophene oxidation and is at a less positive potential.

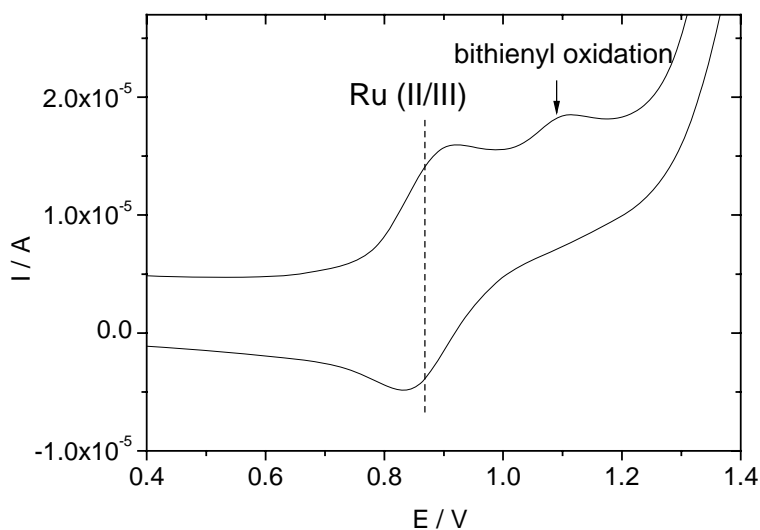


**Figure 3.19** Cyclic voltammogram of [(**3**)Ru(**4**)]<sup>2+</sup>. Measurement made in CH<sub>3</sub>CN (0.1 M TBAPF<sub>6</sub>) with glassy carbon electrode at 100 mV/s with Fc/Fc<sup>+</sup>.

The ligands **2** and **3** have oxidation potentials that partly overlap with the ruthenium II/III process when coordinated. The HOMO energy level appears to be spread across the metal center and the ligands. This is supported by semi-empirical orbital calculations simulated using HyperChem<sup>TM</sup> (version 7.01). In figure 3.20 a plot of the

calculated HOMO orbital of  $[(\mathbf{3})\text{Ru}(\mathbf{5})]^{2+}$  shows the HOMO partly localized on ligand  $\mathbf{3}$  and partly on the ruthenium metal center.<sup>[9, 42]</sup>

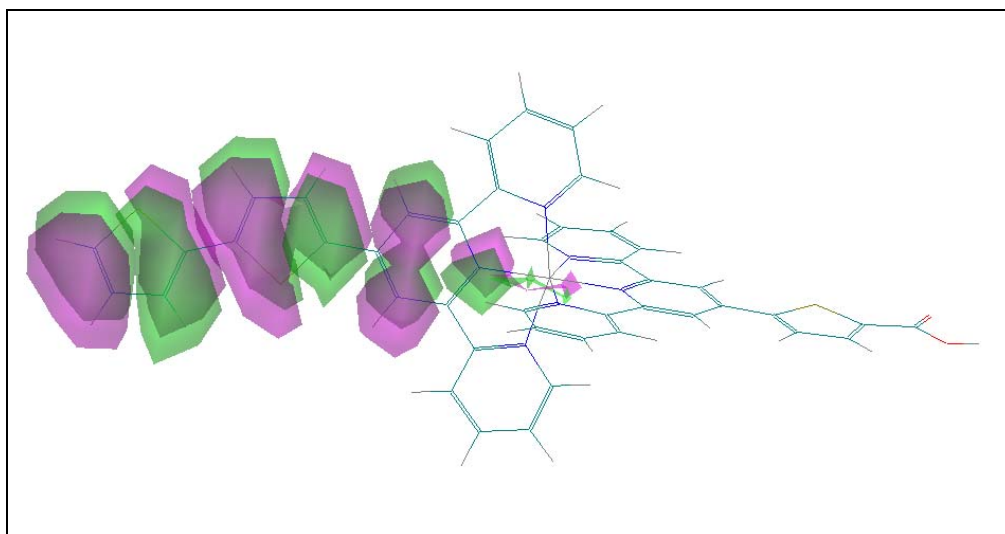


**Figure 3.20** Semi-empirical ZINDO-1 calculation of HOMO of  $[(\mathbf{3})\text{Ru}(\mathbf{5})]^{2+}$ .

**Table 3.10** Redox potentials of ruthenium complexes in anhydrous MeCN with TBAPF<sub>6</sub> (0.1 M) as supporting electrolyte with potentials quoted versus Fc/Fc<sup>+</sup>. Values measured with SWV. CV measurements were performed to control reversibility. All the cations have 2 PF<sub>6</sub><sup>-</sup> as counter anions.

Compound	Ox. Ru (V)	Ox. Lig. (V)	Red. 1(V)	Red. 2 (V)
$[\text{Ru}(\text{tpy})_2]^{2+}$ *	+ 0.91		- 1.66	- 1.87
$[\text{Ru}(\mathbf{4})_2]^{2+}$	+ 0.89		- 1.56	- 1.78
$[\text{Ru}(\mathbf{5})_2]^{2+}$	+ 0.89	+ 1.04, + 1.42	- 1.49	- 1.69
$[\text{Ru}(\mathbf{6})_2]^{2+}$	+ 0.86		- 1.53	- 1.73
$[(\text{tpy})\text{Ru}(\mathbf{1})]^{2+}$	+ 0.86	+ 1.64	- 1.60	- 1.87
$[\text{Ru}(\mathbf{1})_2]^{2+}$ *	+ 0.83	+ 1.65	- 1.60	- 1.82
$[(\text{tpy})\text{Ru}(\mathbf{3})]^{2+}$	+ 0.86	(o.l.)* + 1.50	- 1.57	- 1.85
$[\text{Ru}(\mathbf{3})_2]^{2+}$ *	+ 0.84	(o.l.)*	- 1.59	- 1.87
$[(\text{tpy})\text{Ru}(\mathbf{2})]^{2+}$	+ 0.82	+ 1.34	- 1.63	- 1.87
$[\text{Ru}(\mathbf{2})_2]^{2+}$	+ 0.77	+ 1.04, + 1.32	- 1.64	- 1.86
$[(\text{tpy})\text{Ru}(\mathbf{8})]^{2+}$	+ 0.88	+ 1.18, + 1.35	- 1.66	- 1.89
$[\text{Ru}(\mathbf{8})_2]^{2+}$	+ 0.88	+ 1.23, + 1.34	- 1.57	- 1.76

\*o.l. stands for over lapping with metal centred process.

The redox potentials of the ruthenium couples shift slightly due to the substituent on the 4'-position on the terpyridine ligands. Differences in electron-donating/-

withdrawing capability of the ligands and the changes in conjugation lengths have been reported to shift the redox potentials.<sup>1,2</sup>

From the values of the redox potentials of the ruthenium metal centers in table 3.10 it appears that the potential is less positive for the complexes with oligo thienyl functionalised ligands. This suggests a weak electron donating ability of the ligands, which can easier stabilise the higher oxidation state. With the data from the homoleptic complexes the order of the electron donation strength is tpy < tpySBS < tpySS ≤ tpyS < tpyEDOT with tpyEDOT being the most donating. The first oxidation potential is shifted to more positive values by the electron rich ethylene-dioxy bridge on the EDOT substituent. The first reduction potential is shifted to more negative values the most by the tpySS and tpySBS ligands. Complexes with the carboxylate ligands have the largest shift towards less negative reduction potentials. The trends follow those for the free ligands (see table 3.3).

The iron complexes have lower oxidation potentials than the ruthenium complexes and the reduction potentials are also slightly less negative but the trends for the different ligands are the same as for ruthenium complexes. In table 3.11 all the electrochemical potentials for the iron complexes are collected.

**Table 3.11** Redox potentials of iron complexes in anhydrous MeCN with TBAPF<sub>6</sub> (0.1 M) as supporting electrolyte with potentials quoted versus Fc/Fc<sup>+</sup>. Ag wire as pseudo reference and values from SWV.

Compound	Ox. Fe (V)	Ox. Lig. (V)	Red. 1 (V)	Red. 2 (V)
[Fe(tpy) <sub>2</sub> ] <sup>2+*</sup>	+ 0.73		- 1.64	- 1.82
[Fe(1) <sub>2</sub> ] <sup>2+</sup>	+ 0.69	+ 1.44	- 1.57	- 1.71, - 2.32
[Fe(3) <sub>2</sub> ] <sup>2+</sup>	+ 0.68	+ 1.12, + 1.26	-1.36	-1.73
[Fe(4) <sub>2</sub> ] <sup>2+</sup>	+ 0.70			- 1.71
[Fe(2) <sub>2</sub> ] <sup>2+</sup>	+ 0.64	+ 1.00	- 1.61	- 1.71
[Fe(8) <sub>2</sub> ] <sup>2+</sup>	+ 0.73	+ 1.25, + 1.43	- 1.49	- 1.59, -1.72

As was discussed in section 1.2, the energy gap between the HOMO and LUMO of the complexes can be related to the metal to ligand charge transfer transition as an approximation of the energy in the transition.<sup>[43, 44]</sup> The <sup>1</sup>MLCT absorption bands in figure 3.11 are more intense when the first reduction and oxidation potentials are

close, which is often the case when the metal gets easier to oxidise and the ligand easier to reduce.<sup>[45]</sup>

In figure 3.21a the potential difference of the 1<sup>st</sup> oxidation potential and the 1<sup>st</sup> reduction potentials are plotted against the MLCT absorption maximum.<sup>[43]</sup> Although there is no linear trend among the complexes with substitutions, the change in the energy gap (between the HOMO and LUMO) and the shift in MLCT wavelength maximum for the 4'-substituted 2,2':6',2''-terpyridines compared to the unsubstituted terpyridines is clear. Also the difference between the iron and ruthenium complexes is large. In the broad <sup>1</sup>MLCT absorbance, several bands overlap and not all the absorbance bands correspond to the lowest <sup>1</sup>MLCT transition.<sup>[4]</sup> In figure 3.21b the emission maximum band energies have a more linear relation with the  $\Delta E_{1/2}$  energies although the complexes with ligands **5**, **8** and especially **3** deviate. The emission is only from the ground state of the <sup>3</sup>MLCT (Kasha's rule) and so should have a more linear relation with  $\Delta E_{1/2}$ .<sup>[6]</sup>

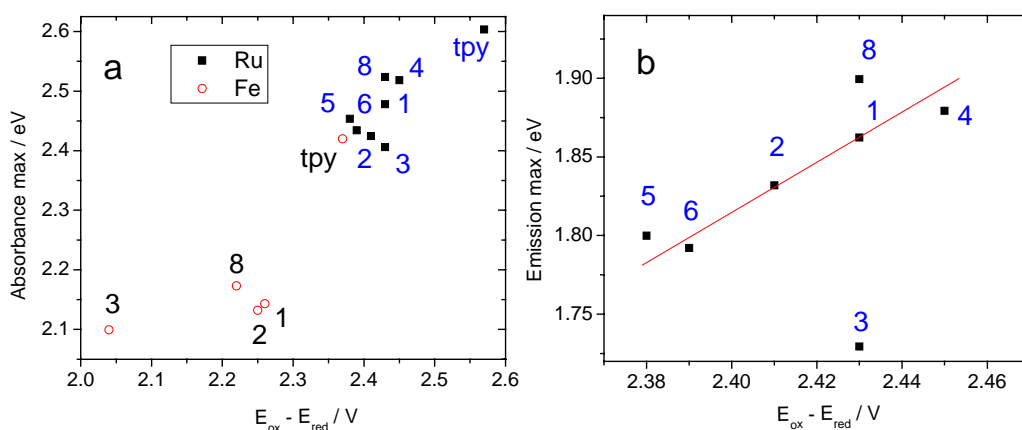


**Figure 3.21** The values of  $|E_{ox} - E_{red}|$  plotted against the (a) absorption maxima for the homoleptic iron and ruthenium complexes. In (b) the emission maxima for the ruthenium complexes are plotted. The squares are the ruthenium complexes and the circles the iron complexes. The numbers stand for the ligand in the ruthenium and iron homoleptic complexes.

### Complexes with anchoring ligand

The electrochemistry of heteroleptic complexes with one anchoring ligand gave important information concerning their suitability as dyes in the dye sensitised solar cell. The potentials need to match the energy levels of the other components in the DNSC, as was discussed in section 2.2. For the photoelectrochemical polymerisation

of oligo-thiophene monomers by the excited dye, there needs to be an oxidising ability that is strong enough.

Electrochemical data for all the ruthenium complexes with an anchoring ligand are collected in table 3.12. In section 3.5.2 further investigation into these dye molecules will be discussed including photovoltaic measurements.

**Table 3.12** Electrochemical data for the ruthenium complexes with one anchoring ligand. All measurements were performed in dry CH<sub>3</sub>CN, under Ar atmosphere, with glassy carbon (GC) working electrode and versus the ferrocene/ferrocinium redox couple set as 0 V. The values are from SWV but all samples have been measured with CV to control reversibility of processes. The electrolyte was TBAPF<sub>6</sub> (0.1 M).

Compound	Ox. Ru (V)	Ox. Lig. (V)	Red. 1(V)	Red. 2 (V)
[(tpy)Ru(4)] <sup>2+</sup>	+ 0.88		- 1.63	- 1.84
[(tpy)Ru(5)] <sup>2+</sup>	+ 0.87		- 1.58	- 1.80
[(1)Ru(4)] <sup>2+</sup>	+ 0.89	+ 1.35	- 1.56	- 1.78
[(1)Ru(5)] <sup>2+</sup>	+ 0.86		- 1.57	- 1.78
[(1)Ru(6)] <sup>2+</sup>	+ 0.84	+ 1.47	- 1.55	- 1.81
[(3)Ru(4)] <sup>2+</sup>	+ 0.84	+ 1.04	- 1.56	- 1.80
[(3)Ru(5)] <sup>2+</sup>	+ 0.87	(o.l.), + 1.10	- 1.52	- 1.74
[(2)Ru(4)] <sup>2+</sup>	+ 0.81	+ 1.03	- 1.61	- 1.79
[(2)Ru(5)] <sup>2+</sup>	+ 0.83	+ 0.96, +1.07	- 1.60	- 1.86
[(2)Ru(6)] <sup>2+</sup>	+ 0.81	(o.l.), + 1.36	- 1.56	- 1.83
[(8)Ru(4)] <sup>2+</sup>	+ 0.89	+ 1.48	- 1.62	- 2.10
[(9)Ru(4)] <sup>2+</sup>	+ 0.88	+ 0.19 (Fc)	- 1.63	- 2.21

### Ruthenium complex with ferrocene functionalised ligand

Cyclic voltammetry of the ruthenium complex with a ferrocenyl group ([**(9)Ru(4)**][PF<sub>6</sub>]<sub>2</sub>), shows the expected peak for ferrocene oxidation and thereafter the ruthenium peak. The ferrocene redox couple is shifted to more positive values by about 200 mV compared to ferrocene alone in solution. This has been reported for [Ru(**9**)<sub>2</sub>][PF<sub>6</sub>]<sub>2</sub> earlier.<sup>[7]</sup> Switching the voltage after the ferrocene peak but prior to the ruthenium, a reversible process for the ferrocene is seen. When the ruthenium process is included in the sweep, the reduction peak of the ferrocene is less intense. At a scan



rate of 100 mV/s, the reduction peak for the ruthenium process is absent as can be seen in figure 3.22. One possible explanation is that the oxidized ruthenium can be reduced by the ferrocenyl group (if it has remained un-oxidised by the electrode). This may be possible if un-oxidised compound is within the diffusion field of the electrode.

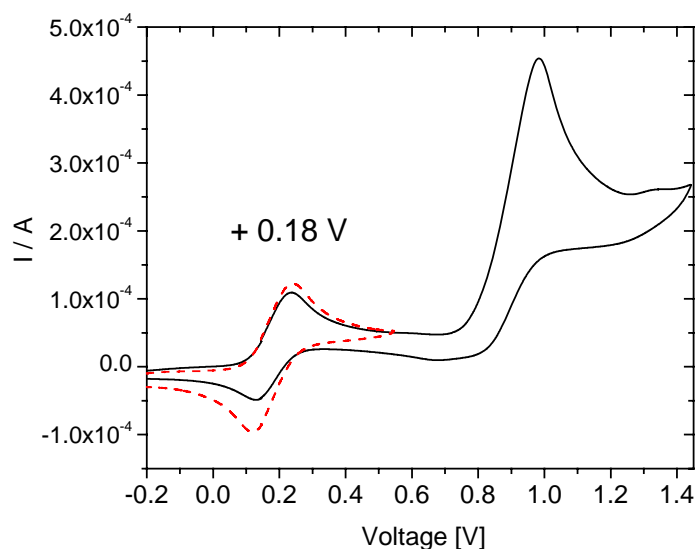


**Figure 3.22** CV of  $[(9)Ru(4)]^{2+}$  in  $CH_3CN$  at 100 mV/s with the  $Fc/Fc^+$  redox couple in solution set as 0V. The red voltammogram shows the ferrocene from ligand **9** (dashed line) when the cycling range is restricted to the range 0-0.5 V.

In figure 3.22 the voltammogram of the complex when the range is restricted to 0-0.5 V is overlapped with the full voltammogram. In the full voltammogram the ferrocene peak also has its reduction peak reduced.

In figure 3.23, the SWV measurement quantifies the ferrocene and ruthenium processes to two one-electron oxidations (if the ferrocene redox couple is considered a one electron process, which the peak separations in the cyclic voltammetry suggest,  $\Delta E_p = 59/n$  mV). To reduce the range of the diffusion field, cyclic voltammetry with higher scan rates was used (diffusion-field range  $\sim \sqrt{(D_o/t)}$ ).<sup>[46]</sup> The macro-electrode was used up to 5 V/s and beyond that (up to 30 V/s) a microelectrode was employed. At higher scan rates, from about 1 V/s, a reduction peak was visible but it was not very large, which can be seen in figure 3.24.

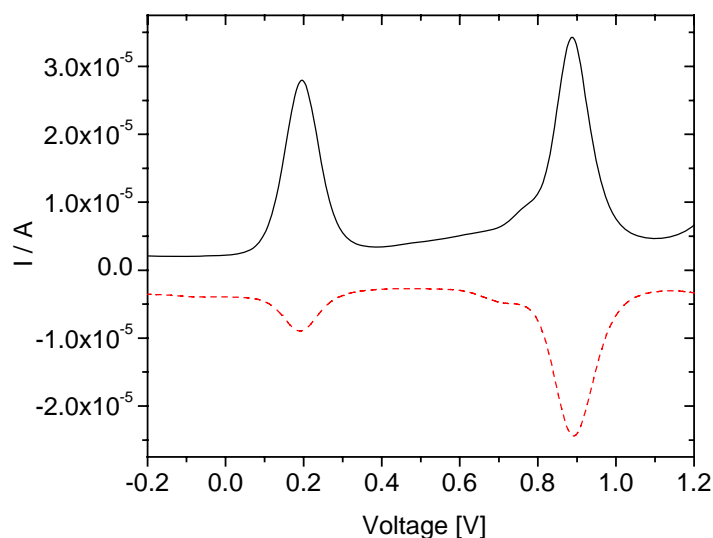


**Figure 3.23** SWV of  $[(9)\text{Ru}(4)]^{2+}$  with the anodic current and the reverse cathodic current (dashed line). Measured with glassy carbon indicator electrode in  $\text{CH}_3\text{CN}$  (0.1 M TBAPF<sub>6</sub>).

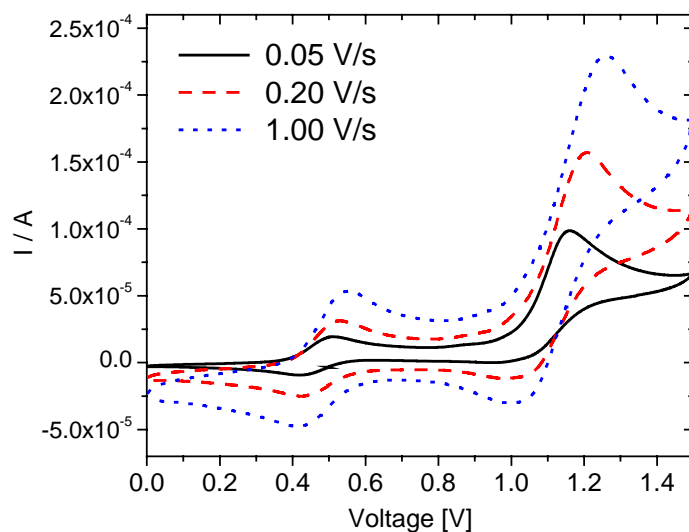


**Figure 3.24** CV of  $[(9)\text{Ru}(4)]^{2+}$  in  $\text{CH}_3\text{CN}$  at 50, 200 and 1000 mV/s. Measured with glassy carbon indicator electrode in  $\text{CH}_3\text{CN}$  (0.1 M TBAPF<sub>6</sub>) at different scan-rates.

The electrochemistry of  $[(9)\text{Ru}(4)][\text{PF}_6]_2$  suggests that there is electron transfer between the oxidized ruthenium and the ferrocene moiety. This ability is used in section 3.3.2 when the complex is adsorbed to  $\text{TiO}_2$  thin films. The close proximity of the two metal centers allows a strong intramolecular electron transfer, however when

the ferrocene and ruthenium complex are separate in the solution, they are too far away from each other for an equally efficient electron transfer.

The diffusion constants of the  $[\text{Ru}(\text{II})(\text{terpy})_2]^{2+}$  complexes can be measured with a microelectrode (electrode  $d=25\mu\text{m}$ ) when low scan rates are applied.\* A cyclic voltammogram of a reversible process gives a sigmoidal curve shape (see section 1.2) where the diffusion constant,  $D_O$ , can be calculated from the limiting state current by equation 27 from chapter 2.

$$i_{SS} = 4nFD_O C_O^* r_0 \quad (27)$$

The steady state current is  $i_{SS}$ ,  $n$  the number of electrons in the process,  $F$  is Faraday's constant,  $D_O$  the diffusion constant,  $C_O^*$  the bulk concentration and  $r_0$  is the microelectrode radius. A typical scan is plotted in figure 3.25 where  $[\text{Ru}(\mathbf{4})_2][\text{PF}_6]_2$  in  $\text{CH}_3\text{CN}$  gives a steady state current of  $\sim 5.5$  nA. Together with the other values that are known, a diffusion constant of  $1.5 \pm 0.1 \cdot 10^{-5} \text{ cm}^2 \text{ s}^{-1}$  is calculated. The values are probably very similar for the other ruthenium complexes as they are close in size. The diffusion layer thickness grows approximately by  $2(D_O t)^{1/2}$  with time ( $t$ ).<sup>[46]</sup> With the value of  $D_O$  for  $[\text{Ru}(\mathbf{4})_2][\text{PF}_6]_2$ , and a scan rates of 30 V/s, the diffusion layer thickness will reach circa 10  $\mu\text{m}$ .

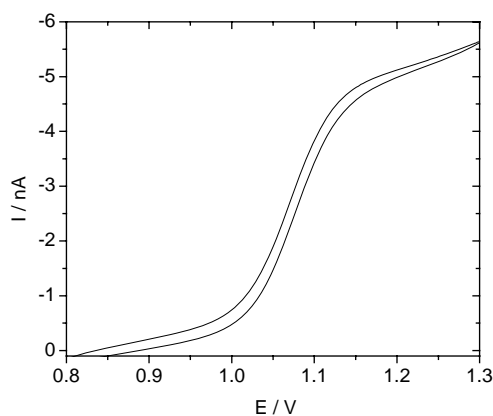


**Figure 3.25** Steady-state voltammogram of  $[(\text{tpy})\text{Ru}(\mathbf{1})]^{2+}$  (0.73 mM) in  $\text{CH}_3\text{CN}$  at 10 mV/s with a 25  $\mu\text{m}$  diameter microelectrode in  $\text{CH}_3\text{CN}$ .

\* In sections 1.1 and 1.2 the electrochemistry of microelectrodes is further discussed.

### 3.2.5 Crystal-structure

A crystal structure for  $[\text{Fe}(\mathbf{2})_2][\text{PF}_6]_2 \cdot (\text{CH}_3)_2\text{CO} \cdot 0.4(\text{CH}_2\text{Cl}_2) \cdot 0.6(\text{H}_2\text{O})$  was obtained. To obtain the crystals, the complexes were dissolved in MeCN and put in sample vials. The tubes were put on the bottom of glass jars containing  $\text{Et}_2\text{O}$ . A lid on the jar prevents solvents from evaporating and allows the ether to slowly diffuse into the MeCN solution. Over time the complex crystallises from the solution.

In figure 3.26, the structure of the  $[\text{Fe}(\mathbf{2})_2]^{2+}$  ion in the above complex shows that the bite angles for the coordinating nitrogen atoms are  $81.17(6)^\circ$  for N1-Fe-N2 and  $81.13(6)^\circ$  for N3-Fe-N2. The Fe-N distance is  $1.9688(15) \text{ \AA}$  for N1-Fe,  $1.9780(15) \text{ \AA}$  for N3-Fe and  $1.8782(14) \text{ \AA}$  for the central pyridine iron distance (see table 3.13). These values are usual in the case of octahedral complexes with terpyridine, where the two ligands are orthogonal with the central metal ion in a distorted octahedral environment.<sup>[47]</sup> This distortion differs from the ideal angle of  $90^\circ$  for octahedral geometry. It can be seen that the terpyridine ligand is close to planar. The angles between the mean planes defined for the central terpyridine ring (N2-C10) and the other two terpyridine rings (N1-C1) and (N3-C11) are  $2.11^\circ$  and  $5.27^\circ$  respectively. The angle between the mean planes defined for the central terpyridine ring (N2-C10) and the thiophene ring (S1-C17) is  $2.85^\circ$ . The carbon and oxygen atoms in the dioxyethylene bridges of the EDOT groups are slightly out of plane due to the  $\text{sp}^3$  hybridisation.

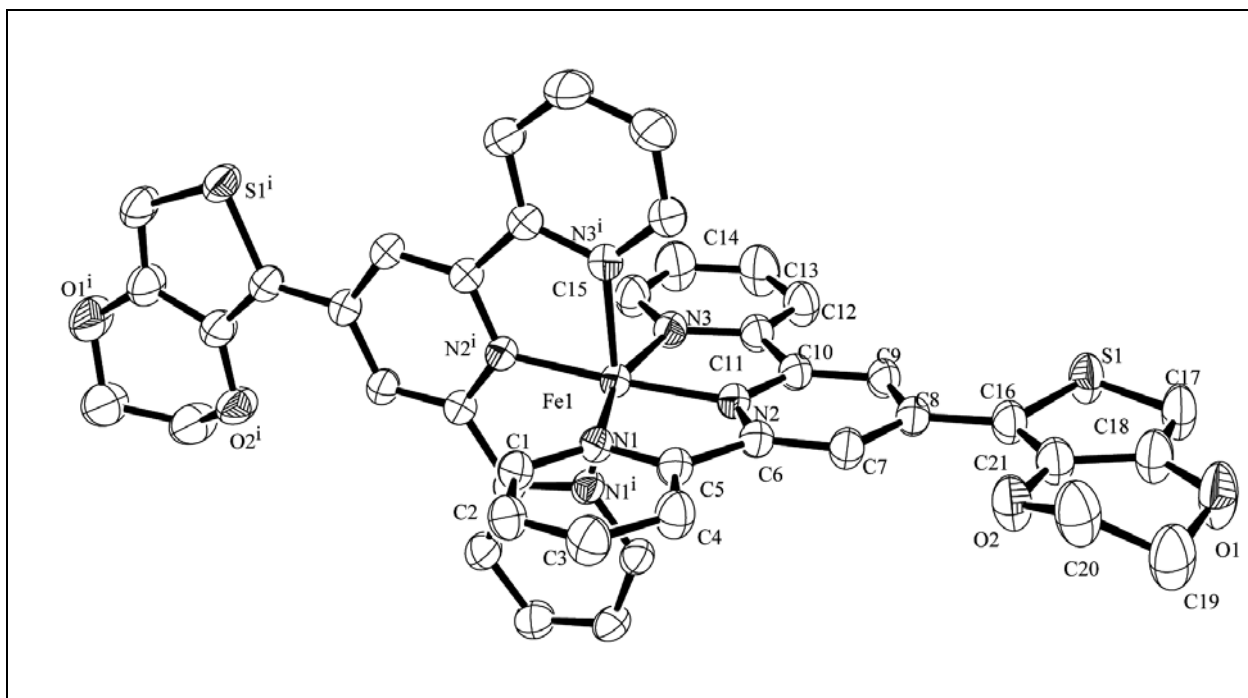


**Figure 3.26** ORTEP representation of the  $[\text{Fe}(\mathbf{2})_2]^{2+}$  cation. The counter ions ( $2\text{PF}_6^-$ ), hydrogens and solvent molecules (Acetone,  $\text{CH}_2\text{Cl}_2$  and  $\text{H}_2\text{O}$ ) have been omitted for clarity. The molecule is plotted as thermal ellipsoids at 50% probability level. (i)  $-x+1, y, -z+0.5$

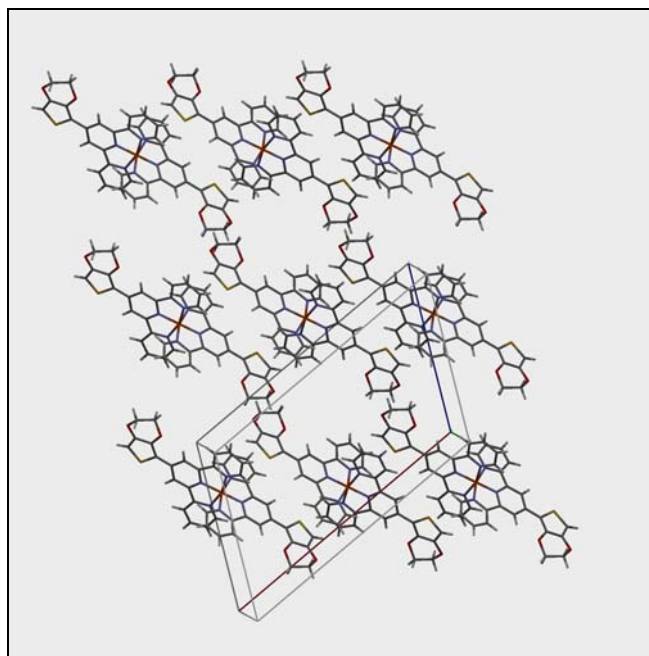


**Figure 3.27** The ac plane in the unit cell of the  $[\text{Fe}(\mathbf{2})_2][\text{PF}_6]_2 \cdot (\text{CH}_3)_2\text{CO} \cdot 0.4(\text{CH}_2\text{Cl}_2) \cdot 0.6(\text{H}_2\text{O})$  crystal structure. The  $\text{PF}_6^-$  anions, hydrogens and solvent molecules have been omitted for clarity.

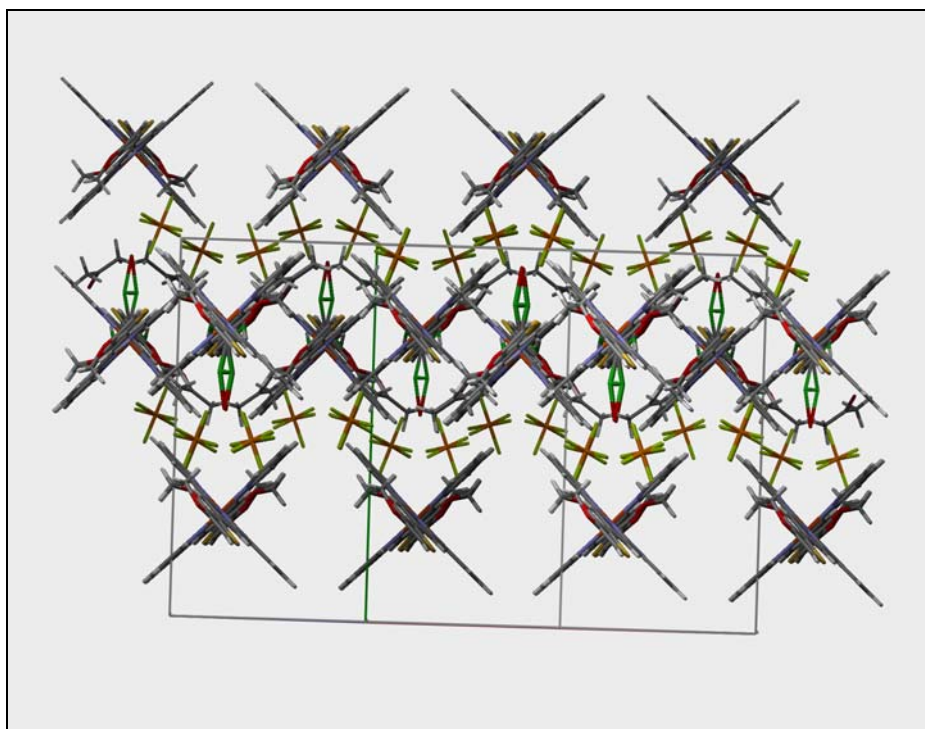


**Figure 3.28** Planes form the *ac*-axis of the unit cell  $[\text{Fe}(\mathbf{2})_2][\text{PF}_6]_2 \cdot \text{acetone} \cdot 0.4(\text{CH}_2\text{Cl}_2) \cdot 0.6(\text{H}_2\text{O})$  with the  $\text{PF}_6^-$  counter ions (yellow and orange) sitting in between the stacks.

The shortest distances between the  $[\text{Fe}(\mathbf{2})_2]^{2+}$  ions are between the EDOT groups, where the shortest distance ( $\sim 3.3 \text{ \AA}$ ) is between the dioxyethylene bridges, and between the outer 2,2':6',2''-terpyridine ring and the thiophene ring ( $\sim 3.3 \text{ \AA}$ ). The latter interaction appears to be an offset face-to-face interaction.<sup>[29]</sup> The packing consists of sheets of the complex ions in the *ac*-plane with the  $\text{PF}_6^-$  counter ions sitting in between. In figures 3.27 and 3.28 this is shown with a view down onto a sheet (3.27) and one along the planes (3.28).

The asymmetric unit of the structure consists of one ligand and half the metal ion together with a  $\text{PF}_6^-$  anion, half an acetone and half a second solvent molecules that is partially occupied by  $\text{CH}_2\text{Cl}_2$  and partially  $\text{H}_2\text{O}$  and is situated on a symmetry site. Within the molecule there is a  $C_2$  symmetry relationship. From analysing the packing, the solvent molecules (two acetone molecules together with either a dichloromethane molecule or a water molecule) appear to form clusters, with hydrogen bonding, that lie in cavities between the complexes. There appears to be no channels.

The X-ray data is in the appendix A. Table 3.13 lists some selected data from the crystal structure.

**Table 3.13** Selected bond lengths and angles from the crystal structure of  $[\text{Fe}(\mathbf{2})_2][\text{PF}_6]_2 \cdot \text{CO}(\text{CH}_3)_2 \cdot 0.4(\text{CH}_2\text{Cl}_2) \cdot 0.6(\text{H}_2\text{O})$ .

Atoms	Length (Å)	Atoms	Angle (°)
N1-Fe	1.9688(15)	N1-Fe-N3'	162.24(6)
N2-Fe	1.8782(14)	N1-Fe-N2'	81.17(6)
N3-Fe	1.9780(15)	N1-Fe-N3'	91.76(6)
		N2-Fe-N2'	176.53(9)
		N2-Fe-N3'	96.43(6)
		N3-Fe-N3'	91.68(9)
		N2-C10-C11	111.65(15)
		N1-C5-C6	113.47(15)
		N3-Fe-N2	81.13(6)
		N1-Fe-N2	81.17(6)
		N1-Fe-N3	162.25(6)

## 3.2.7 Experimental

1. [(tpy)Ru(**1**)][PF<sub>6</sub>]<sub>2</sub> [35]
2. [(tpy)Ru(**3**)][PF<sub>6</sub>]<sub>2</sub> [14]
3. [(tpy)Ru(**2**)][PF<sub>6</sub>]<sub>2</sub>
4. [Ru(**2**)<sub>2</sub>][PF<sub>6</sub>]<sub>2</sub>
5. [(tpy)Ru(**8**)][PF<sub>6</sub>]<sub>2</sub>
6. [Ru(**8**)<sub>2</sub>][PF<sub>6</sub>]<sub>2</sub>
7. [(tpy)Ru(**4**)][PF<sub>6</sub>]<sub>2</sub> [9]
8. [Ru(**4**)<sub>2</sub>][PF<sub>6</sub>]<sub>2</sub> [15]
9. [(tpy)Ru(**5**)][PF<sub>6</sub>]<sub>2</sub> donated<sup>Jullien, V.</sup>
10. [Ru(**5**)<sub>2</sub>][PF<sub>6</sub>]<sub>2</sub>
11. [Ru(**6**)<sub>2</sub>][PF<sub>6</sub>]<sub>2</sub>
12. [(**3**)Ru(**4**)][PF<sub>6</sub>]<sub>2</sub>
13. [(**3**)Ru(**5**)][PF<sub>6</sub>]<sub>2</sub>
14. [(**1**)Ru(**4**)][PF<sub>6</sub>]<sub>2</sub> donated<sup>[9], Jullien, V.</sup>
15. [(**1**)Ru(**5**)][PF<sub>6</sub>]<sub>2</sub> donated<sup>Jullien, V.</sup>
16. [(**1**)Ru(**6**)][PF<sub>6</sub>]<sub>2</sub>
17. [(**2**)Ru(**4**)][PF<sub>6</sub>]<sub>2</sub>
18. [(**2**)Ru(**5**)][PF<sub>6</sub>]<sub>2</sub>
19. [(**2**)Ru(**6**)][PF<sub>6</sub>]<sub>2</sub>
20. [(**8**)Ru(**4**)][PF<sub>6</sub>]<sub>2</sub>
21. [(**9**)Ru(**4**)][PF<sub>6</sub>]<sub>2</sub>
22. [(**2**)Ru(**7**)][PF<sub>6</sub>]<sub>2</sub>
23. [Fe(**1**)<sub>2</sub>][PF<sub>6</sub>]<sub>2</sub> [33]
24. [Fe(**2**)<sub>2</sub>][PF<sub>6</sub>]<sub>2</sub>
25. [Fe(**3**)<sub>2</sub>][PF<sub>6</sub>]<sub>2</sub>
26. [Fe(**4**)<sub>2</sub>][PF<sub>6</sub>]<sub>2</sub>
27. [Fe(**8**)<sub>2</sub>][PF<sub>6</sub>]<sub>2</sub>

Donated compounds are from colleagues in the laboratory who worked in collaboration. UV-vis and electrochemical data are in tables 3.5-3.8 and 3.8-3.10 respectively. Number codes are given for some of the complexes (the free acids) at the bottom right of the structures and are repeated in scheme 3.10 on page 207.

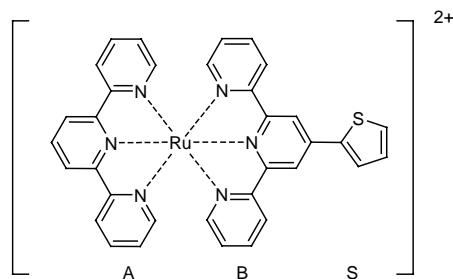


**[(tpy)Ru(1)][PF<sub>6</sub>]<sub>2</sub>**

Previously reported in reference [34].

Formula: C<sub>34</sub>H<sub>24</sub>N<sub>6</sub>RuSP<sub>2</sub>F<sub>12</sub>

Formula weight: 939.7



52 mg (0.118 mmol) [(tpy)RuCl<sub>3</sub>] was added to 37 mg (0.117 mmol) ligand **1** in a round bottom flask with 20 ml EtOH. An addition of 2 drops of N-ethylmorpholine was followed by reflux for 3 hours. NH<sub>4</sub>PF<sub>6</sub> in water was added to the cooled red solution to yield the PF<sub>6</sub><sup>-</sup> salt. After isolation and washing (water and EtOH) a red solid was obtained.

Yield: 50 mg, 0.053 mmol (45%);

<sup>1</sup>H-NMR (CD<sub>3</sub>CN, 500 MHz): δ = 8.92 (s, 2H, B3'), 8.74 (s, 2H, A3'), 8.64 (d, J= 7.73, 2H, A3), 8.49 (d, J= 8.12 Hz, 2H, B3), 8.40 (t, J= 8.16 Hz, 1H, A4'), 8.18 (d, J= 3.72 Hz, 1H, S3), 7.93 (m, 4H, A4+B4), 7.83 (d, J= 5.11 Hz, 1H, S5), 7.42 (m, 3H, B6+S4), 7.34 (d, J= 4.13 Hz, 2H, A6), 7.16 (m, 4H, A5+B5);

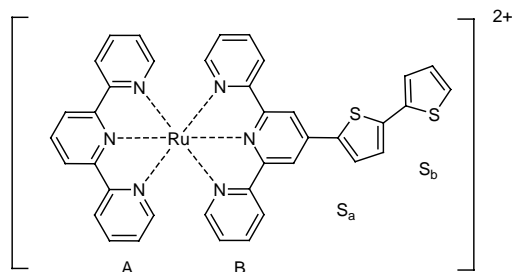
ES-MS *m/z* (calc.): 324.9 ([M-2PF<sub>6</sub>]<sup>2+</sup>).

**[(tpy)Ru(3)][PF<sub>6</sub>]<sub>2</sub>**

Previously reported in reference [14].

Formula: C<sub>38</sub>H<sub>26</sub>N<sub>6</sub>RuS<sub>2</sub>P<sub>2</sub>F<sub>12</sub>

Formula weight: 1021.9



27.8 mg (0.046 mmol) [(3)RuCl<sub>3</sub>] was added to 11.0 mg (0.047 mmol) 2,2':6',2''-terpyridine in 40 ml EtOH. The reaction was refluxed for 2.5 hours. Precipitation with aqueous NH<sub>4</sub>PF<sub>6</sub> yielded a red solid. After filtration and washing in water and ethanol, the clean product was afforded.

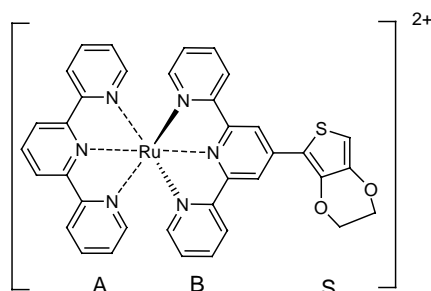
Yield: 14 mg, 0.014 mmol (30%)

<sup>1</sup>H-NMR (CD<sub>3</sub>CN, 400 MHz): δ = 8.89 (s, 2H, B3'), 8.75 (d, J= 8.17 Hz, 2H, A3'), 8.64 (d, J= 7.78, 2H, B3), 8.49 (d, J= 8.14 Hz, 2H, A3), 8.41 (t, J= 8.16 Hz, 1H, A4'), 8.13 (d, J= 3.93 Hz, 1H, S<sub>a</sub>3), 7.93 (m, 4H, A4+B4), 7.55 (d, J= 3.91 Hz, 1H, S<sub>a</sub>4), 7.51 (m, 2H, S<sub>b</sub>3+S<sub>b</sub>5), 7.44 (d, J= 4.88 Hz, 2H, A6), 7.34 (d, J= 4.83 Hz, 2H, B6), 7.18 (m, 5H, A5+B5+ S<sub>b</sub>4);

ES-MS *m/z* (calc.): 366.0 ([M-2PF<sub>6</sub>]<sup>2+</sup>)

**[(tpy)Ru(2)][PF<sub>6</sub>]<sub>2</sub>**Formula: C<sub>34</sub>H<sub>26</sub>N<sub>6</sub>O<sub>2</sub>RuSP<sub>2</sub>F<sub>12</sub>

Formula weight: 997.7



14.0 mg (0.06 mmol) 2,2':6',2''-terpyridine was added to 34.9 mg (0.06 mmol) [(2)RuCl<sub>3</sub>] in 15 ml EtOH. 2 drops of NEM were then added and the reaction refluxed in the microwave reactor for 15 minutes at 145°C. A red powder was precipitated with NH<sub>4</sub>PF<sub>6</sub> (aq.). TLC with MeCN, KCl (sat'd) and H<sub>2</sub>O eluent (14:2:1) showed one red spot.

Yield: 25 mg, 0.025 mmol (42%)

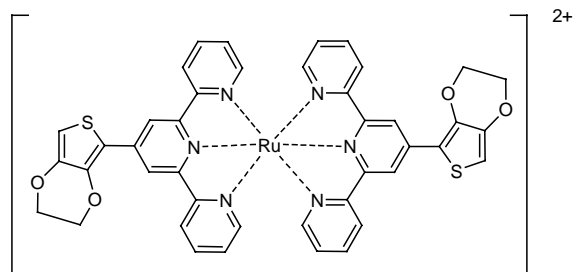
<sup>1</sup>H-NMR (CD<sub>3</sub>CN, 500 MHz): δ = 8.96 (s, 2H, B3'), 8.74 (d, J= 8.16 Hz, 2H, A3'), 8.57 (d, J= 7.83 Hz, 2H, B3), 8.49 (d, J= 8.13 Hz, 2H, A3), 8.40 (t, J= 8.15 Hz, 1H, A4'), 7.92 (m, 2H, A4+B4), 7.44 (d, J= 4.88 Hz, 2H, B6), 7.33 (d, J= 4.34 Hz, 2H, A6), 7.16 (m, 4H, A5+B5), 6.85 (s, 1H, S5), 4.62 (m, 2H, CH<sub>2</sub>O), 4.42 (m, 2H, CH<sub>2</sub>O);

ES-MS *m/z* (calc.): 354.1 ([M-2PF<sub>6</sub>]<sup>2+</sup>).

**Anal.** Calcd for C<sub>36</sub>H<sub>26</sub>N<sub>6</sub>O<sub>2</sub>SRuP<sub>2</sub>F<sub>12</sub>·2H<sub>2</sub>O: C, 41.83; H, 2.93; N, 8.13; found; C, 40.84; H, 2.83; N, 8.14 %

**[Ru(2)<sub>2</sub>][PF<sub>6</sub>]**Formula: C<sub>42</sub>H<sub>30</sub>N<sub>6</sub>O<sub>4</sub>RuS<sub>2</sub>P<sub>2</sub>F<sub>12</sub>

Formula weight: 1138.0



20 mg (~0.054 mmol) of ligand **2** and 13.0 mg (~0.027 mmol) Ru(DMSO)<sub>4</sub>Cl<sub>2</sub> was added to 30 ml EtOH. Under stirring the solution was refluxed at 85°C for 2 hours. The resulting red solution was collected and aqueous NH<sub>4</sub>PF<sub>6</sub> was added to precipitate the PF<sub>6</sub><sup>-</sup> salt. The solid was collected on Celite and washed with water, EtOH and ether. The compound was then redissolved in MeCN and the solvent removed *in vacuo*.

Yield: 15 mg, 0.013 mmol (48%)

**<sup>1</sup>H-NMR** (CD<sub>3</sub>CN, 400 MHz): δ = 8.96 (s, 4H, N3'), 8.57 (d, J= 7.10 Hz, 4H, N3), 7.91 (td, J= 1.49, 7.94, 7.88 Hz, 4H, N4), 7.42 (d, J= 6.30 Hz, 4H, N6), 7.18 (td, J= 1.27, 5.58, 7.50 Hz, 4H, N5), 6.85 (s, 2H, S), 4.61 (m, 4H, CH<sub>2</sub>O), 4.42 (m, 4H, CH<sub>2</sub>O);

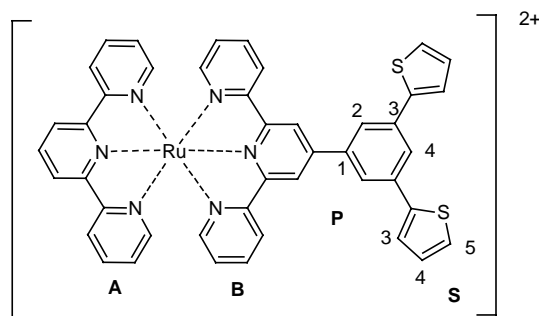
**ES-MS** *m/z* (calc.): 424.0 ([M-2PF<sub>6</sub>]<sup>2+</sup>)

**IR** (solid, cm<sup>-1</sup>): 2920w, 1659m, 1603m, 1495m, 1421m, 1364m, 1252w, 1173m, 1067m, 827s, 785m, 754m, 692m, 611m;

**Anal.** Calcd for C<sub>42</sub>H<sub>30</sub>N<sub>6</sub>O<sub>4</sub>S<sub>2</sub>RuP<sub>2</sub>F<sub>12</sub>·2H<sub>2</sub>O: C, 42.97; H, 2.92; N, 7.16; found; C, 42.36; H, 2.99; N, 8.05 %

**[(tpy)Ru(8)][PF<sub>6</sub>]<sub>2</sub>**Formula: C<sub>44</sub>H<sub>30</sub>N<sub>6</sub>RuS<sub>2</sub>P<sub>2</sub>F<sub>12</sub>

Formula weight: 1098



18.0 mg (0.041 mmol) (tpy)RuCl<sub>3</sub> and 19.2 mg (0.041 mmol) were added to a round bottom flask with 20 ml EtOH. 2 drops of n-ethylmorpholine were added and the reaction refluxed for 2.5 hours. Precipitation with aqueous NH<sub>4</sub>PF<sub>6</sub> resulted in a dark red solid. TLC with CH<sub>3</sub>CN, saturated KNO<sub>3</sub> (aq.) and H<sub>2</sub>O (14:2:1) showed two red spots. One of them was probably [Ru(tpy)<sub>2</sub>]<sup>2+</sup>. The spots were separated with silica column chromatography. The second, larger fraction was the product.

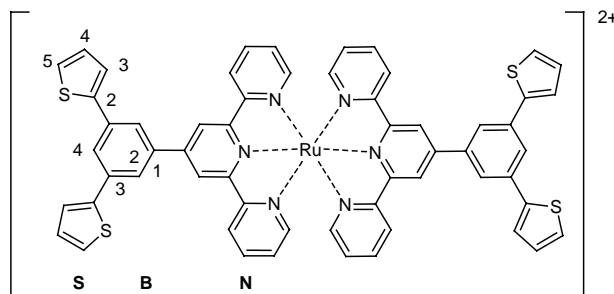
Yield: 7 mg, 0.006 mmol (16%);

<sup>1</sup>H-NMR (CD<sub>3</sub>CN, 400 MHz): δ = 9.14 (s, 4H, B3'), 8.79 (d, J= 8.17 Hz, 2H, A3'), 8.72 (d, J= 8.07 Hz, 2H, B3), 8.53 (d, J= 8.52 Hz, 2H, A3), 8.42 (t, J= 8.16 Hz, 1H, A4'), 8.34 (d, J= 1.61 Hz, 2H, P2), 8.17 (t, J= 1.59 Hz, 1H, P4), 7.94 (dd, J= 8.80, 16.55 Hz, A4+B4), 7.80 (dd, J= 1.14, 3.64 Hz, 2H, S3), 7.58 (dd, J=1.11, 5.08 Hz, 2H, S5), 7.44 (d, J= 6.29 Hz, 2H, B4), 7.37 (d, J= 4.80 Hz, 2H, A4), 7.27 (dd, J= 3.65, 5.08 Hz, 2H, B5), 7.18 (m, 4H, A5+S4);

ES-MS *m/z* (calc.): 443 ([M-2PF<sub>6</sub>]<sup>2+</sup>), 1031 ([M-PF<sub>6</sub>]<sup>+</sup>)

**[Ru(8)]<sub>2</sub>[(PF<sub>6</sub>)<sub>2</sub>]**Formula: C<sub>58</sub>H<sub>38</sub>N<sub>6</sub>RuS<sub>4</sub>P<sub>2</sub>F<sub>12</sub>

Formula weight: 1338.3



35.0 mg (0.074 mmol) of ligand **8** were added to 17.9 mg (0.037 mmol) Ru(II)(DMSO)<sub>4</sub>Cl<sub>2</sub> in 15 ml EtOH. The mixture was refluxed in a microwave reactor for 15 minutes at 145°C. The solution had turned clear red. The product was precipitated out with aqueous NH<sub>4</sub>PF<sub>6</sub> and filtered off on Celite, washed with water, EtOH and ether, and redissolved in MeCN. After evaporation of solvent *in vacuo*, a rather pure red powder product was recovered.

Yield: 22 mg, 0.016 mmol (43%)

<sup>1</sup>H-NMR (CD<sub>3</sub>CN, COSY, 500 MHz): δ = 9.13 (s, 4H, N3'), 8.72 (d, J= 7.91 Hz, 4H, N3), 8.34 (d, J= 1.60 Hz, 4H, B2+B6), 8.18 (s, 2H, B4), 7.97 (dt, J= 1.46, 7.98, 8.00, 4H, N4), 7.80 (dd, J= 1.12, 3.64 Hz, 4H, S3), 7.59 (dd, J= 1.09, 5.07 Hz, 4H, S5), 7.47 (d, J= 4.08 Hz, 4H, N6), 7.28 (m, 4H, N5), 7.22(m, 4H, S4);

ES-MS *m/z* (calc.): 524 ([M-2PF<sub>6</sub>]<sup>2+</sup>);

IR (solid, cm<sup>-1</sup>): 3076w, 1661m, 1593m, 1402m, 1242w, 1207w, 1036w, 825s, 785m, 752m, 692m;

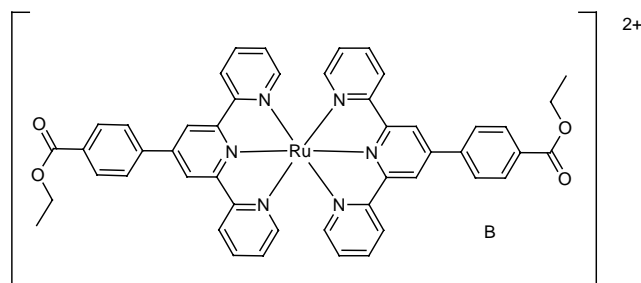
Anal. Calcd for C<sub>58</sub>H<sub>38</sub>N<sub>6</sub>S<sub>4</sub>RuP<sub>2</sub>F<sub>12</sub>·3H<sub>2</sub>O: C, 50.03; H, 3.19; N, 6.04; found; C, 49.77; H, 3.15; N, 6.57 %

**[Ru(4)]<sub>2</sub>[PF<sub>6</sub>]<sub>2</sub>**

Previously reported in reference [15].

Formula: C<sub>48</sub>H<sub>38</sub>N<sub>6</sub>O<sub>4</sub>RuP<sub>2</sub>F<sub>12</sub>

Formula weight: 1153.9



13 mg (0.034 mmol) terpyridine-benzoic-ester was added to a solution of 8.3 mg (0.017 mmol) of [Ru(DMSO)<sub>4</sub>Cl<sub>2</sub>] in 20 ml EtOH. The mixture was refluxed in microwave oven at 145 C° for 15 minutes. A red clear solution was afforded. Aqueous NH<sub>4</sub>PF<sub>6</sub> was added and a precipitate was formed. The precipitate was collected by Celite in a glass frit and washed with water and ethanol. The product was then redissolved in acetonitrile and the solvent evaporated *in vacuo*. TLC with an eluent of MeCN, *sat.* KNO<sub>3</sub> and H<sub>2</sub>O (14:2:1) showed one red spot.

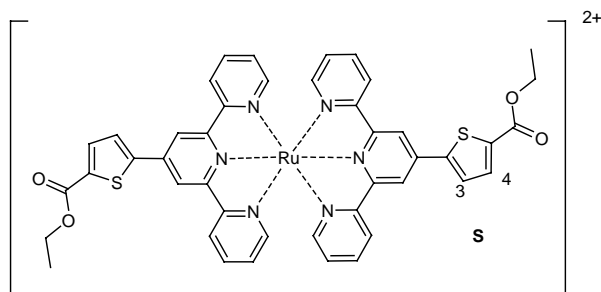
Yield: red brown solid, 12 mg (61%)

<sup>1</sup>H-NMR (CD<sub>3</sub>CN, 250 MHz): δ = 9.04 (s, 2H, N3'), 8.66 (d, J= 8.01 Hz, 2H, N3), 8.34 (dd, J= 8.53, 26.93 Hz, 4H, B), 7.96 (t, J= 7.20 Hz, 2H, N4), 7.44 (d, J= 5.45 Hz, 2H, N6), 7.19 (m, 2H, N5), 4.46 (q, J= 14.2, 7.1 Hz, 2H, CH<sub>2</sub>), 1.44 (t, J= 7.1 Hz, 3H, CH<sub>3</sub>);

ES-MS *m/z* (calc.): 432.1 ([M-2PF<sub>6</sub>]<sup>2+</sup>), 1009.3 ([M-PF<sub>6</sub>]<sup>+</sup>);

**[Ru(5)<sub>2</sub>][PF<sub>6</sub>]<sub>2</sub>**Formula: C<sub>44</sub>H<sub>34</sub>N<sub>6</sub>O<sub>4</sub>RuS<sub>2</sub>P<sub>2</sub>F<sub>12</sub>

Formula weight: 1166.0



12 mg (0.031 mmol) of ligand **5** was added to 18 mg (0.031 mmol) (tpy)RuCl<sub>3</sub> in 20 ml EtOH. 2 drops of N-ethylmorpholine was added as reductant and the reaction was refluxed for 3 hours. After cooling, a solid was precipitated from the ethanol with aqueous NH<sub>4</sub>PF<sub>6</sub>. After isolation of complex, a red solid was recovered.

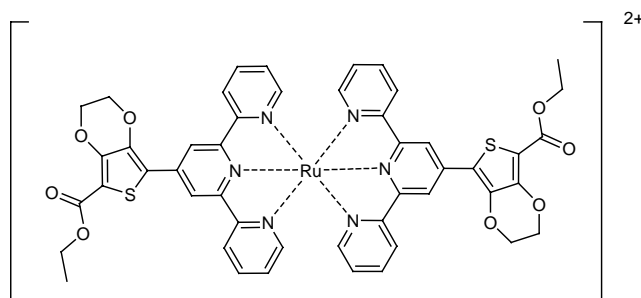
Yield: 11 mg, 0.009 mmol (30%)

<sup>1</sup>H-NMR (CD<sub>3</sub>CN, 400 MHz): δ = 8.97 (s, 4H, N3'), 8.67 (d, J= 7.91 Hz, 4H, N3), 8.17 (d, J= 4.03, 2H, S3), 8.02 (d, J= 4.04 Hz, 2H, S4), 7.95 (t, J= 7.89 Hz, 4H, N4), 7.42 (d, J= 6.13 Hz, 4H, N6), 7.19 (m, 4H, N5), 4.44 (q, J= 7.23, 7.22 Hz, 4H, CH<sub>2</sub>), 1.43 (t, J= 7.12 Hz, 3H, CH<sub>3</sub>);

ES-MS *m/z* (calc.): 438.0 ([M-2PF<sub>6</sub>]<sup>2+</sup>), 1020.9 ([M-PF<sub>6</sub>]);

**[Ru(6)<sub>2</sub>][PF<sub>6</sub>]<sub>2</sub>**Formula: C<sub>48</sub>H<sub>38</sub>N<sub>6</sub>O<sub>8</sub>RuS<sub>2</sub>P<sub>2</sub>F<sub>12</sub>

Formula weight: 1282.1



12 mg (0.027 mmol) of ligand **6** and 6.5 mg (0.014 mmol) Ru(DMSO)<sub>4</sub>Cl<sub>2</sub> were put in a reaction flask with some EtOH. The reaction was refluxed in a microwave reactor for 15



minutes at 145°C under stirring. Solution is dark red after reaction. Aqueous  $\text{NH}_4\text{PF}_6$  was added to give a precipitate that was filtered off through Celite, washed with EtOH, water and ether, redissolved in MeCN and finally the solvent removed *in vacuo*.

Yield: red solid, 4.5 mg, 0.035 mmol (25%)

$^1\text{H-NMR}$  ( $\text{CD}_3\text{CN}$ , COSY, 500 MHz):  $\delta = 9.03$  (s, 4H, N3'), 8.60 (d,  $J = 8.06$  Hz, 4H, N3), 7.93 (t,  $J = 7.60$  Hz, 4H, N4), 7.42 (d,  $J = 4.81$  Hz, 4H, N6), 7.17 (m, 4H, N5), 4.62 (m, 4H,  $\text{CH}_2\text{O}$ ), 4.56 (m, 4H,  $\text{CH}_2\text{O}$ ), 4.39 (q,  $J = 7.12$  Hz, 4H,  $\text{CH}_2$ ), 1.42 (t,  $J = 7.11$  Hz, 3H,  $\text{CH}_3$ );

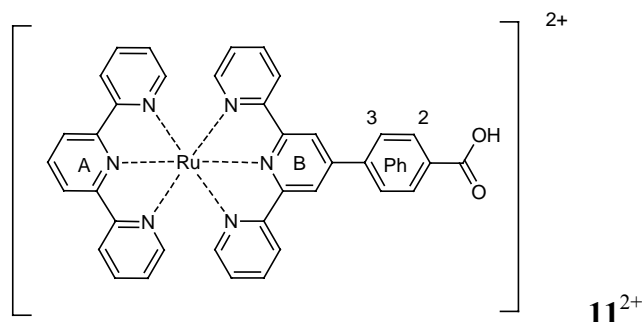
ES-MS  $m/z$  (calc.): 496.1 ( $[\text{M}-2\text{PF}_6]^{2+}$ ), 1137 ( $[\text{M}-\text{PF}_6]^+$ )

### **$[(\text{tpy})\text{Ru}(\mathbf{4})][\text{PF}_6]_2$**

Previously reported in reference [9].

Formula:  $\text{C}_{37}\text{H}_{26}\text{N}_6\text{O}_2\text{RuP}_2\text{F}_{12}$

Formula weight: 997.7



112 mg (0.2 mmol)  $[(\mathbf{4})\text{RuCl}_3]$  was added to a solution of 47 mg (0.2 mmol) tpy in 40 ml MeOH. To the solution 2 drops of NEM was added and the solution was stirred at reflux for 3 hours. A drop of  $\text{HPF}_6$  was added followed by aqueous  $\text{NH}_4\text{PF}_6$  to precipitate product. The solid was filtered off and washed with MeOH and water. Redissolved in MeCN, which was removed *in vacuo*. TLC (MeCN,  $\text{H}_2\text{O}$ , sat.  $\text{KNO}_3$ , 14:2:1) showed one red spot.

Yield: red solid, 60 mg, 0.060 mmol (30%)

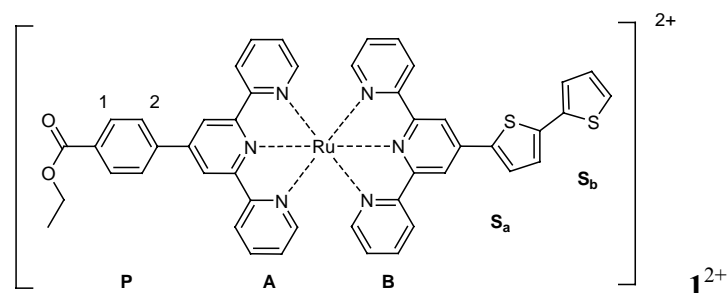
$^1\text{H-NMR}$  ( $\text{CD}_3\text{CN}$ , 250 MHz):  $\delta = 8.75$  (s, 2H, B3'), 8.74 (d,  $J = 8.03$  Hz, 2H, A3'), 8.64 (d,  $J = 8.03$  Hz, 2H, B3), 8.48 (d,  $J = 7.68$  Hz, 2H, A3), 8.42 (t,  $J = 8.04$  Hz, 1H, A4'), 8.38 (d,  $J = 8.40$  Hz, 2H, C3), 8.22 (d,  $J = 8.40$ , 2H, C2), 7.94 (dt,  $J = 1.46, 8.04$  Hz, 2H, B4), 7.91 (dt,  $J = 1.46, 8.04$  Hz, 2H, A4), 7.41 (d,  $J = 5.84$  Hz, 2H, B6), 7.33 (d,  $J = 5.45$  Hz, 2H, A6), 7.15 (m, 4H, A5+B5);

**ES-MS**  $m/z$  (calc.): 356.0 ( $[M-H+Na-2PF_6]^{2+}$ ), 854.1 ( $[M-H+Na-PF_6]^+$ );

**[(3)Ru(4)][PF<sub>6</sub>]<sub>2</sub>**

Formula: C<sub>47</sub>H<sub>34</sub>N<sub>6</sub>O<sub>2</sub>RuS<sub>2</sub>P<sub>2</sub>F<sub>12</sub>

Formula weight: 1170



60 mg (0.099 mmol) (3)RuCl<sub>3</sub> and 35 mg (0.099 mmol) of ligand 4 (acid form) were added to 50 ml MeOH in a round bottom flask. 2 drops of N-ethylmorpholine were added. The reaction was refluxed for 3 hours. After cooling to room temperature the two drops of HPF<sub>6</sub> was added to ensure a protonated carboxylate. Aqueous NH<sub>4</sub>PF<sub>6</sub> was added to precipitate the complex. The precipitate was filtered off through Celite and washed with water and MeOH. After re-dissolving the complex in MeCN, the solvent was removed *in vacuo* to yield a red solid.

Yield: 42 mg, 0.036 mmol (36%).

The ethyl group was added by reacting 30 mg (0.0263 mmol) of the acid in 5 ml DMF with 2 equivalents of C<sub>2</sub>H<sub>5</sub>I and 5 equivalents Na<sub>2</sub>CO<sub>3</sub> at room temperature overnight. Water, NH<sub>4</sub>PF<sub>6</sub> and ethyl acetate were added to precipitate ester. Ester was isolated as red powder.

Yield: 9 mg, 0.0077 mmol (21%)

**Ester**

<sup>1</sup>H-NMR (CD<sub>3</sub>CN, 400 MHz): δ = 9.03 (s, 2H, A3'), 8.90 (s, 2H, B3'), 8.65 (dd, J= 2.98, 7.74 Hz, 4H, A3+B3), 8.33 (dd, J= 8.67, 28.13 Hz, 4H, P1+P2), 8.13 (d, J= 3.93, 1H, S<sub>a</sub>3), 7.96 (t, J= 7.87 Hz, 4H, A4+B4), 7.56 (d, J= 3.90 Hz, 1H, S<sub>b</sub>3), 7.52 (m, 4H, S<sub>a</sub>4+S<sub>b</sub>5), 7.46 (d, J= 3.48 Hz, 2H, A6), 7.42 (d, J= 4.82 Hz, 2H, B6), 7.91 (m, 5H, A5+B5+S<sub>b</sub>4), 4.45 (q, J= 7.12, 7.15 Hz, 2H, CH<sub>2</sub>), 1.45 (t, J= 7.14 Hz, 3H, CH<sub>3</sub>);

**EI MS**  $m/z$  (calc.): 440.2 ( $[M-2PF_6]^{2+}$ ), 1024.9 ( $[M-PF_6]^+$ );

**Acid**

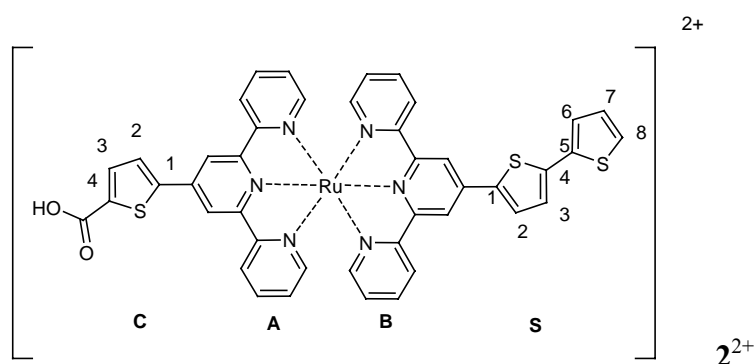
**ES-MS**  $m/z$  (calc.): 426.1 ( $[M-2PF_6]^{2+}$ ), 1040.9 ( $[M-PF_6]^+$ );

**Anal.** Calcd for  $C_{45}H_{30}N_6O_2RuS_2P_2F_{12}$ : C, 47.33; H, 2.65; N, 7.36; found; C, 47.19; H, 3.31; N, 7.40 %

**[(3)Ru(5)][PF<sub>6</sub>]<sub>2</sub>**

Formula:  $C_{43}H_{28}N_6O_2RuS_3P_2F_{12}$

Formula weight: 1148



18 mg (0.036 mmol)  $[Ru(3)Cl_3]$  was added to a solution of 14 mg (0.036 mmol) of tpySCOOEt in 15 ml MeOH. 2 drops of N-ethylmorpholine (NEM) were added. The solution was stirred for 3 hours under reflux. After cooling the solution to room temperature aqueous  $NH_4PF_6$  was added and a red precipitate was formed. The precipitate was collected on celite on a frit and washed with water and methanol. The product was then redissolved in acetonitrile and the solvent evaporated *in vacuo*. TLC with MeCN,  $KNO_3$ (sat) and  $H_2O$  (14:2:1) showed a red spot. The red product was purified on a silica column.

Yield: red solid, 28 mg, 0.024 mmol, (66%)

**Ester**

**<sup>1</sup>H-NMR** ( $CD_3CN$ , COSY, 500 MHz):  $\delta$  = 8.98 (s, 2H, A3'), 8.90 (s, 2H, B3'), 8.66 (m, 4H, A3+B3), 8.16 (d,  $J=3.95$  Hz, 1H, C2), 8.13 (d,  $J=3.89$  Hz, 1H, S2), 8.02 (d,  $J=3.95$  Hz, 1H, C3), 7.95 (m, 4H, A4+B4), 7.55 (d,  $J=3.87$  Hz, 1H, S6), 7.51 (m, 2H, S3+S8), 7.45 (d,  $J=5.66$  Hz, 2H, A6), 7.41 (d, 2H, B6) 7.19 (m, 5H, A5+B5+S7), 4.43 (q,  $J=7.13$  Hz, 2H,  $CH_2$ ), 1.42 (t,  $J=7.12$  Hz, 3H,  $CH_3$ );

**<sup>13</sup>C-NMR** (CD<sub>3</sub>CN, 500 MHz, DEPT 500 MHz): δ = 162.8 (COOEt, quat), 159.2 (A2/B2, quat), 159.0 (A2'/B2', quat), 157.0 (, quat), 156.5 (, quat), 153.8 (A6+B6, tert), 139.4 (A4+B4, tert), 135.9 (, tert), 130.7 (Sa, tert), 130.0 (Ca, tert), 129.7 (, tert), 129.0 (, tert), 128.8.0 (, tert), 128.0 (, tert), 127.0 (Sc, tert), 126.7 (, tert), 126 (Sb+Se, tert), 125.9 (A3+B3, tert), 121.3 (B3', tert), 120.4 (A3', tert), 63.1 (CH<sub>2</sub>, sec), 14.9 (CH<sub>3</sub>, tert);

**ES-MS** *m/z* (calc.): 443 ([M-2PF<sub>6</sub>]<sup>2+</sup>), 1031 ([M-PF<sub>6</sub>]<sup>+</sup>)

**IR** (solid, cm<sup>-1</sup>): 1695m, 1603m, 1466s, 1448m, 1425m, 1398m, 1331s, 1277m, 1242m, 1155m, 1084s, 1053s, 878m, 827m, 789s [PF<sub>6</sub>], 746s, 729m, 704m;

### Acid

To a solution of 18 mg (0.0153 mmol) [Ru(tpySS)(tpySCOOEt)][PF<sub>6</sub>]<sub>2</sub> in 2 ml ACN, 1 ml NaOH (2M) was slowly added. The mixture was heated to 70°C for 3 hours. After cooling to room temperature and addition of a few drops of HPF<sub>6</sub>, the compound was precipitated by adding aqueous NH<sub>4</sub>PF<sub>6</sub>.

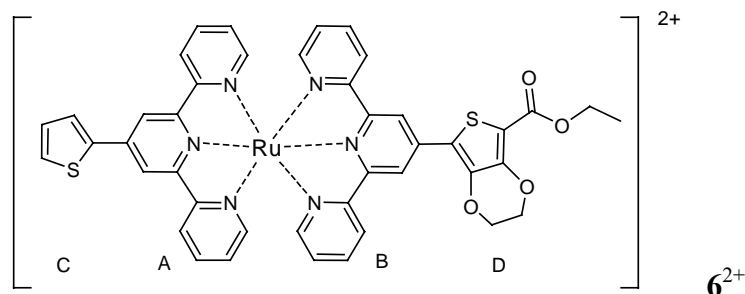
Yield: 14 mg (79%)

**<sup>1</sup>H-NMR** (CD<sub>3</sub>CN, 400 MHz): δ = 8.96 (s, 2H, A3'), 8.89 (s, 2H, B3'), 8.66 (t, J=8.73 Hz, 4H, A3+B3), 8.12 (dd, J=3.95 Hz, 1H, C2), 8.10 (s, 3.89 Hz, 1H, S2), 7.94 (m, 4H, A4+B4), 7.66 (s, 3.95 Hz, 1H, C3), 7.55 (s, 4H, S6), 7.52 (1H, A6), 7.51 (m, 2H, S3+S8), 7.41 (1H, B6), 7.19 (m, 5H, A5+B5+S7);

**ES-MS** *m/z* (calc.): 440.2 ([M-2PF<sub>6</sub>+Na-H]<sup>2+</sup>), 857.3 ([M-2PF<sub>6</sub>-H]<sup>+</sup>)

**IR** (solid, cm<sup>-1</sup>): 1666m, 1607m, 1537m, 1468w, 1452w, 1427m, 1398m, 1371m, 1317w, 1232m, 1161m, 1082m, 1053w, 1028w, 968s, 824s [PF<sub>6</sub>], 787m, 752m, 652m, 555s [PF<sub>6</sub>];

**Anal.** Calcd for C<sub>43</sub>H<sub>28</sub>N<sub>6</sub>O<sub>2</sub>RuS<sub>3</sub>P<sub>2</sub>F<sub>12</sub>·7H<sub>2</sub>O·NaPF<sub>6</sub>: C, 35.82; H, 2.94; N, 5.83; found; C, 35.26; H, 2.91; N, 5.81 %

**[(1)Ru(6)][PF<sub>6</sub>]<sub>2</sub>**Formula: C<sub>43</sub>H<sub>32</sub>N<sub>6</sub>O<sub>4</sub>RuS<sub>2</sub>Formula weight: 862 (+2PF<sub>6</sub>: 1152)

10 mg (0.0245 mmol) terpyridine-ethylenedioxythienyl carboxylate was added to a solution of 11 mg (0.0210 mmol) of (1)RuCl<sub>3</sub> in 20 ml EtOH. Two drops of NEM were added for reduction of Ru(III). The mixture was refluxed in microwave oven at 145 C° for 15 minutes. A red clear solution was afforded. Aqueous NH<sub>4</sub>PF<sub>6</sub> was added and a precipitate was formed. The precipitate was collected by Celite in a frit and washed with water and ethanol. The product was then redissolved in acetonitrile and the solvent evaporated *in vacuo*. TLC with an eluent of MeCN, KNO<sub>3</sub>(sat) and H<sub>2</sub>O (14:2:1), showed one large red spot and another weak spot (Maybe the acid).

Yield: red solid, 12 mg (61%)

<sup>1</sup>H-NMR (CD<sub>3</sub>CN, COSY, 400 MHz): δ = 9.03 (s, 2H, B3'), 8.93 (s, 2H, A3'), 8.66 (m, 4H, A3+B3), 8.18 (dd, J = 3.68, 1.09 Hz, 1H, C3), 7.94 (m, 4H, A6+B6), 7.84 (dd, J = 5.09, 1.02 Hz, 1H, C5), 7.43 (m, 5H, A4+B4+C4), 7.17 (m, 4H, A5+B5), 4.64 (m, 2H, D<sup>CH2</sup>), 4.56 (m, 2H, D<sup>CH2</sup>), 4.38 (q, J = 7.12 Hz, 2H, CH<sub>2</sub>), 1.39 (t, J = 7.13 Hz, 3H, CH<sub>3</sub>);

ES-MS *m/z* (calc.): 430.9 ([M-2PF<sub>6</sub>]<sup>2+</sup>)**Acid**

Synthesis of acid: 10 mg of the ester was dissolved in 2 ml CH<sub>3</sub>CN. 1 ml NaOH (2M) was added drop-wise while stirring. Solution was heated to 80 C° for 2 hours. After 2 hours the solution was cooled to room temperature and a few drops of HCl (1.5 M) were added slowly. The solid was filtered through Celite and washed with water and EtOH.

Yield: red solid, 2 mg (20%)

<sup>1</sup>H-NMR (CD<sub>3</sub>CN, 400 MHz): δ = 9.03 (s, 2H, B3'), 8.93 (s, 2H, A3'), 8.64 (m, 4H, A3+B3), 8.18 (dd, J = 3.68, 1.09 Hz, 1H, C3), 7.94 (m, 4H, A6+B6), 7.84 (dd, J = 5.09, 1.02 Hz, 1H,

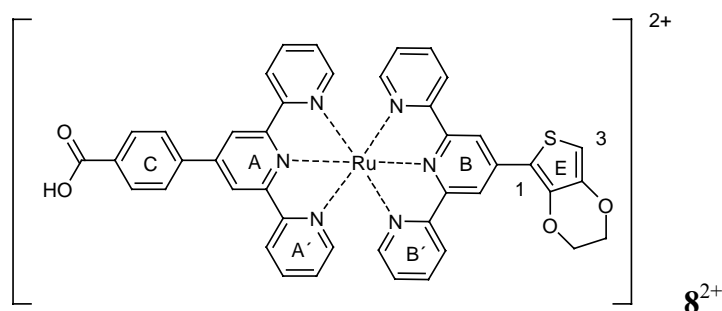
C5), 7.42 (m, 5H, A4+B4+C4), 7.17 (m, 4H, A5+B5), 4.64 (m, 2H, D<sup>CH2</sup>), 4.56 (m, 2H, D<sup>CH2</sup>), 4.38 (q, J = 7.12 Hz, 2H, CH<sub>2</sub>);

**ES-MS** *m/z* (calc.): 416.2 ([M-2PF<sub>6</sub>]<sup>2+</sup>);

**[(2)Ru(4)][PF<sub>6</sub>]<sub>2</sub>**

Formula: C<sub>45</sub>H<sub>34</sub>N<sub>6</sub>O<sub>4</sub>RuSP<sub>2</sub>F<sub>12</sub>

Formula weight: 1145.9



10 mg (0.028 mmol) **4** was added to 7.4 mg (0.028 mmol) RuCl<sub>3</sub>·3H<sub>2</sub>O in 15 ml EtOH. The reaction mixture was heated in microwave at 145°C for 15 minutes. After having cooled down to room temperature, the solution had 10.6 mg (0.028 mmol) of **2** and 1 drop NEM added to it. The reaction is heated in microwave at 145°C for 15 minutes. After reflux a drop of HPF<sub>6</sub> was added and then NH<sub>4</sub>PF<sub>2</sub> in some water to precipitate the PF<sub>6</sub> salt.

**Yield:** red solid, 20 mg (64%)

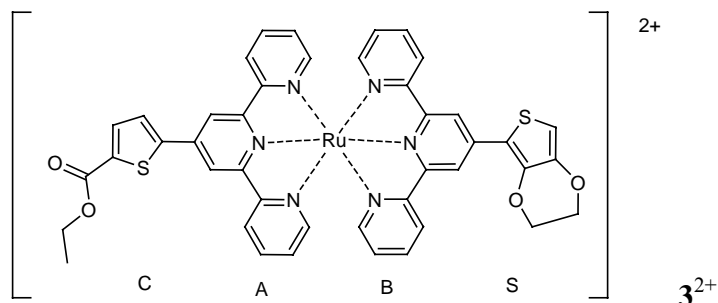
<sup>1</sup>H-NMR (CD<sub>3</sub>CN, 400 MHz): δ = 9.03 (s, 2H, A3'), 8.98 (s, 2H, B3'), 8.65 (d, J= 7.94 Hz, 2H, A3), 8.59 (d, J= 8.23 Hz, 2H, B3), 8.33 (dd, J= 8.68, 28.34 Hz, 4H, C2+C3), 7.94 (dd, J= 6.41, 14.29 Hz, 4H, A4+B4), 7.46 (d, J= 4.78 Hz, 2H, A6), 7.40 (d, J= 6.30 Hz, 2H, B6), 7.17 (m, 4H, A5+B5), 6.85 (s, 1H, E3), 4.61 (m, 2H, E<sup>CHO</sup>), 4.41 (m, 2H, E<sup>CHO</sup>);

**ES-MS** *m/z* (calc.): 414 ([M-2PF<sub>6</sub>]<sup>2+</sup>), 973 ([M-PF<sub>6</sub>]<sup>+</sup>)

**Anal.** Calcd for C<sub>43</sub>H<sub>30</sub>N<sub>6</sub>O<sub>4</sub>RuSP<sub>2</sub>F<sub>12</sub>·4H<sub>2</sub>O·NH<sub>4</sub>PF<sub>6</sub>: C, 38.18; H, 3.13; N, 7.25; found; C, 38.95; H, 3.20; N, 7.10 %

**[(2)Ru(5)][PF<sub>6</sub>]<sub>2</sub>**Formula: C<sub>45</sub>H<sub>34</sub>N<sub>6</sub>O<sub>6</sub>RuS<sub>2</sub>

Formula weight: 1152



To a 100 ml round bottom flask 13.0 mg of **5** (0.034 mmol) was mixed with 20 mg (0.034 mmol) (2)RuCl<sub>3</sub> in 20 ml of EtOH. 2 drops of NEM was added and the solution heated to reflux for 3 hours. After the reaction has cooled to room temperature aqueous NH<sub>4</sub>PF<sub>6</sub> is added to get precipitation. The precipitate was filtered through celite and washed with water and ethanol. Complex was purified by column chromatography with eluent of MeCN, KNO<sub>3</sub>(sat) and H<sub>2</sub>O (14:2:1).

<sup>1</sup>H-NMR (CD<sub>3</sub>CN, 400 MHz): δ = 8.97 (s, 2H, A3'), 8.96 (s, 2H, B3'), 8.66 (d, J=8.06 Hz, 2H, A3), 8.58 (d, J=8.10, 2H, B3), 8.16 (d, J=3.97 Hz, 1H, Ca), 8.03 (d, J=3.98 Hz, 1H, Ca), 7.93 (m, 4H, A4+B4), 7.41 (m, 4H, A6+B6), 7.18 (m, 4H, A5+B5), 6.86 (s, 1H, S), 4.61 (m, 2H, S<sup>CHO</sup>), 4.44 (q, J= 4.93 Hz, 2H, CH<sub>2</sub>), 4.41 (m, 2H, S<sup>CHO</sup>), 1.43 (t, J= 7.12 Hz, 3H, CH<sub>3</sub>).

ES-MS *m/z* (calc.): 443 ([M-2PF<sub>6</sub>]<sup>2+</sup>), 1031 ([M-PF<sub>6</sub>]<sup>+</sup>)

IR (solid, cm<sup>-1</sup>):

**Acid**

The hydrolysis of the ester was done with the standard procedure described in chapter 3.1 and for the hydrolysis of [(3)Ru(5)][PF<sub>6</sub>].

<sup>1</sup>H-NMR (CD<sub>3</sub>CN, 400 MHz): δ = 8.98 (s, 2H, A3'), 8.97 (s, 2H, B3'), 8.69 (d, J= Hz, 2H, A3), 8.59 (d, J= Hz, 2H, B3), 8.15 (d, J=3.97 Hz, 1H, Ca), 7.92 (m, 4H, A4+B4), 7.45 (m, 4H, A6+B6), 7.18 (m, 4H, A5+B5), 6.84 (s, 1H, S), 4.61 (4.61 (m, 2H, S<sup>CHO</sup>)), 4.42 (m, 2H, S<sup>CHO</sup>).

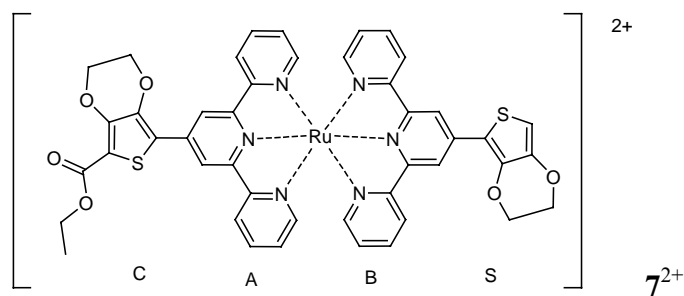
ES-MS *m/z* (calc.): 429.5 ([M-H+Na-2PF<sub>6</sub>]<sup>2+</sup>)

**Anal.** Calcd for  $C_{41}H_{28}N_6O_4RuS_2P_2F_{12} \cdot 9H_2O \cdot NaPF_6$ : C, 33.87; H, 3.19; N, 5.78; found; C, 33.45; H, 2.84; N, 5.93 %

**[(2)Ru(6)][PF<sub>6</sub>]<sub>2</sub>**

Formula:  $C_{45}H_{34}N_6O_6RuS_2$

Formula weight: 1210



30 mg (0.046 mmol) of the previously prepared  $[Ru(6)Cl_3]$  was added to an EtOH solution with 17 mg (0.047 mmol) of **2**. Two drops of NEM were added and the solution refluxed for 3 hours. TLC (MeCN,  $KNO_3$  sat. and  $H_2O$ ; 14:2:1) showed one red spot. The product was precipitated with aqueous  $NH_4PF_6$ , washed with water and ethanol and redissolved in acetonitrile. Evaporation of solvent *in vacuo* afforded the product as a red solid.

Yield: 14 mg, 0.012 mmol (25%)

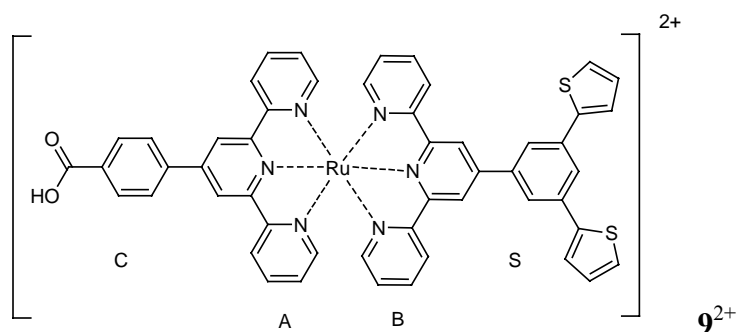
**<sup>1</sup>H-NMR** ( $CD_3CN$ , 500 MHz):  $\delta$  = 9.01 (s, 2H, A3'), 8.96 (s, 2H, B3'), 8.59 (dd, 4H, J= 8.02, 12.38 Hz, A3+B3), 7.91 (m, 4H, A4+B4), 7.42 (m, 4H, A4+B4), 7.17 (m, 4H, A5+B5), 6.85 (s, 1H, S5), 4.65 (m, 2H, C<sup>CHO</sup>), 4.61 (m, 2H, S<sup>CHO</sup>), 4.55 (m, 2H, C<sup>CHO</sup>), 4.42 (m, 2H, S<sup>CHO</sup>), 4.38 (q, J= 7.11 Hz, 2H, CH<sub>2</sub>), 1.39 (t, J= 7.12 Hz, 3H, CH<sub>3</sub>).

**ES-MS**  $m/z$  (calc.): 460.1 ( $[M-2PF_6]^{2+}$ ), 1064.7 ( $[M-PF_6]^+$ ).



**[(8)Ru(4)][PF<sub>6</sub>]<sub>2</sub>**Formula: C<sub>51</sub>H<sub>34</sub>N<sub>6</sub>O<sub>2</sub>RuS<sub>2</sub>

Formula weight: 1218.0



12.0 mg (~0.02 mmol) (4)RuCl<sub>3</sub> and 9.7 mg (~0.02 mmol) 4'-[2,5-(dithiophene)phenyl]-2,2':6',2''-terpyridine were put in ~30 ml EtOH and refluxed for 3 hours under stirring with two drops of NEM added. The solution turns red and when it reached room temperature it was precipitated with aqueous NH<sub>4</sub>PF<sub>6</sub>. The product was collected on Celite, redissolved in MeCN and the solvent was then removed *in vacuo*.

The ester was dissolved in a small amount of MeCN (~3 ml). 1 ml NaOH (2M) was added dropwise and the reaction refluxed 3 hours. When the reaction had cooled to room temperature, 2 drops of HPF<sub>6</sub> were added. The acid was isolated the same way as the ester.

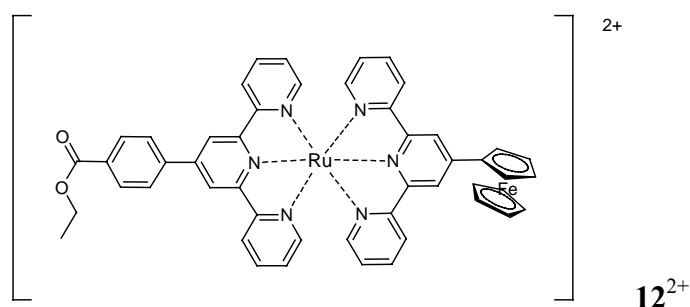
<sup>1</sup>H-NMR (CD<sub>3</sub>CN, 400 MHz): δ = 9.12 (s, 2H, B3'), 9.06 (s, 2H, A3'), 8.69 (m, 2H, A3+B3), 8.29 (m, 4H, C2+C3+C5+C6), 8.19 (s, 1H, D4), 7.96 (m, 4H, A4+B4), 7.79 (m, 2H, B6), 7.59 (d, J = 4.38 Hz, 2H, S3), 7.45 (m, 4H, A6+S5), 7.20 (m, 4H, A5+B5+S4);

ES-MS *m/z* (calc.): 927 ([M-H-2PF<sub>6</sub>]<sup>+</sup>), 1073 ([M-PF<sub>6</sub>]<sup>+</sup>), 478 ([M ester-2PF<sub>6</sub>]<sup>2+</sup>), 1101 ([M ester-PF<sub>6</sub>]<sup>+</sup>)

**Anal.** Calcd for C<sub>51</sub>H<sub>34</sub>N<sub>6</sub>O<sub>2</sub>RuS<sub>2</sub>P<sub>2</sub>F<sub>12</sub>·8H<sub>2</sub>O·NaPF<sub>6</sub>: C, 40.03; H, 3.29; N, 5.49; found; C, 40.37; H, 3.30; N, 5.40 %

**[(9)Ru(4)][PF<sub>6</sub>]<sub>2</sub>**Formula: C<sub>49</sub>H<sub>38</sub>FeN<sub>6</sub>O<sub>2</sub>Ru

Formula weight: 1189.8



10 mg (0.017 mmol) [Ru(tpyPhenylCOOEt)Cl<sub>3</sub>] was added to a solution of 7 mg (0.017 mmol) of tpyFc in 20 ml EtOH. 2 drops of N-ethylmorpholine (NEM) were added. The solution was stirred for 2 hours under reflux. After cooling the solution to room temperature aqueous NH<sub>4</sub>PF<sub>6</sub> was added and a red precipitate was formed. The precipitate was collected by celite in a frit and washed with water and methanol. The product was then redissolved in acetonitrile and the solvent evaporated *in vacuo*. TLC with A-sol showed a red spot and a weak spot of purple that could be iron complex. Purification with column chromatography yielded the product.

Yield: red solid, 7 mg, 0.006 mmol, (35%)

**Ester**

<sup>1</sup>H-NMR (CD<sub>3</sub>CN): δ = 9.03 (s, 2H, A3'), 8.75 (s, 2H, B3'), 8.65 (t, J= 8.96 Hz, 4H, A3+B3), 8.34 (dd, J= 8.27, 37.18 Hz, 4H, Phenyl), 7.95 (m, J=3.89 Hz, 4H, A4+B4), 7.42 (dd, J= 5.29, 28.35 Hz, 2H, N6), 7.22 (m, 2H, B5), 7.17 (m, 2H, A5), 5.36 (s, 2H, Fc), 4.80 (s, 2H, Fc), 4.36 (s, 4H, Fc), 3.12 (q, J=7.12, 14.2 Hz, 2H, CH<sub>2</sub>), 1.28 (t, J= 7.1 Hz, 3H, CH<sub>3</sub>);

ES-MS *m/z* (calc.): 450.0 ([M-2PF<sub>6</sub>]<sup>2+</sup>), 1045.2 ([M-PF<sub>6</sub>]<sup>+</sup>);

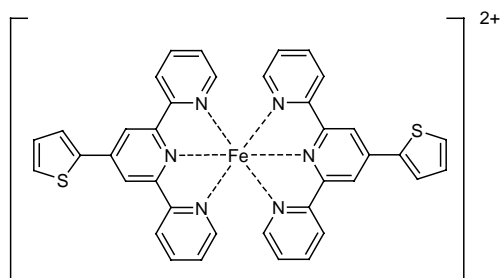
**Anal.** Calcd for C<sub>47</sub>H<sub>34</sub>FeN<sub>6</sub>O<sub>2</sub>RuP<sub>2</sub>F<sub>12</sub>: C, 48.60; H, 2.95; N, 7.23; found; C, 48.04; H, 3.08; N, 7.04 %

## Iron Complexes

### [Fe(**1**)<sub>2</sub>][PF<sub>6</sub>]<sub>2</sub>

Formula: C<sub>38</sub>H<sub>26</sub>FeN<sub>6</sub>S<sub>2</sub>P<sub>2</sub>F<sub>12</sub>

Formula weight: 976.6



22 mg (0.070 mmol) of ligand **1** was added to 12 mg (0.036 mmol) [Fe(H<sub>2</sub>O)<sub>6</sub>][BF<sub>4</sub>]<sub>2</sub> in 20 ml CH<sub>3</sub>CN/CH<sub>3</sub>OH (1:1). The solution was stirred for 15 minutes at room temperature. Aqueous NH<sub>4</sub>PF<sub>6</sub> was added to precipitate the complex as a blue solid.

Yield: 28 mg, 0.028 mmol (80%)

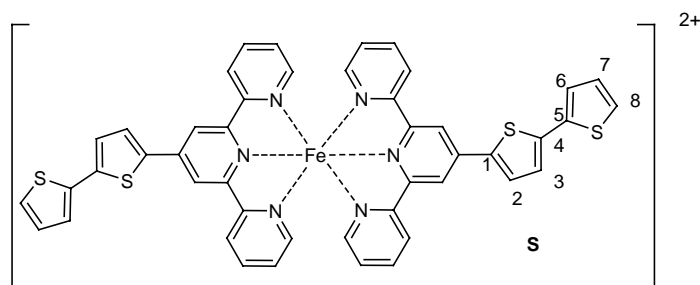
<sup>1</sup>H-NMR (CD<sub>3</sub>CN, 400 MHz): δ = 9.09 (s, 4H, N3'), 8.61 (d, J= 6.81 Hz, 4H, N3), 8.30 (dd, J= 1.13, 3.71 Hz, 2H, S3), 7.90 (m, 6H, N4+S5), 7.47 (dd, J= 3.73, 5.11 Hz, 2H, S4), 7.19 (d, J= 5.80 Hz, 4H, N6), 7.08 (m, 4H, N5);

ES-MS *m/z* (calc.): 343.9 ([M-2PF<sub>6</sub>]<sup>2+</sup>)

**Anal.** Calcd for C<sub>38</sub>H<sub>26</sub>FeN<sub>6</sub>S<sub>2</sub>P<sub>2</sub>F<sub>12</sub>•H<sub>2</sub>O: C, 45.89; H, 2.84; N, 8.45; found; C, 45.07; H, 2.87; N, 8.45 %

**[Fe(3)<sub>2</sub>][PF<sub>6</sub>]<sub>2</sub>**Formula: C<sub>46</sub>H<sub>30</sub>FeN<sub>6</sub>S<sub>4</sub>P<sub>2</sub>F<sub>12</sub>

Formula weight: 1140.6



20 mg (0.050 mmol) of **3** was added to 8.5 mg (0.025 mmol) [Fe(H<sub>2</sub>O)<sub>6</sub>][BF<sub>4</sub>]<sub>2</sub> in 20 ml CH<sub>3</sub>CN/CH<sub>3</sub>OH (1:1). The solution was stirred for 15 minutes at room temperature. Aqueous NH<sub>4</sub>PF<sub>6</sub> was added to precipitate the complex as a blue solid.

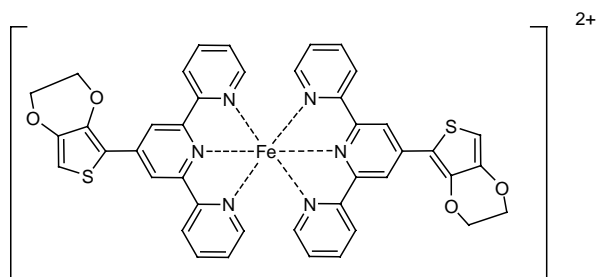
Yield: 24 mg, 0.021 mmol (85%)

<sup>1</sup>H-NMR (CD<sub>3</sub>CN, 400 MHz): δ = 9.06 (s, 4H, N3'), 8.61 (d, J= 8.56 Hz, 4H, N3), 8.25 (d, J= 3.90 Hz, 2H, S2), 7.91 (t, J= 7.12 Hz, 4H, N4), 7.61 (d, J= 3.86 Hz, 2H, S6), 7.55 (d, J= 4.64 Hz, 4H, S3+S8), 7.21 (m, 6H, N6+S7), 7.09 (t, J= 6.55 Hz, 4H, N5);

ES-MS *m/z* (calc.): 425.3 ([M-2PF<sub>6</sub>]<sup>2+</sup>), 996.0 ([M-PF<sub>6</sub>]<sup>+</sup>)

**[Fe(2)<sub>2</sub>][PF<sub>6</sub>]<sub>2</sub>**Formula: C<sub>42</sub>H<sub>30</sub>FeN<sub>6</sub>O<sub>4</sub>S<sub>4</sub>P<sub>2</sub>F<sub>12</sub>

Formula weight: 1092.6



18.0 mg (0.048 mmol) of **2** was added to 8.4 mg (0.025 mmol) [Fe(H<sub>2</sub>O)<sub>6</sub>][BF<sub>4</sub>]<sub>2</sub> in 20 ml CH<sub>3</sub>CN/CH<sub>3</sub>OH (1:1). The solution was stirred for 15 minutes at room temperature. Aqueous NH<sub>4</sub>PF<sub>6</sub> was added to precipitate the complex as a blue solid.

Yield: 23 mg, 0.021 mmol (85%)

<sup>1</sup>H-NMR (CD<sub>3</sub>CN, 400 MHz): δ = 9.12 (s, 4H, N3'), 8.54 (d, J= 7.86 Hz, 4H, N3), 7.87 (t, J= 7.83 Hz, 4H, N4), 7.18 (d, J= 5.70 Hz, 4H, N6), 7.06 (t, J= 5.98 Hz, 4H, N5), 6.91 (s, 2H, S5), 4.65 (m, 4H, CH<sub>2</sub>O), 4.45 (m, 4H, CH<sub>2</sub>O);

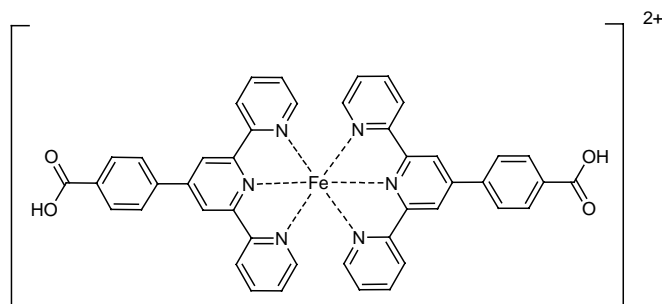
ES-MS *m/z* (calc.): 401.4 ([M-2PF<sub>6</sub>]<sup>2+</sup>)

Anal. Calcd for C<sub>42</sub>H<sub>30</sub>FeN<sub>6</sub>O<sub>4</sub>S<sub>2</sub>P<sub>2</sub>F<sub>12</sub>•2H<sub>2</sub>O: C, 44.69; H, 3.04; N, 7.56; found; C, 44.46; H, 2.89; N, 7.56 %

### [Fe(4)<sub>2</sub>][PF<sub>6</sub>]<sub>2</sub>

Formula: C<sub>44</sub>H<sub>30</sub>FeN<sub>6</sub>O<sub>4</sub>P<sub>2</sub>F<sub>12</sub>

Formula weight: 1052.6



35.0 mg (0.099 mmol) of **4** was added to 16.7 mg (0.049 mmol) [Fe(H<sub>2</sub>O)<sub>6</sub>][BF<sub>4</sub>]<sub>2</sub> in 20 ml CH<sub>3</sub>CN/CH<sub>3</sub>OH (1:1). The solution was stirred for 30 minutes at room temperature. Aqueous NH<sub>4</sub>PF<sub>6</sub> was added to precipitate the complex as a purple solid. A substantial amount of the complex stuck in the celite probably due to the acid groups and was lost.

Yield: 24 mg, 0.0225 mmol (46%);

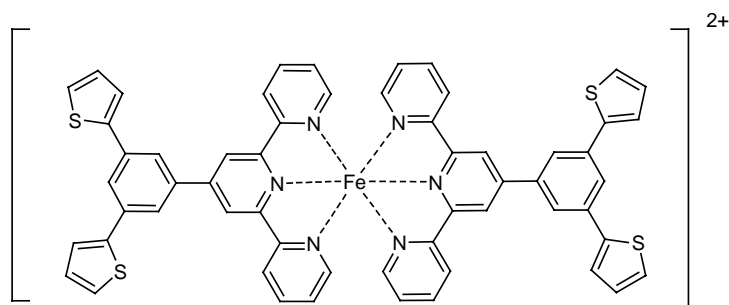
<sup>1</sup>H-NMR (CD<sub>3</sub>CN, 400 MHz): δ = 9.22 (s, 4H, N3'), 8.62 (d, J= 7.77 Hz, 4H, N3), 8.41 (s, 8H, Phenyl), 7.92 (t, J= 7.80 Hz, 4H, N4), 7.19 (d, J= 5.62 Hz, 4H, N6), 7.09 (t, J= 6.60 Hz, 4H, N5).

ES-MS *m/z* (calc.): 381.5 ([M-2PF<sub>6</sub>]<sup>2+</sup>), 761.4 ([M-2PF<sub>6</sub>-H]<sup>+</sup>), 907.2 ([M-PF<sub>6</sub>]<sup>+</sup>)

Anal. Calcd for C<sub>42</sub>H<sub>30</sub>FeN<sub>6</sub>O<sub>4</sub>S<sub>2</sub>P<sub>2</sub>F<sub>12</sub>•3H<sub>2</sub>O: C, 47.76; H, 3.28; N, 7.59; found; C, 47.12; H, 3.18; N, 8.04 %

**[Fe(8)<sub>2</sub>][PF<sub>6</sub>]<sub>2</sub>**Formula: C<sub>58</sub>H<sub>38</sub>FeN<sub>6</sub>S<sub>4</sub>P<sub>2</sub>F<sub>12</sub>

Formula weight: 1293.1



15.0 mg ( $3.17 \cdot 10^{-5}$  mole) of **8** was added to 5.3 mg ( $1.59 \cdot 10^{-5}$  mole) [Fe(H<sub>2</sub>O)<sub>6</sub>][BF<sub>4</sub>]<sub>2</sub> in 20 ml CH<sub>3</sub>CN/CH<sub>3</sub>OH (1:1). The solution was stirred for 30 minutes at room temperature. Aqueous NH<sub>4</sub>PF<sub>6</sub> was added to precipitate the complex as a purple solid. The complexation was slow and not complete.

Yield: 7.2 mg,  $5.57 \cdot 10^{-6}$  mole, (45%);

<sup>1</sup>H-NMR (CD<sub>3</sub>CN, 400 MHz): δ = 9.30 (s, 4H, N3'), 8.68 (d, J= 7.80 Hz, 4H, N3), 8.44 (d, J= 1.60 Hz, 4H, B2), 8.24 (t, J= 1.57 Hz, 2H, B4), 7.94 (td, J= 1.43, 7.88, 7.91 Hz, 4H, N4), 7.82 (dd, J= 1.13, 3.64 Hz, 4H, S3), 7.61 (dd, J= 1.10, 5.07 Hz, 4H, S5), 7.30 (dd, J= 3.66, 5.07 Hz, 4H, N5), 7.22 (d, J= 6.23 Hz, 4H, N6), 7.12 (m, 4H, S4);

ES-MS *m/z* (calc.): 501.8 ([M-2PF<sub>6</sub>]<sup>2+</sup>)

### 3.3 Electrochemical and Photo-Electrochemical Polymerisation

#### 3.3.1 Electrochemical Polymerisation

Electrochemical polymerisation is a very convenient route to produce polymeric thin films. The polymerisation can be anodic or cathodic depending on the polymerisable parts.<sup>[48]</sup> Polythiophenes and other derivatised thiophene systems have been extensively studied due to their interesting electrochemical and photophysical properties.<sup>[49, 50]</sup> They are also relatively robust and easy to work with. Figure 3.29 shows CVs of deposited PEDOT and polythiophene on Pt electrodes.

Poly(3,4-ethylenedioxythiophene), (PEDOT), is an especially interesting system for several reasons: due to its electron rich oxygen groups the oxidation potential of the monomer is low and the polymer is easily produced by anodic electrochemical oxidation. The resulting p-doped polymer is relatively highly conducting, typically ranging between  $10^0$ - $10^2$  S/cm for the electrochemically prepared films.<sup>[51]</sup> The ethylenedioxy groups on the  $\beta$ -position give it stability and minimise cross-linking. The spectroscopy of PEDOT differs from other polythiophenes in that its p-doped conducting state is almost completely transparent but the neutral state blue. Unsubstituted polythiophene is red when neutral and turns blue when p-doped.<sup>[52]</sup>

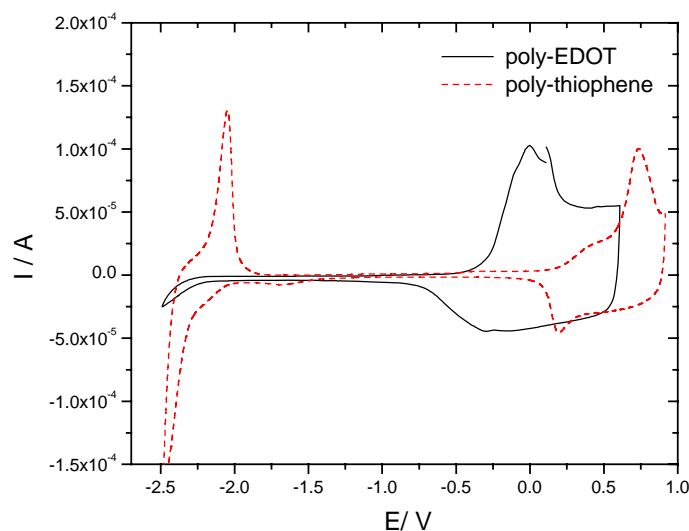


**Figure 3.29** Cyclic voltammograms of electrodeposited terthiophene (dashed line) and electrodeposited bis-EDOT (solid line) films on glassy-carbon electrode in MeCN (0.1 M TBAPF<sub>6</sub>). Fc/Fc<sup>+</sup> set as 0 V.

As discussed in chapter 1, conjugated electroactive polymer films have different absorbance depending on the doping. The band-gap determines the absorbance in neutral form but upon doping new electronic states in the band-gap are formed and will give rise to optical transitions at lower energies. One example is poly(3,4-ethylenedioxythiophene) (PEDOT). The oxidised form is almost transparent with a light blue hue (absorbance maximum at  $\sim 760$  nm) and the neutral form of the solid polymer is deep blue (absorbance maximum at 610 nm).<sup>[53]</sup> Applying a potential to the film changes the doping level and in this way the bandgap is affected. The relatively low bandgap is located near the visible and NIR and any change will affect the colour. In figure 3.30 an electrodeposited film of PEDOT on FTO glass is connected to a potentiostat and a potential is applied. The absorbance was monitored over time with different potentials being applied. The change of absorbance reflects the doping levels at various potentials. In figure 3.30 it can be seen that the doping is reversible.

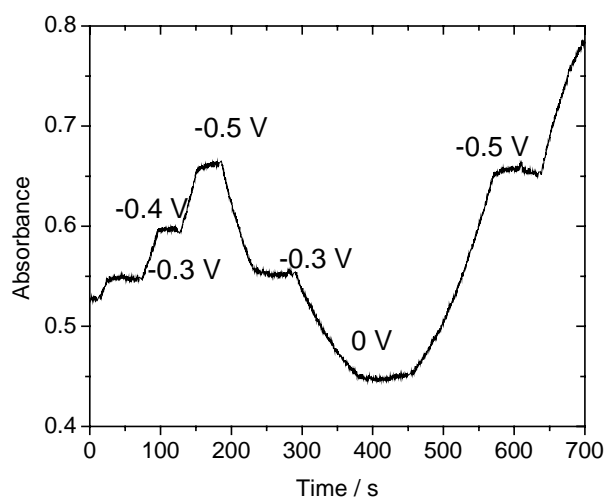


**Figure 3.30** Absorbance change at 600 nm of PEDOT film with different potentials applied.

Conducting polymers with in chain metal centers are of interest for the tuning possibilities of their photophysical and electrochemical properties through choice of their metal center and substituents.<sup>[54, 55]</sup> It has earlier been reported that  $[\text{Ru}(3)_2][\text{PF}_6]_2$  form polymers upon electrochemical oxidation.<sup>[13]</sup> The  $[\text{Ru}(2)_2][\text{PF}_6]_2$ ,  $[\text{Fe}(2)_2][\text{PF}_6]_2$  and  $[\text{Ru}(8)_2][\text{PF}_6]_2$  compounds showed electro-deposition when oxidized in  $\text{CH}_2\text{Cl}_2$  with  $\text{TBAPF}_6$ . In MeCN the two compounds with the EDOT groups show normal solution semi-infinite diffusion. Changing to a solvent with less base character, such as DCM, may lead to some polymerization as discussed in



chapter 2. The cation radicals that are electro-generated at the electrode are very susceptible to nucleophilic attack and thus the lifetime of the radical cation is prolonged in DCM.<sup>[26]</sup>

### Solution electrochemistry in MeCN

Before presenting the results of electrochemical polymerization of compounds  $[\text{Ru}(\mathbf{8})_2][\text{PF}_6]_2$  and  $[\text{Ru}(\mathbf{2})_2][\text{PF}_6]_2$  in DCM, it is interesting to look at the electrochemistry of these compounds in acetonitrile, where they did not deposit on the electrode, to get some indications of in what order the ligands are oxidised. In figure 3.31 the cyclic voltammetry of  $[\text{Ru}(\mathbf{8})_2][\text{PF}_6]_2$  and  $[(\text{tpy})\text{Ru}(\mathbf{8})][\text{PF}_6]_2$  in MeCN (0.1 M TBAPF<sub>6</sub>) are plotted. The amount of charge used for the ligand oxidations can be calculated from the integrals under the peaks and preferably from the square wave voltammetry (SWV) where the charging current has been subtracted.

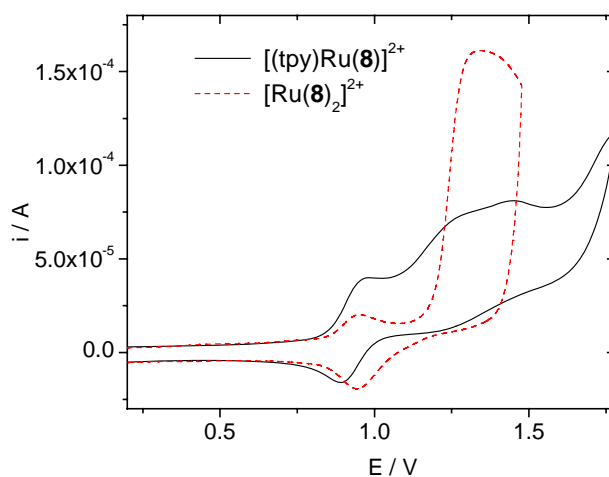


**Figure 3.31** CVs of  $[\text{Ru}(\mathbf{8})_2][\text{PF}_6]_2$  (solid line) and  $[(\text{tpy})\text{Ru}(\mathbf{8})][\text{PF}_6]_2$  (dashed line) in MeCN. (0.1 M TBAPF<sub>6</sub> as electrolyte and GC indicator electrode with Fc/Fc<sup>+</sup> set as 0 V).

From the SWV in figure 3.32 it appears that there are two oxidation processes after the ruthenium redox process. From estimating the charge (area) of the peaks from the SWV (figure 3.32), the oxidation peaks from  $[(\text{tpy})\text{Ru}(\mathbf{8})][\text{PF}_6]_2$  are equivalent to two subsequent one-electron processes, separated by about 200 mV. Doing the same analysis to the SWV of  $[\text{Ru}(\mathbf{8})_2][\text{PF}_6]_2$  gives us peaks at the same potentials but larger and corresponding to just over twice the charge. These results indicate that, on ligand **8** in these measurements, one thiophene is first oxidized and the second oxidation

occurs at a higher potential. For the homoleptic complex, one thienyl from each opposing ligand is oxidised at the same potential and possibly simultaneously.

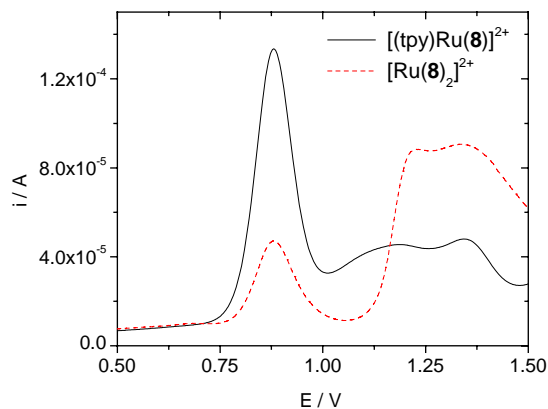


**Figure 3.32** SWVs of  $[\text{Ru}(\mathbf{8})_2][\text{PF}_6]_2$  (solid line) and  $[(\text{tpy})\text{Ru}(\mathbf{8})][\text{PF}_6]_2$  (dashed line) in MeCN. (0.1 M TBAPF<sub>6</sub> as electrolyte and GC indicator electrode with Fc/Fc<sup>+</sup> set as 0 V).

In figures 3.33 and 3.34 the square wave voltammograms of  $[\text{Ru}(\mathbf{2})_2][\text{PF}_6]_2$ ,  $[(\text{tpy})\text{Ru}(\mathbf{2})][\text{PF}_6]_2$  and  $[\text{Fe}(\mathbf{2})_2][\text{PF}_6]_2$  in MeCN are plotted and compared. The concentrations of the solutions are about 1mM.

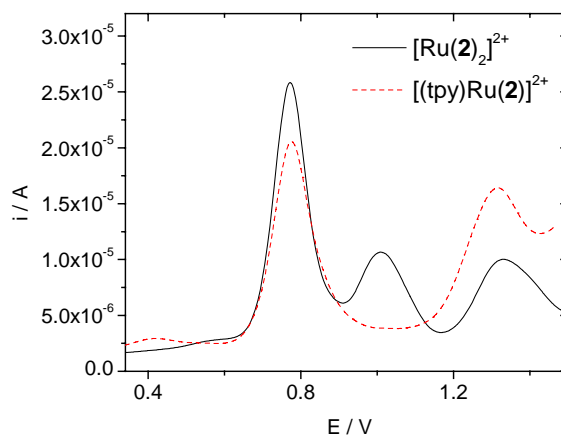


**Figure 3.33** SWVs of  $[\text{Ru}(\mathbf{2})_2][\text{PF}_6]_2$  (solid line) and  $[(\text{tpy})\text{Ru}(\mathbf{2})][\text{PF}_6]_2$  (dashed line) in MeCN. (0.1 M TBAPF<sub>6</sub> as electrolyte and GC indicator electrode with Fc/Fc<sup>+</sup> set as 0 V).

As is seen in figure 3.33 the oxidation peaks of the ligand with an EDOT group (**2**) come one after the other for the homoleptic ruthenium complex while the heteroleptic complex with one EDOT group has only one peak at the higher oxidation potential.

The iron complex has the first oxidation of the ligand at the same potential but with a bigger gap between the metal redox process and the ligand process (figure 3.34). Together, figures 3.33 and 3.34 suggest that in the homoleptic complex one EDOT is first oxidised and the second one is oxidised at  $\sim 200\text{mV}$  higher potential.

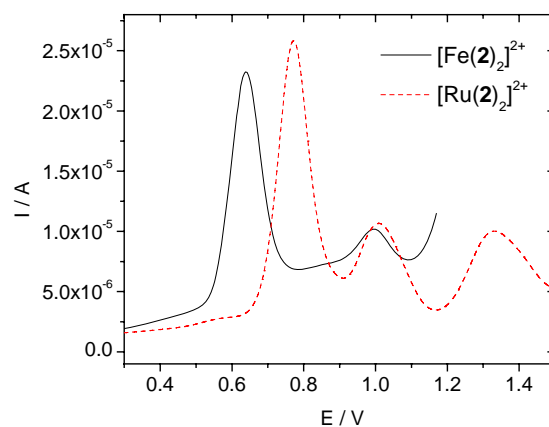
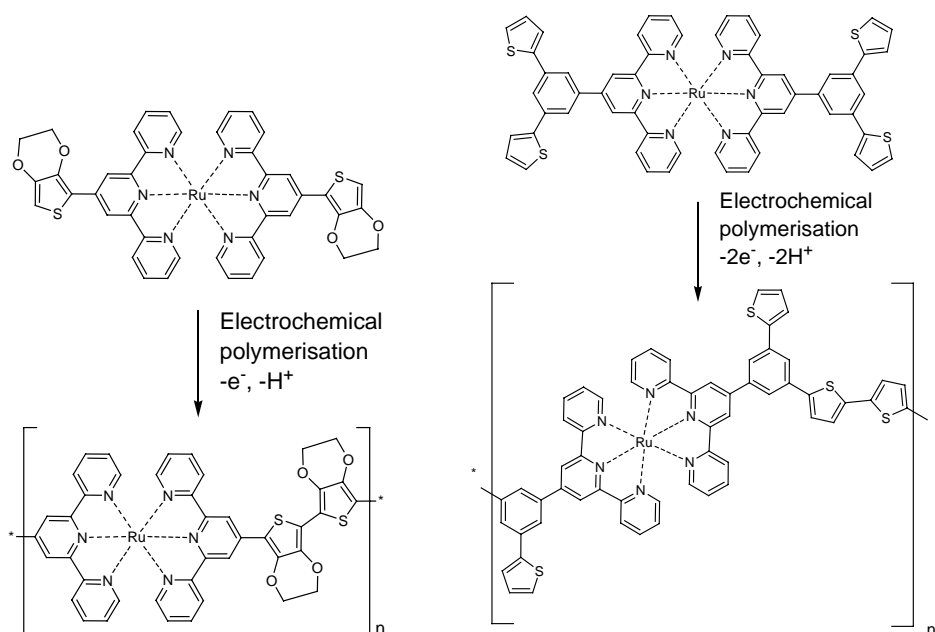


**Figure 3.34** SWVs of  $[\text{Fe}(\mathbf{2})_2][\text{PF}_6]_2$  (solid line) and  $[\text{Ru}(\mathbf{2})_2][\text{PF}_6]_2$  (dashed line) in MeCN. (0.1 M TBAPF<sub>6</sub> as electrolyte and GC indicator electrode with Fc/Fc<sup>+</sup> set as 0 V).

### Electrochemical polymerisation

Electrochemical oxidation in DCM (0.1 M TBAPF<sub>6</sub>) of the iron and ruthenium complexes with ligands **2** and **8** afforded smooth and coloured thin films on the electrode surface. The energy difference between the redox potential of the metal center and the coordinating ligands oxidation potential seems to have a large influence on the polymerization efficiency. The iron complex produced thinner films than the ruthenium complexes at the same oxidation potentials and same number of voltammetric cycles. AFM images of the films also show less polymer growth for the iron monomer. Scheme 3.6 depicts the possible electrochemical polymerization reactions of complexes with ligands **2** and **8**. Figure 3.35 shows an example of cyclic voltammetry of the monomer in DCM and the linearly growing peak current suggesting an accumulation of redox-active film on the electrode surface.

While depositing the iron complex polymer it was necessary to go to a potential beyond that of the iron II/III redox process to get an electrodeposition. For the ruthenium complex the polymerisation occurred at the onset of ruthenium (II) oxidation as there is some overlap of the ligand oxidation.



**Scheme 3.6** Depiction of electrochemical reaction with two different complexes being electrochemically oxidised.

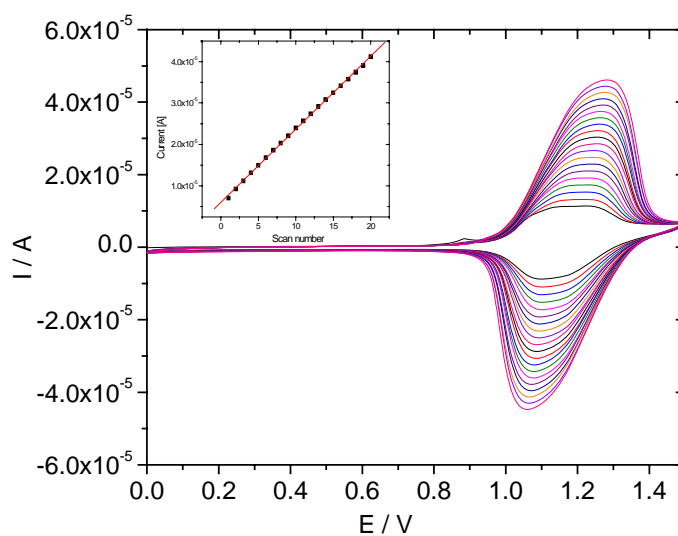


**Figure 3.35** Cyclic voltammetry of  $[\text{Ru}(\mathbf{2})_2]^{2+}$  in DCM during electrodeposition. Inset in left hand corner plots peak current with number of scans.

After deposition, CV recordings were done on the films in MeCN (0.1 M TBAPF<sub>6</sub>) without monomer in the solution to investigate how the redox properties are modified. Figure 3.36 is a CV of poly- $[\text{Ru}(\mathbf{2})_2][\text{PF}_6]_2$  deposited on a GC electrode and table 3.14 shows the redox potentials of the complexes in solution and as electrodeposited.

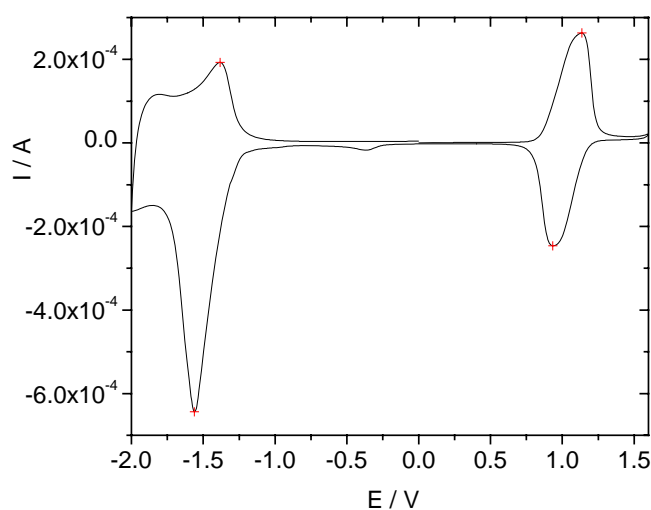


**Figure 3.36** CV of  $[\text{Ru}(\mathbf{2})_2][\text{PF}_6]_2$  film on glassy carbon electrode measured in MeCN (0.1 M TBAPF<sub>6</sub>) without the monomer.

**Table 3.14** Electrochemical redox potentials for complex in solution and as polymeric film. Potentials are quoted versus Fc/Fc<sup>+</sup>.

Complex	Ox. <sub>1</sub> in MeCN	Red. <sub>1</sub> in MeCN	Ox. <sub>1</sub> polymer	Red. <sub>1</sub> polymer
$[\text{Fe}(\mathbf{2})_2][\text{PF}_6]_2$	+ 0.64	- 1.74	+ 0.75	- 1.25
$[\text{Ru}(\mathbf{2})_2][\text{PF}_6]_2$	+ 0.98	- 1.65	+ 1.05	- 1.57
$[\text{Ru}(\mathbf{8})_2][\text{PF}_6]_2$	+ 0.88	- 1.57	+ 0.97	- 1.72*
$[\text{Fe}(\mathbf{8})_2][\text{PF}_6]_2$	+ 0.68	- 1.36	+ 0.74	- 1.50

\* The reduction was very sensitive and afterwards the polymer film gives no response and seems to degrade.

At lower scan rates (<50 mV/s) the peak potential differences of the anodic and cathodic waves ( $\Delta E_p$ ) were between 10 and 30 mV and the peak shapes were symmetrical rather than having the diffusion shaped curves of dissolved species. For one-electron processes, this is indicative of surface bound species although ideally for molecules on a surface without lateral interactions between the redox centers, and where a rapid equilibrium is established with the electrode, the peak separation ( $\Delta E_p$ ) is 0 V.<sup>[46]</sup> The peaks are also broader than expected for a Nernstian system; the full width at half maximum (*fwhm*) being 100-110 mV compared to the ideal value 90.6 mV. These observations indicate weak destabilizing interactions between the adsorbed molecules. For scan rates beyond 50 mV/s the  $\Delta E_p$  increases to 70 mV and

even higher at 200 mV/s. When the scan rate is high, the depletion layer thickness will be less than the film thickness and the cyclic voltammetry response will behave more like it does for molecules in solution with semi-infinite linear diffusion. The Randles-Sevcik equation from chapter 2 (equation 21) should give a straight line for a plot of  $I_p$  against  $v^{1/2}$  when the redox couple is under semi-infinite diffusion conditions. It also permits the product  $D_{CT}^{1/2}C$  to be determined from the slope of a plot and when the concentration is known the diffusion constant can be calculated. For a nernstian adsorbate layer, equation 5 from chapter 2 is analogous. Plotting  $i_p$  against  $v$  should give a straight line that is in accordance to equation (22) (chapter 2).

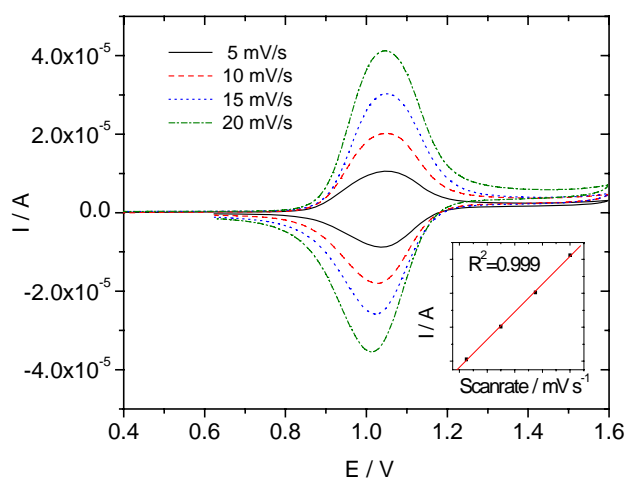


**Figure 3.37** Cyclic voltammetry at different scan rates up to 20 mV/s for poly[Ru(2)<sub>2</sub>]<sup>2+</sup> on GC electrode in MeCN. (vs Ag/AgNO<sub>3</sub>).

In figures 3.37 and 3.38 CV curves of the electrochemically polymerised [Ru(2)<sub>2</sub>]<sup>2+</sup> on glassy carbon electrodes are plotted. In figure 3.37 the shapes from measurements of the polymer films at scan-rates below 20 mVs<sup>-1</sup> appear as surface adsorbate response with a ΔE<sub>p</sub> close to 0 V, symmetrical shape and as seen from the inset a linear relation between peak current and the scan rate. At scan rates above 50 mVs<sup>-1</sup> the CV curves are similar to those expected for electrochemically reversible couple in solution with a ΔE<sub>p</sub> > 59 mV and a linear relation between the peak current and the square root of the scan rate as shown in figure 3.38.

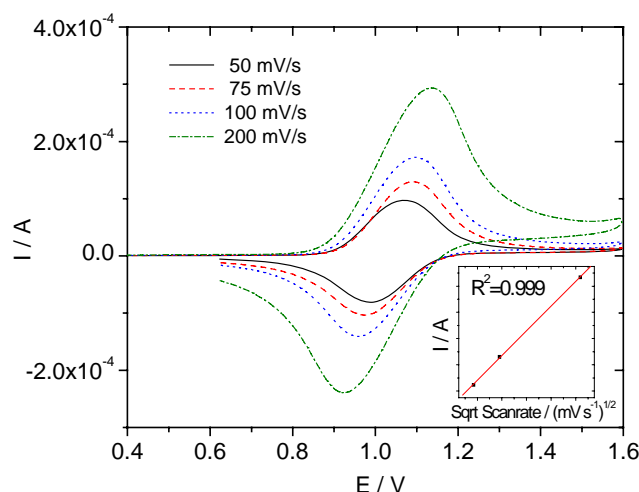


**Figure 3.38** Cyclic voltammetry at different scan rates from 50 to 200 mV/s for poly[Ru(2)<sub>2</sub>]<sup>2+</sup> on GC electrode in MeCN. (vs Ag/AgNO<sub>3</sub>).

In the faster scans ( $>50 \text{ mVs}^{-1}$ ) the entire polymer film does not have time to oxidise or reduce during a sweep so the effective current density depends on how fast charge can diffuse in the polymer. The slower scans allow for complete oxidation or reduction of the polymer film and thus lead to surface adsorbate behaviour. The integral (charge) of the anodic or cathodic CV at scan rates slow enough for complete oxidation or reduction gives the surface coverage and by estimating the concentration, the thickness of the film can be approximated. The charge under the poly-[Ru(2)<sub>2</sub>] peak is  $2.55 \times 10^{-4} \text{ C}$ , which means  $\Gamma_{\text{Ru}2} = 37 \text{ nmole/cm}^2$ . The poly-[Fe(2)<sub>2</sub>] peak integral is  $1.19 \times 10^{-4} \text{ C}$  with  $\Gamma_{\text{Fe}2} = 17 \text{ nmole/cm}^2$ . These values are from the films deposited by cycling the potential between +0.4 and +1.1 V for 12 scans. It appears the efficiency of the polymerisation for the ruthenium complex is twice that of the iron complex. If one molecule takes up the space of a circle with the radius of the molecule ( $\sim 17 \text{ \AA}$  from the [Fe(2)<sub>2</sub>]<sup>2+</sup> crystal structure in section 3.2.5), one layer is estimated to  $\sim 1.3 \times 10^{-12} \text{ mole}$ . This makes the iron complex polymer  $\sim 13\,000$  layers and the ruthenium complex polymer  $\sim 29\,000$  layers thick.

### Charge transport

As previously mentioned, the Randles-Sevcik equation permits the product  $D_{CT}^{1/2}C$  to be determined from the slope of a plot of  $i_p$  vs  $v^{1/2}$  for the faster scans where there is semi-infinite linear diffusion:

$$i_p = (2.69 \times 10^5) n^{3/2} A D_{CT}^{1/2} C v^{1/2} \quad (4)$$

Two other techniques that can be used to evaluate the diffusion constants for the transport of redox-mediated charge are chronoamperometry and chronocoulometry. In table 3.15 the values obtained for  $D_{CT}^{1/2}C$  with the different techniques for the polymers with iron and ruthenium metal center are listed. The ruthenium polymer has values 2-3 times greater than the iron complex suggesting better charge transport.

**Table 3.15**  $D_{CT}^{1/2}C$  values as measured by three different techniques.

Technique	Poly-[Fe(2)]	Poly-[Ru(2)]
	$D_{CT}^{1/2}C / \text{mol cm}^2 \text{s}^{1/2}$	$D_{CT}^{1/2}C / \text{mol cm}^2 \text{s}^{1/2}$
Cyclic-voltammetry	$(2.4 \pm 0.5) \times 10^{-8}$	$(4.8 \pm 0.5) \times 10^{-8}$
Chronoamperometry	$(1.5 \pm 0.5) \times 10^{-8}$	$(4.2 \pm 0.5) \times 10^{-8}$
Chronocoulometry	$(2.0 \pm 0.5) \times 10^{-9}$	$(9.8 \pm 0.5) \times 10^{-9}$

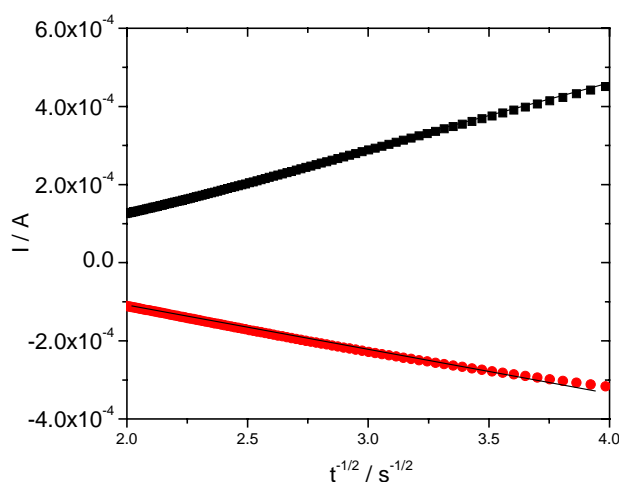


**Figure 3.39** Cottrell plots of the anodic current (squares) and the cathodic current (circles) from chronoamperometric experiments on the poly-[Ru(2)<sub>2</sub>] coated GC electrode.

In figure 3.39 the Cottrell plots of the poly-[Ru(2)<sub>2</sub>] deposit on the GC electrode are measured for the oxidation and reduction of the metal redox process. The potential was stepped to a potential 300 mV more positive or negative than  $E_{Ru}^{0, 2+/3+}$  to ensure



that the heterogeneous electron transfer is fast enough that the current response is controlled by the rate of homogeneous charge transport within the polymer film. The linear response for both the anodic and cathodic currents in figure 3.39, indicate that the transport is consistent with semi-infinite linear diffusion control over this time scale (60-250 ms).<sup>[56]</sup> The values from table 3.15 indicate a faster transport of charge in the polymer with the ruthenium complex than that with the iron metal centers. Having the redox potential close to the energy level of the bridging ligands should enhance the conductivity, even though the conductivity has more ionic character than electronic. This also manifests itself during the electrochemical polymerisation where the ruthenium complex has a much faster growth due to better transport of electrons through the deposit. To avoid time and ohmic affects these measurements could be made with microelectrodes for more precise measurements.<sup>[46]</sup>

### Optical properties

UV-Vis absorbance of the electrodeposited complexes on TCO glass (SnO:F) have a green colour coming from absorption bands at 502 and 620 nm for the ruthenium based complex and blue colour from absorption bands at 586 and 718 nm for the iron based polymer. The UV-Vis absorbance spectra can give information on the conjugation effects. Longer conjugation length of the ligands should shift the <sup>1</sup>MLCT absorbance maximum to the red. Comparing the solution <sup>1</sup>MLCT absorbance with that of the electrodeposited complex on the TCO glass shows the <sup>1</sup>MLCT band slightly red shifted for the iron complex as polymer, but surprisingly the ruthenium complex polymer shows a blue shift. The blue shift could be due to over-oxidation that interrupts conjugation. There is also a new band at higher wavelength in both cases. This is probably the ligand to metal charge transfer (LMCT) due to some ruthenium ions being in the +III oxidation state.<sup>[57]</sup> The LMCT appears to be relatively stable over time.

Immersing the polymer films into an electrolyte with  $\Gamma/\text{I}_3^-$  changes their colour to red. The UV-Vis absorbance of the films reveal that the LMCT bands have vanished and that the MLCT bands have been red shifted. The  $\Gamma/\text{I}_3^-$  redox electrolyte appears to reduce the  $\text{Ru}^{+\text{III}}$  centers of the polymer film. The oxidation potentials of the  $\text{Ru}^{+\text{II}}$  metal centers suggest that, when oxidised to  $\text{Ru}^{+\text{III}}$ , they are likely to oxidise the  $\Gamma/\text{I}_3^-$  redox couple. Table 3.16 has all the wavelengths of the UV-Vis absorbance

measurements before and after polymerisation and after immersion in the electrolyte with the  $\Gamma/\text{I}_3^-$  redox couple.

**Table 3.16** UV-vis spectra of the complexes in solution and of the oxidised forms of the polymers with  $[\text{Ru}(\mathbf{2})_2]^{2+}$  and  $[\text{Fe}(\mathbf{2})_2]^{2+}$ . The films were later immersed in solutions of 3-MPN with  $\text{I}_2 / \Gamma^-$  and measured on.

Complex	$\lambda_{\text{max}}$ solution	$\lambda_{\text{max}}$ Ox. polymer	$\lambda_{\text{max}}$ $\text{I}_2 / \Gamma^-$
$[\text{Fe}(\mathbf{2})_2]^{2+}$	581 nm	586 nm, 718 nm	590 nm
$[\text{Fe}(\mathbf{3})_2]^{2+}$	589 nm	596 nm	600 nm
$[\text{Ru}(\mathbf{2})_2]^{2+}$	506 nm	502 nm, 620 nm	512 nm
$[\text{Ru}(\mathbf{8})_2]^{2+}$	490 nm	493 nm, (665 nm)	499 nm

\*The polymer films deposited on  $\text{TiO}_2$  are investigated as dyes in chapter 3.5.

### Surface topography

The deposited films of poly- $[\text{Ru}(\mathbf{2})_2]^{2+}$  and poly- $[\text{Fe}(\mathbf{2})_2]^{2+}$  on FTO glass were measured by AFM (Atomic Force Microscopy) to evaluate the topography. In figures 3.40 and 3.41,  $5 \times 5 \mu\text{m}$  scans of the surface are shown of poly- $[\text{Ru}(\mathbf{2})_2]^{2+}$  after 4 and 20 cycles of cyclic voltammetric deposition respectively. From the images it appears that the polymer grows in globular shapes at nucleation sites that grow in size after more cycles of voltammetric deposition. The depth of the pores is about 300 nm for the sample of 4 scans while for the 20 scans the depth is almost 600nm. The images of poly- $[\text{Fe}(\mathbf{2})_2]^{2+}$  are similar but with visibly less growth than the ruthenium complex for the same amount of scans. The surface of the FTO substrate, which was used when doing the AFM images, is different from the glassy carbon electrode and may influence the topography of the electrodeposited polymer. A control image of the FTO glass surface was taken as a reference.

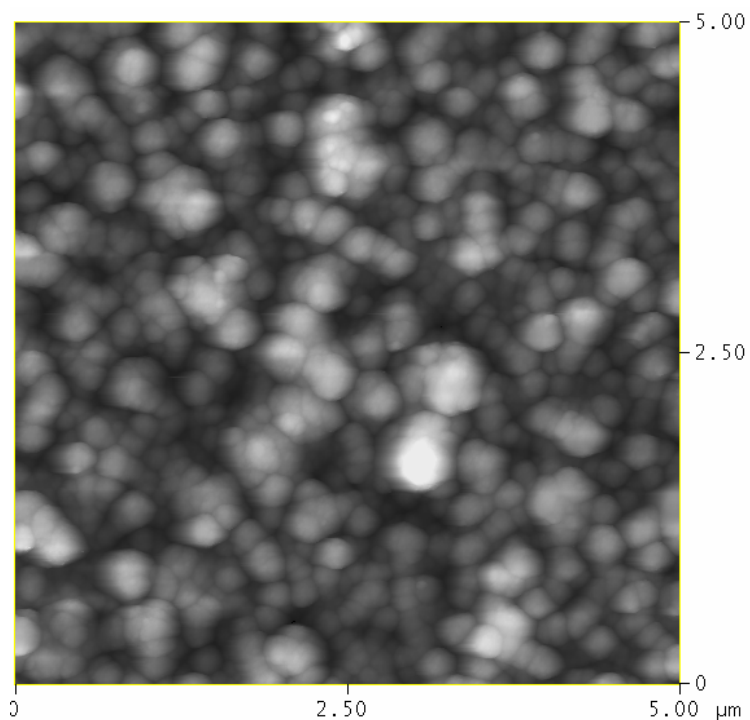


**Figure 3.40** 5x5 μm AFM image of deposited  $[\text{Ru}(\text{2})_2]^{2+}$  on FTO glass after four scans.

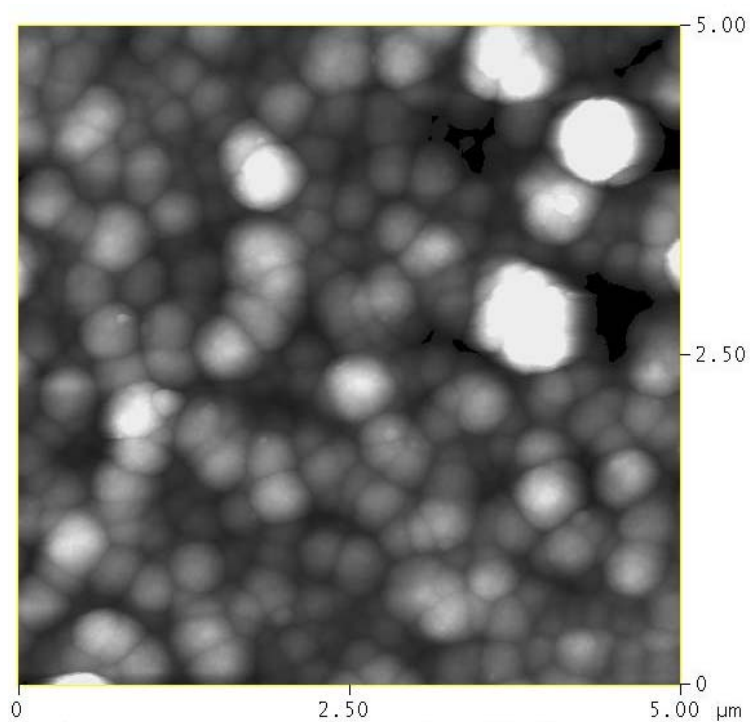
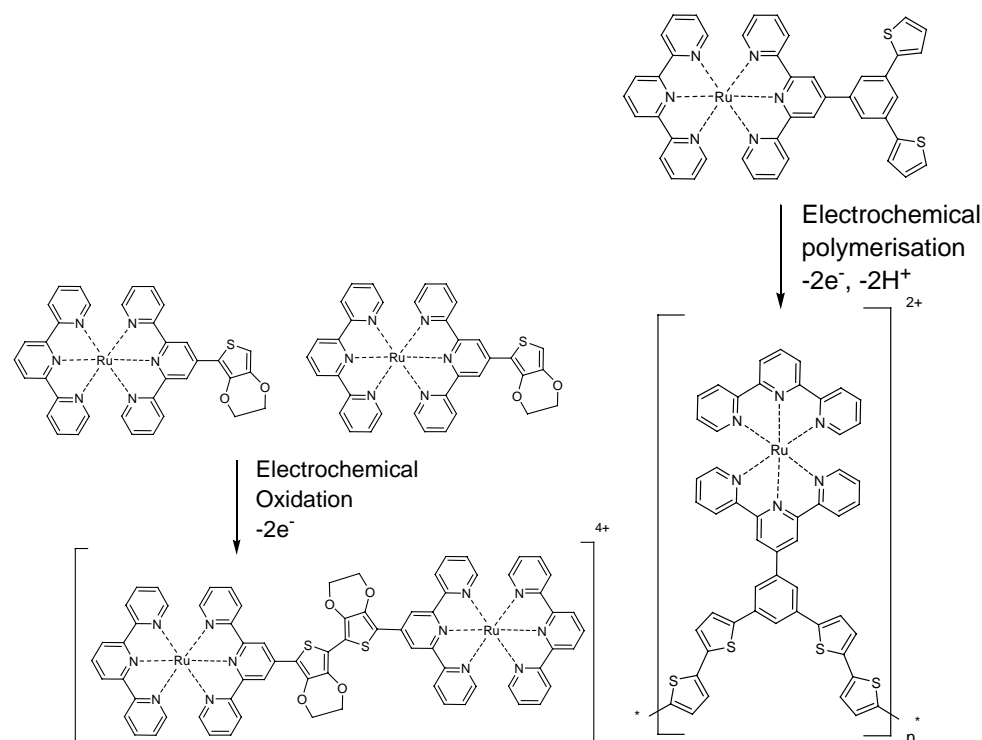


**Figure 3.41** 5x5 μm AFM image of deposited  $[\text{Ru}(\text{2})_2]^{2+}$  on FTO glass after twenty scans.

### Heteroleptic analogues

Electrochemical polymerisation experiments were also performed on the heteroleptic ruthenium complexes of ligands **2** and **8** where the counter ligand is unsubstituted 2,2';6'-terpyridine. Scheme 3.7 projects a possible outcome of the experiments.  $[(\text{tpy})\text{Ru}(\mathbf{2})][\text{PF}_6]_2$  is not expected to form a polymer but  $[(\text{tpy})\text{Ru}(\mathbf{8})][\text{PF}_6]_2$  may form polymer chains. The experimental details were identical to those used for the homoleptic complexes.



**Scheme 3.7** Possible reactions of the electrochemical oxidation of the heteroleptic complexes  $[(\text{tpy})\text{Ru}(\mathbf{2})][\text{PF}_6]_2$  (left) and  $[(\text{tpy})\text{Ru}(\mathbf{8})][\text{PF}_6]_2$  (right).

For both cases there was evidence of some deposition but not for many cycles. No stable polymeric films were obtained and further information on products would require deeper investigation.

### SECM approach curves

One characteristic of the polymer films that may be of interest is the lateral conductivity of holes or electrons across the films. To measure this, SECM approach curve experiments were performed, which were discussed in section 2.2. The technique has been used to measure lateral charge transport in homogenous ultrathin films of, for example, polyaniline layers.<sup>[58]</sup> The electrodeposited films of the redox

polymers had relatively rough topography (see figure 3.41), which is not ideal for the measurements. To start with, bi-thiophene was electrochemically deposited on FTO glass by cyclic voltammetry. The oxidatively doped state is relatively stable and can be attained by applying a positive potential to the FTO glass substrate. Several measurements were done to get reliable data. Ferrocene (0.1 mM) in 3-MPN was used as the redox mediator in the electrolyte. The curves chosen for figure 3.42 give the trend that most of the results support. The increased feedback when the film is doped suggests that the p-doped state has an improved ability to transport electrons laterally than the neutral state.

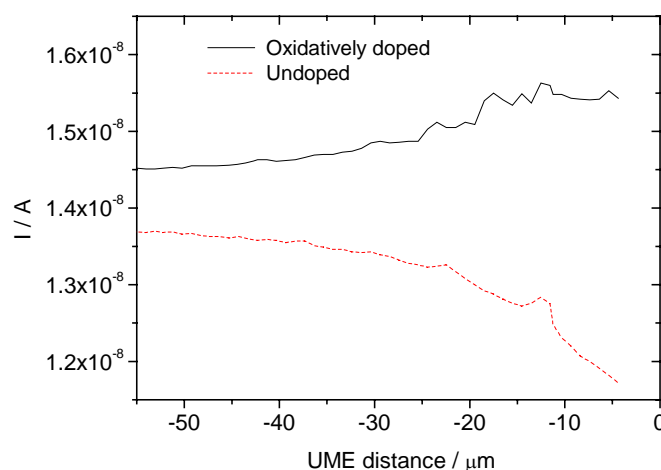


**Figure 3.42** Approach curves towards undoped and anodically doped polythiophene. The microelectrode tip diameter is 10  $\mu\text{m}$ .

To measure the charge transport qualities of the redox polymer films with ruthenium and iron centers, the ferrocene needed to be exchanged for another redox mediator because the metal redox centers of the polymer, where the presumed charge conduction primarily takes place, have oxidation potentials that are too high for the ferrocene to be reduced. The polymer complex with the iron complex should, however, be able to reduce oxidised  $[\text{Ru}(\text{bipy})_3][\text{PF}_6]_2$  as can be seen in the energy scheme of figure 3.43.

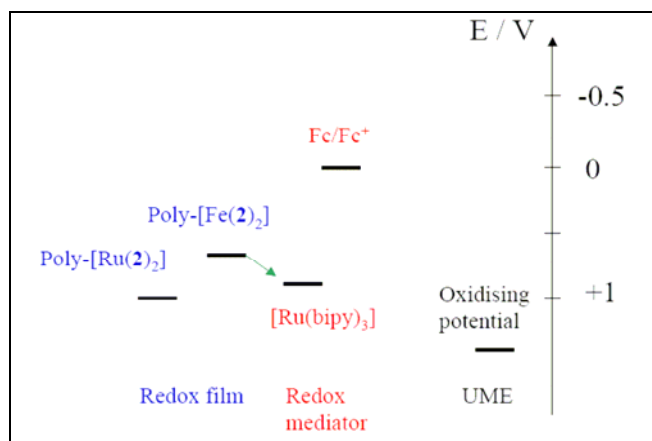


**Figure 3.43** Redox potentials of the different components in the approach curve experiment. The potential scale is with  $\text{Fc}/\text{Fc}^+$  set as 0 V. The arrow points out a possible reduction of the oxidised  $[\text{Ru}(\text{bipy})_3]^{3+}$  by the poly- $[\text{Fe}(\mathbf{2})_2]$  film.

In figure 3.44, two typical approach curves from the SECM experiments with the deposited films are plotted. The poly- $[\text{Ru}(\mathbf{2})_2]^{2+}$  film seems to be blocking the FTO surface from conducting when the redox mediator is ferrocene (inset in figure 3.44) or  $[\text{Ru}(\text{bipy})_3]^{2+}$ . The poly- $[\text{Fe}(\mathbf{2})_2]^{2+}$  film however, appears to generate a feed back current when the UME approaches the surface but only when the redox mediator consists of  $[\text{Ru}(\text{bipy})_3]^{2+}$ . This suggests that the polymer film is reducing the oxidised  $[\text{Ru}(\text{bipy})_3]^{3+}$  and that the surface is transporting charge to compensate the charge transfer. Despite the general trend indicating lateral conduction, the data was not reproducible enough to determine a value for the conductivity.

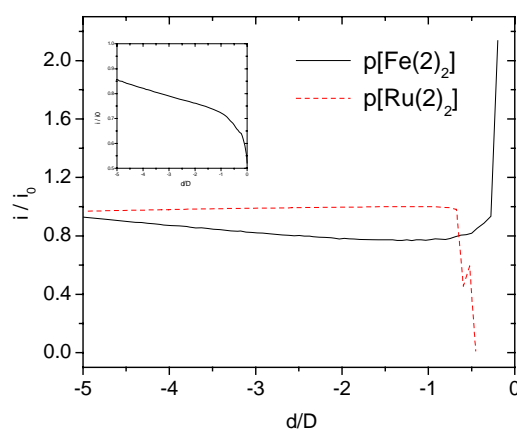


**Figure 3.44** Approach curves towards electrochemically deposited films of  $[\text{Ru}(\mathbf{2})_2][\text{PF}_6]_2$  (dotted line) and  $[\text{Fe}(\mathbf{2})_2][\text{PF}_6]_2$  (solid line) with  $[\text{Ru}(\text{bipy})_3][\text{PF}_6]_2$  as redox mediator. The microelectrode tip diameter is 10  $\mu\text{m}$ . The inset is an approach curve towards the  $[\text{Fe}(\mathbf{2})_2][\text{PF}_6]_2$  film with ferrocene as redox mediator.

### 3.3.2 Photo-Electrochemical Polymerisation

As was discussed in chapter 1 the dye-sensitised solar cell (DNOSC) would for several reasons improve by having a solid-state hole-conductor in place of the liquid electrolyte.<sup>[59]</sup> The main reason is avoiding volatile electrolyte leaking. Many groups have previously reported different materials and methods of applying them. Conducting polymers are good candidates due to their flexibility.<sup>[60]</sup> In this chapter we report on some ruthenium bis-terpyridine complexes that have been tested as dyes for DNOSC and their ability to *in-situ* polymerise hole-conducting polymers. The method used for applying the polymer was *in-situ* photo-electrochemical polymerisation (PEP) where the surface attached dye is used as a photo-oxidant to polymerise monomers in solution.<sup>[59]</sup> It was hoped that this method would lead to good electronic coupling between the dye and the polymer material and that the polymerisation is localised close to the dye molecules instead of directly on the TiO<sub>2</sub> surface or the FTO substrate.

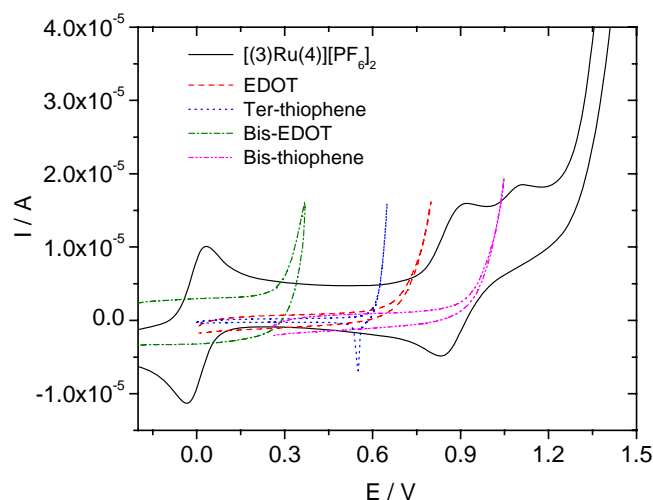


**Figure 3.45** CV of [(3)Ru(4)][PF<sub>6</sub>]<sub>2</sub> in solution with the ferrocene included. Oxidation onsets of monomers are overlapped as comparison.

For the ruthenium complex to be able to oxidise the monomer in solution, the oxidation potential should be higher than that of the monomer. In figure 3.45 a CV of [(3)Ru(4)][PF<sub>6</sub>]<sub>2</sub> is shown together with the CVs of some thiophene monomers. From the spectrum it is likely that bis-thiophene is not a good candidate but terthiophene, bis-EDOT and EDOT should have sufficiently low oxidation potentials. The

suitability of the monomers for being used in PEP was tested in experiments and all of them apart from bis-thiophene showed signs of being oxidised by the ruthenium complexes.

The different dyes used for the photo-oxidation had different groups on the 4'-position of the 2,2':6',2''-terpyridine counter ligand. The three main types of modification on the R position in figure 3.46 (ID numbers for dye molecules in scheme 3.10, page 207):

- Different thiophene groups with different oxidation potentials.
- No 4'-substituent.
- A 'quenching' unit that itself cannot oxidise the monomers in oxidised form (ferrocenyl).

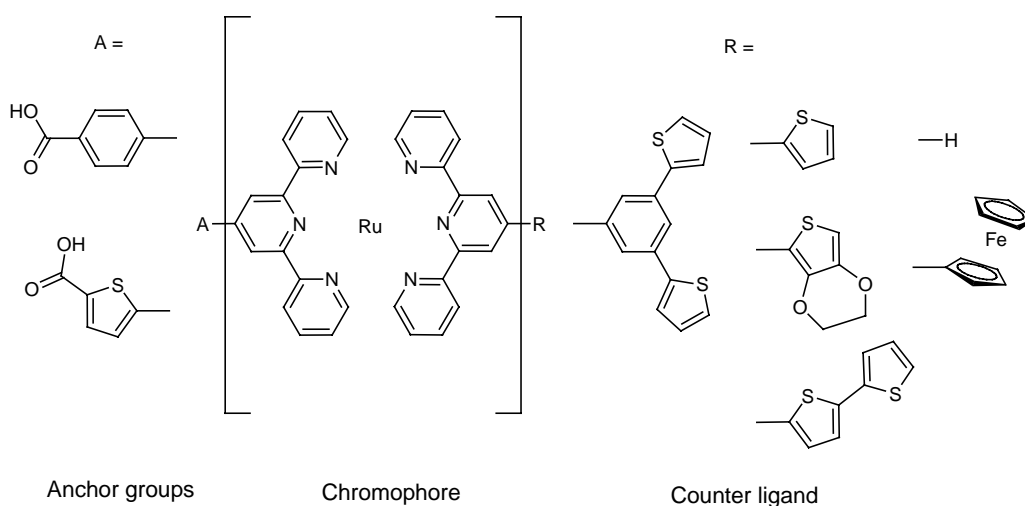


**Figure 3.46** The different complexes used in photo-electrochemical oxidation experiments. There are two different anchoring groups and six different counter ligands. The number tags for the compounds can be found in scheme 3.10 on page 207.

To probe the photo-electrochemical-oxidation as it happens different techniques were used. The main techniques:

- Chronoamperometry and chronocoulometry
- Transient UV-vis spectroscopy
- SECM probing

### No monomer in solution

The ligands with the thienyl groups are more sensitive to oxidation and subsequent reactions. This may lead to a higher probability of coupling with the cation radical monomers in the PEP process. TiO<sub>2</sub> films sensitised with the complexes that had 3



and **2** as counter ligands could not be used in a solar cell after cyclic voltammetry or PEP had been performed on them (without monomer in the electrolyte) (table 3.17). The complexes without thienyl groups on the counter ligand could however later be used in DNSC. This indicates that the thienyl groups may be undergoing reactions on the surface when oxidised by electrochemical or photoelectrochemical means.

### EDOT and bis-EDOT as monomer

In one experiment, complexes with three different thiophene groups on the counter ligand and one with a ferrocenyl group were compared to simple terpyridine. All the complexes apart from the ferrocene-modified terpyridine showed a change in current and in the UV-vis absorbance spectrum when illuminated with an applied potential (0 V, vs Ag/AgNO<sub>3</sub>) in the presence of bis-EDOT. A reason for this may be that the ferrocenyl group is oxidised by the Ru<sup>+III</sup> that results from the electron injection. In this case it would not be able to oxidise the bis-EDOT. Using [(**9**)Ru(**4**)]<sup>2+</sup> in a DNSC indicates that there is electron injection upon illumination but in the PEP the monomers are not able to reduce the oxidised ferrocenyl. In figure 3.47, the transient charge density from the PEP, indicates that the modified 2,2';6',2''-terpyridines respond to illumination with increased anodic current while the ferrocenyl modified 2,2';6',2''-terpyridine shows no response. The current ( $\Delta C/\Delta t$ ) appears to be the same for the three dyes and are assumed to be oxidising monomers. At a point the currents decrease to that before illumination or even lower. This could be the point where the polymer is blocking further reaction and the process is saturated.

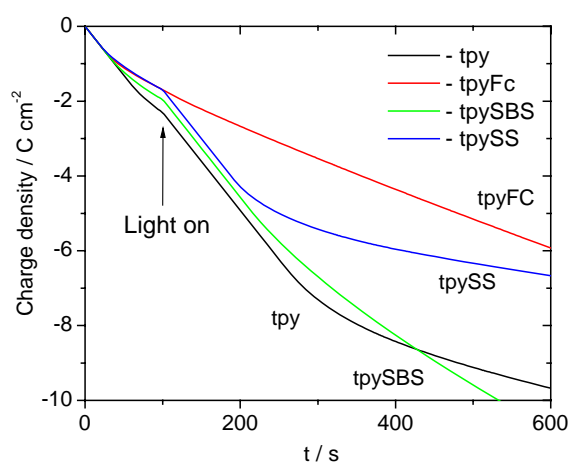


**Figure 3.47** Chronocoulometry of photo-electrochemical oxidation with the different colour codes for the lines in the inset.

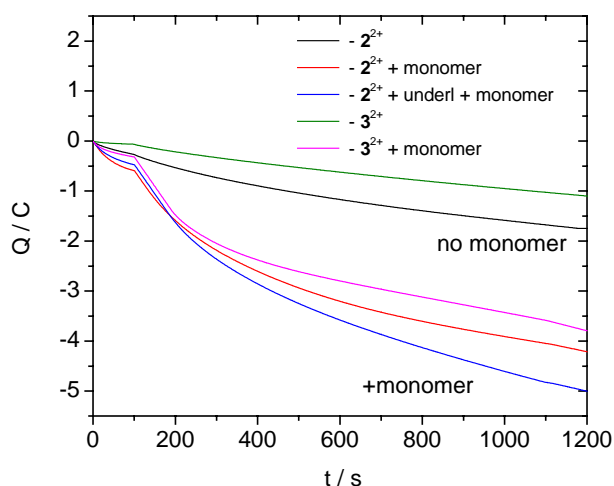


**Figure 3.48** Chronocoulometry experiment that is measured with monomer in the solution (pink, red and blue lines) and without (green and black lines).

Figure 3.48 shows the charge from photo-oxidation for the process with and without monomers in solution and with and without the compact  $\text{TiO}_2$ -underlayer. The samples without monomer in solution to oxidise showed no change in their colour while the samples with monomers in solution did. This change is shown in UV-vis spectra below in figures 3.49-51. Table 3.17 has a summary of some films that underwent PEP with or without monomers and their photovoltaic performances in DNSC after PEP. From the amount of charge used for the oxidation of monomer it appears that between 500-1000 monomers per dye molecule were oxidised.

**Table 3.17** Summary of one of the PEP experiments with and without monomers in solution after 20 minutes photo-oxidation. The monomer was bis-EDOT. The photovoltaic data after the treatment is presented in the two columns with  $V_{oc}$  and  $J_{sc}$ . The cells were made as described in chapter 2.

Dye	Charge ( $\text{C cm}^{-2}$ )	Mole $\text{e}^-/\text{cm}^2$	$V_{oc}$ (V)	$J_{sc}$ ( $\text{A cm}^{-2}$ )	Coverage ( $\text{nmol cm}^{-2}$ )
$2^{2+}$	9.3 (5.4*)	56 $\mu\text{mol}$	0.020	$4.0 \times 10^{-5}$	73
$2^{2+}$ with u	11.1 (7.2*)	75 $\mu\text{mol}$	0.004	$3.0 \times 10^{-5}$	73
$3^{2+}$	8.4 (6.0*)	62 $\mu\text{mol}$	0.001	0	63
<b>No monomer</b>					
$2^{2+}$	3.9	40 $\mu\text{mol}$	0.510	$7.8 \times 10^{-5}$	73
$3^{2+}$	2.4	25 $\mu\text{mol}$	0.450	$8.4 \times 10^{-5}$	63
$10^{2+}$	1.7	18 $\mu\text{mol}$	0.580	$1.2 \times 10^{-3}$	38

\*When the charge from the monomer free photo-oxidation is subtracted.

The photovoltaic performances of the complexes (table 3.17) after the PEP process, with or without monomer, are all reduced compared to the untreated complexes on TiO<sub>2</sub>. The exception was the dye without a substituent on the counter ligand (**10**<sup>2+</sup>). This suggests that the sensitive counter ligands **2** and **3** may react irreversibly upon photo-oxidation and possibly lead to coupling between complexes on the surface.

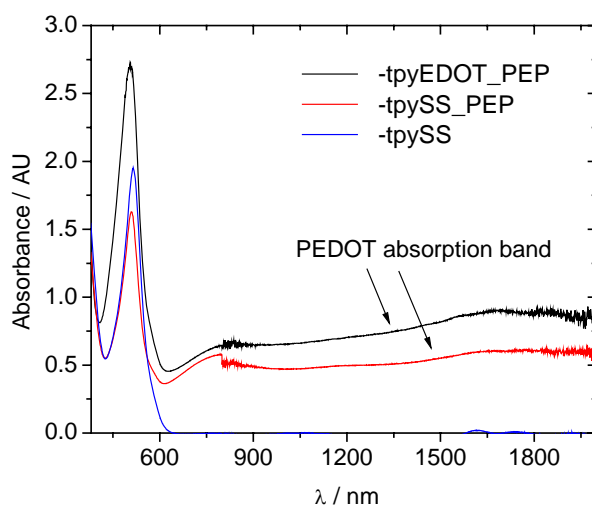


**Figure 3.49** Corresponding UV-vis changes for the films photo-oxidised with monomers and without monomers in the electrolyte. PEP=Photoelectrochemical polymerisation with monomers.

The changes in the UV-vis spectra of the film after the photo-oxidation were recorded. For the EDOT and bis-EDOT monomers the PEP led to a broad band starting from around 700-750 nm as seen in figures 3.49-3.51. This is indicative of p-doped PEDOT that has absorption bands from about 740 nm and into the infrared.<sup>[61]</sup>

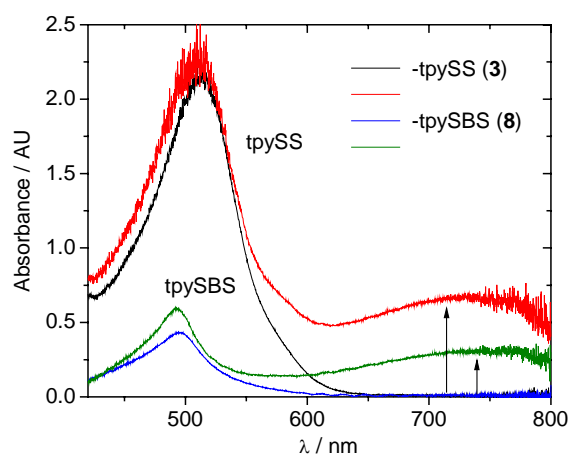


**Figure 3.50** UV-vis changes to complexes with **3** and **8** counter ligands after 20 minutes illumination.

The complexes with ligand **8** (tpySBS) has a smaller coverage as can be seen in figure 3.50, but has a slightly larger photo-oxidation current and the absorbance band at 750 nm has grown more in proportion to the  $^1\text{MLCT}$  band than the others. This might be due to its two thienyl groups on the terpyridine instead of one and they may act as nucleation centers.

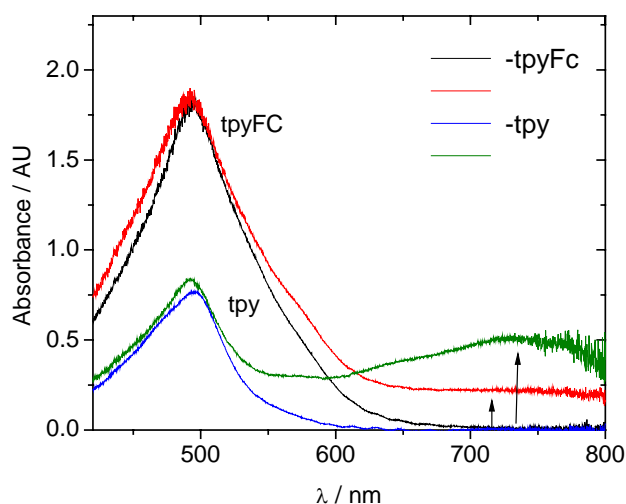


**Figure 3.51** UV-vis changes of surface bound complex with **9** (tpyFc) and tpy after PEP for 20 minutes.

After 20 minutes PEP, the film sensitised with  $\mathbf{12}^{2+}$  (**9** as counter ligand) has not resulted in new bands arising, confirming the control experiment with the ferrocenyl. In all the PEP experiments there is no redshift of the  $^1\text{MLCT}$  bands, which is contradictory to longer thiophene chains covalently coupled to the terpyridine. Attempts to desorb the product in basic water or ethanol and analyse the product with ESI-MS only showed the complex while the polymer appears difficult to desorb. This result suggests that the dye molecules do not couple directly with the longer thienyl oligomers.

### **Terthiophene as monomer**

The samples that are exposed to PEP in a solution of terthiophene display a colour change from red to a darker red that corresponds to a growing band at around 440 nm (As seen in figure 3.52). This is an observation of possible polymerisation and would be consistent with longer thienyl oligomers.

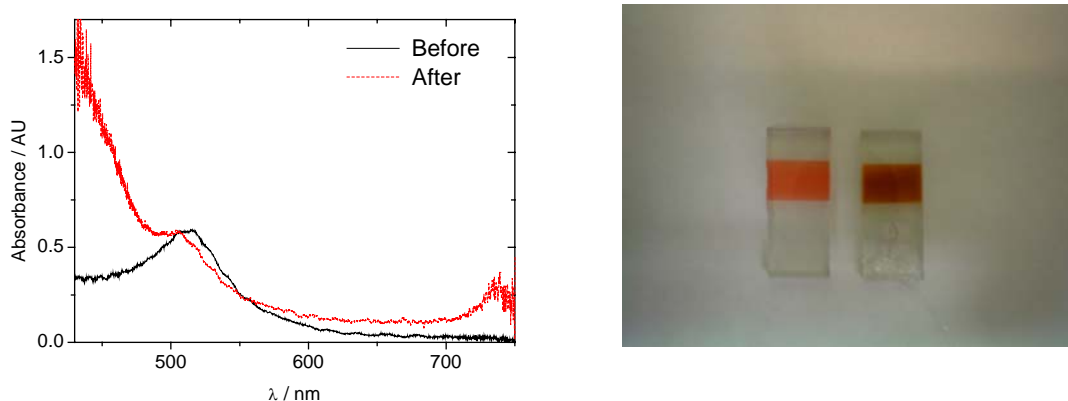


**Figure 3.52** The UV-Vis absorbance spectrum of the TiO<sub>2</sub> film before and after PEP (left). How the change of colour looks (right).

Bi-thiophene has an absorbance maximum at 350 nm, terthiophene at 390 nm and as the chains grow the absorbance maximum moves towards longer wavelengths with longer conjugation length. It has been reported that ter-thiophene, when electrochemically oxidised, only couples to create the dimer, hexa-thiophene, and possibly the dimer of the hexamer.<sup>[62, 63]</sup> This suggests that poly-terthiophene will not form very long chains. The PEP process was probed by transient UV-Vis by measuring the absorbance at 440 nm with time (figure 3.54).

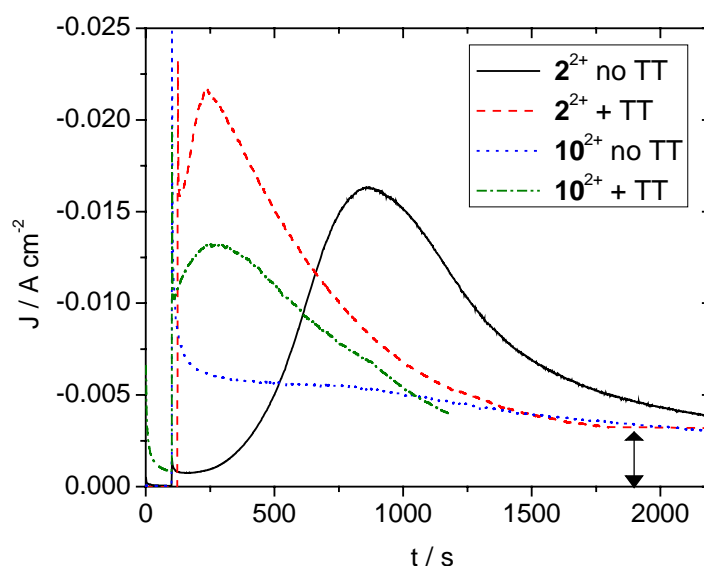


**Figure 3.53** Current during PEP experiment with complexes 2<sup>2+</sup> and 10<sup>2+</sup> with and without monomer in the solution. TT=Terthiophene.

In figure 3.53 some typical transient currents for the photo-oxidation are shown. For the samples with monomer in solution there is a rapid increase in current when the illumination is started and a peak current that then decays to a constant background current (dashed line in figure 3.53). This is compared to the response for the PEP without monomer in solution. In the case of  $2^{2+}$  there is an equal current in magnitude but the peak comes at a later time (900 s compared to 250 s) than the peak in monomer solution. The bi-thienyl ligand in  $2^{2+}$  is reactive and may be photo-oxidised itself during the process. This is supported by the information in table 3.17 where the data for a DNSC with the  $2^{2+}$  sensitised  $\text{TiO}_2$  film after PEP yields a non-working device while  $10^{2+}$  that does not have the reactive bithienyl ligand survives the PEP without monomers and can be used in a DNSC. The current from the PEP in figure 3.53 appears to decrease and level off after about 1600 seconds, which is supported by figure 3.54 where the transient UV-vis absorbance of 440 nm is displayed. At 1600-1800 seconds there is a change in the transient absorbance and a lower increase.

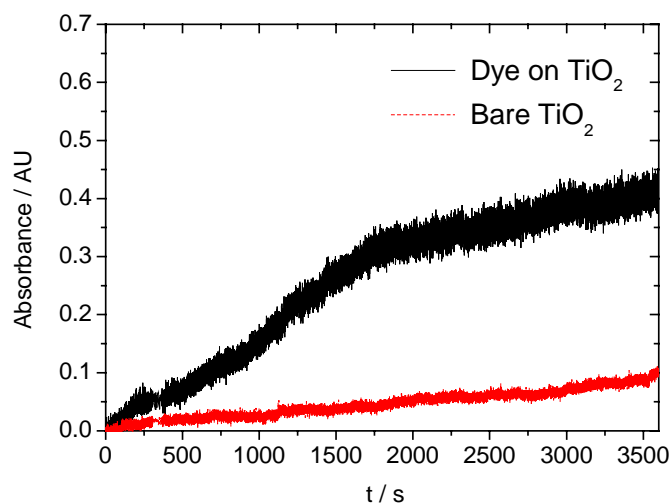


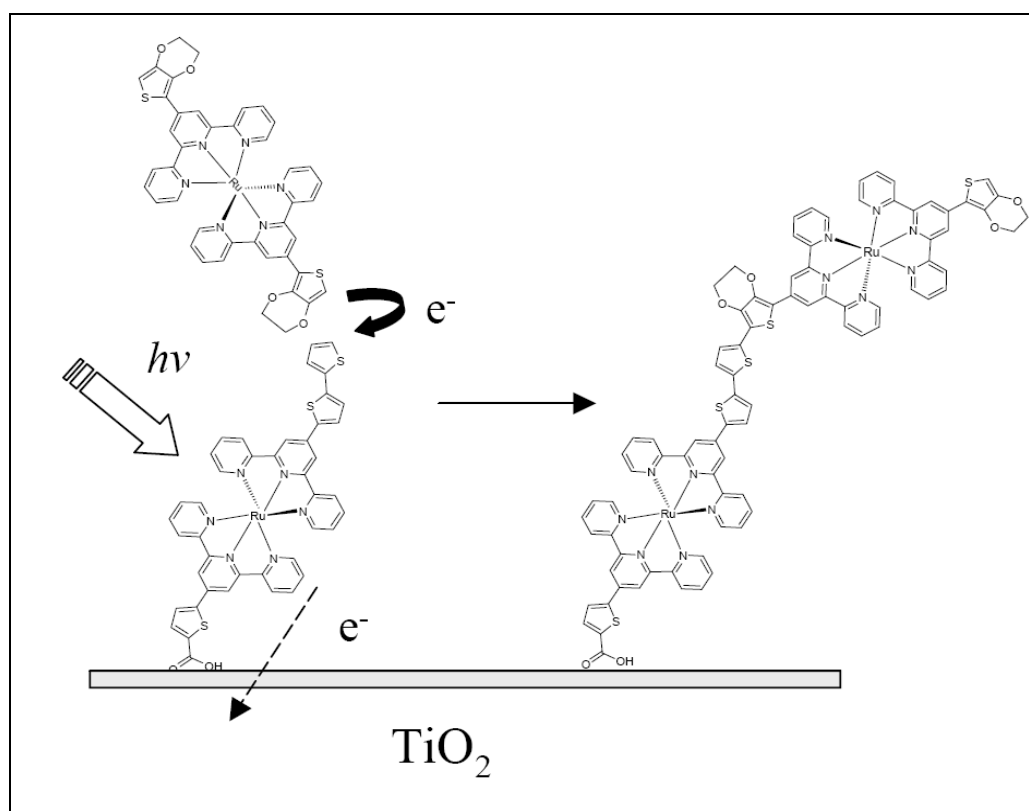
**Figure 3.54** Transient UV-Vis absorbance at 440 nm. The bare  $\text{TiO}_2$  also shows signs of some UV-vis change.

Control experiments were done switching on and off light, switching on and off bias potential and doing the measurements with and without dye and monomers. They indicate that both illumination and bias potential are important for the polymer growth. In figure 3.54 it can be seen that there is possible oxidation on bare  $\text{TiO}_2$ . This is not expected because the light source has a cut off filter at 400 nm so that the

light reaching the  $\text{TiO}_2$  does not have the energy to exceed the band gap of  $\text{TiO}_2$  and create holes in the valence band. The absorbance maximum of terthiophene is at 390 nm, which suggests there may be some photochemical oxidation of the terthiophene. After 60 minutes of the photo-oxidation in the terthiophene solution, UV-vis absorbance on the solution was measured to control how much the terthiophene concentration had changed. The concentration has decreased from 10 mM to  $\sim 7.8$  mM. This translates to 6.6  $\mu\text{mole}$  or 14.7  $\mu\text{mole per cm}^2$  of  $\text{TiO}_2$  film. Taking into consideration the surface coverage of  $2^{2+}$  ( $\sim 70 \text{ nmole cm}^{-2}$ ) it means that for every dye molecule on the surface,  $\sim 210$  monomer molecules have been deposited on the surface during the photo-oxidation reaction.

As well as an increase in absorbance at 440 nm, there is an increase in the absorbance at longer wavelengths ( $\sim 600\text{-}700 \text{ nm}$ ). This signal could be due to oxidative doping of polythiophene that is formed from oxidation. The absorbance bands of this type are from bipolaron transitions.<sup>[64]</sup>

### Complexes as monomers



**Scheme 3.8** Scheme for coupling metal complex to surface bound metal complex via photo-electrochemical methods.

Instead of trying to couple an organic oligomer to the surface bound molecules, it may be possible to couple them with ruthenium or iron complexes. An experiment with the concept of scheme 3.8 was performed with TiO<sub>2</sub> sensitised with **3**<sup>2+</sup> and complexes [Fe(**2**)<sub>2</sub>][PF<sub>6</sub>]<sub>2</sub> and [Ru(**2**)<sub>2</sub>][PF<sub>6</sub>]<sub>2</sub> in solutions of CCl<sub>2</sub>H<sub>2</sub> (0.1 M LiClO<sub>4</sub>).

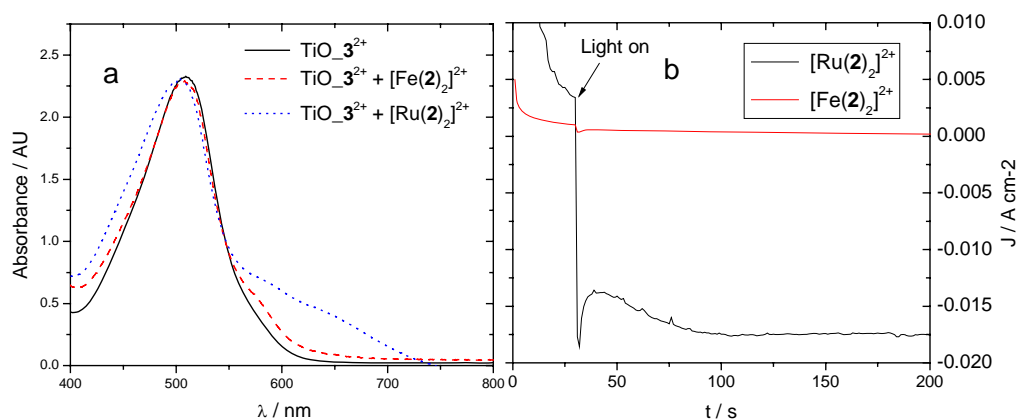


**Figure 3.55** Photo-electrochemical polymerisation of the ruthenium and iron complexes coordinated to **2** in DCM.

In figure 3.55b the current of the contacted FTO substrate with the TiO<sub>2</sub> film sensitised with **3**<sup>2+</sup> at 0 V is plotted with time. Upon illumination the anodic current is increased due to injected electrons in the TiO<sub>2</sub> and the applied potential (0 V) that acts as an electron sink. When a complex such as [Ru(**2**)<sub>2</sub>][PF<sub>6</sub>]<sub>2</sub> is added to the solution (1 mM) the anodic current is increased. Replacing the ruthenium complex with its iron version, [Fe(**2**)<sub>2</sub>][PF<sub>6</sub>]<sub>2</sub>, results in a much lower photocurrent (figure 3.55b). In figure 3.55a, the UV-vis spectra of the TiO<sub>2</sub> films were measured after illumination for 300 seconds. The film from the solution with ruthenium complex shows a new band centred between 600 and 700 nm, which is similar to the band at 620 nm from table 3.16 for the UV-vis of the electrochemically polymerised poly-[Ru(**2**)<sub>2</sub>][PF<sub>6</sub>]<sub>2</sub>. It appears that **3**<sup>2+</sup> on TiO<sub>2</sub> can photo-oxidise the ruthenium complex and lead to oxidative coupling and possible polymerisation. In the case of the iron complex there seems to be no photo-oxidation, which probably is due to the iron (II/III) process having a low oxidation potential that is removed from the oxidation of the ligand. The HOMO of the ruthenium complex has more contribution from the ligand than in the iron complex and the ligand will be easier to oxidise in the ruthenium complex.



### PECM probing of photo-oxidation

To probe the PEP *in-situ* with the PECM technique (chapter 2) it is necessary to probe a redox couple that is oxidised or reduced by the process, but not irreversibly. One way to do this is to probe the reduction of ferrocene and see how this current is affected by competition with bis-EDOT for oxidation by the dye sensitised TiO<sub>2</sub>. When the excited dye molecules are oxidising thiophene monomers instead of the ferrocene, there is a competition that can be probed. The UME electrode is set at  $-0.4$  V (vs. Ag/AgNO<sub>3</sub>) and an electron draining potential of 0 V is set for the FTO substrate. The UME electrode is withdrawn 30  $\mu$ m from the TiO<sub>2</sub> surface and the steady state current measured. In figure 3.56a the current from only ferrocene is measured and when EDOT monomer is added (10 mM). There is no great difference at this point. In figure 3.56b bis-EDOT, which has a lower oxidation potential, is added. As can be seen there is a smaller response to the ferrocene when the monomer is added. Measuring again after 5 minutes, it appears the photocurrent is approaching the earlier value of steady state current. This suggests it is possible to measure the photo-oxidation of the monomers in an indirect mode where the competition between the UME and TiO<sub>2</sub>, when they are both oxidising, is probed.

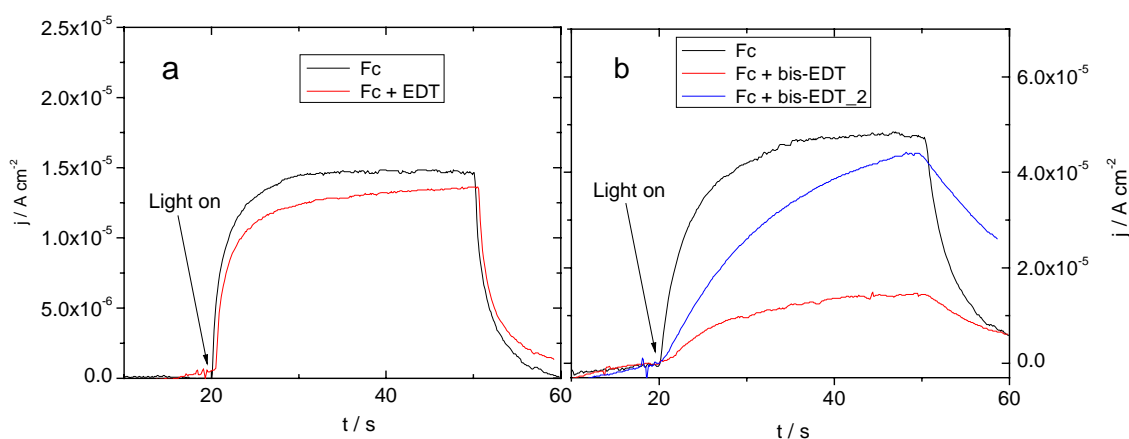


**Figure 3.56** (a) UME response to reduction of ferrocene close to dye sensitised TiO<sub>2</sub> under illumination when EDT is added. (b) The response when bis-EDOT is added just after adding and two minutes after adding. Ferrocene, EDT and bis-EDOT concentrations are 10 mM. The light is switched on between 20 and 50 seconds. The light intensity was  $25 \text{ mWcm}^{-2}$ .

$$(a)[J_{UME}] \propto k_{red}[Fc^+]$$

$$(b)[Fc^+] \propto k_{OxFc}[Fc] \quad (20a-c)$$

$$(c)[Fc^+] \propto k_{OxFc}[Fc] - k_{OxbiEDOT}[bis - EDOT]$$

A simplified model to describe the current and its dependence on the concentrations of ferrocene and bis-EDOT, is applied in equations 20a-c. In equations 20a-c, the current density at the UME is mainly dependent on the concentration of  $Fc^+$  and the rate constant of reduction (equation 20a). The concentration of  $Fc^+$  is dependent on the oxidation rate of Fc at the  $TiO_2$  surface (equation 20b). Finally, when bis-EDOT is added, the concentration of  $Fc^+$  will depend on the concentrations of ferrocene and bis-EDOT as it is written in equation 20c. In figure 3.56b the decrease of current supports equations 20a-c at the start but the current returns to something close to the current with no added bis-EDOT. This may be caused by the fact that the oxidation of bis-EDOT is irreversible and at a certain point further oxidation of bis-EDOT is blocked.

### 3.4 Electrochemistry of Dye Sensitised TiO<sub>2</sub>

#### 3.4.1 CVs of Dye sensitised Electrodes

The electrochemistry of nanoporous TiO<sub>2</sub> has been reported on many times. As was discussed in chapter 1, there are many potential applications of such a material. In applications where electron injection into the material is important the energy levels are of high significance. The conduction band energy level is shifted when influenced by pH, solvent, surface adsorbants and different cations.<sup>[65]</sup> In figure 3.57 the recorded CV of nanoporous TiO<sub>2</sub> thin films on FTO glass in 3-MPN and MeCN with TBAPF<sub>6</sub> (0.1 M) are shown. These two solvents are the main ones used in this work and from the figure they influence the reduction potentials of the TiO<sub>2</sub> differently. The onset of reduction is shifted more negative in 3-MPN.

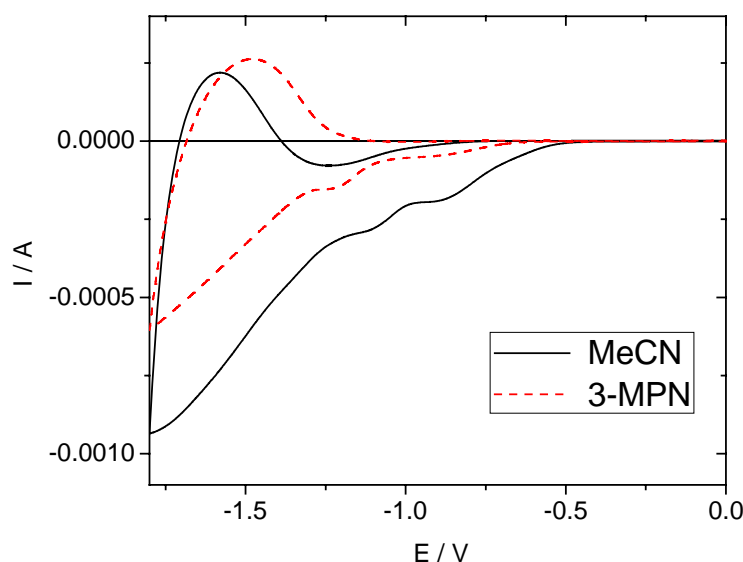


**Figure 3.57** Cyclic voltammetry on FTO glass with TiO<sub>2</sub> film in MeCN and 3-MPN (0.1 M TBAPF<sub>6</sub>) with scan rate of 100 mV/s. Reference electrode was Ag/AgNO<sub>3</sub>.

Cyclic voltammetry on molecules adsorbed to nanoporous TiO<sub>2</sub> that are supported on an electrode, such as FTO covered glass, is possible because of the porous nature of the TiO<sub>2</sub> that allows contact of the electrolyte with the FTO surface.<sup>[66-69]</sup> A signal from the dye molecules redox process, which is within the bandgap of TiO<sub>2</sub>, is present due to lateral charge transport along the surface of the TiO<sub>2</sub>. Upon applying a positive polarization to the electrode, positive holes are injected into the film via the surface

adsorbed complexes that are oxidised. The oxidised sensitiser then mediates the oxidation of TiO<sub>2</sub>-bound sensitizers by self-exchange electron transfer across the nanocrystalline surface. Counter ions in the electrolyte diffuse to counter balance the oxidized molecules.<sup>[69]</sup> This results in semi-infinite diffusion controlled charge transport, as one would expect from a species in solution although the peak-to-peak splitting is large and the redox process quasi-reversible. In figure 3.58 dyes **2**<sup>2+</sup> and **10**<sup>2+</sup> on TiO<sub>2</sub> are investigated. At a similar dye loading there is still a big difference in current response. Integration of the oxidation peaks to find the amount of charge, it is found that for dye **2**<sup>2+</sup> about 5 nmol of the 48 nmol total surface coverage are electroactive in the experiment (~10%), while for dye **10**<sup>2+</sup> only about 0.2 nmol of the total 39 nmol surface adsorbed molecules are oxidised (~0.5%).

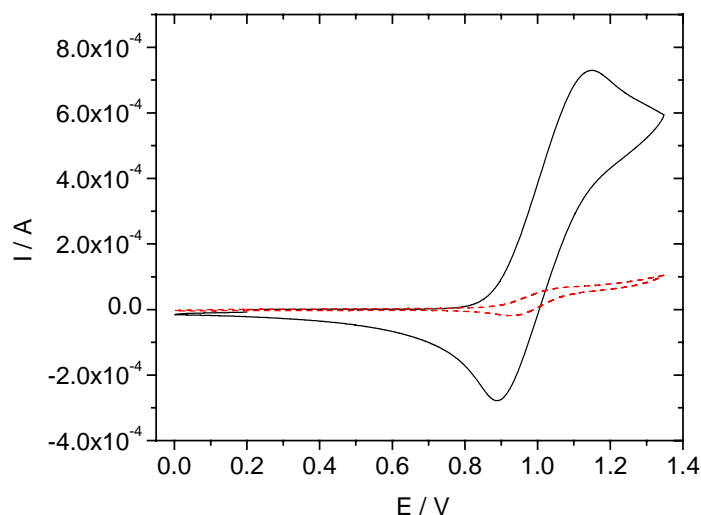


**Figure 3.58** Cyclic voltammograms of **2**<sup>2+</sup> (solid line) and **10**<sup>2+</sup> (dashed line) adsorbed to nanoporous TiO<sub>2</sub> measured in MeCN (0.1M TBAPF<sub>6</sub>) at 100 mV/s.

There is an apparent larger current density for **2**<sup>2+</sup>, that has a bi-thienyl group on the counter ligand, than for **10**<sup>2+</sup> that has no modifying group on the outer terpyridine. It appears that the bi-thienyl groups may aid in transferring the positive charges. Wang *et al.* found that surface adsorbed complexes with thiocyanate groups gave higher diffusion constants than the complexes without.<sup>[69]</sup> The HOMO of the complex was extended by the thiocyanate groups and allowed for closer proximity of the positive charges between the adsorbed molecules. This is similar to the case of the bithienyl groups on the bis-terpyridine complexes, which also appears to extend the HOMO

(from electrochemical and modeling experiments in section 3.2.4). The electron rich sulfur atom that is present in both cases may thus be stabilizing any positive charges on the ligand. There appears to be some irreversible oxidation of the thienyl groups upon oxidation, which results in a slight change in the absorbance spectrum in the form of a shoulder on the MLCT at longer wavelengths. Later experiments with these films in DNSC give cells that do not work for  $2^{2+}$ , while  $10^{2+}$  (no thienyl counter ligand) could still perform in a DNSC. Prior to cyclic voltammetry,  $2^{2+}$  desorbed readily from  $\text{TiO}_2$  when immersed in ethanol but after the electrochemical measurement, the dye does not desorb. These observations suggest that the  $2^{2+}$  molecules indeed undergo an irreversible process when an oxidative potential is applied and result in a film that is harder to dissolve.

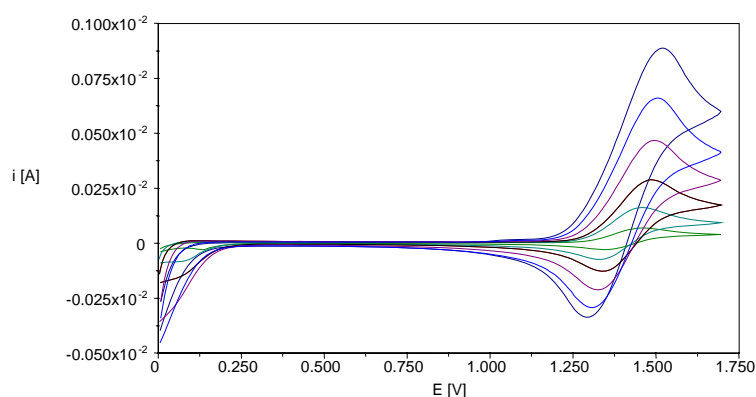


**Figure 3.59** CV's of [(2)Ru(5)]-TiO<sub>2</sub> in MeCN (0.1 M TBAPF<sub>6</sub>) at different scan rates.

Cyclic voltammetry of the ruthenium + II/III process at different scan rates can give information on the diffusion kinetics.<sup>[69]</sup> In figure 3.59 CV's of [(2)Ru(5)]-TiO<sub>2</sub> at different scan rates are plotted. In figure 3.60 the square root of the scan rate is plotted against the current at  $E_p$  for the anodic and cathodic currents. The fact that the plots are linear suggest that the charge transport is semi-infinite diffusion controlled according to the Randles-Sevcik relationship,  $I_p = (2.69 \times 10^5)n^{3/2}AD_+^{1/2}C_0v^{1/2}$ . In the equation,  $A$  is the surface area of the electrode,  $n$  the amount of electrons in the process,  $D_{+/-}$ , the diffusion constant,  $C_0$  the concentration and  $v$  the scan rate.

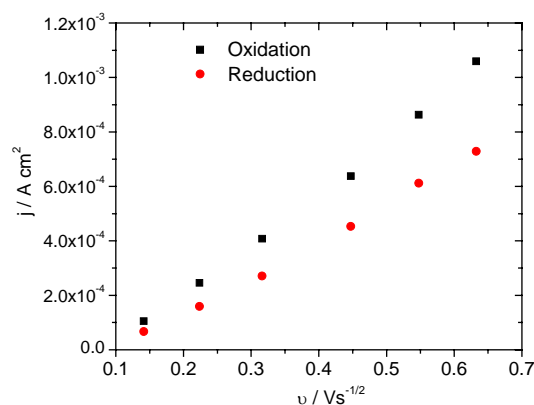


**Figure 3.60** Plots of current versus the square root of the scan rate for the anodic and cathodic peak current.

As can be seen in figure 3.60 the cathodic current peaks (oxidation) increase less than the anodic peaks (reduction). This may be because of irreversible reactions or due to slower percolation of the negative charges than the positive charges along the monolayer. The CV of the complex with counter ligand **3** in the place of **2** in [(**2**)Ru(**5**)]-TiO<sub>2</sub> is similar.

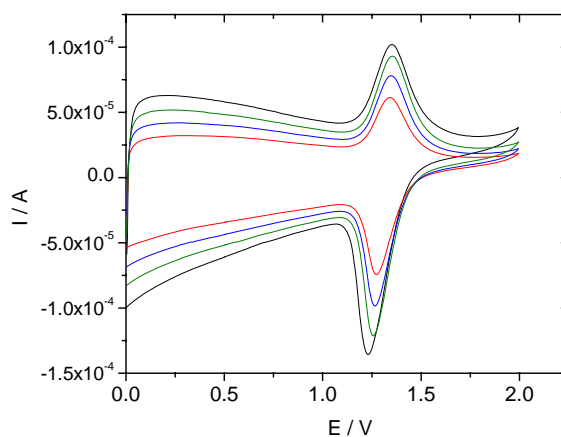


**Figure 3.61** CVs on dye sensitised mesoscopic conducting F-doped SnO<sub>2</sub> at different scan rates.

In figure 3.61 the cyclic voltammograms of the complex adsorbed to mesoscopic Sb-doped SnO<sub>2</sub> is shown. The more symmetrical shape of the peaks suggests surface adsorbed monolayer (see chapter 2). The Sb-doped SnO<sub>2</sub> nanoparticles have a considerably higher conductivity than the TiO<sub>2</sub> so the CV should behave more as one for a surface monolayer adsorbed directly to an electrode.<sup>[70]</sup>

The redox potentials of the  $\text{Ru}^{2+}/\text{Ru}^{3+}$  processes for the dyes that showed a clear signal on  $\text{TiO}_2$ , measured against the  $\text{Ag}/\text{Ag}^+$  reference electrode, are collected in table 3.18. The potentials are consistently at higher values on the  $\text{TiO}_2$  surface than in the solution phase. This is similar to previous reports on voltammetry of ruthenium poly-pyridyl complexes bound by carboxylic acids to nanocrystalline  $\text{TiO}_2$ .<sup>[71, 72]</sup> The suggested explanation was that the bond formation between the  $\text{TiO}_2$  surface and the carboxylic groups increased the electron withdrawing character of that ligand, thus shifting the oxidation potential of the  $\text{Ru}^{2+}/\text{Ru}^{3+}$  process to more positive potentials. The larger peak split may be due to the reorganization energy required for a molecule solvated on the surface compared to in solution.<sup>[73, 74]</sup>

**Table 3.18** The redox potentials of some complexes in solution and adsorbed to  $\text{TiO}_2$  surfaces. The reference is ferrocene.

Complex	$E_{1/2}$ (solution)	$E_{1/2}$ (on $\text{TiO}_2$ )
<b>11</b> <sup>2+</sup>	+ 0.87	+ 0.96
<b>3</b> <sup>2+</sup>	+ 0.83	+ 0.99
<b>8</b> <sup>2+</sup>	+ 0.81	+ 0.99
<b>2</b> <sup>2+</sup>	+ 0.87	+ 0.97

## 3.5 Photoelectrochemistry of Metal Complexes

### 3.5.1 Spectroelectrochemistry

To probe how the frontier orbitals energy levels change when the HOMO is oxidized, spectroelectrochemistry was conducted on some of the ruthenium complexes. The complexes used for the experiment had thienyl groups on the 4'-position of the terpyridine that contribute to different extents the HOMO.

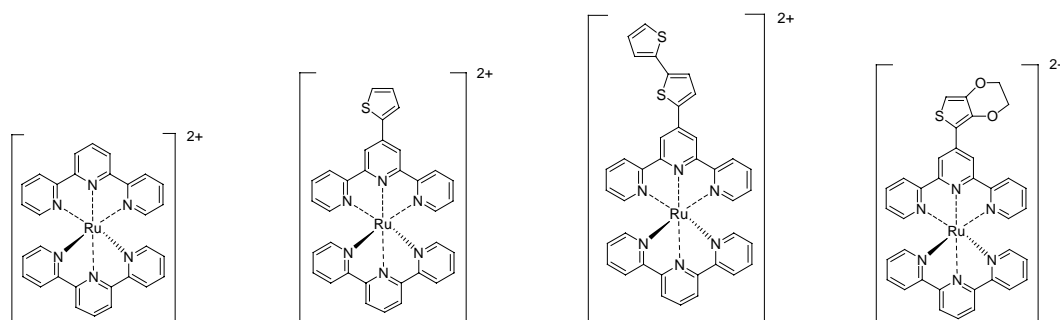


**Figure 3.62** The four different ruthenium complexes that were used in the spectro-electrochemical experiments. From left to right they are named as **20a-20d**.

The complexes were in their heteroleptic forms, with unsubstituted terpyridine as counter ligand, to avoid any polymerisation when oxidation may lead to radical cations, although some dimerisation may take place (see figure 3.62).

A thin platinum mesh was cut to fit in a thin optical cell. The thin platinum mesh was working as an optically transparent electrode (OTE). Together with a platinum counter electrode and a silver reference wire a three-electrode set-up was prepared. The small thickness of the optical cell allows the OTE to oxidise/reduce all the surrounding solute and changes in the UV-vis spectrum are easily detected.

For all the samples the potential was increased from 400 mV less positive of the  $E_p$  of the ruthenium +II/+III process to ~200 mV more positive of it in steps of 100 mV. The relatively long time (1-2 minutes) it takes to scan the NIR-vis-UV range (200-2000 nm) decreases the accuracy of the measurement as changes may occur during the time when the spectrometer is not measuring the specific wavelength. On the other hand, the in-homogenous nature of the platinum mesh makes it necessary to let the diffusion layer thickness to grow larger than the openings of the mesh, which takes a certain time.<sup>[46]</sup>



The spectroelectrochemical graphs for the four different compounds are collected in figure 3.63. All the compounds show bleaching at their MLCT bands with increasing oxidation potentials as is reported for oxidation of  $[\text{Ru}(\text{bipy})_3]^{2+}$ .<sup>[75]</sup> In all of the compounds a new band between 600 and 900 nm emerges as the applied potential reaches that of the redox couple, in this case  $\text{Ru}^{2+}/\text{Ru}^{3+}$ , and about 200 mV beyond. This could be the ligand to metal charge transfer transition (LMCT) that is rather weak for **20a** but much stronger for the complexes with thienyl groups. The electron rich thiophene groups lower the  $\pi$  orbital energy of the ligand and allow a stronger transfer. Complex **20b** had a more intense and red-shifted band at 800 nm. For the complexes with bi-thienyl and EDOT groups there were several new bands.

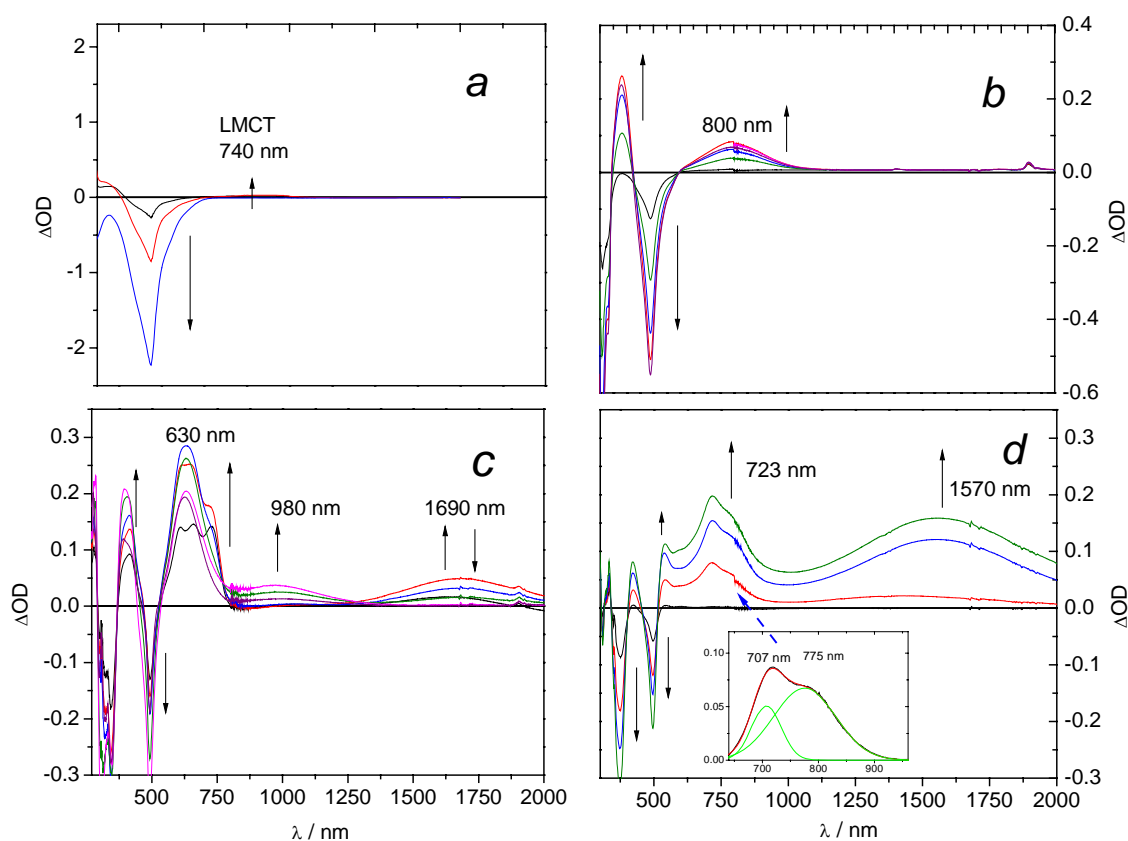


**Figure 3.63** Spectroelectrochemistry of compounds **20a** (a)  $[\text{Ru}(\text{tpy})_2][\text{PF}_6]_2$ , **20b** (b)  $[(\text{tpy})\text{Ru}(\mathbf{1})][\text{PF}_6]_2$ , **20c** (c)  $[(\text{tpy})\text{Ru}(\mathbf{2})][\text{PF}_6]_2$ , and **20d** (d)  $[(\text{tpy})\text{Ru}(\mathbf{3})][\text{PF}_6]_2$  in MeCN (0.1 M TBAPF<sub>6</sub>). The spectra are plotted as the change in absorbance compared to the spectrum when no potential is applied ( $\Delta\text{OD}$ ). The inset in figure 2d shows that the peak at 723 nm may consist of two smaller peaks at 707 and 775 nm that are overlapping.

An LMCT transition between an electron donating ligand and ruthenium in its +III oxidation state will often occur but the transitions above 500 nm in figures 3.63b-d have other origins. Apart from the bands between 600-800 nm there were broad bands at 1690 nm for **20c** and 1570 nm for **20d**. Moorlag *et al.* reported absorption bands close to these wavelengths for spectroelectrochemistry on ruthenium complexes with incorporated oligothiophenes.<sup>[75]</sup> Other experiments have shown that singly oxidised oligothiophenes have two electronic transitions.<sup>[76]</sup> The energies and intensities fit in with the two absorption bands at 600-800 nm and 1500-1600 nm seen in figures 3.63c-d. The transitions at higher energy (shown as A in figure 3.64) correspond to SOMO→LUMO  $\pi$ - $\pi^*$  transitions. In figure 3.64 the molecular orbitals of the ruthenium d-orbitals and the ligands  $\pi$ -orbitals are mixed to a certain extent and combine into the molecules HOMO.<sup>[75]</sup> The low energy absorptions are proposed to be the transitions (B in figure 3.64) between mixed Ru/oligothiophenes orbitals close in energy. Bands of intermediate energy may be transitions from lower lying  $\pi$ -orbitals to the SOMO.

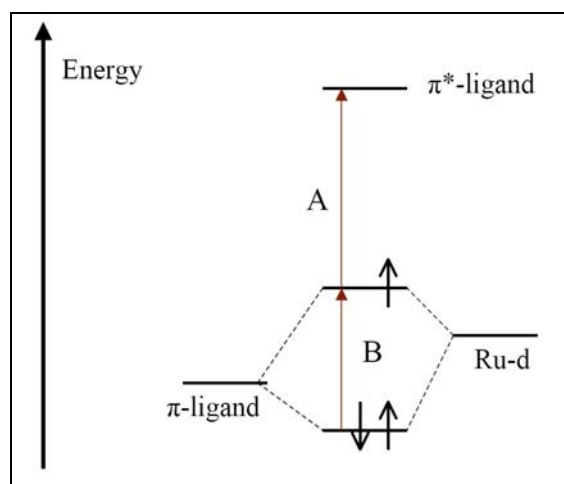


**Figure 3.64** A qualitative molecular orbital diagram for the oxidised ruthenium complex where the HOMO has contributions from the ligand  $\pi$ -orbitals and the ruthenium d-orbitals. Reproduced from reference [72].

In table 3.19 the absorption bands from the spectroelectrochemistry are collected. The bands at 630 nm and 723 nm in figure 3.63 c and d show some complexity and are probably made up of overlapping bands as the inset in figure 3.63d proposes. In figure 3.63c, the low energy band at 1690 nm diminishes as the potential is increased beyond the redox peak potential. At the same time a new band arises at 980 nm, which

suggests a shift in an energy level. The spectra for complexes **20c** and **20d** show bleaching at about 350 nm, as well as for the MLCT band. The neutral oligothiophenes have  $\pi$ - $\pi^*$  transitions in this region and as they are oxidised this absorption diminishes.

**Table 3.19** The peaks in the UV-vis absorbance between 300 and 2000 nm that emerge during the electrochemical oxidation.

Complex	MLCT bleaching (nm)	New bands (nm)	(nm)	(nm)
$[\text{Ru}(\text{tpy})_2]^{2+}$	475	740		
$[(\text{tpy})\text{Ru}(\mathbf{1})]^{2+}$	488	800		
$[(\text{tpy})\text{Ru}(\mathbf{2})]^{2+}$	490	630	980	1690
$[(\text{tpy})\text{Ru}(\mathbf{3})]^{2+}$	495	723		1570

A ruthenium complex that was used as a dye for the  $\text{TiO}_2$  was measured upon in a spectroelectrochemical experiment. The ester of  $\mathbf{1}^{2+}$  has a carboxylate anchoring group and ligand **3**. Applying the same range of potentials (to about 0.2 V above the redox potential of the  $\text{Ru}^{2+}/\text{Ru}^{3+}$  process) results in the spectra in figure 3.65 that is similar to the one in figure 3.63d. As with  $[(\text{tpy})\text{Ru}(\mathbf{3})]^{2+}$  (**20d**), there is a peak at 723 nm that appears to be made up of two or more overlapping peaks (see figure 3.63d).

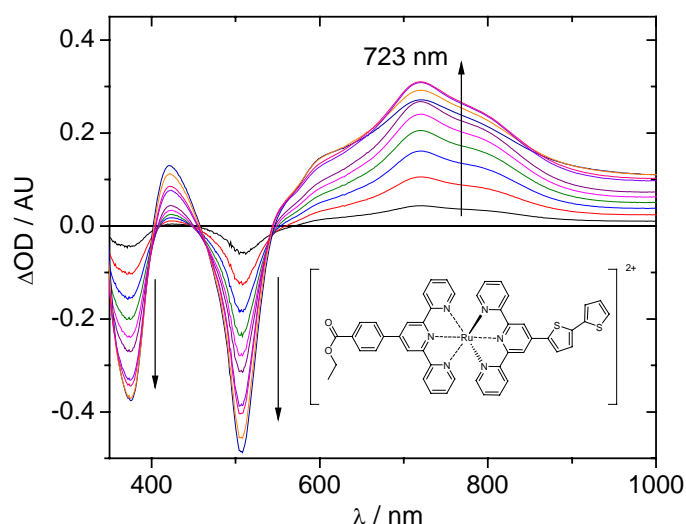


**Figure 3.65** The changes in the UV-vis spectrum when an oxidative potential is applied around the potential of the  $\text{Ru}^{2+}/\text{Ru}^{3+}$  process ( $\pm\sim 200$  mV). Done in MeCN (0.1 M TBAPF<sub>6</sub>).

**Conclusion on spectroelectrochemistry**

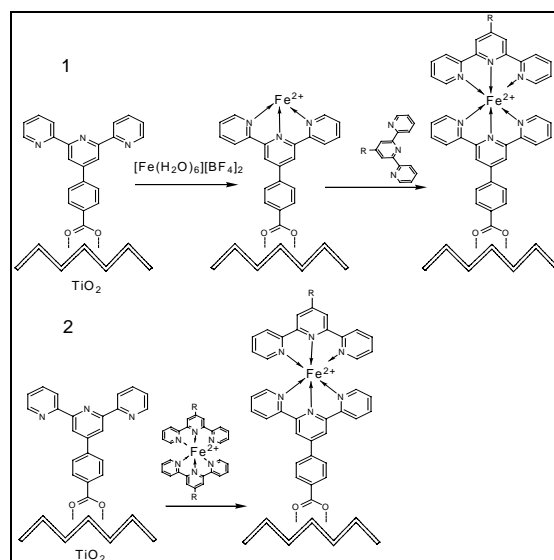
From the spectra it appears that oxidising the complexes at potentials close to the redox potential of the compounds can reveal simultaneous oxidation of the ligand. It appears that for the compounds **20b-20d** there is a degree of orbital mixing between the ruthenium d-orbitals and the ligand  $\pi$ -orbitals.

### 3.5.2 Photovoltaic (PV) Performance of Metal Complexes

#### Iron dyes

Labile metal ligand systems like copper and iron are difficult to turn into heteroleptic complexes due to ligand exchange resulting in statistical mixtures.<sup>[32]</sup> A molecular dye in a DNSC has improved electron injection ability when there is a good electron / hole separation after excitation. Metal complexes with 2,2':6',2''-terpyridine ligands may have a more directed charge transfer as heteroleptic complexes than as homoleptic. In order to sensitise TiO<sub>2</sub> with heteroleptic iron compounds, it has been intended to be built-up on TiO<sub>2</sub> surface *in-situ*, using a bottom up approach where an anchoring ligand was first attached and then iron ions added as a salt or as a complex.<sup>[37]</sup>

TiO<sub>2</sub> films on FTO glass were immersed in DMSO solutions of anchoring ligand **4** overnight. UV-vis spectra of the solutions confirmed that some of the ligand had been adsorbed to the TiO<sub>2</sub> surface (~20 nmol / projected cm<sup>2</sup>). The films were rinsed afterwards in DMSO and acetone to wash off any unattached ligand. Then the films were put in a solution of an iron salt or alternatively a solution of an iron bis-terpyridine complex (see scheme 3.9). The complex in solution, hopefully participates in ligand exchange with the anchoring ligand on the TiO<sub>2</sub> surface.



**Scheme 3.9** Different pathways towards in-situ synthesised iron heteroleptic complexes attached to TiO<sub>2</sub> surface labelled as bottom-up synthesis method 1 and 2.

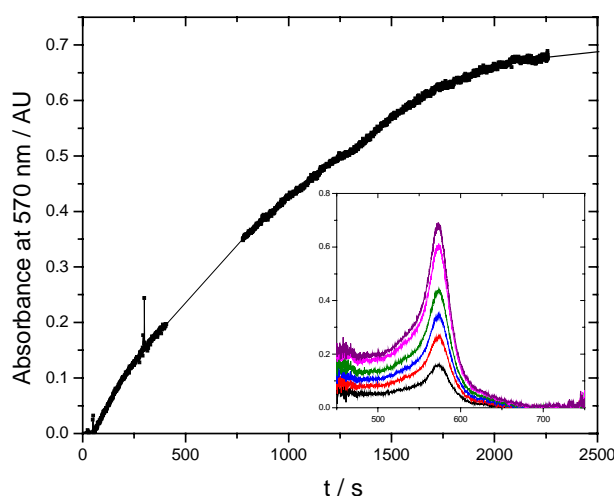


**Figure 3.66** Transient absorbance at 570 nm of a TiO<sub>2</sub> film immersed in anchoring ligand **4** into the surface is immersed in a solution of [Fe(II)(H<sub>2</sub>O)<sub>6</sub>][BF<sub>4</sub>]<sub>2</sub> (~2 mM). The inset shows the individual spectra.

### Method 1

Surface attached dyes were visible after the two steps while control experiments showed that the bottom up approach was only possible when an acid functionalised ligand was first adsorbed. Control experiments with TiO<sub>2</sub> films without any anchoring ligand **4** and control experiments with ligand **7** did not result in coloured films when iron salt was added. Figure 3.66 shows how the Fe(II) ion in solution coordinates to the TiO<sub>2</sub> surface adsorbed ligand **4** and gives rise to an MLCT transition. Two ligands on the surface may also form a bis-terpyridine complex with the ion. After about 40 minutes it has reached a maximum of Absorbance (A)=0.7 at 572 nm. That is ~30 nmoles per projected cm<sup>2</sup>, a little more than the ~20 nmole of **4** on the surface.

### Method 2

Another TiO<sub>2</sub> film, sensitised with ligand **4**, was put into a solution of [Fe(III)]<sup>2+</sup> (~1mM) overnight. It had a light blue colour after this. The absorbance maximum of the TiO<sub>2</sub> sensitised with ligand **4** + complex [Fe(III)]<sup>2+</sup> was at about 600 nm and the absorbance A=0.2. This is a red-shift of 10 nm from the [Fe(III)]<sup>2+</sup> complex (589 nm) in solution and 30 nm from the TiO<sub>2</sub>-**4**-Fe(II) compound (570 nm). The red shift is consistent with those of some of the ruthenium dyes adsorbed to TiO<sub>2</sub>. As will be discussed, this might be due to the effect of an anchoring ligand that is somewhat

covalently bonded to the surface, which may lower the LUMO of the molecule and cause a smaller bandgap. Despite the low absorption of the TiO<sub>2</sub> film with the *in-situ* synthesised [(4)Fe(3)]<sup>2+</sup> due to low coverage (A=0.2), the performance is far better than for the bottom-up synthesis *method 1* (A=0.7). Table 3.20 summarises the UV-vis absorbance and photovoltaic data. TiO<sub>2</sub> films sensitised with [Fe(4)<sub>2</sub>][PF<sub>6</sub>]<sub>2</sub> had similar PV performance but with a far higher optical density (A=1.6). The same experiment was done with [Fe(2)<sub>2</sub>][PF<sub>6</sub>]<sub>2</sub> to build the iron complex [(2)Fe(4)]<sup>2+</sup> (see table 3.20) on the TiO<sub>2</sub> surface. An even better efficiency was reached for a very low coverage.

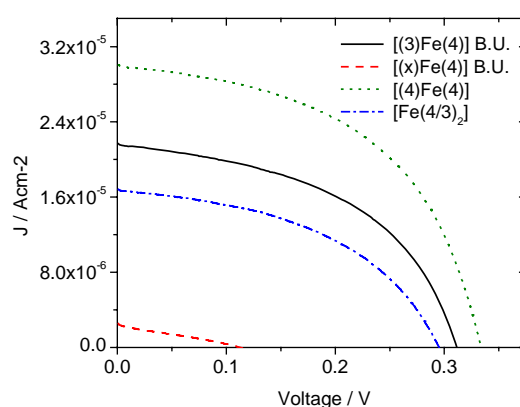


**Figure 3.67** I-V curves for PV cells with TiO<sub>2</sub> films sensitised with anchor-ligand **4** and *in-situ* added [Fe(II)(H<sub>2</sub>O)<sub>6</sub>][BF<sub>4</sub>]<sub>2</sub> or [Fe(3)<sub>2</sub>][PF<sub>6</sub>]<sub>2</sub>. They are compared to the TiO<sub>2</sub> films sensitised in solutions of [Fe(4)<sub>2</sub>][PF<sub>6</sub>]<sub>2</sub> and [Fe(3/4)][PF<sub>6</sub>]<sub>2</sub>. Electrolyte standard 2 was used.

In figure 3.67, the I-V curves from the photovoltaic cells are plotted. Attempts at synthesis of [(3)Fe(4)][PF<sub>6</sub>]<sub>2</sub> result in a mixture of three complexes. Synthesis using stoichiometric mixtures of the ligands (1:1), with and without precipitation with NH<sub>4</sub>PF<sub>6</sub>, only led to very low yields of [(3)Fe(4)][PF<sub>6</sub>]<sub>2</sub> with the ligands preferring to coordinate as homoleptic complexes. The wavelength of the absorbance maximum of [Fe(3/4)][PF<sub>6</sub>]<sub>2</sub> on TiO<sub>2</sub> (table 3.20) suggests that it is mostly [Fe(4)<sub>2</sub>][PF<sub>6</sub>]<sub>2</sub> on the surface. Two other combinations for building up [(3)Fe(4)]<sup>2+</sup> were tried: (3) first adsorbing [Fe(4)<sub>2</sub>][PF<sub>6</sub>]<sub>2</sub> followed by immersion in a solution of [Fe(3)<sub>2</sub>][PF<sub>6</sub>]<sub>2</sub> did not result in a change of the UV-vis absorbance spectrum, (4) first adsorbing **4** to the surface, then adding the iron salt and finally immersing in a solution of [Fe(3)<sub>2</sub>][PF<sub>6</sub>]<sub>2</sub>. This did not either result in a substantial change of the UV-Vis spectrum.

**Table 3.20** Values from iron dyes adsorbed to TiO<sub>2</sub> and their photovoltaic performances.

Dye	$\lambda_{\max}$ on TiO <sub>2</sub> / nm (in solution)	Abs.	J <sub>sc</sub> (mA/cm <sup>2</sup> )	V <sub>oc</sub> (V)
[Fe(4) <sub>2</sub> ][PF <sub>6</sub> ] <sub>2</sub>	572 (570)	1.6	0.030	0.33
[Fe(3/4)][PF <sub>6</sub> ] <sub>2</sub>	572	1.0	0.017	0.30
[Fe(3) <sub>2</sub> ][PF <sub>6</sub> ] <sub>2</sub> **	-(589)	-	-	-
[(X)Fe(4)][PF <sub>6</sub> ] <sub>2</sub> (B.U.)*	570	0.7	0.003	0.11
[(3)Fe(4)][PF <sub>6</sub> ] <sub>2</sub> (B.U.)*	600	0.2	0.022	0.31
[(2)Fe(4)][PF <sub>6</sub> ] <sub>2</sub> (B.U.)*	582	0.1	0.078	0.34

\* B.U.: Bottom up synthesis, i.e. in two steps on the surface. X = Cl<sup>-</sup> or other ligand.

\*\*Did not adsorb to TiO<sub>2</sub>.

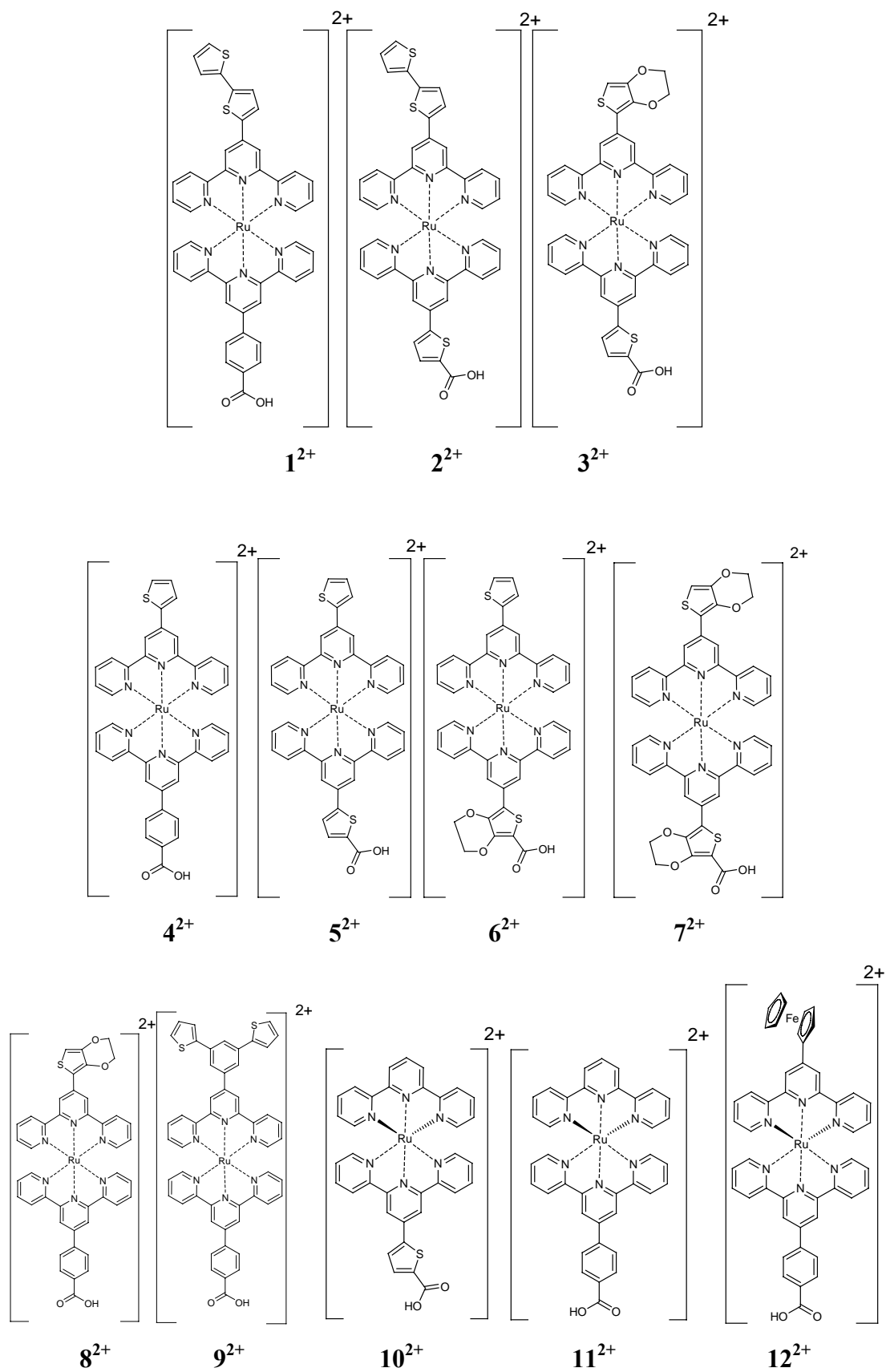
### Conclusion on Iron dyes

In conclusion, the method of building up heteroleptic iron complexes *in-situ* on TiO<sub>2</sub> surfaces seems to work (especially method 2) but only very low coverages were reached. With optimisation the method could provide new and maybe improved dyes with a labile metal ions such as iron or alternatively copper. The bottom-up synthesis of [(3)Fe(4)]<sup>2+</sup> on the TiO<sub>2</sub> gave a very low absorbance and comparing to the extinction coefficients a quite low surface coverage. This needs to be improved if better PV performances are to be reached. The donating properties of the thienyl ligands (**2** and **3**) may promote stabilising the MLCT levels and move it away from the deactivating <sup>3</sup>MC state.<sup>[28, 77]</sup> This would help improve electron injection.

### Ruthenium dyes

Several different ruthenium terpyridine dyes with varying thiophene functional groups were tested in photovoltaic cells (scheme 3.10). As standard dye, N719 (Solaronix) is used, which is described in chapter 1. It is widely recognised as one of the best dyes for the DNSC with a measured efficiency of around 10%. The practical preparations of the photovoltaic devices and the measuring instruments are described in section 2.2. The electrolytes used in these measurements are labelled as *standard 1* and *standard 2* (see section 2.2 for further details). Unless other is stated, electrolyte *standard 2* is used in the DNSC measurements.





**Scheme 3.10** The ruthenium complexes with the identification numbers that are used in the text. All the complexes are PF<sub>6</sub><sup>-</sup> salts.

### Anchoring groups

The anchoring groups that attach the complexes to the surface have been made with a spacer group between the terpyridine and the carboxylic acid. One of the essential qualities of a semiconductor/molecular junction for light harvesting is the directionality of the excited state orbital. The electron withdrawing quality of the carboxylic acid group lowers the LUMO of the ligand to make it a better acceptor.<sup>[78]</sup> In order to direct the excited electrons from the dye to the semiconductor a good orbital overlap with the titania is needed. Therefore the geometry is also important. Octahedral metal complexes with 2,2':6',2''-terpyridine ligands with substitutions on the 4'-position, may have vectorial advantages over, for example, bipyridine ligands.<sup>[9]</sup>

To compare the photophysics and electrochemistry of the 2,2':6',2''-terpyridine anchoring ligands when coordinated to ruthenium, homoleptic complexes of the carboxylate esters were made as seen in figure 3.68. The first reduction potential corresponds to the LUMO, which is mainly ligand centered. In an MLCT transition the excited electron should be directed into the ligand with the more (lowest lying) accepting orbital. For efficient electron injection the anchoring ligand needs to be the acceptor ligand. As was discussed earlier in chapter 1, electron injection into the TiO<sub>2</sub> from ruthenium polypyridyls is ultra-fast from the excited singlet state but there is also a slower injection rate from relaxed excited states, which time resolved spectroscopy has suggested.<sup>[79, 80]</sup> The electrochemical reduction potential relates to the energy of the lowest lying ligand orbitals in the ground state. Luminescence from the ruthenium polypyridine compound is a transition from the relaxed lowest lying excited state, <sup>3</sup>MLCT, to the ground state HOMO (see figure 3.69). The ground state or the HOMO is experimentally measured with electrochemistry as the first oxidation onset potential. The excited oxidation potential of dye is then calculated by subtracting the 0-0 emission in energy from the first oxidation potential of the compound according to  $E_{1/2}^*(\text{Ru}^{\text{III}}/\text{Ru}^{\text{III}}) = E_{1/2}(\text{Ru}^{\text{II}}/\text{Ru}^{\text{III}}) - E_{0-0}(\text{}^3\text{MLCT})$ .<sup>[81]</sup> The zeroth-zeroth transition,  $E_{0-0}$ , is estimated by taking the middle overlap point between the absorbance maximum and the emission maximum.

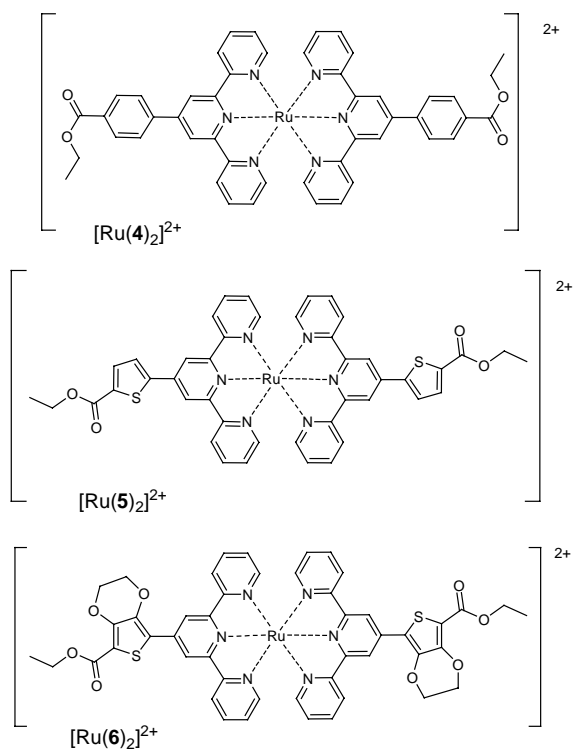


**Figure 3.68** Homoleptic ruthenium (II) complexes  $[\text{Ru}(\mathbf{4})_2][\text{PF}_6]_2$ ,  $[\text{Ru}(\mathbf{5})_2][\text{PF}_6]_2$  and  $[\text{Ru}(\mathbf{6})_2][\text{PF}_6]_2$ . The complexes are  $\text{PF}_6^-$  salts.

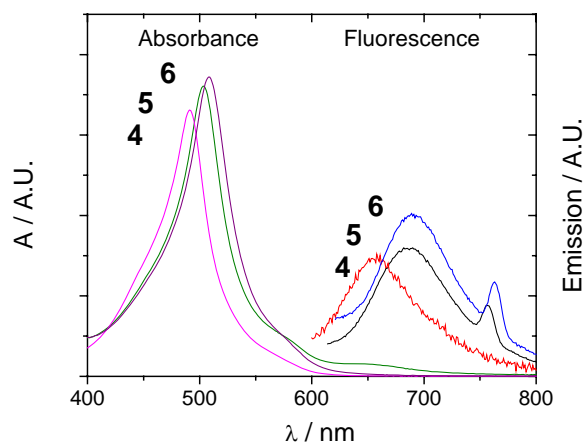


**Figure 3.69** Homoleptic complexes of anchoring ligands and their MLCT absorbance and fluorescence spectra. The numbers refer to the ligand of the ruthenium complex. Note that the intensities of the peaks are not to scale with each other.

### Solar cell measurements of the dyes

The sensitised TiO<sub>2</sub> films were prepared as described in chapter 2. All the dye solutions had concentrations between 0.7-1.0 mM with CH<sub>3</sub>CN used as solvent. In tables 3.21 and 3.22 data for the three dyes comparing anchoring ligands are presented. Table 3.21 presents electrochemical information that is relevant for the PV performance.

**Table 3.21** The electrochemical data and excited state oxidation potentials for the three homo-leptic complexes with ligands **4**, **5** and **6**.

Complex	E <sub>red1</sub> (V)	E <sub>ox</sub> (V)	E <sub>0-0</sub> (eV)	E* <sub>ox</sub> (V)
[Ru( <b>4</b> ) <sub>2</sub> ] <sup>2+</sup>	-1.56	+ 0.89	2.15	-1.26
[Ru( <b>5</b> ) <sub>2</sub> ] <sup>2+</sup>	-1.49	+ 0.90	2.08	-1.18
[Ru( <b>6</b> ) <sub>2</sub> ] <sup>2+</sup>	-1.53	+ 0.85	2.07	-1.22

From the data in table 3.21 it appears the ligand in [Ru(**5**)<sub>2</sub>]<sup>2+</sup> might be the most suitable anchor ligand when considering electron injection. This is confirmed with PV cell testing (table 3.22) where the dyes [(**1**)Ru(anchorligand **4/5/6**)]<sup>2+</sup> are compared. Comparing the photovoltaic data from the measurements in table 3.22 it appears that **5**<sup>2+</sup> is slightly better than **4**<sup>2+</sup> and **6**<sup>2+</sup> by far the most efficient. Taking into account the different coverages the trend is different though. In this test the dye with anchor ligand **5** gave a very low coverage, **4** a very good one and **6** an intermediate value. In figure 3.70 the photocurrent density divided by the surface coverage (mA per nanomole dye) from the measurements in table 3.22 are plotted against the excited state potentials and first reduction potentials, of the respective anchoring ligand complexes (table 3.21), to show the trends of the photocurrents. Now the dye with anchoring ligand **5** is almost twice as efficient as **6** and five times that of **4**. Table 3.24 will show that the counter ligands also have a large effect on electron injection and adsorption capabilities.

**Table 3.22** Photovoltaic values of dyes with the anchoring ligands that were compared. The cells were illuminated with light of 100 mW/cm<sup>2</sup> intensity.

Dye	J <sub>sc</sub> (mA/cm <sup>2</sup> )	V <sub>oc</sub> (V)	η (%)	Absorbance at λ <sub>max</sub> <sup>TiO</sup>	Coverage nmole/cm <sup>2</sup>	J <sub>sc</sub> /Cov. mA/nmol
4 <sup>2+</sup>	0.88	0.50	0.30	1.75	159	0.006
5 <sup>2+</sup>	1.00	0.56	0.38	0.55	14	0.071
6 <sup>2+</sup>	1.81	0.52	0.62	2.49	61	0.030

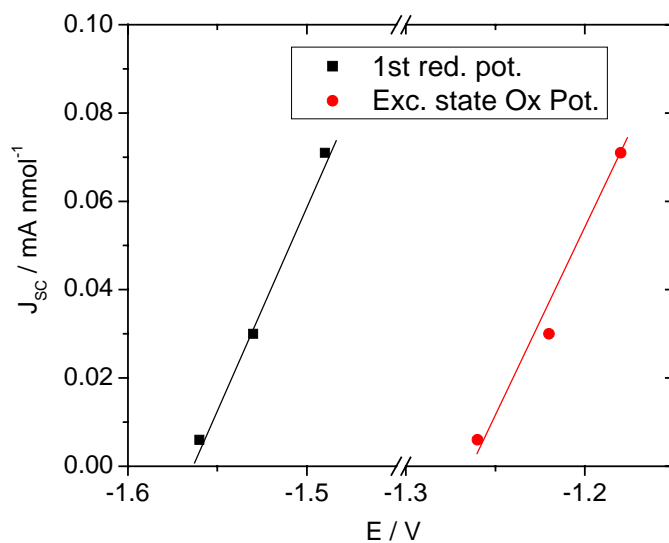


**Figure 3.70** The photocurrent density (current per nano-mole of the dye) of the solar cells with the dyes 4<sup>2+</sup>, 5<sup>2+</sup> and 6<sup>2+</sup>, plotted against the excited state oxidation potentials (circles) and the first reduction potentials (squares) of the homoleptic complexes of the anchoring ligands 4, 5, and 6.

Solar cell measurements of the ruthenium complexes were done in several batches to have reproducible values. Each dye has been measured in complete DNSC 3-4 times in different batches. The electrochemical data that is pertinent for the PV-cell performance is listed in table 3.23 for all the dyes.

**Table 3.23** Electrochemical potentials (in MeCN) and UV-vis MLCT values.

Dye	1 <sup>st</sup> E <sub>ox</sub> (V)	1 <sup>st</sup> E <sub>red</sub> (V)	E <sub>ox.</sub> * (V)*	λ <sub>max</sub> (nm)ε(10 <sup>4</sup> )
<b>1</b> <sup>2+</sup>	+ 0.84	- 1.56	- 1.29	503 (3.5)
<b>2</b> <sup>2+</sup>	+ 0.87	- 1.52	- 1.14	509 (3.0)
<b>3</b> <sup>2+</sup>	+ 0.83	- 1.60	- 1.26	505 (3.6)
<b>4</b> <sup>2+</sup>	+ 0.89	- 1.56	- 1.22	495 (1.1)
<b>5</b> <sup>2+</sup>	+ 0.86	- 1.57	- 1.24	502 (4.0)
<b>6</b> <sup>2+</sup>	+ 0.84	- 1.55	- 1.26	504 (4.1)
<b>7</b> <sup>2+</sup>	+ 0.81	- 1.56	- 1.24	508 (3.4)
<b>8</b> <sup>2+</sup>	+ 0.81	- 1.61	- 1.22	501 (3.1)
<b>9</b> <sup>2+</sup>	+ 0.89	- 1.62	- 1.32	491 (3.0)
<b>10</b> <sup>2+</sup>	+ 0.87	- 1.58	- 1.22	491 (2.5)
<b>11</b> <sup>2+</sup>	+ 0.87	- 1.64	- 1.30	483 (1.2)
<b>12</b> <sup>2+</sup>	+0.89 (+ 0.19)	- 1.63	-**	491 (4.0)

\* E<sub>ox</sub>\* (V) = E<sub>ox</sub> (V) – E<sub>00</sub>; E<sub>0-0</sub> is estimated from the wavelength lying between λ<sub>max</sub><sup>abs.</sup> And λ<sub>max</sub><sup>em.</sup>.

\*\*No fluorescence from excited MLCT band.

In table 3.24 the measured values for the PV measurements (under illumination) are collected. In this table the absorbance values at the maximum MLCT peak that can be used to estimate the coverage of the dye are also collected. In the column furthest to the right is the ratio of the photocurrent density to the projected coverage absorption. This value allows us to compare the different dyes regardless of dye loading.

**Table 3.24** The photoelectric measurements for all the dyes are presented. The samples were measured in one batch and in control batches of 2-4 dyes. The electrolyte was *standard 2*.

Dye	J <sub>sc</sub> (mA/cm <sup>2</sup> )	V <sub>oc</sub> (V)	FF	η (%)	Abs. (AU)	Cov. (nmol/cm <sup>2</sup> )	J <sub>sc</sub> /Cov. mA/nmol
<b>1<sup>2+</sup></b>	0.97	0.45	0.64	0.28	1.70	49	0.020
<b>2<sup>2+</sup></b>	1.87	0.52	0.61	0.59	2.20	73	0.026
<b>3<sup>2+</sup></b>	1.77	0.50	0.65	0.58	2.50	63	0.028
<b>4<sup>2+</sup></b>	0.63	0.49	0.68	0.21	2.20	200	0.003
<b>5<sup>2+</sup></b>	1.00	0.56	0.66	0.38	0.55	18	0.056
<b>6<sup>2+</sup></b>	1.81	0.52	0.66	0.62	2.49	61	0.030
<b>7<sup>2+</sup></b>	1.20	0.53	0.66	0.42	1.65	43	0.028
<b>8<sup>2+</sup></b>	0.81	0.49	0.59	0.23	2.40	77	0.011
<b>9<sup>2+</sup></b>	0.76	0.53	0.68	0.27	0.44	15	0.051
<b>10<sup>2+</sup></b>	1.17	0.57	0.66	0.44	0.95	38	0.031
<b>11<sup>2+</sup></b>	1.44	0.52	0.67	0.50	2.31	192	0.008
<b>12<sup>2+</sup></b>	1.14	0.45	0.67	0.34	1.79	45	0.025
<b>N719</b>	12.64	0.74	0.55	5.18	1.43	110	0.115

From table 3.24, the influence from the counter ligand on electron injection ability and adsorption is noticeable. For example, ligand **3** gives the dye a higher extinction coefficient but at the same time offsets the electron injection, which will be less directed towards the anchoring group.

**Comparing dyes with anchoring ligand 5 (thienyl spacer, table 3.24)**

Comparing dyes **2<sup>2+</sup>**, **5<sup>2+</sup>** and **10<sup>2+</sup>** (all having the anchoring ligand 5), the effect of extending the 4'-substituted 2,2':6',2''-terpyridines can be monitored. To start with, the dye loadings vary with dye **5<sup>2+</sup>** (monothienyl) having a very low loading (14 nmol/cm<sup>2</sup>), dye **2<sup>2+</sup>** (bithienyl) having a higher (73 nmol/cm<sup>2</sup>) and dye **10<sup>2+</sup>** an intermediate value (38 nmol/cm<sup>2</sup>). Dye **3<sup>2+</sup>** gives a similar performance to **2<sup>2+</sup>**. The monothienyl group seems to enhance the performance compared to the unsubstituted 2,2':6',2''-terpyridine while the bithienyl group reduces the photocurrent density per dye molecule. The conclusion here is that the thienyl substituents on the counter ligand increase the extinction coefficients of the MLCT transition but they also direct the excited state LUMO away from the anchoring ligand, which decreases the

injection rate.<sup>[9]</sup> The bithienyl group does this to a greater extent than the monothienyl.

#### ***Comparing dyes with anchoring ligand 4 (phenyl spacer, table 3.24)***

The dyes with anchoring ligand 4 give high surface coverage when the counter ligand is the unsubstituted 2,2':6',2''-terpyridine (208 nmol/cm<sup>2</sup>) or the 4'-thienyl-2,2':6',2''-terpyridine (159 nmol/cm<sup>2</sup>). Interestingly the bithienyl counter ligand yields lower coverage (49 nmol/cm<sup>2</sup>) but much higher photocurrent density. The dyes **4**<sup>2+</sup> and **11**<sup>2+</sup> have low photo-current per projected cm<sup>2</sup> per mole coverage at 0.003 and 0.008 mA/nmol while dye **1**<sup>2+</sup> has a three times higher photo-current per projected cm<sup>2</sup> per mole coverage at 0.020 mA/nmol. This result contradicts the measurements of dyes with anchoring ligand **5** above. No obvious explanation for this was found. As has been reported, the photocurrent is higher (>2 times) for the complex with an unsubstituted terpyridine than for the complex with a thienyl-substituted terpyridine on the counter ligand position.<sup>[9]</sup> This is explained by the LUMO being more localised on the counter ligand and away from the TiO<sub>2</sub> when there is a thienyl group on it. The plots in figure 3.70 support this explanation.

#### ***Dye coverage***

The relationship between the photocurrent density and the surface coverage of a dye in a DNSC, can give information on possible aggregation of the dye molecules, which would lead to lower efficiencies.<sup>[82]</sup> If a monolayer were growing proportionally with the amount of dye loading, the photocurrent density would do the same. If there were aggregation of the dye molecules, that is dye molecules aggregating with other dye molecules instead of adsorbing to the surface with the carboxylic acid groups, the photocurrent density will increase with a lower rate than the coverage. This may also be the case if the charge transport through the electrolyte or TiO<sub>2</sub> is hindered. It has been reported, that above a certain coverage the conversion efficiency of the dye N3 improves drastically.<sup>[83]</sup> It is suggested that this may be due to hole (positive charge) percolation between the dye molecules that improves charge separation. Two possible explanations for the efficiency increase at higher coverages follow.

1. At a critical coverage (around 50%) the molecules are close enough to transport holes between them that prolong the charge separation. Grätzel et al. came



to the same conclusion when studying charge percolation through dye sensitized TiO<sub>2</sub> electrodes with cyclic voltammograms in a three electrode setup.<sup>[69]</sup>

2. At high coverage the dye molecules may act as barriers towards recombination reactions between electrons in the TiO<sub>2</sub> conduction band and triiodide in the electrolyte, and therefore prevent dark current.<sup>[84]</sup>

It should be kept in mind that at a certain point higher surface coverage might not be important for the magnitude of photocurrent. This is due to that it is thought that only one or two electrons are injected per TiO<sub>2</sub> particle at any time. More important may be the light harvesting efficiency ( $LHE=1-10^{1-A}$ ) that takes into account the percentage of the incident light that is absorbed. When the light harvesting efficiency is higher than 99% ( $Abs = 2.0$ ) differences in absorbance does not matter as much. In the case of the dyes in this work, surface coverage appeared to have an influence even at the higher coverages.

As was described in chapter 2, the dye solutions for the measurements in table 3.21 had concentrations between 0.7 and 1 mM. The solvent used was CH<sub>3</sub>CN as it dissolves all the dyes although some of the dyes with thiophene groups needed some CH<sub>3</sub>OH added for complete dissolution. The extent of adsorption from different concentrations was measured as well as what affect the coverage had on PV performance for some of the dyes.

In figure 3.71 the surface coverage is plotted against concentration of the solutions for dyes **4**<sup>2+</sup>, **5**<sup>2+</sup>, **10**<sup>2+</sup> and **11**<sup>2+</sup>. These plots give an indication of binding strength.<sup>[83]</sup> The dyes **11**<sup>2+</sup> and **4**<sup>2+</sup> (both have anchoring ligand **4**) show higher adsorption strength (~4 times the coverage) than those with anchor ligand **5**. The difference may also be due to different footprint areas. While the dyes with anchor ligand **4** (phenyl spacer) have no angle between the ruthenium centre and the carboxylic group, those with ligand **5** (thienyl spacer) have an angle of about 18° (from crystal structure in section 3.2.6). This may increase the footprint area 3-6 times depending on whether the rotation around the bond to the carboxylic group is included. This could account for the ~4 times higher surface coverage of dyes with **4** as anchor ligand. In solutions of 0.5 mM all of the dyes more or less reach a saturated adsorption. The linear increase of photocurrent with projected surface coverage in figure 3.72 of dyes **10**<sup>2+</sup> and **11**<sup>2+</sup> suggest that there is no aggregation. Dyes **4**<sup>2+</sup> and **5**<sup>2+</sup> have a different behaviour and

have a very steep improvement in photocurrent and then reach a plateau of maximum photocurrent at much lower coverage than dyes  $10^{2+}$  and  $11^{2+}$ .

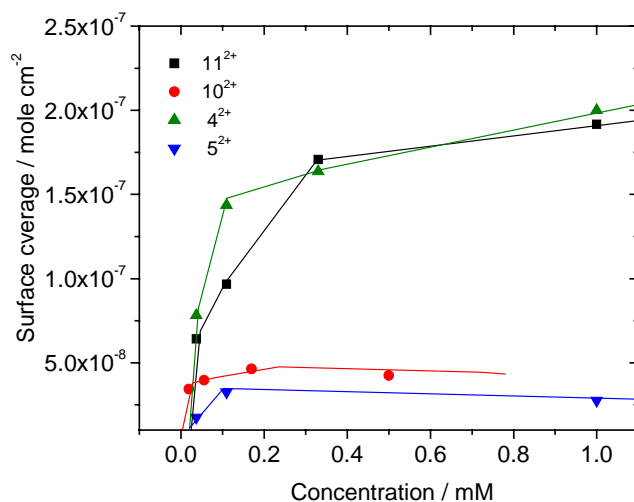


**Figure 3.71** Plots of solution concentration versus the adsorbed amount of dye.

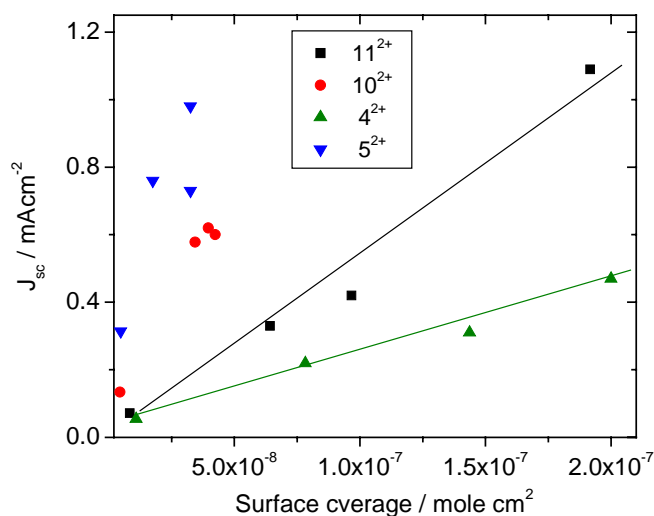


**Figure 3.72** The short circuit photocurrent densities are related to their projected surface areas.

### ***Comparing coverage of the three anchor-ligands***

In figure 3.73 the adsorption of dyes  $4^{2+}$ ,  $5^{2+}$  and  $6^{2+}$  as a function of the concentrations of the solutions used for sensitization are plotted. Anchor-ligands **5** and **6** lead to lower coverages than the dye with anchor-ligand **4**. The dyes reach adsorption maximums in solutions with concentrations of about 0.4 mM. The three dyes in figure 3.73 have ligand **1** as counter ligand.

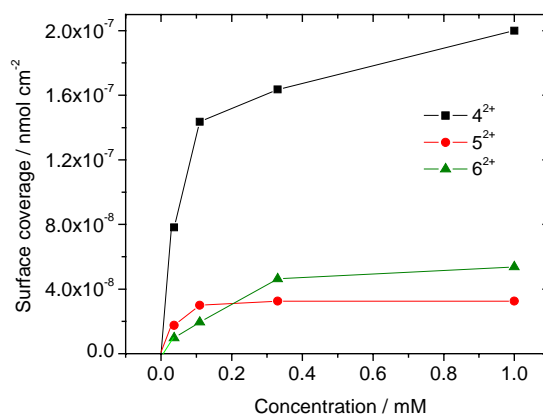


**Figure 3.73** Adsorption of three dyes with anchorligands having different spacers. The phenyl spacer is in squares, the thienyl spacer in circles and the diethoxythienyl spacer in triangles.

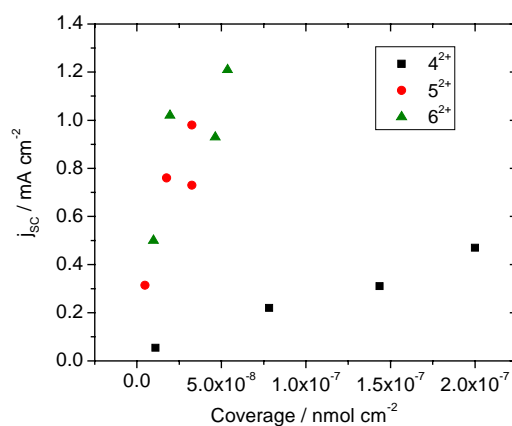


**Figure 3.74** Dye coverages plotted against short circuit current. The thienyl spacer is marked with circles, the diethoxy-thienyl with triangles and the phenyl with squares. All three dyes have 1 as counter ligand.

Figure 3.74 shows that the photocurrents with anchoring ligands **5** and **6** are similar and both higher than that of the dye with **4** as anchorligand. **4**<sup>2+</sup> has a close to linear increase in photo-current with coverage, but **5**<sup>2+</sup> and **6**<sup>2+</sup> have more irregular changes in photo-current at coverages of above 20 nmole cm<sup>-2</sup>. This may be aggregation that ligands **5** and **6** perhaps promote. The higher photocurrents for complexes with **5** and **6** indicate that they perform better than complexes with **4** when adsorbed in the same fashion.

**Comparing dyes with 2 (tpyEDOT) as counter ligand**

The dyes with **2** as counter ligand do not have an increase in photocurrent when the coverage reaches a certain point. In figure 3.75 this trend is plotted. The ligand may be causing aggregation between dye molecules so that at higher concentrations the ligands interact. The crystal structures in section 3.2 suggests some interaction between the EDOT groups of  $[\text{Fe}(\mathbf{2})_2]^{2+}$  ions in crystal form, which may be similar to any eventual interaction on the  $\text{TiO}_2$  surface. As is seen in figure 3.75 the dyes with anchoring ligands **4** ( $8^{2+}$ ) and **5** ( $3^{2+}$ ) give very similar plots with photocurrents that start to decrease at higher coverages.

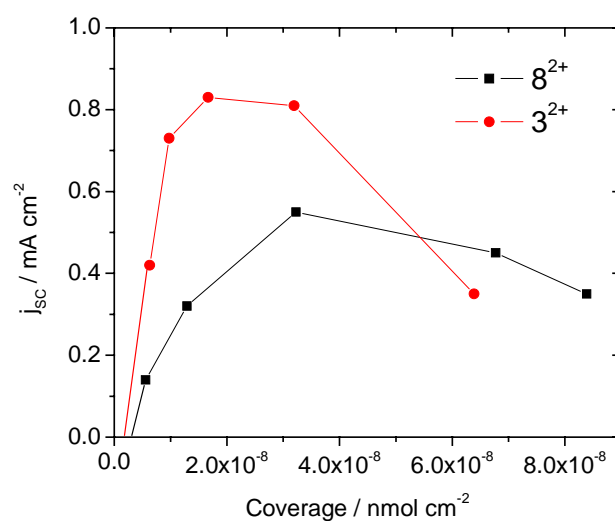


**Figure 3.75** The projected surface coverage in mole/cm<sup>2</sup> is plotted against the projected surface coverage. The squares are dye  $8^{2+}$  and the circles dye  $3^{2+}$ .

*Comparing the influence of coverage for dyes  $2^{2+}$  and  $10^{2+}$*

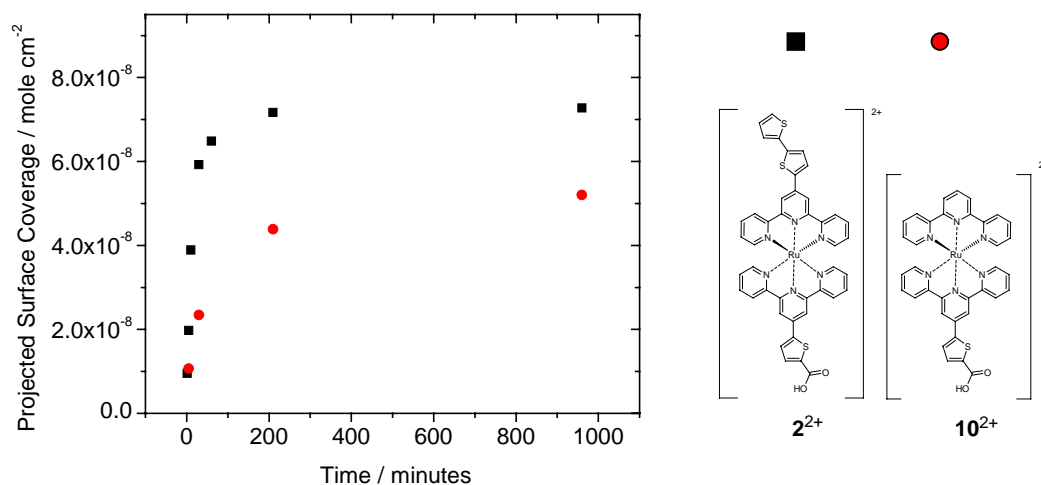


**Figure 3.76** The projected surface coverage in mole/cm<sup>2</sup> is plotted against the adsorption time. The squares are dye  $2^{2+}$  and the circles dye  $10^{2+}$ . Both are 0.8 mM MeCN solutions.

In figure 3.76 the adsorption of dyes  $2^{2+}$  and  $10^{2+}$  are plotted with time. As can be seen, dye  $2^{2+}$  has about 25% higher coverage when the adsorptions have reached saturation. The dye sensitized TiO<sub>2</sub> films were incorporated in DNSC and measured under illumination of 100 mWcm<sup>-2</sup>. While dye  $10^{2+}$  has a linear increase of photocurrent with increasing coverage, dye  $2^{2+}$  has a much lower increase in photocurrent with increasing coverage for the films sensitized up to 4 hours, but the film that was sensitized overnight shows a large improvement (figure 3.77) despite negligible increase in coverage. Leaving the films for longer periods of two nights only resulted in lower photo-currents.

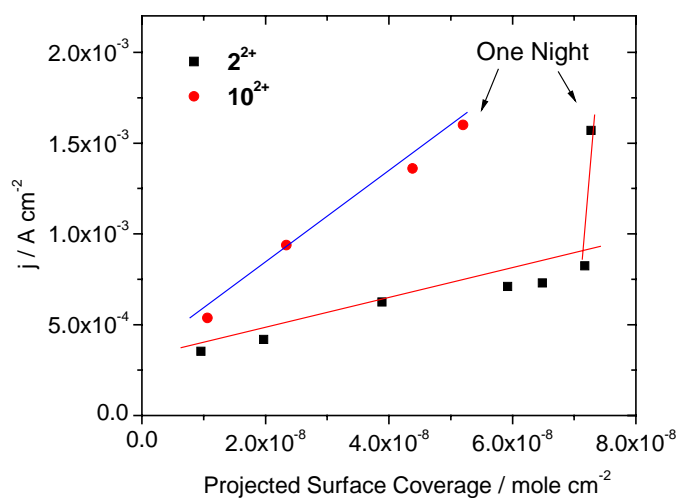


**Figure 3.77** The measured photocurrent densities are plotted against the surface coverage's. The circles represent dye  $2^{2+}$  and the squares dye  $10^{2+}$ .

Figure 3.77 suggests that dye  $2^{2+}$  molecules are ordering themselves on the surface during the time they are in the solution. The time of adsorption seemed to have an effect on the bi-thienyl substituted terpyridine and a jump in efficiency is recorded for the films that were in solution ( $2^{2+}$ ) overnight despite the apparent surface coverage essentially staying the same. The longer time in solution may result in some reordering of the dye molecules on the surface. In a recent experiment, Schwanz *et al.* measured coadsorption of acetonitrile molecules with N3 dye molecules on nc-TiO<sub>2</sub> by SXPS (soft X-ray induced photoelectron spectroscopy) and found that the adsorbed solvent quenches surface states that may form recombination paths and deduced a model where the acetonitrile molecules interact with the dye and insulate them from each other and from the substrate by solvation.<sup>[85]</sup> As the authors discussed, this helps directing the counter ligand away from the surface and out towards the electrolyte, which may improve the photovoltaic performance.

#### ***Dyes without carboxylate groups***

The ruthenium complexes  $[\text{Ru}(\text{tpy})_2][\text{PF}_6]_2$  and  $[(\text{tpy})\text{Ru}(\mathbf{3})][\text{PF}_6]_2$  appear to adsorb to the TiO<sub>2</sub> surface when TiO<sub>2</sub> films are immersed in 1 mM solutions of the complexes for 14 hours. The TiO<sub>2</sub> films are coloured after rinsing and show some electron injection when measured in DNSC. Table 3.25 lists the results together with some values from table 3.24 as reference. The two complexes without carboxylic acids

show reasonable performances considering their low coverage. The complex  $[(\text{tpy})\text{Ru}(\mathbf{3})]^{2+}$  is as good as  $\mathbf{11}^{2+}$  when considering the current per mole of dye. This suggests that the acid with a phenyl spacer may be increasing adsorption but much of the electron injection may not be directly through the carboxylic acid.

**Table 3.25** Photoelectric measurements of ruthenium dyes without acid groups. Three other dyes from table 3.24 are added as comparison.

Dye	J <sub>sc</sub> (mA/cm <sup>2</sup> )	V <sub>oc</sub> (V)	η (%)	Absorbance at λ <sub>max</sub> <sup>TiO</sup>	Coverage nmole/cm <sup>2</sup>	J <sub>sc</sub> /Cov. mA/nmol
[Ru(tpy) <sub>2</sub> ] <sup>2+</sup>	0.30	0.39	0.07	0.80	67	0.004
[(tpy)Ru( <b>3</b> )] <sup>2+</sup>	0.24	0.42	0.06	0.55	23*	0.010
<b>10</b> <sup>2+</sup>	1.17	0.57	0.44	0.95	38	0.031
<b>11</b> <sup>2+</sup>	1.44	0.52	0.50	2.31	192	0.008
<b>1</b> <sup>2+</sup>	0.97	0.45	0.28	1.70	49	0.020

\*ε = 2.4 x 10<sup>4</sup> M<sup>-1</sup>cm<sup>-1</sup> for [(tpy)Ru(**3**)]PF<sub>6</sub>]<sub>2</sub>.<sup>ref</sup>

#### Additive in electrolyte

Adding 1-Methylbenzimidazole (MBI) to the electrolyte is known to raise the conduction band edge of the TiO<sub>2</sub> to give better energy matching with dyes such as N719.<sup>[73]</sup> This usually increases the photo-voltage and FF without decreasing the photocurrent. The excited state oxidation potential of N719 and similar dyes is around -1.41 V (vs Fc/Fc<sup>+</sup>) while for the ruthenium complexes **1**<sup>2+</sup>-**12**<sup>2+</sup> they are roughly between -1.20 and -1.30. This is often quoted as the potential of the excited electrons that will inject into the TiO<sub>2</sub>. It is therefore important with a potential negative enough to be above the conduction band of the TiO<sub>2</sub> (~-1.1 V vs Fc/Fc<sup>+</sup> in MeCN).

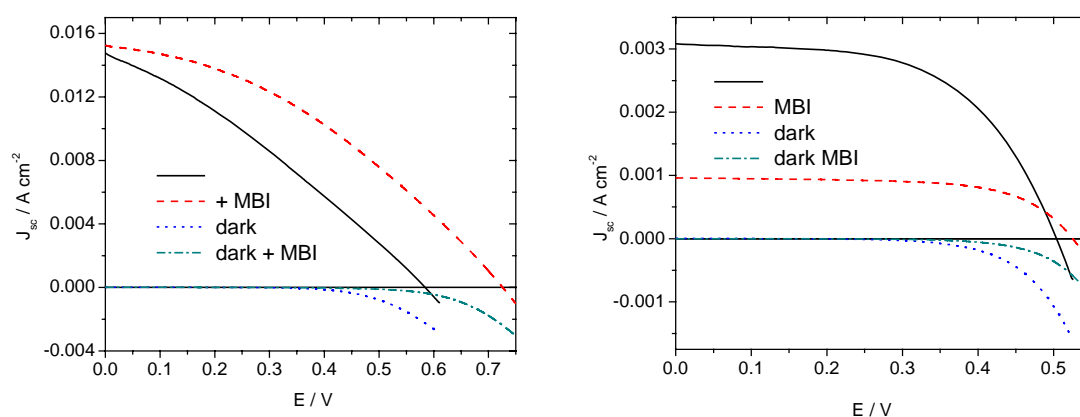


**Figure 3.78** I-V curves of N719 (left) and for **5**<sup>2+</sup> (right) under illumination and in dark.

Dyes  $5^{2+}$ ,  $12^{2+}$  and N719 were measured in electrolyte (*Standard 1*) with and without MBI additive. In figure 3.78 the short circuit current ( $J_{sc}$ ) for N719 remains much the same while the open circuit voltage increases a little. In the left box of figure 3.78, the same measurements on  $5^{2+}$  give a large difference in  $J_{sc}$  with the addition of MBI decreasing the current substantially. The result with  $12^{2+}$  was similar. The difference is attributed to the difference in the potential of the conduction band. A higher conduction band (more negative) will hinder the injection from  $5^{2+}$  while the injection from N719 will not be affected. The dark currents (figure 3.78) support this conclusion with an onset at a more positive potential for the electrolyte with MBI. The composition of electrolyte *standard 2* (see chapter 2), which is mainly used in this work, appears to have an intermediate affect on the efficiencies of complexes  $1^{2+}$ - $12^{2+}$  with photocurrents between those in figure 3.78 (right-hand side).

### **Conclusion**

The photovoltaic performances of the dye molecules were in general about one order of magnitude lower than for N719. The main points of N719 compared to  $1^{2+}$ - $12^{2+}$  are: bipyridine ligands instead of terpyridine, two carboxylic acid groups for better attachment to the  $TiO_2$  surface and two electron-donating thiocyanate ligands.

The properties of both the anchoring ligand and the opposing ligands for the electron injection has been found to be very important for complexes  $1^{2+}$ - $12^{2+}$  in this work. This is evident from comparing the different bis-terpyridine dyes (scheme 3.10). Generally a lower lying LUMO of the counter ligand, will result in less electrons being directed towards the  $TiO_2$  surface while a lower lying LUMO of the anchoring ligand will promote electron injection.



### 3.5.3 Four-Electrode PECM Measurements

The basic theory on the photo-electrochemical microscopy (PECM) and the experimental details on the set-up were discussed earlier in chapter 1 and 2 respectively. The application of the SECM to the dye-sensitized solar cell (DSSC) was tested with two of the ruthenium dyes ( $2^{2+}$  and  $10^{2+}$ ) and the commercially available ruthenium dye N719. The potentials of the FTO glass support of the  $\text{TiO}_2$  and the UME-tip could both be addressed by the bipotentiostat used. In figure 3.78 the response to illumination of N719 sensitised  $\text{TiO}_2$  in an electrolyte containing either ferrocene or the  $\text{I}_3^-/\text{I}^-$  redox couple in 0.5 M concentrations are shown.

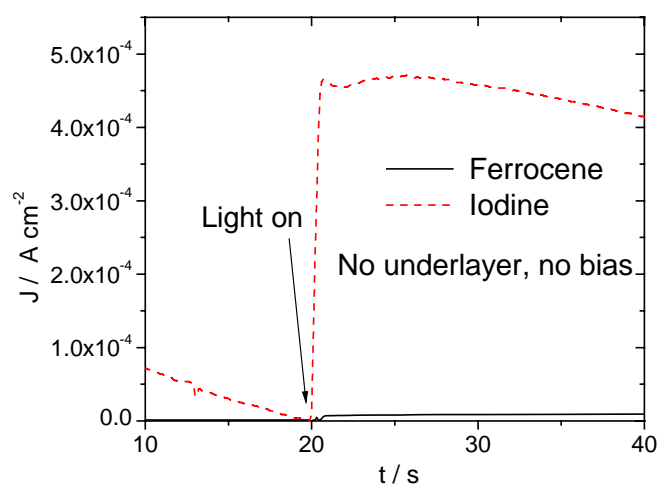


**Figure 3.79** Cathodic current at UME tip when  $-0.5$  V potential is applied in electrolytes of ferrocene or  $\text{I}^-/\text{I}_3^-$ . The measurements were made with no under-layer and no bias potential.

#### Electrolyte

As is seen in figure 3.79 the  $\text{I}^-/\text{I}_3^-$  is more efficient than the ferrocene in a PECM experiment. As expected, the iodine/iodide has a far better performance than ferrocene/ferrocinium as a redox couple for regenerating the oxidised dye.<sup>[86]</sup> The main advantage of the iodide electrolyte is assumed to be the slow kinetics for  $\text{I}_2$  reduction at  $\text{SnO}_2$  and  $\text{TiO}_2$  surfaces.<sup>[87]</sup> This prevents the back reaction of injected electrons with iodide under working conditions and make the cells function efficiently. The ferrocene however is easily reduced at  $\text{SnO}_2$  and  $\text{TiO}_2$ .

## Ferrocene

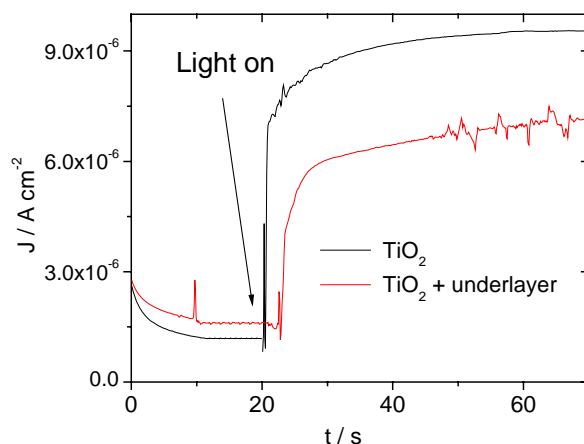


**Figure 3.80** PECM measurement of ferrocene over an N719 sensitised  $\text{TiO}_2$  film with (red line) and without (black line) a compact  $\text{TiO}_2$  underlayer.

In figure 3.80 the difference of a compact under-layer when ferrocene is the redox mediator is small and actually decreases the current. The reduction of ferrocene is expected to happen mostly at the  $\text{TiO}_2$  and not at the FTO surface.

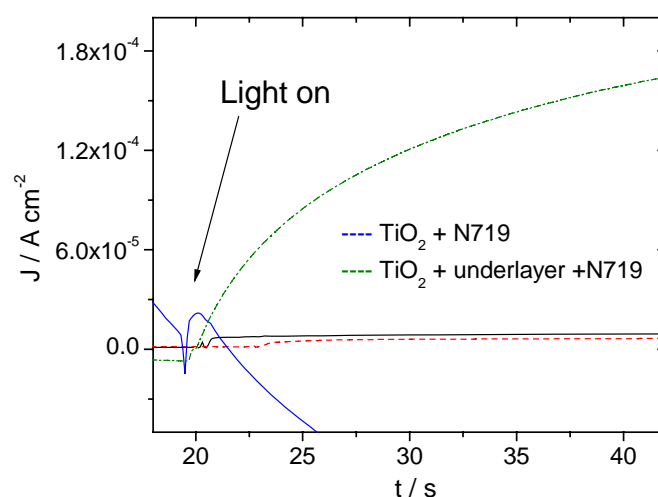


**Figure 3.81** UME tip response over N719 sensitised  $\text{TiO}_2$  with a  $-0.4$  V bias potential applied, in an electrolyte of ferrocene. The dashed line shows the photocurrent when a compact under-layer is present. The solid line is the response when no under-layer is present. The smaller solid and dashed lines show the magnitude of the currents from figure 3.69 (no bias-potential).

The applied bias potential improves the electron injection by acting as a sink for the electrons. In working conditions of the solar cell, a concentration gradient of electrons

is believed to drive electrons towards the anode.<sup>[88]</sup> Applying a negative potential to the anode and thereby depleting the  $\text{TiO}_2$  closest to the anode of electrons should amplify the concentration gradient. In the case of ferrocene, the photocurrent is increased only when a compact under-layer (as described in chapter 2) is present, in the other case the negative potential of the FTO glass in contact with the electrolyte is enough to reduce the oxidised ferrocene. In figure 3.81 the plots of this data are presented.

### Iodide / tri-Iodide

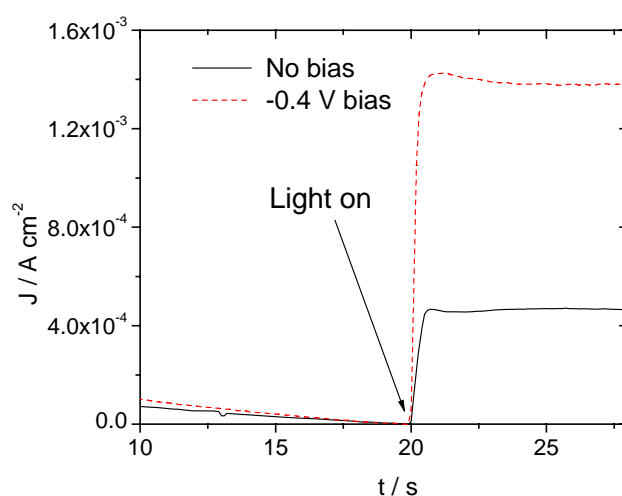


**Figure 3.82** UME tip response over N719 sensitised  $\text{TiO}_2$  with and without a  $-0.4$  V bias in an electrolyte with the  $\text{I}_3^-/\text{I}^-$  couple.

In figure 3.82 the UME tip current is measured in an electrolyte with the  $\text{I}^-/\text{I}_3^-$  redox couple when illuminated. The  $\text{I}_3^-$  ions do not get reduced by the bias potential at the FTO glass and can be re-reduced at the UME tip and result in a photocurrent even when there is no under-layer. The applied voltage bias results in an improved electron yield as can be seen in figure 3.82. With the applied potential working as an electron sink, the photo-generated conduction band electrons can be drained and avoid recombining with  $\text{I}_3^-$  at the  $\text{TiO}_2$ / electrolyte interface.

### Evaluating dyes for the DNSC with PECM

In chapter 2 the PECM set-up was discussed and the potential to use it to study the photo-electrochemical system of the DNSC. The measurement can be done in a three-

electrode configuration, but using 4-electrodes has the advantage of controlling the potential of both the FTO substrate and the UME tip. The photocurrent that the UME tip probes (defined in chapter 2) can be used to evaluate the electron injection efficiency of the particular dye. In Figure 3.83 three dyes are compared;  $1^{2+}$ ,  $2^{2+}$  and N719, with the PECM method. The steady state current density for the reduction of  $I_3^-$  to  $I^-$  at the UME is probed in the dark and with illumination (1 sun). The magnitudes of the photo current densities are comparable to those measured in solar cells of  $0.45\text{cm}^2$  size. The conditions in figure 3.83 are somewhere between open circuit voltage and short-circuit current with the difference in the applied potentials of the two electrodes smaller than for the open circuit conditions. The maximum photocurrents obtainable were used for the plot.

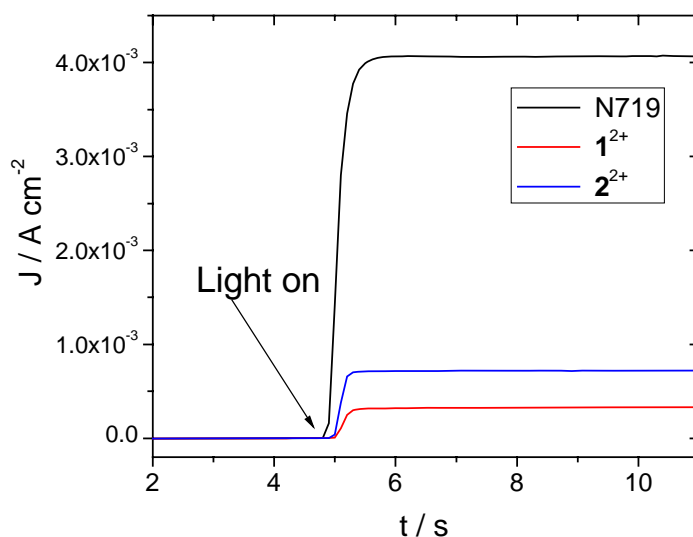


**Figure 3.83** Steady-state currents at 25  $\mu\text{m}$  diameter Pt UME over dye sensitized  $\text{TiO}_2$  in 3-MPN with  $I^-/I_3^-$  as redox mediator. Upon illumination the photocurrents can be measured. The applied potentials are  $-0.3\text{ V}$  for  $\text{TiO}_2$  substrate and  $-0.1\text{ V}$  for the UME tip (vs.  $\text{Fc}/\text{Fc}^+$ ). The positions of the currents have been normalized for easier comparison.

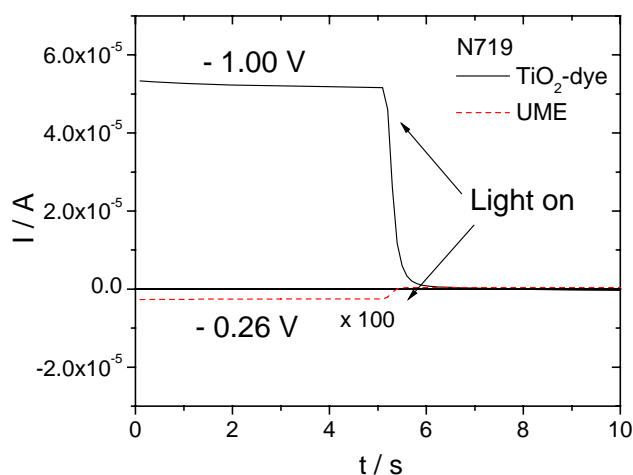


**Figure 3.84** The steady-state currents of the UME tip (dashed) and the FTO glass substrate (solid) in the dark and upon illumination for N719 dye. The potentials of the electrodes are included (vs. Ag/AgNO<sub>3</sub>). The UME current is magnified 100 times.

In figures 3.84 and 3.85 the steady-state currents of the UME-tip above TiO<sub>2</sub> sensitised with dyes  $2^{2+}$  (3.84) and N719 (3.85) are shown together with the currents from the TiO<sub>2</sub> substrate when the potentials applied to the electrodes result in zero photocurrent (current when illuminated) at the respective electrodes. This represents open circuit conditions with the electron injection and back reactions cancelling each other out and no net current flows.

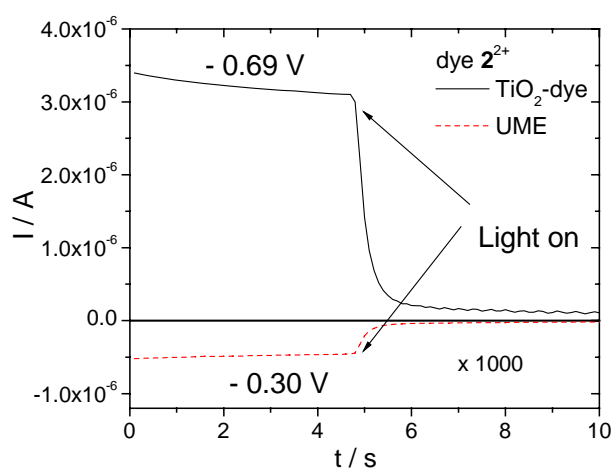


**Figure 3.85** The steady-state currents of the UME tip (dashed) and the FTO glass substrate (solid) in the dark and upon illumination for dye  $2^{2+}$ . The potentials of the electrodes are included (vs. Ag/AgNO<sub>3</sub>). The UME current is magnified 1000 times.

The open-circuit voltage of a dye-sensitised solar cell has been calculated as the difference of the potentials of the anode and the cathode (see chapter 2) in the PECM measurements. These potential differences are compared to the measured  $V_{oc}$  in complete solar cells in table 3.26 for dyes  $1^{2+}$ ,  $2^{2+}$  and N719. The SECM measurements show the same trends as the solar cell tests but the ratios between the dyes are not the same. The differences in  $V_{oc}$  for the dyes are consistent but with higher potentials for the complete cells by 60-90 mV. The photocurrent densities at the UME are also consistent, although the current density for N719 sensitised  $TiO_2$  is 7.3 times higher in a complete DNSC while for dyes  $1^{2+}$  and  $2^{2+}$  it is 4.4 and 3.4 times higher respectively.

**Table 3.26** The various values from PECM and solar cell measurements in one table.

Dye	PECM $V_{oc}$ (V)	Cell $V_{oc}$ (V)	$\Delta V_{oc}$ (V)	$J_{UME}$ ( $mA/cm^2$ )	$I_{TiO_2}$ (A)	$J_{sc(cell)}$ ( $mA/cm$ )	$\eta$ (%)
$1^{2+}$	0.26	0.35	0.09	0.13	$1.56 \times 10^{-6}$	0.57	0.12
$2^{2+}$	0.36	0.42	0.06	0.38	$2.01 \times 10^{-6}$	1.29	0.26
N719	0.69	0.76	0.07	1.73	$3.55 \times 10^{-5}$	12.70	5.10

In figure 3.86, the difference between N719 and  $2^{2+}$  when measured by the PECM technique is presented. The absolute currents at the UME for different bias potentials are plotted in figure 3.86. The relative photocurrent ( $\Delta I = I_{light} - I_{dark}$ ) of the N719 sensitised  $TiO_2$  is higher than that of  $2^{2+}$ . The potential of zero photocurrent is shifted more to the positive in the case of N719.

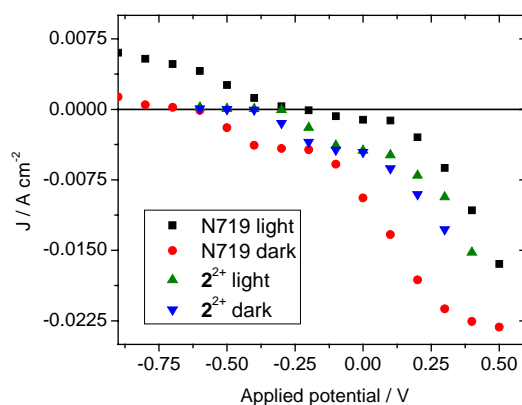


**Figure 3.86** The absolute current of the UME at different potentials for N719 and  $2^{2+}$  in the dark and under illumination.

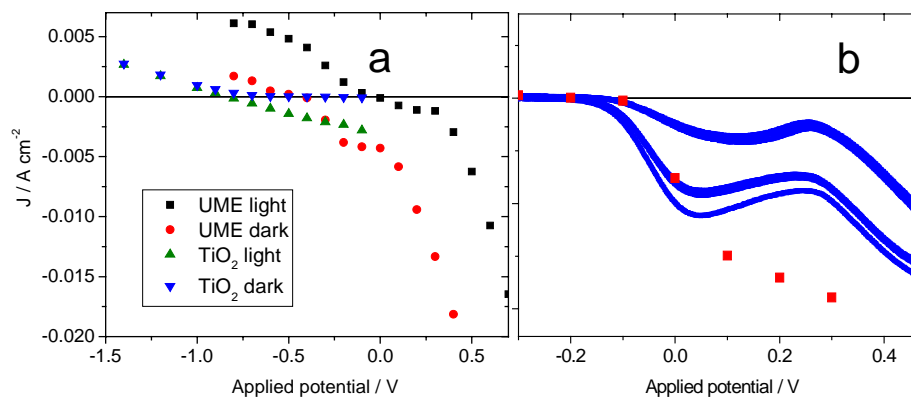


**Figure 3.87** (a) The absolute current in the dark and in illumination, of the UME and  $\text{TiO}_2$  substrate with different potentials being applied. (b) Comparison of the UME current with a superimposed CV of  $\text{I}_2$  and  $\text{I}^-$  in solution (solid line plot).

In figure 3.87a the absolute photocurrents and dark-currents (See chapter 2 for definitions) of the UME and  $\text{TiO}_2$  substrate are plotted against the applied potentials of the respective electrodes (while the applied potential is changed, the opposing electrode is held fixed at the potential where the absolute photocurrent is 0). The values come from measurements like those in figure 3.84 and 3.85. In figure 3.87b the CV of  $\text{I}_2$  with an iodide salt is plotted together with the absolute photocurrent of the UME. The current voltage plot follows the CV of the  $\text{I}_2/\text{I}^-$  at the first oxidation peak. The relative currents are plotted in figure 3.88. The UME current is increased the most close to the redox potential of the  $\text{I}^-/\text{I}_3^-$  redox couple.

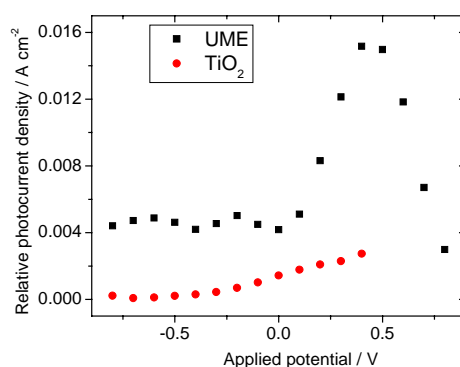


**Figure 3.88** The relative currents of the UME (squares) and  $\text{TiO}_2$  (circles) at different potentials for N719 on  $\text{TiO}_2$ .

The values in table 3.23 were obtained by measuring the steady state current at fixed potentials in the dark and under illumination but can also be obtained by cyclic voltammetry. This makes the analysis faster (no need to measure the potential one value at a time). The draw back is that it is difficult to get the steady state current when the voltage is scanned because of non-faradic currents (see section 2.2). In figure 3.89a and b, the forward and backward sweeps are slightly different, which makes it difficult to pinpoint the zero current points (arrows in figure 3.89b). A lower scan rate should further improve the accuracy. For the substrate with TiO<sub>2</sub> the difference is even larger due to a large undefined electrode area.

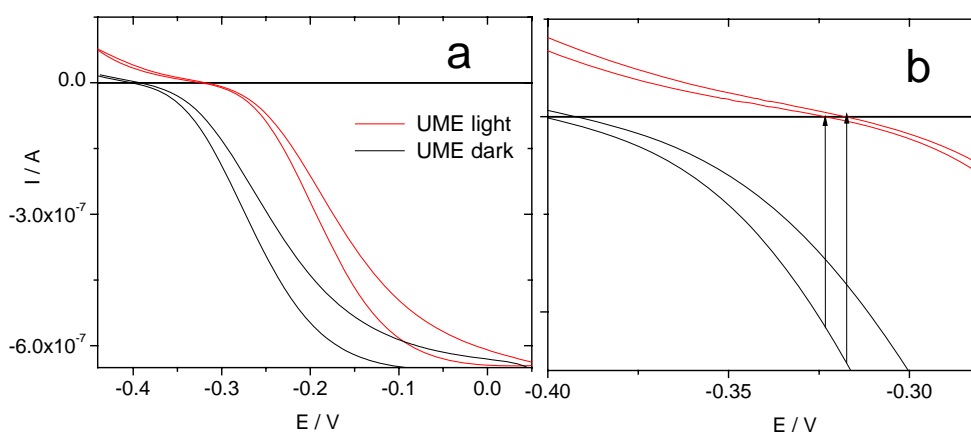


**Figure 3.89** (a) CV at 50 mVs<sup>-1</sup> of UME (TiO<sub>2</sub> fixed at open circuit potential) in the light and in the dark. (b) Close-up of the CV where the open-circuit voltage is located.

### Electrolyte additive

The four-electrode system can be used to probe both electrodes independently against a fourth reference electrode. The additive MBI is used in the electrolyte to increase the photovoltage. It is believed that while the counter electrode has a “pinned” potential that the redox couple in the electrolyte determines, the TiO<sub>2</sub> conduction band (CB) has a potential that changes with surface adsorbates.<sup>[89]</sup> The MBI increases the energy level of the CB when adsorbed to the surface and the  $V_{oc}$  of the entire cell is increased. The PECM measurement was performed on **N719** sensitised TiO<sub>2</sub> in electrolytes with I<sub>3</sub><sup>-</sup>/I<sup>-</sup> and with and without MBI (0.5 M). The measurement with MBI showed open circuit conditions for the electrode with TiO<sub>2</sub> to be -100 mV lower than without, while the counter electrode had an unchanged value. The same difference in



$V_{oc}$  was found for complete solar cells. This supports the idea of the  $TiO_2$  CB being shifted by the MBI additive.<sup>[90]</sup>

### SPECM (Scanning Photo-Electro-Chemical Microscopy)

With the SECM equipment there is the possibility to obtain a scanned image where a surface is probed. This could be a rapid method of evaluating a series of dyes. In figure 3.90 this concept was tested for an illuminated N719 sensitised  $TiO_2$  film. The scan was made at a resolution of  $50 \mu m$  and the current measured for 17 ms. Fine-tuning the parameters did not improve the image. For higher resolution many technical improvements need to be made, such as better shielding against electric noise.

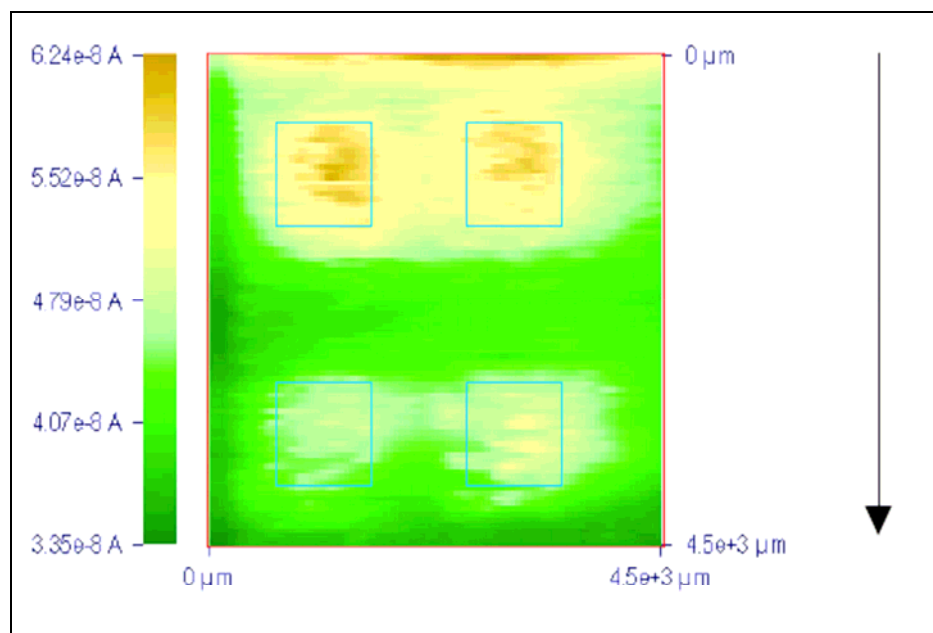


**Figure 3.90** Scanning electrochemical voltammogram over  $0.45 \times 0.45 \text{ mm}$  area of 4 small  $TiO_2$  squares sensitised with N719. The blue rectangles outline the dye sensitised  $TiO_2$  squares. The arrow marks the direction of the sweep.

The current measurement for every position is carried out on a short time span ( $\sim 17 \text{ ms}$ ) in order that the oxidised redox mediator from the surrounding surface has a minimum influence (diffusion layer increases with time; eq.6). While scanning the surface there is a gradient in the current. Because there is a distance dependent current when the UME tip is within a few radii of the surface, this may be due to a slightly tilted surface.<sup>[91]</sup> A second measurement in the dark can be performed to obtain a reference that can be subtracted from the illuminated sample. In figure 3.91 the 3-D

plots of the scan in the light (a) and (b) in the dark. It should be noted that the peak currents, after subtraction of dark current, of the four spots are reasonably equal ( $\sim\pm 10\%$ ) and can be compared.

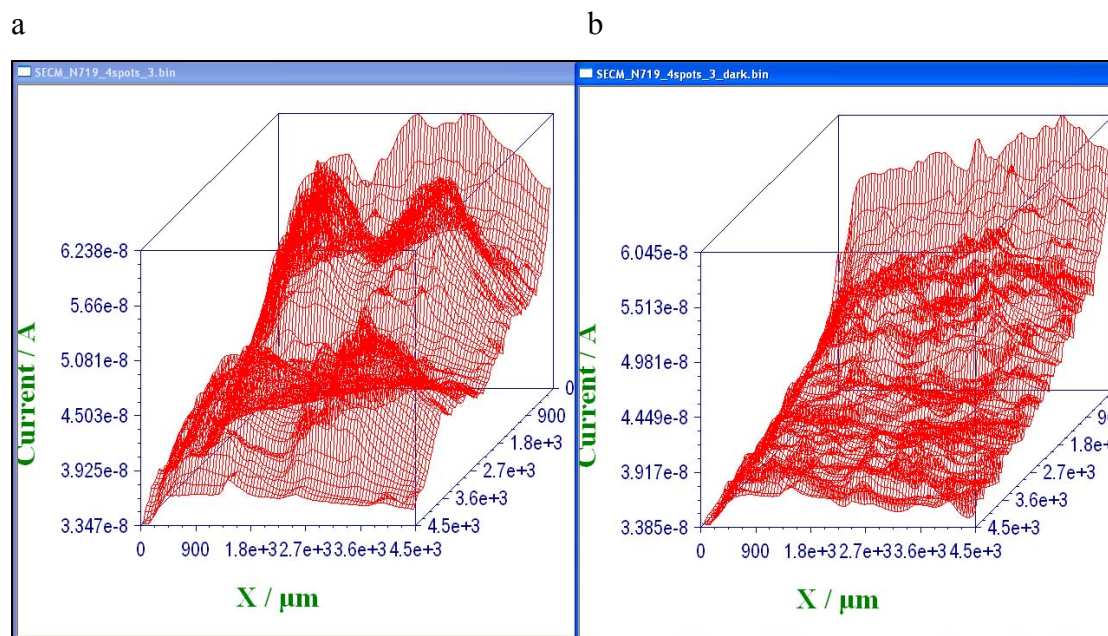


**Figure 3.91** PECM images of a scanned surface with four  $\text{TiO}_2$  spots sensitised with N719. The surface under illumination is presented in (a) and in the dark in (b).

### Conclusion of PECM measurements

The viability of the PECM technique as a tool to investigate the surface photo-electrochemistry of FTO electrodes with mesoscopic  $\text{TiO}_2$  sensitised with dyes (as used in a DNSC) was proven by PECM measurements on dye sensitised substrates that were compared to measurements of complete solar cells with the respective dyes. The results show that PECM measurements are sufficient to probe the photovoltaic properties of the surface. With the scan mode (SPECM) it may be possible to develop a high-speed screening of several dyes on one substrate. There are however difficulties in making arrays of small equal  $\text{TiO}_2$  spots each sensitised with a different dye. The baths of dye need to be large enough to ensure that the bulk concentrations do not decrease too much. This would otherwise lead to incomplete adsorption.

It was also shown that it is possible to control the potentials of both the electrodes with a separate reference electrode under working conditions.

### Electrochemically-polymerised complexes in DNSC

In section 3.2 the polymerisation of the ruthenium complexes was discussed. Experiments were carried out to test the polymer films in dye-sensitised solar cells. TiO<sub>2</sub> films on FTO glass were contacted and immersed in 1 mM CH<sub>2</sub>Cl<sub>2</sub> solution of [Ru(2)<sub>2</sub>][PF<sub>6</sub>]<sub>2</sub> (and 0.1 M LiClO<sub>4</sub>) together with a reference electrode (Ag/AgNO<sub>3</sub>) and an auxiliary electrode (Pt). A positive potential was applied at about 200 mV more positive than the oxidation peak of the complex for different amounts of time. In figure 3.92 the UV-vis spectra of the deposition for different times are plotted. Above 120 seconds the absorbance does not really change and appears to be saturated. The polymeric films have an absorbance peak where the MLCT band is located and a band further into the longer wavelengths, which may be an LMCT band due to Ru<sup>+3</sup>. As is noted in section 3.3.1, the polymeric film of [Ru(2)<sub>2</sub>][PF<sub>6</sub>]<sub>2</sub> has an MLCT band at shorter wavelengths (500 nm) than the species in solution (506 nm), which is the opposite expected for extended length of the ligands. Reducing the films does red shift (511 nm) the polymeric films though. When the TiO<sub>2</sub> films with the polymeric films were immersed in the 3-MPN electrolyte with the I<sup>-</sup>/I<sub>3</sub><sup>-</sup> couple, the UV-vis spectrum changed with the suspected LMCT band disappearing and the MLCT being red shifted from 500 nm to 511 nm. It may be the electrolyte that is reducing the polymer film, which would reduce the Ru<sup>+3</sup> to Ru<sup>+2</sup>. An explanation for the red shift of the MLCT after immersion in the electrolyte was not found.

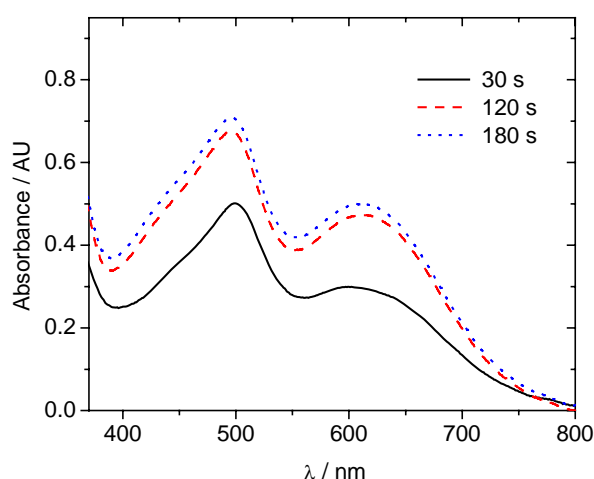


**Figure 3.92** UV-vis spectra of the TiO<sub>2</sub> films after potentiostatic deposition of [Ru(2)<sub>2</sub>][PF<sub>6</sub>]<sub>2</sub> in a 1 mM MeCN solution for different amounts of time (30, 120 and 180 seconds).

Dye sensitised solar cells were prepared with the normal procedures (see section 2.2) from the polymeric films. Possible advantages of this type of cell would be better control of the amount of dye to deposit, broader absorption and better stability of the dye on the TiO<sub>2</sub> (harder to desorb). Electrolyte *standard 2* was used. In figure 3.93 the resulting I-V curves are plotted. The two films with the higher absorbance (red and blue line) have ~25 % lower short circuit currents than the film that was deposited during 30 seconds. There appears to be a point where more deposition will decrease the cell efficiency.

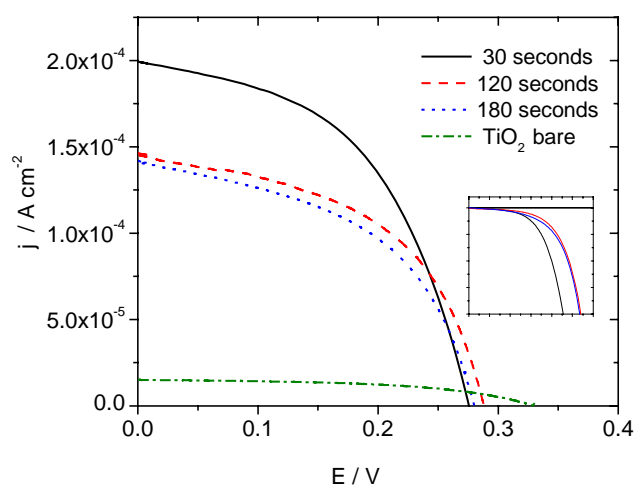


**Figure 3.93** I-V curves of the PV-cells with polymeric films of [Ru(2)<sub>2</sub>][PF<sub>6</sub>]<sub>2</sub> deposited for different times. The measurements were made in 100 mW/cm<sup>2</sup> light. DSSC measurement on bare TiO<sub>2</sub> is also added. The inset shows the dark-currents.

The photo-current can be compared to that of complex **7**<sup>2+</sup> that has the same structure as [Ru(2)<sub>2</sub>][PF<sub>6</sub>]<sub>2</sub> apart from having a carboxylic acid on one of the ligands. The photocurrent is 6 times lower for the polymer although the absorbance is 3 times lower as well. The lower V<sub>OC</sub> may be due to more recombination between the polymer “holes” and the electrons in the FTO and TiO<sub>2</sub>. The inset in figure 3.93 shows the dark currents for the three poly-[Ru(2)<sub>2</sub>] polymer films. The less covered film, the 30 seconds sample, has a dark current onset at lower potentials than the two films with higher coverage. This may be caused by more contact of the TiO<sub>2</sub> with the electrolyte, which is the main recombination pathway.<sup>[86]</sup>

### Dry DNSC with photoelectrochemically oxidised PEDOT

The dye sensitised TiO<sub>2</sub> films with photo-oxidised polymeric thiophene from section 3.3.2, were tested in PV-cells without liquid electrolyte. The four alternative methods for preparing the devices were described in chapter 2. All methods were tested but the only method that gave a measurable signal when the electrolyte had been removed was that of *method 2* in figure 2.5. The films from section 3.3.2 did not give reproducible results as solid-state solar cells. In *method 2* from figure 2.5, the electrodes were assembled and filled with an electrolyte composition of 5 M EDOT and 0.1 M LiClO<sub>4</sub> in 3-MPN. After illuminating (100 mWcm<sup>-2</sup>) the cell under short circuit conditions, for 1 hour, the electrolyte was pulled out by capillary forces with tissue paper and the remaining solvent was left to evaporate overnight. In figure 3.94 the open circuit photo-voltage of the cells before the photo-oxidation and after are shown for the cell with and without TiO<sub>2</sub> compact underlayer and for a control cell that was not illuminated. Dyes **10**<sup>2+</sup>, **2**<sup>2+</sup> and **3**<sup>2+</sup> were tested but it seemed that only **2**<sup>2+</sup> stayed attached during the process. The other dyes were not stable enough on the surface and desorbed during the process. For the cell with **2**<sup>2+</sup>, the open circuit voltage had decreased but the cells that had undergone photo-oxidation had higher photo-voltage (figure 3.94).

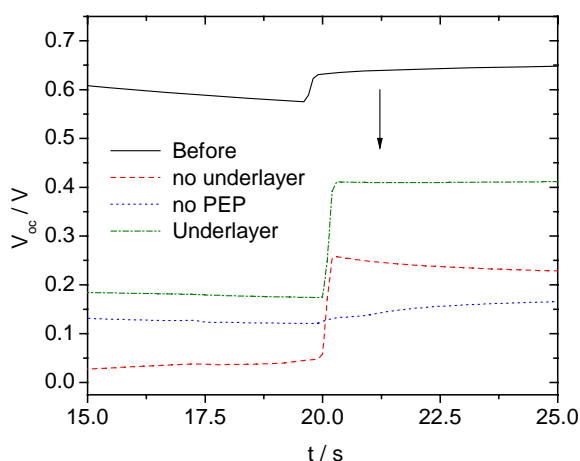


**Figure 3.94** Open circuit voltage ( $V_{OC}$ ) of a DNSC with 5 M EDOT before (solid line) PEP and after removal of electrolyte (dashed, dotted and dashed-dotted lines).

In figure 3.95 the I-V curves for the cells are plotted. It appears that the PEP treated cells indeed have a higher photocurrent than the non-treated cell. The cell with a

compact  $\text{TiO}_2$  under-layer had the highest photocurrent, which would be expected if it insulates the FTO glass from the polymer. The photocurrents are very poor and the FF values are also very low. The hole-conducting polymer must have good contact with the platinum counter electrode to conduct the holes and judging from the low amount of polymer material deposited, which was checked by opening the cell, there was too little contact for good charge transport. Due to the disorder of the polymer chains the diffusion length is very short so there will be large losses in current. The maximum thickness should be less than 100nm, which is around 500 times less than the  $50\mu\text{m}$  gap that is present in this cell design.<sup>[92, 93]</sup>

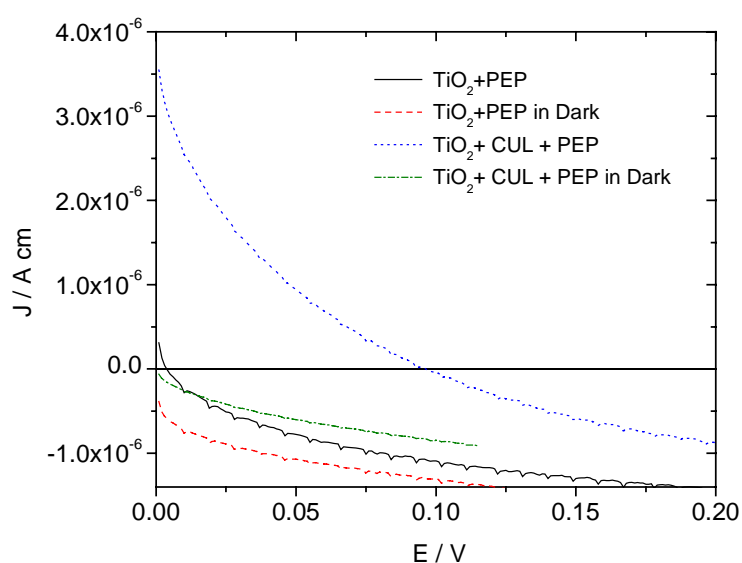


**Figure 3.95** I-V curves of the cells that were PEP treated with (blue line) and without (black line) a compact  $\text{TiO}_2$  underlayer (CUL). The untreated cell (no photoelectrochemical polymerisation) results in a photocurrent close to zero and much smaller than in figure 3.94.

### 3.6 Photoelectrochemistry of non-Metal Containing Dyes

Some alternative dyes to the ruthenium complexes were tried in collaboration with the group of Marcel Mayor. The alternative dyes were purely organic without any metals and synthesised by Alfred Blaszczyk from the group of Mayor. As was discussed in chapter 1, organic dyes applied in light harvesting devices could have several advantages such as high extinction coefficients and cheap starting materials compared to metal containing complexes.<sup>[94, 95]</sup> So far the main drawback with organic dyes has been the stability. One strategy is to first look for the most efficient structure and then to modify the dye to be more stable. Another way is to start with a stable and robust core and then make modifications to improve the conversion efficiency. One such type of molecule is perylene-diimide dyes that are related to the rylenes.<sup>[96, 97]</sup> They are robust, thermally stable and often used as commercial pigments and have been used in DNSCs.<sup>[98, 99]</sup> A similar structure is the naphthalene-diimide, which has optical properties that are tunable by core substituents.<sup>[100]</sup> Seven\* novel naphthalene diimine dyes were tested in dye-sensitised solar cells with  $I^-/I_3^-$  based redox-electrolyte. Figure 3.96 shows the core structure of the dyes. They had varying anchoring groups and electron donating groups to improve them for photovoltaic application. By measuring and comparing the energy levels relevant for the DNSC some conclusions could be made. Dye B7 has an anchoring group that allows more intimate contact with the  $TiO_2$  than the others. All the anchoring groups had catechol binding groups apart from B2 that had a carboxylic acid. The benzyl substituents with tertbutyl groups act to prevent stacking and provide some hydrophobicity. All the dyes were dissolved in DCM for the UV-vis spectroscopy, electrochemistry and dye sensitisation experiments.

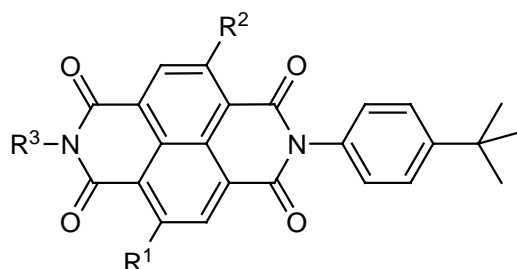


**Figure 3.96** Core structure of the naphthalene-bisimide dyes. Anchoring and modifying groups are positioned on  $R^1$  and  $R^2$ . \* Dye number 7 has the anchoring group on position  $R^3$ .

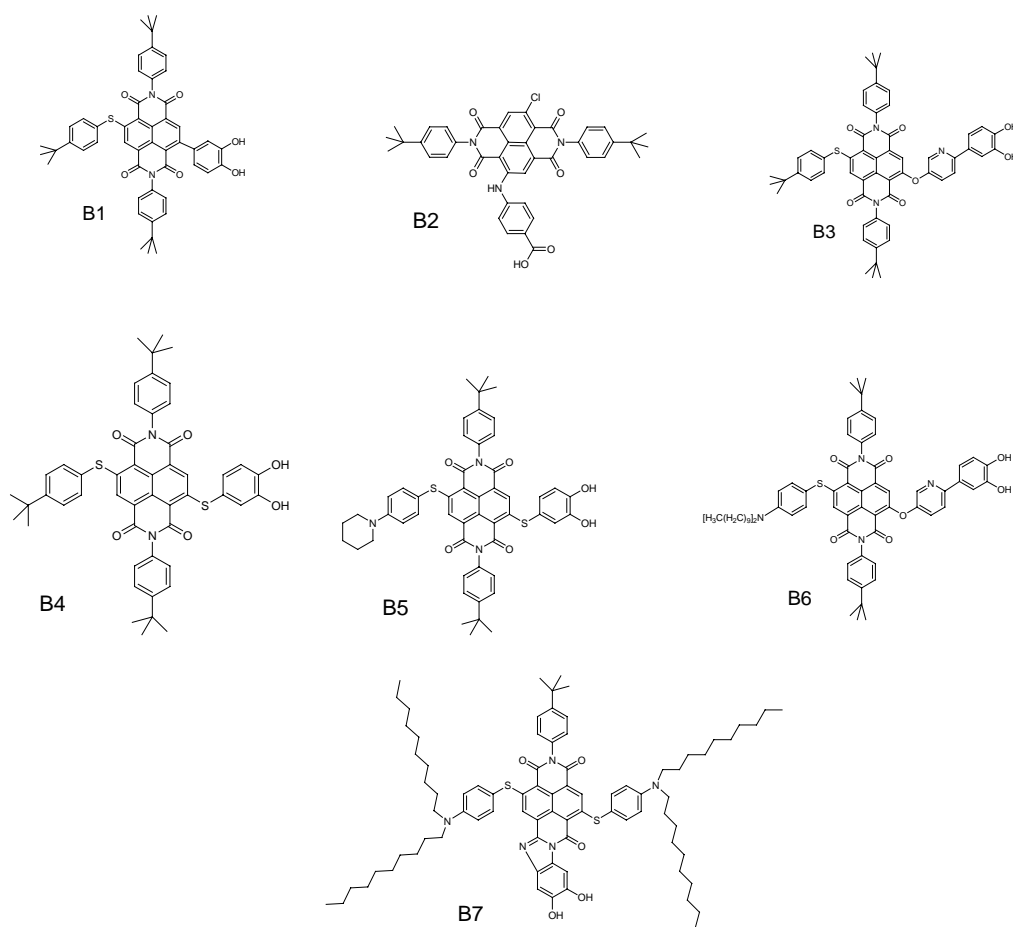


**Figure 3.97** The different dyes with number tags.

The different dyes with their abbreviations are shown in figure 3.97. The amine moieties in dyes **B5**, **B6** and **B7** are good  $\pi$ -donors and contribute to the highest occupied molecular orbital (HOMO), which decreases the voltammetrically measured oxidation potential. Dyes **B5**, **B6** and **B7** have oxidation potentials around + 0.5 V \* while the other dyes have values closer to 1.0 V \*. The chloride in dye **B2** has a weakly electron-withdrawing effect and increases the oxidation potential compared to the others. Importantly, all the dyes have oxidation potentials more positive than the redox couple  $I/I_3^-$  (roughly  $-0.1$  V vs. Ferrocene), thus providing enough driving energy for the regeneration of the dye. The oxidation potentials of the molecules are all irreversible within the time of the voltammetric experiments (100 mV/s – 30 V/s).

\* All potentials quoted versus ferrocene/ferrocinium redox couple.



In the photovoltaic device the regeneration of the oxidised dye by  $I^-$  is much faster ( $\sim 10^{-8}$  s) than the experimental time for the voltammetry so the molecule may be reversible when functioning as a dye in the DNSC.<sup>[101]</sup>

Dye B5 had two oxidation processes within the measured potential window instead of one as the others had. The first oxidation may be attributed to the pendant amino group.<sup>[98]</sup> The electrochemical data of B1-B7 is collected in table 3.27.

**Table 3.27** Electrochemical data for organic dyes in  $CH_2Cl_2$  (Fluka). Potentials quoted versus ferrocene/ferrocinium. Values obtained from cyclic voltammetry. The non-reversible oxidations had 0.02 V subtracted from the anodic peak. All reduction potentials were reversible.  $E_{0-0}$  was estimated from the absorption onset of the dye adsorbed on  $TiO_2$  at 10% of the full amplitude at the absorption maximum.<sup>[102]</sup>

Dye	$E_{1/2}^{Ox}$ (V)	$E_{1/2}^{Red}$ (V)	$E_{1/2}^{Red 2}$ (V)	$E_{0-0}$ (eV) (on $TiO_2$ )	$E_{1/2}^{Ox*}$ (V)
B1	+ 0.97	- 1.09	- 1.50	1.71	- 0.72
B2	+ 1.22	- 1.54		2.02	- 0.79
B3	+ 0.80	- 1.07	- 1.46	2.17	- 1.36
B4	+ 0.93	- 1.05	- 1.48	1.77	- 0.82
B5	+ 0.47, + 0.93	- 1.15	- 1.59	1.83	- 1.34
B6	+ 0.48	- 1.11	- 1.55	1.90	- 1.40
B7	+ 0.54	- 1.26	- 1.68	1.62	-1.06

All compounds had two reversible reduction processes. The excited state oxidation potentials were also estimated to complement the electrochemical data. The excited state oxidation potential and the 1<sup>st</sup> reduction potential give information regarding the potential of the LUMO. This is important for the energy matching of the excited electronic state with the  $TiO_2$  conduction band. The conduction band of  $TiO_2$  in 3-MPN was earlier (chapter 3.2) estimated to be around  $-1.0$  V (versus  $Fc/Fc^+$ ) so the values of  $E_{1/2}^{Red}$  and  $E_{1/2}^{Ox*}$  for the dyes are not perfect for good electron injection. It is probable that the energy levels of the HOMO and LUMO are perturbed by the adsorption of the dye to  $TiO_2$  and are different to the solution-measured potentials. The UV-vis absorbance data from table 3.28 with the peak shifts upon adsorption suggest this.

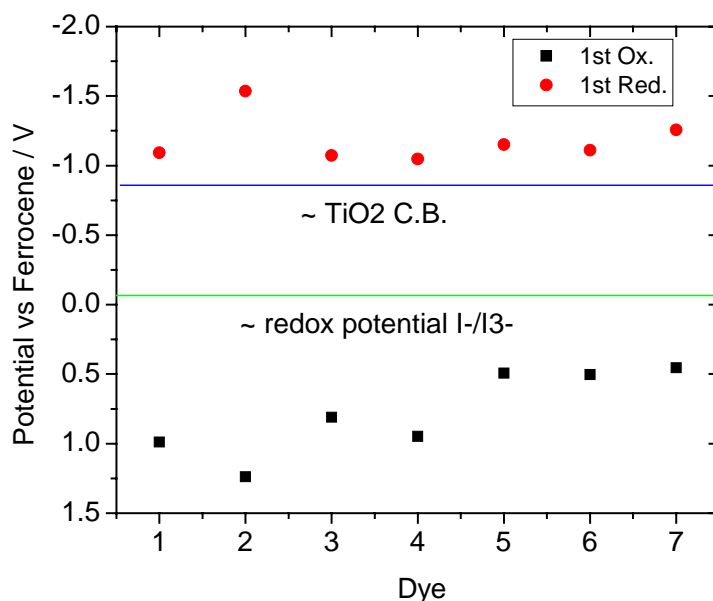


**Figure 3.98** First oxidation and reduction potentials from CVs plotted for every dye.

Figure 3.98 summarises the electrochemical data from solution measurements and relates them to  $\text{TiO}_2$  conduction band potential and the redox potential of  $\text{I}_3^-/\text{I}^-$ . Dye B2 has the most diverging values and it was also the dye that gave the poorest performance in a DNSC.

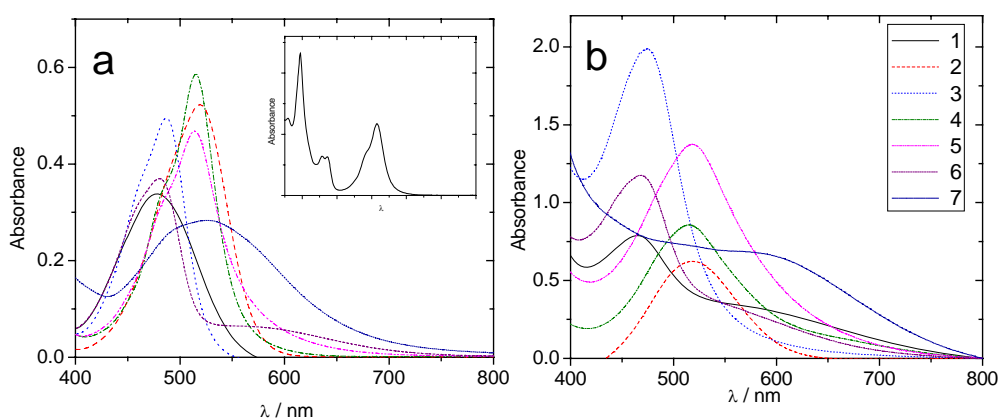


**Figure 3.99** UV-vis absorption spectra of dyes (a) in DCM solutions and (b) attached to transparent  $\text{TiO}_2$  films. The DCM solutions have concentrations between  $2 \times 10^{-4}$  and  $3 \times 10^{-4}$  M. The inset in a is the complete spectra of B4 and is typical for the compounds B1-B7.

In figure 3.99a the UV-vis absorbance spectra for the dyes in  $\text{CH}_2\text{Cl}_2$  solutions are plotted and in figure 3.99b the UV-vis spectra for the dyes adsorbed to  $\text{TiO}_2$ . All the

dyes, apart from **B2** and **B4**, show shifts in the absorbance maximum when attached to the TiO<sub>2</sub> surface. **B1**, **B3** and **B6** show blue shifts of the absorbance maximum that suggests that the conjugation is shortened upon adsorption.<sup>[102]</sup> **B5** and **B7** show red shifts when adsorbed and might be indications of an extended conjugation. **B7** has a different kind of anchoring group and has the broadest absorbance band in solution. Upon adsorption to TiO<sub>2</sub>, **B7** has the largest shift and the widest absorbance range, which suggests an intimate binding with the TiO<sub>2</sub>. Relating the quantity of absorbance at the absorbance maximum to the extinction coefficients gives an estimate of the projected surface coverage as was discussed in chapter 2. This assumes that the extinction coefficient is the same in solution as it is attached to a TiO<sub>2</sub> surface.

**Table 3.28** The absorbance maxima (>400 nm) of the organic dyes in solution (CH<sub>2</sub>Cl<sub>2</sub>) and on TiO<sub>2</sub> surface with extinction coefficients and projected surface coverage added.

	$\lambda$ max in sol. (nm)	$\lambda$ max on TiO (nm)	Abs. $\lambda_{\max}$ On TiO <sub>2</sub>	Ex.Coeff. $\lambda$ max	Cov. nmole/cm <sup>2</sup>
<b>B1</b>	479	465	0.79	11 100	71
<b>B2</b>	519	518	0.62	20 900	30
<b>B3</b>	487	474	1.99	15 900	125
<b>B4</b>	515	515	0.86	23 400	37
<b>B5</b>	514	518	1.37	16 800	81
<b>B6</b>	480	469	1.17	13 100	89
<b>B7</b>	526	580	0.68	14 900	46

### Photo-electrochemical measurements

Photo-electrochemical measurements of the dyes were done with the standard method described in chapter 2. The electrolyte used was *standard 2*. All the dyes showed similar open circuit voltage except **B2** that had less than half. The best performing dye, **B7**, had a  $V_{oc}$  of 0.36 V. Especially at low photocurrents the  $V_{oc}$  is closely linked to the photocurrent and the concentration of electrons in the conduction band of the TiO<sub>2</sub>.<sup>[103]</sup> The short circuit current followed the same trend as the open circuit voltage. Dye **B7** had the highest and dye **B2** the lowest. The photo-electrochemical measurements are collected in table 3.29.

**Comparison of dyes:**

**Anchoring groups:** Dyes B1, B3 and B4 have the same structures but different anchoring groups. Comparing the photocurrents, show B1 and B3 having very similar values but B4 having about 30 % lower. From the UV-vis absorbance it seems the adsorption is greatest for dye B3. It appears the anchoring group of dye B3 with a pyridine spacer gives the best performance.

**Counter groups:** Dyes B6 and B3 have the same anchoring ligands but different groups on the opposite side. The amino group of B6 gives it a slightly better performance. Dyes B5 and B4 can also be compared in this way. B5 has a better photocurrent than B4 and the higher conversion efficiency (0.019 to 0.006 %).

Dye B2 with its' electron withdrawing chloro-group is clearly not a good modification for the dye. Dye B7 is the best performer in the DNSC. It has an anchoring group that has more conjugation with the core than the others and there is no torsion between the anchoring group and the core. It also has two electron donating amino groups. Additionally it has hydrophobic alkyl chains to minimize water at the interface.

**Table 3.29** Photoelectric data in 1 sun illumination.

Dye	Voc (V)	Jsc (mA/cm <sup>2</sup> )	FF	η (%)
1	0.28	0.091	0.19	0.012
2	0.11	0.009	0.18	<0.001
3	0.30	0.112	0.58	0.020
4	0.20	0.068	0.44	0.006
5	0.33	0.100	0.56	0.019
6	0.33	0.134	0.61	0.027
7	0.36	0.143	0.60	0.031

**Conclusion on organic dyes**

The anchoring group is a very important part of a successful organic dye as has been reported from other groups. Measurements of dye B7 have shown slightly improved conversion efficiency with an anchoring group that should give the chromophoric core a better electric connection to the TiO<sub>2</sub>. The broadened UV-vis absorbance on TiO<sub>2</sub> compared to solution supports this conclusion. The amine groups improve the performance probably by directing the electron injection towards the TiO<sub>2</sub>.

## Reference list

- [1] P. G. Sammes, G. Yahioğlu, *Chem. Soc. Rev.* **1994**, *23*, 327.
- [2] M. Gerloch, E. C. Constable, *Transition Metal Chemistry*, VCH, **1994**.
- [3] E. C. Constable, *Chem. Soc. Rev.* **2007**, *36*, 246.
- [4] V. Balzani, G. Bergamini, S. Campagna, F. Puntoriero, in *Photochemistry and Photophysics of Coordination Compounds I, Vol. 280*, Springer-Verlag Berlin, Berlin, **2007**, pp. 1.
- [5] H. Hofmeier, U. S. Schubert, *Chem. Soc. Rev.* **2004**, *33*, 373.
- [6] E. C. Constable, A. M. W. Cargill-Thompson, D. A. Tocher, M. A. M. Daniels, *New J. Chem.* **1992**, *16*, 855.
- [7] E. C. Constable, A. J. Edwards, R. Martinez-Manez, P. R. Raithby, A. M. W. Cargill-Thompson, *J. Chem. Soc., Dalton Trans.* **1994**, 645.
- [8] E. C. Constable, A. J. Edwards, R. Martinez-manez, P. R. Raithby.
- [9] E. Figgemeier, V. Aranyos, E. C. Constable, R. W. Handel, C. E. Housecroft, C. Risinger, A. Hagfeldt, E. Mukhtar, *Inorg. Chem. Commun.* **2004**, *7*, 117.
- [10] E. C. Constable, J. Lewis, M. C. Liptrot, P. R. Raithby, *Inorg. Chim. Acta* **1990**, *178*, 47.
- [11] J. H. Wang, G. S. Hanan, *Synlett.* **2005**, 1251.
- [12] E. C. Constable, M. W. C. Thompson, *New J. Chem.* **1992**, *16*, 855.
- [13] J. Hjelm, R. W. Handel, A. Hagfeldt, E. C. Constable, C. E. Housecroft, R. J. Forster, *Inorg. Chem.* **2005**, *44*, 1073.
- [14] R. W. Handel, PhD thesis, University of Birmingham **2002**.
- [15] E. C. Constable, E. L. Dunphy, C. E. Housecroft, M. Neuburger, S. Schaffner, F. Schaper, S. R. Batten, *Dalton Trans.* **2007**, 4323.
- [16] E. C. Constable, C. E. Housecroft, E. A. Medlycott, M. Neuburger, F. Reinders, S. Reymann, S. Schaffner, *Inorg. Chem. Commun.* **2008**, *11*, 805.
- [17] R. O. Steen, L. J. Nurkkala, S. J. Angus-Dunne, C. X. Schmitt, E. C. Constable, M. J. Riley, P. V. Bernhardt, S. J. Dunne, *Eur. J. Inorg. Chem.* **2008**, 1784.
- [18] W. Goodall, K. Wild, K. J. Arm, J. A. G. Williams, *J. Chem. Soc., Perkin Trans. 2* **2002**, 1669.
- [19] T. Laue, A. Plagens, *Namen- und Schlagwort-Reaktionen der Organischen Chemie*, Teubner Studienbücher, **1998**.
- [20] T. Renouard, M. Gratzel, *Tetrahedron* **2001**, *57*, 8145.
- [21] A. J. Carpenter, D. J. Chadwick, *Tetrahedron* **1985**, *41*, 3803.
- [22] J. Kagan, S. K. Arora, *Heterocycles* **1983**, *20*, 1937.
- [23] S. Akoudad, J. Roncali, *Synth. Met.* **1998**, *93*, 111.
- [24] P. W. Atkins, *Physical Chemistry*, 6 ed., Oxford University Press, **1999**.
- [25] C. Y. Chen, S. J. Wu, C. G. Wu, J. G. Chen, K. C. Ho, *Angew. Chem., Int. Ed. Engl.* **2006**, *45*, 5822.
- [26] D. T. Sawyer, A. Sobkowiak, R. L. R., *Electrochemistry for chemists*, 2 ed., **1995**.
- [27] E. R. Schofield, PhD thesis, Universität Basel **1999**.
- [28] E. A. Medlycott, G. S. Hanan, *Chem. Soc. Rev.* **2005**, *34*, 133.
- [29] C. Janiak, *J. Chem. Soc., Dalton Trans.* **2000**, 3885.
- [30] B. P. Sullivan, J. M. Calvert, T. J. Meyer, *Inorg. Chem.* **1980**, *19*, 1404.
- [31] B. Brisig, E. C. Constable, C. E. Housecroft, *New J. Chem.* **2007**, *31*, 1437.
- [32] R. Hogg, R. G. Wilkins, *J. Chem. Soc.* **1962**, 341.

- [33] E. C. Constable, R. Handel, C. E. Housecroft, M. Neuburger, E. R. Schofield, M. Zehnder, *Polyhedron* **2004**, *23*, 135.
- [34] E. C. Constable, A. Thompson, D. A. Tocher, M. A. M. Daniels, *New Journal of Chemistry* **1992**, *16*, 855.
- [35] E. C. Constable, C. E. Housecroft, E. R. Schofield, S. Encinas, N. Armaroli, F. Barigelletti, L. Flamigni, E. Figgemeier, J. G. Vos, *Chem. Commun.* **1999**, 869.
- [36] M. K. Nazeeruddin, A. Kay, I. Rodicio, R. Humphrybaker, E. Muller, P. Liska, N. Vlachopoulos, M. Gratzel, *J. Am. Chem. Soc.* **1993**, *115*, 6382.
- [37] S. Anderson, E. C. Constable, M. P. Dareedwards, J. B. Goodenough, A. Hamnett, K. R. Seddon, R. D. Wright, *Nature* **1979**, *280*, 571.
- [38] A. B. P. Lever, *Inorganic Electronic Spectroscopy*, 2 ed., elsevier, **1984**.
- [39] S. Ferrere, *Inorg. Chim. Acta* **2002**, *329*, 79.
- [40] E. Figgemeier, E. C. Constable, C. E. Housecroft, Y. C. Zimmermann, *Langmuir* **2004**, *20*, 9242.
- [41] J. Hjelm, E. C. Constable, E. Figgemeier, A. Hagfeldt, R. Handel, C. E. Housecroft, E. Mukhtar, E. Schofield, *Chem. Commun.* **2002**, 284.
- [42] H. Rensmo, S. Lunell, H. Siegbahn, *J. Photochem. Photobiol., A* **1998**, *114*, 117.
- [43] M. Maestri, N. Armaroli, V. Balzani, E. C. Constable, A. Thompson, *Inorg. Chem.* **1995**, *34*, 2759.
- [44] A. A. Vlcek, E. S. Dodsworth, W. J. Pietro, A. B. P. Lever, *Inorg. Chem.* **1995**, *34*, 1906.
- [45] C. E. Housecroft, A. G. Sharpe, *Inorganic Chemistry*, 3 ed., Prentice Hall, **2007**.
- [46] A. J. Bard, F. L. R., *Electrochemical Methods, Fundamentals and Applications*, 2 ed., Wiley, **2001**.
- [47] E. C. Constable, C. E. Housecroft, E. Medlycott, M. Neuburger, F. Reinders, S. Reymann, S. Schaffner, *Inorg. Chem. Commun.* **2008**, *11*, 518.
- [48] V. Aranyos, J. Hjelm, A. Hagfeldt, H. Grennberg, *J. Chem. Soc., Dalton Trans.* **2001**, 1319.
- [49] Z. G. Xu, G. Horowitz, *J. Electroanal. Chem.* **1992**, *335*, 123.
- [50] H. Randriamahazaka, V. Noel, C. Chevrot, *J. Electroanal. Chem.* **1999**, *472*, 103.
- [51] L. Groenendaal, F. Jonas, D. Freitag, H. Pielartzik, J. R. Reynolds, *Adv. Mater.* **2000**, *12*, 481.
- [52] G. Zotti, G. Schiavon, *Synth. Met.* **1990**, *39*, 183.
- [53] C. Carlberg, X. W. Chen, O. Inganas, *Solid State Ionics* **1996**, *85*, 73.
- [54] D. D. Graf, K. R. Mann, *Inorg. Chem.* **1997**, *36*, 150.
- [55] P. G. Pickup, *J. Mater. Chem.* **1999**, *9*, 1641.
- [56] J. Hjelm, R. W. Handel, A. Hagfeldt, E. C. Constable, C. E. Housecroft, R. J. Forster, *J. Phys. Chem. B* **2003**, *107*, 10431.
- [57] P. S. Braterman, J. I. Song, R. D. Peacock, *Spectrochim. Acta, Part A* **1992**, *48*, 899.
- [58] J. Zhang, A. L. Barker, D. Mandler, P. R. Unwin, *J. Am. Chem. Soc.* **2003**, *125*, 9312.
- [59] S. Yanagida, G. K. R. Senadeera, T. Nakamura, T. Kitamura, Y. Wada, *J. Photochem. Photobiol., A* **2004**, *166*, 75.
- [60] B. Li, L. D. Wang, B. N. Kang, P. Wang, Y. Qiu, *Sol. Energy Mater. Sol. Cells* **2006**, *90*, 549.

- [61] Q. B. Pei, G. Zuccarello, M. Ahlskog, O. Inganäs, *Polymer* **1994**, *35*, 1347.
- [62] J. Roncali, F. Garnier, M. Lemaire, R. Garreau, *Synth. Met.* **1986**, *15*, 323.
- [63] G. Zotti, S. Zecchin, G. Schiavon, B. Vercelli, A. Berlin, *J. Electroanal. Chem.* **2005**, *575*, 169.
- [64] A. Pron, P. Rannou, *Prog. Polym. Science* **2002**, *27*, 135.
- [65] H. L. Wang, J. J. He, G. Boschloo, H. Lindstrom, A. Hagfeldt, S. E. Lindquist, *J. Phys. Chem. B* **2001**, *105*, 2529.
- [66] P. Bonhôte, E. Gogniat, S. Tingry, C. Barbe, N. Vlachopoulos, F. Lenzmann, P. Comte, M. Grätzel, *J. Phys. Chem. B* **1998**, *102*, 1498.
- [67] Q. Wang, S. M. Zakeeruddin, J. Cremer, P. Bauerle, R. Humphry-Baker, M. Grätzel, *J. Am. Chem. Soc.* **2005**, *127*, 5706.
- [68] N. Papageorgiou, M. Grätzel, O. Enger, D. Bonifazi, F. Diederich, *J. Phys. Chem. B* **2002**, *106*, 3813.
- [69] Q. Wang, S. M. Zakeeruddin, M. K. Nazeeruddin, R. Humphry-Baker, M. Grätzel, *J. Am. Chem. Soc.* **2006**, *128*, 4446.
- [70] G. Boschloo, D. Fitzmaurice, *J. Phys. Chem. B* **1999**, *103*, 3093.
- [71] V. Aranyos, H. Grennberg, S. Tingry, S. E. Lindquist, A. Hagfeldt, *Sol. Energy Mater. Sol. Cells* **2000**, *64*, 97.
- [72] T. A. Heimer, S. T. D'Arcangelis, F. Farzad, J. M. Stipkala, G. J. Meyer, *Inorg. Chem.* **1996**, *35*, 5319.
- [73] G. Boschloo, J. Lindstrom, E. Magnusson, A. Holmberg, A. Hagfeldt, *J. Photochem. Photobiol., A* **2002**, *148*, 11.
- [74] R. A. Marcus, *J. Phys. Chem.* **1990**, *94*, 1050.
- [75] C. Moorlag, B. Sarkar, N. Sanrame, P. Bauerle, W. Kaim, M. O. Wolf, *Inorg. Chem.* **2006**, *45*, 7044.
- [76] P. Bauerle, U. Segelbacher, A. Maier, M. Mehring, *J. Am. Chem. Soc.* **1993**, *115*, 10217.
- [77] E. C. Constable, R. W. Handel, C. E. Housecroft, A. F. Morales, B. Ventura, L. Flamigni, F. Barigelletti, *Chem. Eur. J.* **2005**, *11*, 4024.
- [78] T. W. G. Solomons, C. B. Fryhle, *Organic Chemistry*, 7 ed., Wiley, **2000**.
- [79] Y. Tachibana, J. E. Moser, M. Grätzel, D. R. Klug, J. R. Durrant, *J. Phys. Chem.* **1996**, *100*, 20056.
- [80] R. Katoh, A. Furube, K. Hara, S. Murata, H. Sugihara, H. Arakawa, M. Tachiya, *J. Phys. Chem. B* **2002**, *106*, 12957.
- [81] A. Juris, V. Balzani, F. Barigelletti, S. Campagna, P. Belser, A. Von Zelewsky, *Coord. Chem. Rev.* **1988**, *84*, 85.
- [82] K. Sayama, S. Tsukagoshi, T. Mori, K. Hara, Y. Ohga, A. Shinpou, Y. Abe, S. Suga, H. Arakawa, *Sol. Energy Mater. Sol. Cells* **2003**, *80*, 47.
- [83] A. Fillinger, B. A. Parkinson, *J. Electrochem. Soc.* **1999**, *146*, 4559.
- [84] M. Grätzel, *Inorg. Chem.* **2005**, *44*, 6841.
- [85] K. Schwanz, E. Mankel, R. Hunger, T. Mayer, W. Jaegermann, *Chimia* **2007**, *61*, 796.
- [86] B. A. Gregg, F. Pichot, S. Ferrere, C. L. Fields, *J. Phys. Chem. B* **2001**, *105*, 1422.
- [87] H. Tributsch, *Coord. Chem. Rev.* **2004**, *248*, 1511.
- [88] S. Södergren, A. Hagfeldt, J. Olsson, S. E. Lindquist, *J. Phys. Chem.* **1994**, *98*, 5552.
- [89] J. Bisquert, F. Fabregat-Santiago, I. Mora-Sero, G. Garcia-Belmonte, E. M. Barea, E. Palomares, *Inorg. Chim. Acta* **2008**, *361*, 684.



- [90] F. Nour-Mohammadi, H. T. Nguyen, G. Boschloo, T. Lund, *J. Photochem. Photobiol., A* **2007**, *187*, 348.
- [91] M. V. Mirkin, B. R. Horrocks, *Anal. Chim. Acta* **2000**, *406*, 119.
- [92] F. Monestier, J. J. Simon, P. Torchio, L. Escoubas, B. Ratier, W. Hojeij, B. Lucas, A. Moliton, M. Cathelinaud, C. Defranoux, F. Flory, *Appl. Opt.* **2008**, *47*, C251.
- [93] H. Benten, M. Ogawa, H. Ohkita, S. Ito, *Adv. Funct. Mater.* **2008**, *18*, 1563.
- [94] D. P. Hagberg, T. Edvinsson, T. Marinado, G. Boschloo, A. Hagfeldt, L. C. Sun, *Chem. Commun.* **2006**, 2245.
- [95] S. L. Li, K. J. Jiang, K. F. Shao, L. M. Yang, *Chem. Commun.* **2006**, 2792.
- [96] S. Erten, S. Alp, S. Icli, *J. Photochem. Photobiol., A* **2005**, *175*, 214.
- [97] Y. Shibano, T. Umeyama, Y. Matano, H. Imahori, *Org. Lett.* **2007**, *9*, 1971.
- [98] S. Ferrere, B. A. Gregg, *New J. Chem.* **2002**, *26*, 1155.
- [99] Y. Avlasevich, K. Mullen, *Chem. Commun.* **2006**, 4440.
- [100] A. Blaszczyk, M. Fischer, C. von Hanisch, M. Mayor, *Helv. Chim. Acta* **2006**, *89*, 1986.
- [101] I. Montanari, J. Nelson, J. R. Durrant, *J. Phys. Chem. B* **2002**, *106*, 12203.
- [102] T. Edvinsson, C. Li, N. Pschirer, J. Schoneboom, F. Eickemeyer, R. Sens, G. Boschloo, A. Herrmann, K. Mullen, A. Hagfeldt, *J. Phys. Chem. C* **2007**, *111*, 15137.
- [103] K. Fredin, J. Nissfolk, G. Boschloo, A. Hagfeldt, *J. Electroanal. Chem.* **2007**, *609*, 55.

## 4 Summary

Photoelectric measurements on a series of ruthenium complexes with 9 different 2,2',6',2''-terpyridine ligands modified by different thienyl substitutions on the 4'-position were performed. Three of the ligands were novel. Their performances in dye sensitised nanostructured solar cells (DNSC) were compared to their electrochemical and photophysical properties. Adding thienyl substitutes amplified the extinction coefficient and red-shifted the maximum of the  $^1\text{MLCT}$ . The anchoring ligands were found to influence the injection efficiency of the complexes. A less negative reduction potential of the anchoring ligand corresponded to a lower LUMO, which directs the ligand centred excited state electron towards the  $\text{TiO}_2$ . The counter ligand affects the injection efficiency in an opposing way with ligands that have a lower LUMO directing the excited state electrons away from the  $\text{TiO}_2$  surface.

As has been previously reported, it is observed from electrochemical measurements that the HOMO of the complexes with thienyl substituted terpyridines have both ruthenium and ligand contributions. Electrochemical oxidation of homoleptic complexes resulted in electrodeposition and probable polymerisation of metallorganic polymers. The polymers showed modified optical and electrochemical values compared to their monomers. Polymers with iron ions exhibited lower charge transport capabilities than the ruthenium equivalents.

A  $\text{TiO}_2$  surface sensitised with the different dyes were able to photo-electrochemically oxidise and polymerise oligothiophene monomers in solution upon illumination. The process was monitored by chronocoulometry and UV-Vis spectroscopy. The efficiency of polymerisation did not appear to be affected by the substitute on the counter ligand, although saturation occurred at different times. A ferrocene on the counter ligand quenched the polymerisation despite electron injection. This was due to the ferrocene reducing the oxidised ruthenium center before oxidation of monomer could take place.

A technique for analysing a dye sensitised  $\text{TiO}_2$  surfaces was developed using the scanning electrochemical microscope (SECM). By measuring the current voltage characteristics of a  $\text{TiO}_2$  substrate and ultra microelectrode (UME) tip simultaneously upon illumination it was possible to compare dyes, their photocurrents and estimate the open circuit potentials. This could be done on very small areas of  $\text{TiO}_2$ . By

scanning a substrate with an array of dye sensitised TiO<sub>2</sub> spots it may be possible to obtain data on many potential dyes in one scan, which would cut down time requirements for evaluating dyes for DNSC purpose. The technique was given the name photo-electro-chemical microscopy (PECM).

A series of seven organic dyes (synthesised by the group of Marcel Mayor) were tested. The dyes belonged to the naphthalene-diimide family, which are rather robust and stable. Results showed UV-vis and electrochemical characteristics that may give good photoelectric performance. The efficiencies varied with different modifications and on the anchoring group. The dyes that included the donor amine groups into the structure seemed to improve efficiency. Positioning the anchoring group close to the molecular core also increased the efficiency of photovoltaic conversion.



## Appendix A

[Fe(2) <sub>2</sub> ][PF <sub>6</sub> ] <sub>2</sub>	
Model Formula	C <sub>42</sub> H <sub>30</sub> FeN <sub>6</sub> O <sub>4</sub> S <sub>2</sub> ·C <sub>3</sub> H <sub>6</sub> O·0.4(CH <sub>2</sub> Cl <sub>2</sub> )·0.6(H <sub>2</sub> O)·2(PF <sub>6</sub> )
Model Molecular Weight	1194.29
Crystal System	Monoclinic
Space group	C2/c
A	22.6741 (3) Å
B	20.3648 (3) Å
C	14.24870 (10) Å
α	90°
β	115.9673 (6)°
γ	90°
V	5915.16 (13) Å <sup>3</sup>
Z	4
μ(MoK α)	0.50 mm <sup>-1</sup>
T <sub>min/max</sub>	0.92, 0.95
N	51053
N <sub>ind</sub>	7078(R <sub>int</sub> 0.030)
N <sub>obs</sub>	5040(F <sup>2</sup> > 2σ(F <sup>2</sup> ))
Residual R1	0.044
Δρ <sub>max</sub>	0.73 e Å <sup>-3</sup>
F(000)	2422.400
Goodness of fit F <sup>2</sup>	0.9607
R1 all	0.0581
WR2 all	0.0578
R1 ref	0.0440
WR2 ref	0.0500

<b>8</b>	
Model Formula	C <sub>29</sub> H <sub>19</sub> N <sub>3</sub> S <sub>2</sub>
Model Molecular Weight	473.62
Crystal System	Orthorhombic
Space group	<i>Pbca</i>
A	7.8131(3) Å
B	20.4207(6) Å
C	27.9314(9) Å
α	90°
β	90°
γ	90°
V	4456.4(3) Å <sup>3</sup>
Z	8
μ(MoK α)	0.264 mm <sup>-1</sup>
T <sub>min/max</sub>	0.96/0.99
N	96700
N <sub>ind</sub>	6698 (R <sub>int</sub> 0.053)
N <sub>obs</sub>	3076 (I>2.0σ(I))
Residual R1	0.0305
Δρ <sub>max</sub>	-0.24/0.27e Å <sup>-3</sup>
F(000)	1968
Goodness of fit F <sup>2</sup>	1.1155
R1 all	0.0687
WR2 all	0.0573
R1 ref	0.0344
WR2 ref	0.0374

## *Curriculum vitae*

---

William Henrik Kylberg

Frobenstrasse 56a

CH-4056 Basel

061-321 9587

076-583 6374

E-mail: williamkylberg@hotmail.com

Marital status: Single

Nationality: Swedish

Date of birth: 9 April 1977

---



### **Profile**

PhD educated Chemist (Physical and Inorganic chemistry primarily).

### **Experience**

- **Electrochemistry**: Potentiostat for three and four electrode measurements, Scanning Electro-Chemical Microscope (SECM) and electrochemical impedance spectroscopy.
- **Analytical**:  $^1\text{H}/^{13}\text{C}$ -NMR, ES-MS, IR, UV-Vis spectroscopy and Fluorescence spectroscopy.
- **Photo-electrochemistry**: Assembling of dye-sensitised solar cell. Analysis and measurement of photovoltaic performance.
- **Synthetic**: Polypyridines, thiophenes, metal complexes and  $\text{TiO}_2$  nanoparticle-colloids.

### **Employment**

**2003-2004**

Laboratory engineer at the Department of Physical Chemistry at Uppsala University (Sweden) in the group of Prof. Anders Hagfeldt.

## Education

### **2004-2008**

PhD studies in Basel University Chemistry Department. Title of thesis:  
“Photoelectrochemical surface modification and analysis in dye sensitised solar cells” Supervisors: E. Figgemeier and E. C. Constable.

### **1998-2003**

Undergraduate studies at Uppsala University with M.Sc. degree in Chemistry.  
Diploma work in department of Physical chemistry. Title of diploma work:  
“Effects of Aluminium Oxide Layers on Dye Sensitised Nanostructured Solar Cells”  
Supervisor: A. Hagfeldt.

### **1993-1996**

Gångsätra Gymnasium (Stockholm) with Natural sciences.

### **1984-1993**

Högsätra (Stockholm) elementary school.

## Language skills

Languages: English (mother tongue), Swedish (mother tongue), German (good) and French (good).

## Military Service

**1997** 10 months in the Swedish military service as part of the signal troops.

## Publications involved in to date

- [1] E. C. Constable, E. L. Dunphy, C. E. Housecroft, W. Kylberg, M. Neuburger, S. Schaffner, E. R. Schofield, C. B. Smith, *Chemistry-a European Journal* **2006**, 12, 4600.  
*Structural development of free or coordinated 4'-(4-pyridyl)-2,2':6',2''-terpyridine ligands through N-alkylation: New strategies for metallamacrocyclic formation*
- [2] E. Figgemeier, W. Kylberg, E. Constable, M. Scarisoreanu, R. Alexandrescu, I. Morjan, I. Soare, R. Birjega, E. Popovici, C. Fleaca, L. Gavrilă-Florescu, G. Prodan, *Applied Surface Science* **2007**, 254, 1037.  
*Titanium dioxide nanoparticles prepared by laser pyrolysis: Synthesis and photocatalytic properties*
- [3] Figgemeier Egbert ; Kylberg William H. ; Bozic Biljana  
Proceedings of SPIE, the International Society for Optical Engineering  
ISSN 0277-786X, **2006**



*Scanning photoelectrochemical microscopy as versatile tool to investigate dye-sensitized nano-crystalline surfaces for solar cells*

- [4] T. Bessho, E. C. Constable, M. Graetzel, A. Hernandez-Redondo, C. E. Housecroft, W. Kylberg, M. K. Nazeeruddin, M. Neuburger, S. Schaffner, *Chem. Commun.* **2008**, 3717.  
*An element of surprise - efficient copper-functionalised dye-sensitised solar cells*

### Conferences

The following conferences were attended with poster presentations:

- *Grandest 2005 in Mulhouse* (French Chemical Society).
- Spring meeting 2005 of the Swiss Chemical Society.
- IPS-16 in Uppsala, Sweden (16<sup>th</sup> international conference on Photochemical Conversion and Storage of Solar Energy), 2005.
- IPS-17 in Dublin, Ireland (17<sup>th</sup> International Symposium of the Photophysics and Photochemistry of Coordination Compounds), 2007.
- Fall meeting 2006 of the Swiss Chemical Society.
- Fall meeting 2007 of the Swiss Chemical Society.

### Oral presentations

- 5 minute talk at IPS-17 in Dublin, Ireland (17<sup>th</sup> International Symposium of the Photophysics and Photochemistry of Coordination Compounds), 2007.
- 30 minute talk at the 5<sup>th</sup> Swiss Snow Symposium 2007, Swiss Young Chemists Association (JFC).